Combined Spectral and Temporal Analysis

of a

Her X-1 Turn-On

vorgelegt von

Markus Kuster

aus Ebingen
2004

Zusammenfassung

Markus Kuster
Kombinierte Spektrale und Zeitliche Analyse eines Her X-1 Turn-On

Der 35 Tage Zyklus im akkretierenden Röntgenpulsar Her X-1 ist einer der deutlichsten Beobachtungs-Hinweise für eine geneigte, verbogene und präzedierende Akkretionsscheibe in einem Doppelsternsystem. Im September 1997 wurde die Quelle mit dem Röntgensatelliten *RXTE* mit hoher zeitlicher und spektraler Auflösung im Spektralbereich von 2–200 keV beobachtet. Die Beobachtung mit einer Gesamtlänge von 3 Tagen umfasst einen Turn-On des 35^{d} Präzessions-Zyklus der Akkretionsscheibe. Dies entspricht dem Zeitraum, zu dem der äußere Rand der Akkretionsscheibe die Sicht auf den Neutronenstern frei gibt. Diese Arbeit stellt die Ergebnisse einer zeitlichen und spektralen Analyse der Daten vor.

Das phasengemittelte Kontinuum von Her X-1 während des Turn-On wird gut durch ein Partial Covering Modell beschrieben. Dieses Modell setzt sich zusammen aus einer stark absorbierten Power-Law-Komponente ($\alpha \approx 1.0$) mit einem exponentiellen Abfall ($E_{\mathrm{cut}} \approx 21$ keV) und einer zusätzlichen spektralen Komponente mit gleichem Verlauf die nicht absorbiert ist. Das Spektrum weisst eine Eisenfloureszenzlinie bei ≈ 6.4 keV auf und zeigt eine schwache Zyklotronresonanzlinie bei 39.9 keV. Die Energieauflösung des *PCA* von *RXTE* ist zu niedrig, um eine systematische Variation der Eisenlinie mit der Zeit zu untersuchen. Aus der Linienlage der Zyklotronlinie lässt sich direkt eine Magnetfeldstärke von 4.1×10^{12} Gauss ableiten.

Die Rotationsperiode des Neutronensterns wurde aus den Daten bestimmt und ist in guter Übereinstimmung mit den Ergebnissen aus anderen Beobachtungen. Dies bestätigt die lang anhaltende Spin-Up Phase von Her X-1, die sich erst vor kurzer Zeit zu einem Spin-Down geändert hat. Eine Zerlegung des Pulsprofils in die Beiträge der beiden Neutronensternpole liefert ähnliche Ergebnisse für den Turn-On, wie die für das Pulsprofil im Main-On. Das beobachtete Pulsprofil wird bei hohen Energien von einem *Pencil Beam* Anteil dominiert, aber beinhaltet auch Anteile eines *Fan Beams*. Die Änderungen des Pulsprofils und des Anteils an gepulstem Fluss zu Beginn des Turn-On sind konsistent mit der Form eines Main-On Pulsprofils, das durch photoelektrische Absorption und Thomson-Streuung beeinflusst ist.

Die Entwicklung der Wasserstoffsäulendichte N_{H} und der Covering Fraction während des Turn-Ons kann durch ein einfaches geometrisches Modell erklärt werden, das eine Akkretionsscheibenkorona und den äusseren Rand der Akkretionsscheibe mit einbezieht. Das Modell kann auch die beobachtete Entwicklung des Pulsprofils in den unterschiedlichen Energiebereichen erklären. Zusätzlich wurden die zeitliche Signatur einer streuenden heissen Korona auf gepulste und gerichtete Emission untersucht und die Ergebnisse dargestellt. Ein Vergleich der Ergebnisse der Simulation mit den beobachteten Pulsprofilen unterstützt das geometrische Modell des Turn-Ons.

Abstract

Markus Kuster
Combined Spectral and Temporal Analysis of a Her X-1 Turn-On

The $35^{\rm d}$ cycle of the accreting X-ray pulsar Her X-1 provides one of the best evidences for an inclined, warped, and precessing accretion disk in a binary system. In 1997 September the source was observed with the X-ray satellite *RXTE* with high temporal and spectral resolution in the energy band of 2–200 keV. The 3 days long observation covers a full turn-on of the $35^{\rm d}$ precession cycle of the accretion disk, which is the time when the outer edge of the disk frees the line of sight to the neutron star. In this thesis I present results of the temporal and spectral analysis of the data.

The phase averaged continuum spectrum of Her X-1 during the turn-on is well described by a partial covering model, which combines a heavily absorbed power-law spectral component ($\alpha \approx 1.0$) with an exponential cut-off ($E_{\rm cut} \approx 21$ keV) and a similar spectral component which is not affected by absorption. The spectrum shows a strong signature of iron flourescent emission at ≈ 6.4 keV and a weak Cyclotron resonant scattering feature at 39.9 keV. The energy resolution of the *PCA* on-board of *RXTE* is too low for a systematic study of a variation of the iron line with time. The energy of the CRSF indicates a magnetic field strength of 4.1×10^{12} Gauss which confirms recent findings.

The spin period of the neutron star was determined from the data and is in agreement with other observations. This confirms the long spin-up period of Her X-1 which only recently changed to a spin-down. A decomposition of the pulse profile into the contribution of the two neutron star poles gives similar results for the turn-on as for the main-on pulse profile. The observed pulse profile is dominated by a *pencil beam* component at high energies, but shows a signature of a *fan beam* component as well. The changes in shape of the pulse profile and the pulsed flux ratio towards the beginning of the turn-on are consistent with the shape of a main-on pulse profile which is modified by photoelectric absorption and Thomson scattering.

The evolution of the absorbing column $N_{\rm H}$ and the covering fraction during the turn-on can be explained by a simple geometric model which includes an accretion disk corona and the influence of the outer accretion disk rim. This model can also explain the observed pulse evolution in different energy bands. In addition the temporal signature of a partially ionized corona on beamed and pulsed emission is simulated and the results presented. These results in turn are used to simulate the influence of a scattering hot corona on pulsed emission. Comparing the results of the simulations with the observed pulse profiles supports the presented geometric model of the turn-on.

Contents

Chapter 1

Introduction

The history of X-ray astronomy began in the early 1960's when the first galactic X-ray source, was discovered on 1962 June 18. Before then, the only X-ray source known in the sky was the sun. During a rocket flight dedicated to measure X-rays from the moon, a team led by Riccardo Giacconi discovered the very bright galactic X-ray source Sco X-1 (Giacconi et al., 1962). It took more than four additional years to accurately determine the location of Sco X-1 and to reveal the unusual nature of this source. By the time the physical processes which could explain the observed X-ray flux were unknown. After the identification of the optical counterpart of Sco X-1 by Sandage et al. (1966), mass transfer in a close binary system was discussed as a possible mechanism. In addition, X-ray emission of "exotic" objects like neutron stars, was taken into account (e.g., Morton, 1964).

Since then, X-ray astronomy has evolved with an amazing speed into a new and powerful field of science. This progress has gone in parallel and with the advance in space and detector technology. Since the Earth's atmosphere is optically thick for X-rays, rocket or balloon flights, or satellites are indispensable to carry the X-ray detectors to high altitude ($\gtrsim 35 - 50$ km) for observation. The first astronomy satellite mission was launched eight years after the discovery of Sco X-1 in 1970, it was called *UHURU* (Swahili translation for "freedom"). One of the main purposes of *UHURU* was a uniform scan of the whole sky, the first all-sky survey in the energy range of 2–20 keV. With *UHURU* the number of known X-ray sources could be extended to more than 400, among those were the X-ray pulsars Cen X-3 (Giacconi et al., 1971) and Her X-1 (Tananbaum et al., 1972).

Unlike with balloon or rocket flights, satellite based instruments have major advantages since they are able to measure the full energy range of the X-ray spectrum without the influence of atmospheric absorption and long term observations on time scales of months and years are feasible. Soon, other missions such as *ARIEL-5*, *HEAO-1*, and Einstein followed, providing better energy resolution, larger effective collecting area, and imaging capability. After the German *ROSAT* mission in 1999 the number of known X-ray sources in the sky has grown to more than 125000 individual objects. The instrumentation of "modern" X-ray observatories of the twenty-first century like NASA's *RXTE* and *Chandra*, or ESA's *XMM-Newton* can provide spatial resolution comparable with the resolution of Earth bound optical telescopes (0.5 arcsec) in the X-ray band. At the same time spectroscopy with a spectral resolving power of $E/dE \approx 30$–2000 (e.g., *Chandra*'s Low Energy Transmission Grating) is possible, in combination with high time resolution of the order of $dP/P \approx 10^{-9}$ (*RXTE, XMM-Newton*).

In the first decade of X-ray astronomy research, observations were focused on the brightest galactic X-ray sources, which were classified as binary systems (Gursky et al., 1966; Sandage et al., 1966). It was soon recognized that mass accretion in a gravitational field is an important energy source, a theory originally proposed by Salpeter (1964) for quasi-stellar radio sources (Quasars).

This idea was adopted 4 years later by Shklovsky (1967) to explain the energy release of the X-ray binary Sco X-1. Since then the theory of accretion has advanced considerably, as well as the theory of accretion disks. Prendergast & Burbidge (1968) pointed out that even the inner parts of an viscous heated accretion disk can be the source of X-rays in binary systems. The progenitor of the so called "standard model" of X-ray binaries was first published by Zel'dovich & Guseynov (1966) followed by the so called α-disk model of Shakura & Sunyaev (1973). With increasing sensitivity of the detectors the "zoo" of X-ray sources could be extended to fainter objects, such as normal stars, pulsars, active galactic nuclei (AGN), clusters of galaxies, super nova remnants (SNR) to mention some of the classes of galactic and extra galactic X-ray sources known today.

The main topic of this thesis is the accreting X-ray pulsar Her X-1. Her X-1 is one of the best studied X-ray binaries and can be called a kind of "prototype" of an accreting X-ray pulsar, since many of the basic assumptions of the standard model of accreting X-ray pulsars outlined in chapter 2 are based on or verified by observations of Her X-1. Chapter 3 summarizes radiation processes in X-ray pulsars which are of importance to understand the observed spectra discussed in chapter 7. An introduction to the underlying data analysis methods used during this work is given in chapter 4. Chapter 5 introduces the detectors of the X-ray satellite *RXTE* which provided the data for this work.

One of the most intriguing feature of the accreting X-ray pulsar Her X-1 is the variability of its X-ray intensity and spectral shape on several timescales: the neutron star's spin period $P_{\rm spin}$, the orbital period of the binary system $P_{\rm orb}$, quasi-periodic oscillations in the mHz regime, and the 35 d intensity modulation ($P_{\rm disk}$). The 35 d modulation generally is attributed to a warped, precessing, and inclined accretion disk periodically covering the central X-ray source, the neutron star. These and other properties of the binary system Hercules X-1/HZ Her are presented in chapter 6. The observation underlying this thesis covers a period of 4 d at the beginning of the disk precessing cycle, called "turn-on". This observation in 1997 was the first time that such a turn-on could be observed with high spectral and temporal resolution. The results of the spectral and temporal analysis of this data are outlined in chapter 7. In the final part of this thesis, in chapter 8, I try to combine the spectral analysis with an analysis of the pulse profile. A conclusion and discussion of the results is presented in chapter 9.

Chapter 2

Accreting X-Ray Pulsars – The Standard Model

The discovery of Sco X-1 gave rise to discussions among theorists on the origin of the enormous energy release observed and the underlying physical mechanisms. Up to now about 280 X-ray binary systems (150 low-mass X-ray binaries and 130 high-mass X-ray binaries) are known from individual observations and/or systematic surveys (Liu et al., 2000, 2001). In general, X-ray binaries are interacting detached or semi-detached double star systems, consisting of a compact object and a "normal" mass donating companion star orbiting around their common center of mass. The compact object either can be a white dwarf (cataclysmic variable – CV), a neutron star, or a black hole. In the latter case, the binary system is called black hole candidate (BHC), because a direct observational evidence for a black hole such as the presence of the event horizon is still missing.

The type of the compact object, its magnetic field strength, and the accretion mechanism determine the observable spectra, the luminosity, and the temporal behavior of an X-ray binary. A review of X-ray binaries in general and of some individual sources can be found in Lewin et al. (1995). In this work I will concentrate on a subclass of X-ray binaries, the accreting X-ray pulsars (XRP). XRPs are X-ray binaries accreting matter on a strongly magnetized neutron star and the observed X-ray luminosity shows a regular periodical modulation. The first theoretical models of XRPs go back on the work of Pringle & Rees (1972) and Davidson & Ostriker (1973). The central "engine" of such an XRP is a neutron star with a strong dipole like magnetic field. Close to the neutron star, under the increasing influence of the strong magnetic field, the accreted plasma follows the magnetic field lines (section 2.3.4) and is channeled towards the neutron star's magnetic poles (section 2.3.6). At the magnetic poles the plasma interacts with the surface of the neutron star and gives rise for X-ray emission. These processes are still not very well understood in detail, since the physical conditions close to the neutron star are extreme, needing full relativistic and quantum electrodynamic treatment. The emerging emission region is rather small ($A \lesssim 1\,\mathrm{km}^2$), and in case the rotational axis of the neutron star and its magnetic field axis are not aligned, the observed X-ray intensity is modulated with the rotational period of the neutron star. Some accreting X-ray pulsars accrete matter from an accretion disk, which is the accretion scenario observed in the accreting X-ray pulsar Her X-1/HZ Her, on which this thesis focuses on. An introduction to other possible accretion mechanisms, such as accretion from a strong stellar wind, can be found in the literature, e.g., Davidson & Ostriker (1973), or in Kretschmar (1996) and Kreykenbohm (1997), who deal with individual sources such as the X-ray binary system Vela X-1.

During the last decade, the theory of mass accretion and the understanding of accreting X-ray binaries and X-ray pulsars have made rapid progress. Some of these results are presented in this

chapter as far as they are related to the main topic of this thesis. More general considerations like the structure of the gravitational potential in a binary system are given at the beginning in section 2.2, followed by an introduction to accretion by Roche Lobe overflow and the structure of the resulting accretion disk. To understand the large energy release and the long term behavior of neutron star spin periods in XRPs, it is essential to know how angular momentum is transfered to the neutron star and within the accretion disk (section 2.3.2 and section 2.3.5).

2.1   Mass Accretion in X-ray Binaries

The two components of an X-ray binary system can interact by mass transfer from the "normal" star to the compact object. This process is called accretion. The way matter is accreted mainly depends on the spectral type, the mass of the companion star, and the orbital separation of the binary system. From the theoretical understanding, different accretion scenarios are possible. Matter can either be accreted by mass transfer via Roche Lobe overflow, from a strong stellar wind, or through an equatorial mass flow. As an example, a simple estimate for a $1\,M_\odot$ neutron star, assuming that the total gravitational energy of the accreted plasma is converted during accretion, yields an energy release of $\approx 10^{20}\,\mathrm{erg\,g^{-1}}$. This value is one order of magnitude higher compared to the energy gain from nuclear reactions, as e.g. during hydrogen burning (Frank et al., 1995). Therefore mass accretion is a very powerful energy source, which easily can explain the large luminosities and energy release observed in X-ray binaries or XRPs.

On the other hand the accretion rate cannot increase indefinitely since the accreted plasma generates X-ray photons which interact with the electrons of the infalling plasma by scattering. The electrons in turn interact with protons of the plasma by Coulomb scattering. For an idealized accretion model which describes steady and spherical symmetric accretion (see Frank et al., 1995) an upper limit for the accretion rate and the observable luminosity can be calculated. If the accreted material is assumed to be fully ionized hydrogen and radiation pressure due to Thomson scattering off electrons is the force that equals the gas pressure of the infalling material caused by gravitational force, then the upper limit for the observable luminosity is given by the Eddington luminosity:

$$L_{\mathrm{Edd}} = \frac{4\pi\,G M_{\mathrm{x}} m_{\mathrm{p}} c}{\sigma_{\mathrm{T}}} = 1.3 \times 10^{38} \frac{M_{\mathrm{x}}}{M_\odot}\,\mathrm{erg\,s^{-1}} \qquad (2.1)$$

where σ_{T} is the Thomson cross section, M_{x} the mass of the compact object, and m_{p} the proton mass. For a higher luminosity than L_{Edd} the radiation pressure would overcome the gravitational force and make further accretion impossible. For the case that all the gravitational energy is converted to luminosity, the maximum possible accretion rate is:

$$\dot{M}_{\mathrm{Edd}} \approx 1.5 \times 10^{-8} \frac{R}{10\,\mathrm{km}} \frac{M_\odot}{\mathrm{year}} \qquad (2.2)$$

Generally, the observed X-ray luminosity of X-ray binaries is lower than the Eddington limit, there are, however, sources whose luminosity is higher than Eddington limit. This is not in contradiction to the theory, since the Eddington luminosity given in Eq. (2.1) is only valid for the case of spherical symmetric accretion, neglecting e.g. the influence of the magnetic field of the compact object. In binary systems like XRPs the magnetic field plays a dominant role and accretion is concentrated to an a column like geometry (see section 2.3.6).
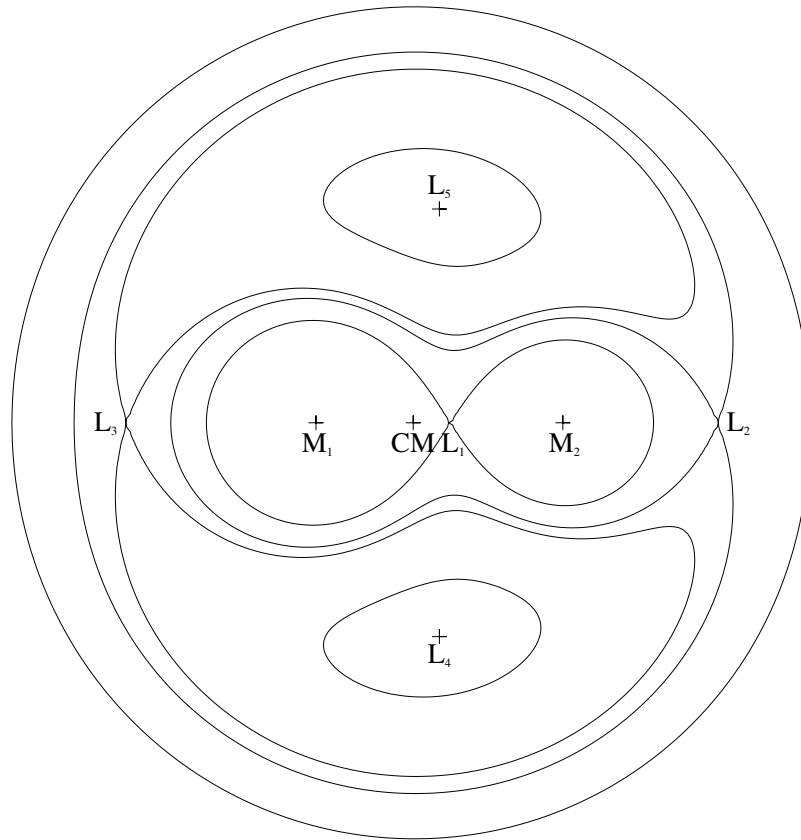
Figure 2.1: Roche equipotential surfaces in the orbital plane of a binary system with a mass ratio $q = \frac{M_2}{M_1} = 0.65$. $M_2 = M_x$ and M_1 mark the positions of the neutron star and the companion star. Similar to the inner Lagrange point L_1, the center of mass (CM) lies on the line of connection between M_1 and M_2 (P. Kretschmar, J. Wilms, priv. comm.).

2.2 The Roche Potential

All accretion mechanisms have in common that gravitational energy is the driving force for accretion, thus the shape and structure of the gravitational potential in a binary system are important. The theoretical description of the total gravitational potential of a binary system is founded on the studies of the French mathematician Eduard Albert Roche (1820–1883). Roche investigated the orbit of a test particle moving in the gravitational potential of two massive bodies. His results can be applied directly to binary star systems assuming that all perturbation on the stars shape caused by the test particle are negligible, the stars are moving on a circular orbit around their common center of mass, and the stars are homogeneous, solid bodies rotating synchronous relative to the orbital motion around their individual axis. Such an idealized model of a binary system is also known as the restricted three body problem (Frank et al., 1995). The total potential of the binary system in the corotating frame of reference is then given by:

$$\Phi(r) = -\frac{GM_1}{|\vec{r} - \vec{r}_1|} - \frac{GM_2}{|\vec{r} - \vec{r}_2|} - \frac{1}{2}(\vec{\omega} \times \vec{r})^2 \tag{2.3}$$

where $\vec{r}_1$ and $\vec{r}_2$ are the position vectors of the center of the two stars, M_1 and M_2 the masses of the two components, and $\vec{\omega}$ is the angular velocity of the binary system. The first two terms in

Eq. (2.3) represent the gravitational potential of each component and the last term the influence of the centrifugal force. This description of the gravitational field is called Roche potential. The equipotential surfaces of the Roche potential in the binary orbital plane for an X-ray binary system, where $M_1 = 2.3\,M_\odot$ is the mass of the companion star and $M_2 = M_x = 1.5\,M_\odot$ the mass of the neutron has the shape shown in Fig. 2.1. The equilibrium points, where the total gravitational force vanishes, are called Lagrange points, and generally are referenced as L_1, L_2, L_3, L_4, and L_5. While L_1, L_2, and L_3 on the line of connection of the two stars, are unstable local maxima of the potential field, L_4 and L_5 are stable solutions. For large distances the equipotential surface is spherically shaped and is similar to the potential of a single point mass in a rotating coordinate system with the total mass $M = M_1 + M_2$. For the opposite case of small distances, the gravitational potential is dominated by the single masses and the equipotential surfaces are spheres. The "eight"-like, closed equipotential surface is called the critical surface. Within the critical surface each star is surrounded by its Roche Lobe. The shape of the Roche Lobe depends on the orbital separation and its size is given by the mass ratio $q = M_1/M_2$. Mass flow from the star to the compact object via the inner Lagrange point L_1 is eminent as soon as the size of a star exceeds the size of its Roche Lobe. This process is called Roche Lobe overflow.

2.3 Roche Lobe Overflow

During the evolutionary process of a binary star, the size of a star can change several times, allowing one component to exceed the size of its Roche lobe and starting an overflow of matter through the inner Lagrange point L_1 (Kopal, 1959). Besides evolutionary processes, removing angular momentum from the binary system can decrease the radius of the Roche lobe inducing mass transfer as well. This Roche Lobe "shrinking" process can either be driven by gravitational waves, magnetic braking, tidal torques, or mass ejection, e.g., by a strong stellar wind (Iben, 1991; Padmanabhan, 2001).

2.3.1 Accretion Disk

Due to thermal motion and the pressure of the gas particles in the photosphere of the star close to L_1, the plasma can leave the gravitational well of the star and enter the gravitational well of the compact object. Since the gas stream carries angular momentum, it cannot be accreted directly by the compact object, instead the gas follows Keplerian trajectories around the neutron star until the stream intercepts itself and forms a ring like structure. The radius of the ring is called circulation radius and depends on the initial energy and angular momentum of the gas stream (which can be written in terms of orbital separation and mass ratio with the aid of Kepler's third law; Frank et al., 1995):

$$r_{\text{circ}} = (1 + q)\,[0.500 - 0.227\log q]^4 a \tag{2.4}$$

where q is the mass ratio and a the orbital separation. Finally, the ring starts to spread under the influence of dissipative processes like, e.g., viscous interaction or shock waves within the plasma of the ring. Thereby the gas looses energy and starts to move inwards towards the neutron star. Because the total amount of angular momentum has to be conserved, material has to spread outwards at the same time compensating the inward motion of the accreting matter (Frank et al., 1995). As a consequence a flat accretion disk forms which extends further inwards and outwards than the circulation radius. The time scale for this process is given by the viscous timescale which
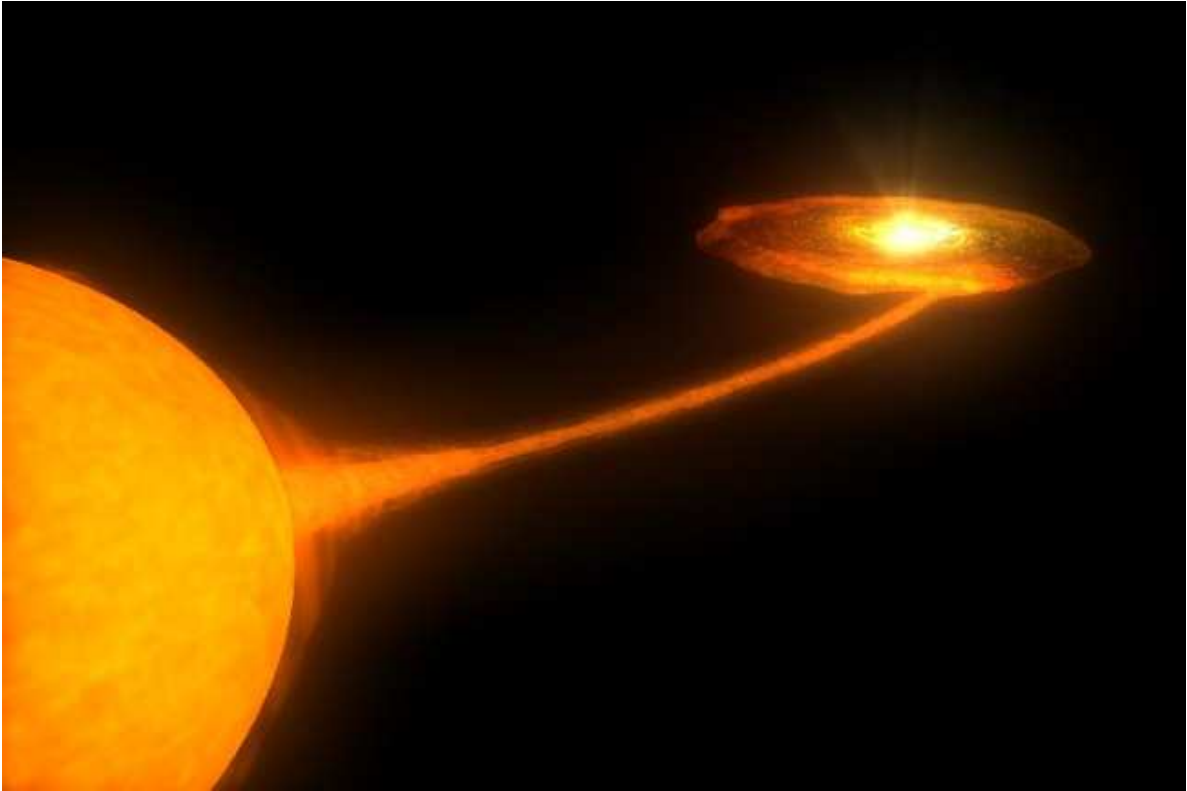
Figure 2.2: Roche Lobe accreting LMXB X-ray binary with an accretion disk. The compact object, a neutron star in this case, is located in the center of the disk. The relative geometrical size of the optical companion and the accretion disk is the same as in the binary system Her X-1/HZ Her (source *USCD*).

can be estimated to:

$$t_{\text{visc}} \approx \frac{r^2}{\nu} \approx \frac{r}{v_r} \tag{2.5}$$

Here r is the radial distance the gas travels, ν the viscosity, and v_r the radial component of the velocity vector.

In the early 1980s the standard accretion disk model was published in the pioneering work of Shakura & Sunyaev (1973). For their hydrodynamic disk model, they assumed the gas in the accretion disk to rotate on Keplerian orbits (v_Φ). The vertical extension of the accretion disk is determined by the internal pressure of the gas, which equalizes the z-component of the gravitational force. Following their hydrodynamical calculations, such a disk is geometrically thin and optically thick. As a mechanism for angular momentum transport they proposed turbulent motion of the gas in the accretion disk. To be able to parameterize turbulence, they introduced the α-parameter, which is the constant of proportionality between the viscous stress tensor t and the disk pressure, such that $t = \alpha p$ with $\alpha < 1$. Unfortunately, using two dimensional hydrodynamics alone, as in α-disk models, is not sufficient to reveal a physical explanation for the large accretion rates and the energy release observed from accretion disks in X-ray binaries. The origin of large scale turbulence during this time was unclear, since it cannot be explained from pure hydrodynamic processes.
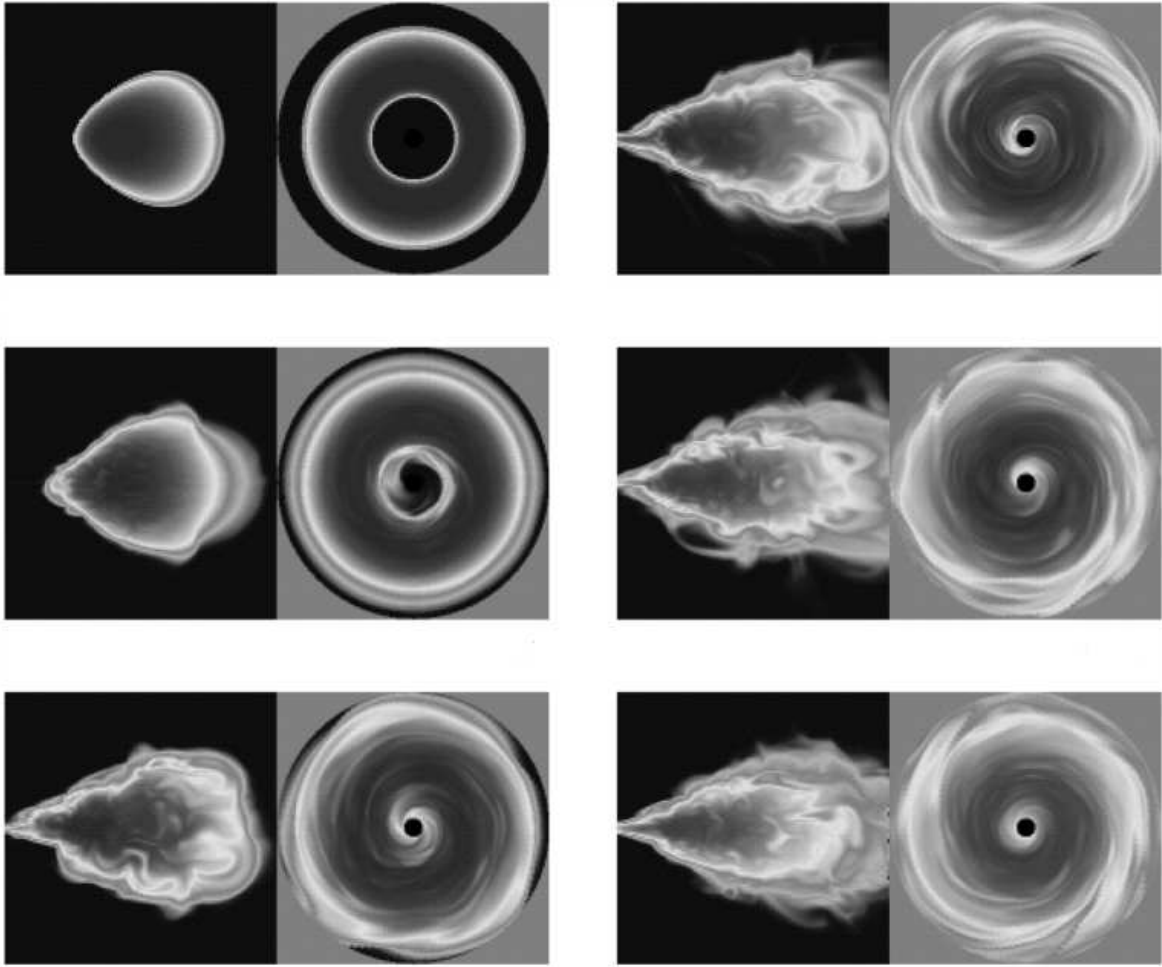
Figure 2.3: This sequence shows an evolving magneto-rotational instability (MRI) in an accretion torus. Each frame gives a side and top view of an accretion torus. The density is shown as a logarithmic gray scale. The initial density distribution is shown in the top left frame. In the middle frame of the left sequence the MRI starts to evolve at the inner edge of the torus and rapidly spreads outwards until the whole disk becomes turbulent (lower right frame). The temporal sequence is from top left to bottom left and top right to bottom right (Hawley, 2000, figure 9).

In an α-disk the Keplerian motion of the gas can reach velocities of about $v_\Phi \approx 1000 \, \mathrm{km\,s^{-1}}$ which is highly supersonic ($c_s \approx 10 \, \mathrm{km\,s^{-1}}$). In contrast, the radial velocity $v_r \approx 0.3 \, \mathrm{km\,s^{-1}}$ of the infalling plasma is slow compared to the speed of sound. From the assumption of a thin but optically thick disk, the emitted spectrum of an α-disk can be assumed as a superposition of single blackbody spectra (multi-color disk blackbody) with variable temperature solely depending on the disk radius according to $T(r) \propto r^{-3/4}$ (e.g., Mitsuda et al., 1984; Makishima et al., 1986).

2.3.2   Angular Momentum Transfer in Accretion Disks

One of the major problems for theorists working in the field of accretion theory is that large energy dissipation in turn needs a very efficient process for angular momentum transport. Instabilities in the disk flow caused by molecular viscosity or radiative processes are far to ineffective to explain the necessary outward angular momentum flow.
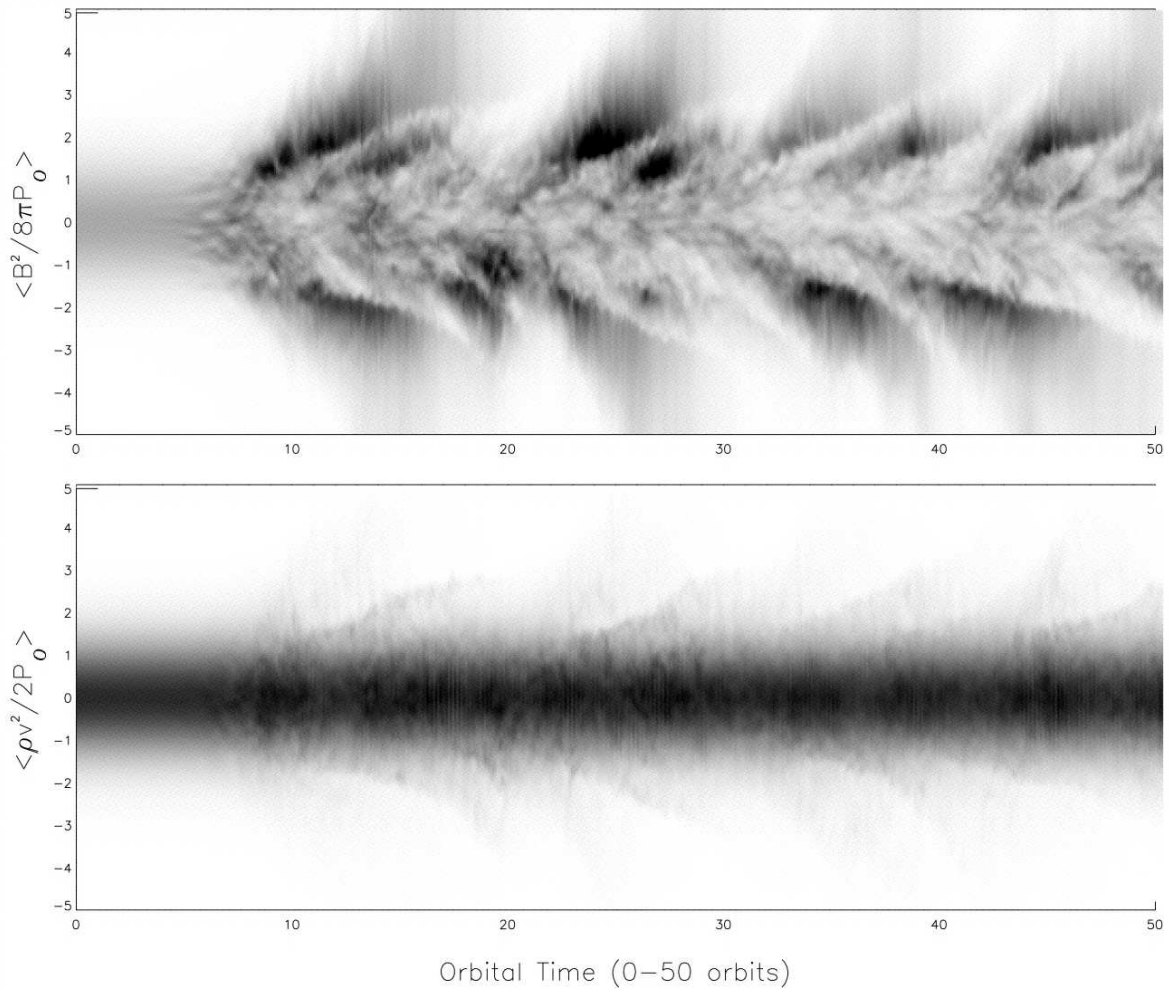
Figure 2.4: Temporal evolution of the vertical structure of a magnetized accretion disk corona. The horizontally averaged magnetic (top images) and kinetic energy distribution (lower panel) of a disk corona are shown. After about 10 orbital periods the buoyant MRI starts to spread up- and downwards from the center of the accretion plane and finally extends to 3–4 scale heights of the accretion disk (Miller, 2000, figure 1).

One of the most promising source of stresses in accretion disks is turbulence caused by weak magnetic fields. Major improvements in understanding angular momentum transfer in accretion disks were made, by including magnetic fields in hydrodynamic calculations. Such magneto-hydrodynamic (MHD) calculations lead to the discovery of magneto-rotational instabilities (MRI) (Chandrasekhar, 1960, 1961), which are the origin of large scale magneto hydrodynamic turbulence called Balbus-Hawley instabilities (Balbus & Hawley, 1991; Hawley & Balbus, 1991). These instabilities act as a kinematic "dynamo", amplifying the initially weak magnetic energy in the accreting plasma by factors of 10^4 on very short time scales (within a few Keplerian timescales, Hawley & Balbus, 1995). In the arising turbulent eddies kinetic energy of a laminar non-turbulent accretion flow is converted into turbulent kinetic and magnetic energy. Such eddies enhance the viscosity and thus the angular momentum transport in the disk becomes very effective. In return to the enormous progress in computer-science and calculation power of modern computers, accretion disk simulations could be extended to three dimensions and even time dependent simulations are
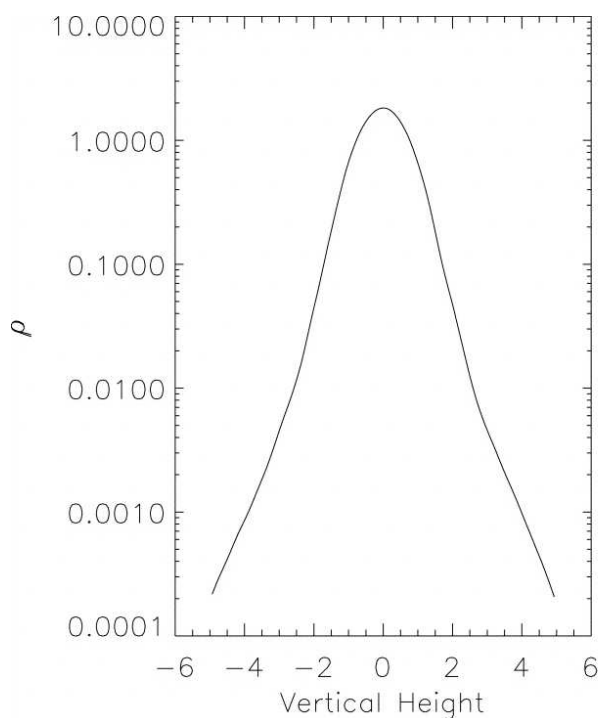
Figure 2.5: Averaged vertical density distribution of an accretion disk corona derived from the simulation shown in Fig. 2.4 (Miller, 2000).

possible for parts of an accretion disk (typically ring like or rectangular sectors of a disk), fully accommodating for the vertical disk structure. As an example, results of such a simulation are shown in Fig. 2.3, giving an impression how MRI triggers a runaway process causing highly turbulent motion in an accretion disk. In the beginning an MRI evolves at the inner edge of the disk (Fig. 2.3, middle frame on the left side) before it spreads quickly throughout the disk. As a consequence, the accretion flow evolves from a laminar flow (Fig. 2.3, top left frame) to an accretion disk which is dominated by turbulent motion of the accreted gas (Fig. 2.3, lower right frame). A recent review on magnetic turbulence in accretion disks and an introduction to the theory of magnetized accretion disks can be found in, e.g., Balbus & Hawley (1998) and Hawley et al. (2001).

2.3.3   Accretion Disk Coronae

Several observations of accreting X-ray binaries indicate that the upper and lower side of an accretion disk is covered by a diffuse low density corona. To explain the origin of such a corona different models exist like, e.g., coronae which evolve from external irradiation of the accretion disk from the central object (Dove et al., 1997; Begelman & McKee, 1983). Other models rely on three dimensional MHD simulations rather than radiative transfer. In MHD models such as the one shown in Fig. 2.4, a corona can evolve from the internal dynamic structure of the disk. Miller & Stone (2000) have demonstrated with 3D MHD simulations of a weakly magnetized accretion disk that a corona can be effectively heated by buoyant flux tubes which dissipate and magnetize the corona while rising upwards from the central region of the turbulent accretion disk. Thereby magnetic energy is converted into kinetic energy which heats the corona by viscous interaction of the plasma. The energy dissipation deduced from such MRI driven disk corona models is of the order of the observed energy dissipation. Fig. 2.4 gives an impression of the evolution of the ver-

tical structure of such an accretion disk corona. The evolving magnetic energy (top panel) and the kinetic energy (lower panel) is shown versus time. Such simulations indicate that the disk corona can extend in vertical direction up to 5 times the scale hight of the disk. The corresponding density profile, giving the averaged vertical structure of the disk is shown in Fig. 2.5.

2.3.4   The Boundary Layer

Contrary to the outer parts of the accretion disk treated in the sections before, the magnetic field of the neutron star dominates the accretion flow close to the neutron star. The detailed physics of this region close to the magnetospheric radius, which is called the boundary layer, is difficult to understand. It was theoretically and quantitatively treated for a Keplerian rotating α-disk in the papers of Ghosh et al. (1977), Ghosh & Lamb (1979a), and Ghosh & Lamb (1979b). In these works the magnetic dipole axis of the neutron star and its rotation axis are aligned (coaligned rotator). The disk structure for an inclined magnetic dipole with respect to the rotation axis can be found in, e.g., Lipunov (1982). Fig. 2.6 shows a schematic picture of the magnetosphere, the inner boundary of the accretion disk, and the transition region for a coaligned rotating neutron star.

In the presence of a strong magnetic field of the order of $\approx 10^{11}$–10^{13} Gauss, which is a typical range for XRPs, the magnetic pressure P_m prevents the inner part of the disk to extend to the surface of the neutron star. At the Alfvén or magnetospheric radius (Nagase, 1989)

$$r_m \simeq 5.2 \times 10^8 \mu_{30}^{4/7} \dot{M}_{16}^{-2/7} M_x^{-1/7} \text{ cm} \tag{2.6}$$

the magnetic pressure equals the radial pressure component of the infalling gas (Davidson & Ostriker, 1973)

$$P_{mag}(r_m) = \frac{B(r_m)^2}{8\pi} = \rho v(r_m)^2 = P_{ram}(r_m) \tag{2.7}$$

which is called ram pressure (P_{ram}). As a condition for accretion to take place, the angular velocity of the neutron star ω_x, which is identical to the angular velocity of the magnetosphere, has to be smaller than the Keplerian velocity of the gas at the magnetospheric radius r_m. This boundary condition can be expressed in terms of the *fastness* parameter, which is defined as (Ghosh & Lamb, 1979b; Nagase, 1989):

$$\omega_s := \frac{\omega_x}{\omega_k(r_M)} = \left(\frac{r_m}{r_{co}}\right)^{2/3} \tag{2.8}$$

The corotation radius r_{co} in Eq. (2.9) is the distance from the neutron star where the angular velocity of the magnetosphere equals the Keplerian velocity of the gas:

$$r_{co} = \left(\frac{GMP_{spin}^2}{4\pi^2}\right)^{1/3} = \left(\frac{GM}{\omega_s}\right)^{1/3} \tag{2.9}$$

For steady accretion to take place, $\omega_s < 1$ must be fulfilled, since otherwise the accreting matter can be repelled by centrifugal forces at the centrifugal barrier. In the transition zone the magnetic field threads the disk, but viscous stress still dominates over magnetic forces. Within the boundary layer the magnetic field is strong enough for magnetic stress to overcome the influence of viscosity and matter is torn off in vertical direction from the accretion disk. Outside the transition region the angular motion of the disk is Keplerian and changes rapidly within the transition region until the disk angular velocity equals the angular velocity of the magnetosphere at the corotation radius r_{co} which lies within the boundary layer. For radii smaller than r_m the magnetic pressure is higher
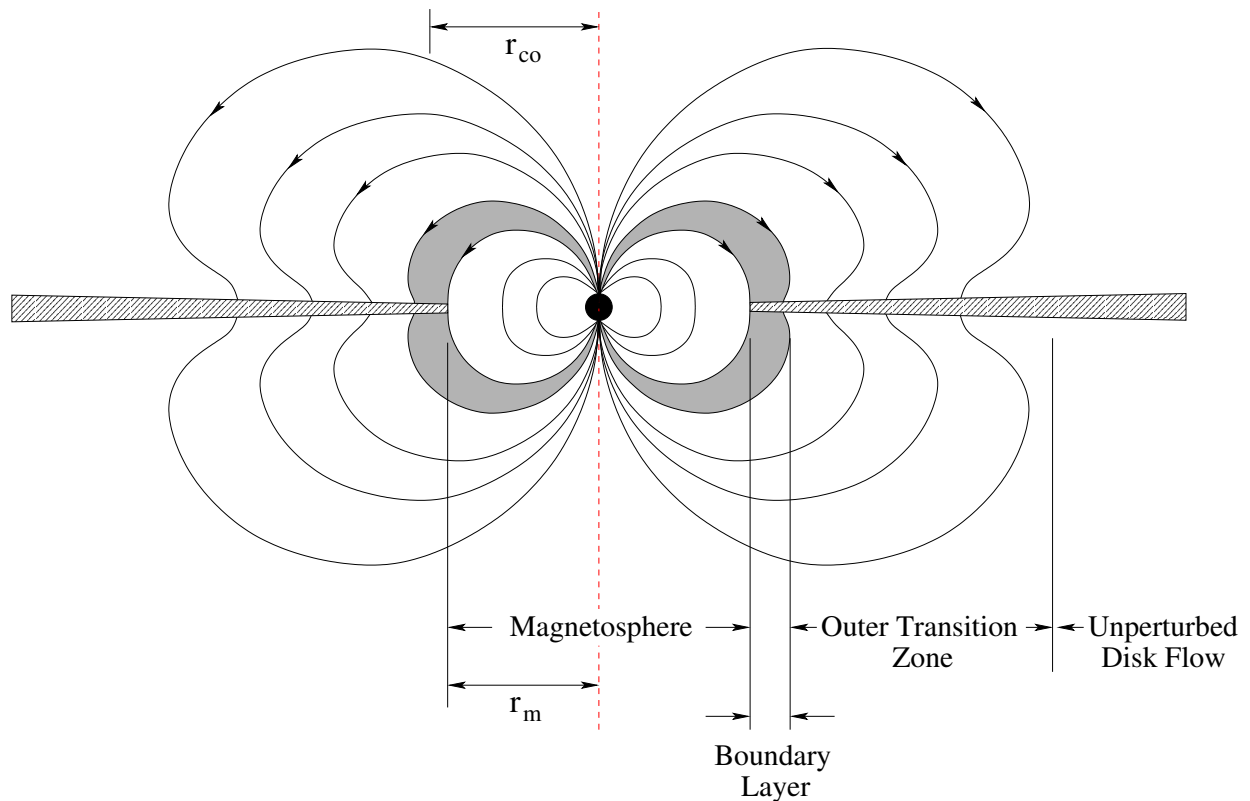
Figure 2.6: Schematic view of the boundary layer of a neutron star with a strong magnetic field and the inner parts of an accretion disk. The boundary layer is indicated by the shaded region. r_{co} is the corotation radius and r_m the magnetospheric radius (adopted from Ghosh & Lamb, 1979b, Fig. 1).

than the ram-pressure of the gas stream in the disk and the plasma has to follow the magnetic field lines towards the poles of the neutron star. Close to the magnetic poles the gas flow is concentrated in an accretion funnel until it reaches the surface of the neutron star at its polar caps.

2.3.5 Angular Momentum Transfer to the Neutron Star

All accreting X-ray pulsars show variations of their rotational period (pulse frequency) on time scales of days to months. Over long periods the pulse frequency typically increases linearly with time (spin-up). This spin-up can erratically be interrupted by short periods of spin-down, where the pulse frequency decreases. Fig. 2.8 clearly demonstrates this behavior for the X-ray binary Her X-1/HZ Her. Spin-up/down variations can either be irregular or correlated with an increasing or decreasing observed luminosity, like it is the case for transient sources and some X-ray binaries. Typical values of $\dot{P}$ range from $10^{-6}\,\mathrm{s\,y^{-1}}$ up to $10^{-3}\,\mathrm{s\,y^{-1}}$ (Frank et al., 1995).

In any case, a spin-up is correlated with an increasing angular momentum of the neutron star and a spin-down with a decreasing amount of angular momentum (e.g., Davidson & Ostriker, 1973). The angular momentum transfer takes place close to the boundary layer and the outer transition zone of the accretion flow by magnetic coupling of the neutron star's magnetosphere to the disk matter causing magnetic torques (Ghosh & Lamb, 1979b; Nagase, 1989). Whether a positive or negative torque is exerted on the neutron star is primarily a function of the fastness parameter ω_s, which depends on the magnetospheric radius r_m, respectively. Following the calculations of
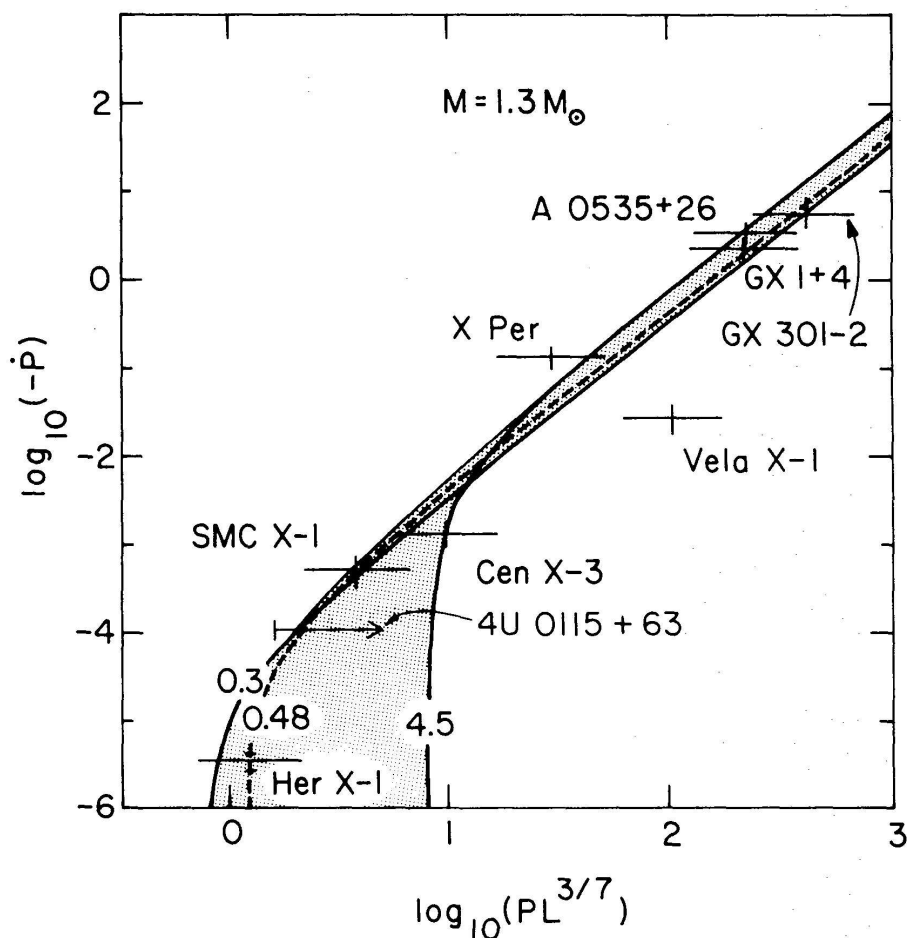
Figure 2.7: Correlation between the spin-up $-\dot{P}$ and $PL^{3/7}$ for nine X-ray pulsars. Theoretical curves are overlaid for different magnetic moments μ_{30}. The dashed line gives the best fit for $\mu_{30} = 0.48$ (Fig. 9, Ghosh & Lamb, 1979b; Rappaport & Joss, 1977).

Ghosh & Lamb (1979b), a spin-up is possible for $r_m \ll r_{co}$, which is equivalent to $\omega_s \ll 1$. When ω_s increases, the net accretion torque gets weaker until the angular momentum transfer stops at a maximum value of the fastness parameter of $\omega_{max} \approx 0.95$ (Ghosh & Lamb, 1979b). The decreasing angular momentum transfer is a consequence of the fact that for fast rotating neutron stars the torques in the outer transition zone, where the magnetic field treads the disk cause a spin-down. If this spin-down torque is of the order of the positive spin-up torque in the boundary layer, both torques cancel out and thus no net angular momentum transfer to the neutron star will take place. In contrast, slowly rotating neutron stars always exert a spin-up and their change in pulse period is given by (Ghosh & Lamb, 1979b, Eq. 15):

$$-\dot{P} = 5.0 \times 10^{-5} \mu_{30}^{2/7} n(\omega_s)\, r_6^{6/7} m_x^{3/7} I_{45}^{-1}\, (PL_{37}^{3/7})^2 \text{ s yr}^{-1} \tag{2.10}$$

where L_{37} is the accretion luminosity in units of 10^{37} erg s^{-1}, r_6 the radius in units of 10^6 cm, I_{45} the moment of inertia in units of 10^{45} g cm^3, μ_{30} the magnetic moment of the neutron star in units of 10^{30} Gauss cm^3, and $n(\omega_s)$ a dimensionless analytic expression for the accretion torque which solely depends on ω_s (see Ghosh & Lamb, 1979b, Eq. 7). Thus the spin-up for a specific object depends on the luminosity and the rotational period by $-\dot{P} \propto (PL_{37}^{3/7})^2$. This relation is shown in Fig. 2.7 for different values of the magnetic moment μ_{30}, including observed data of nine X-
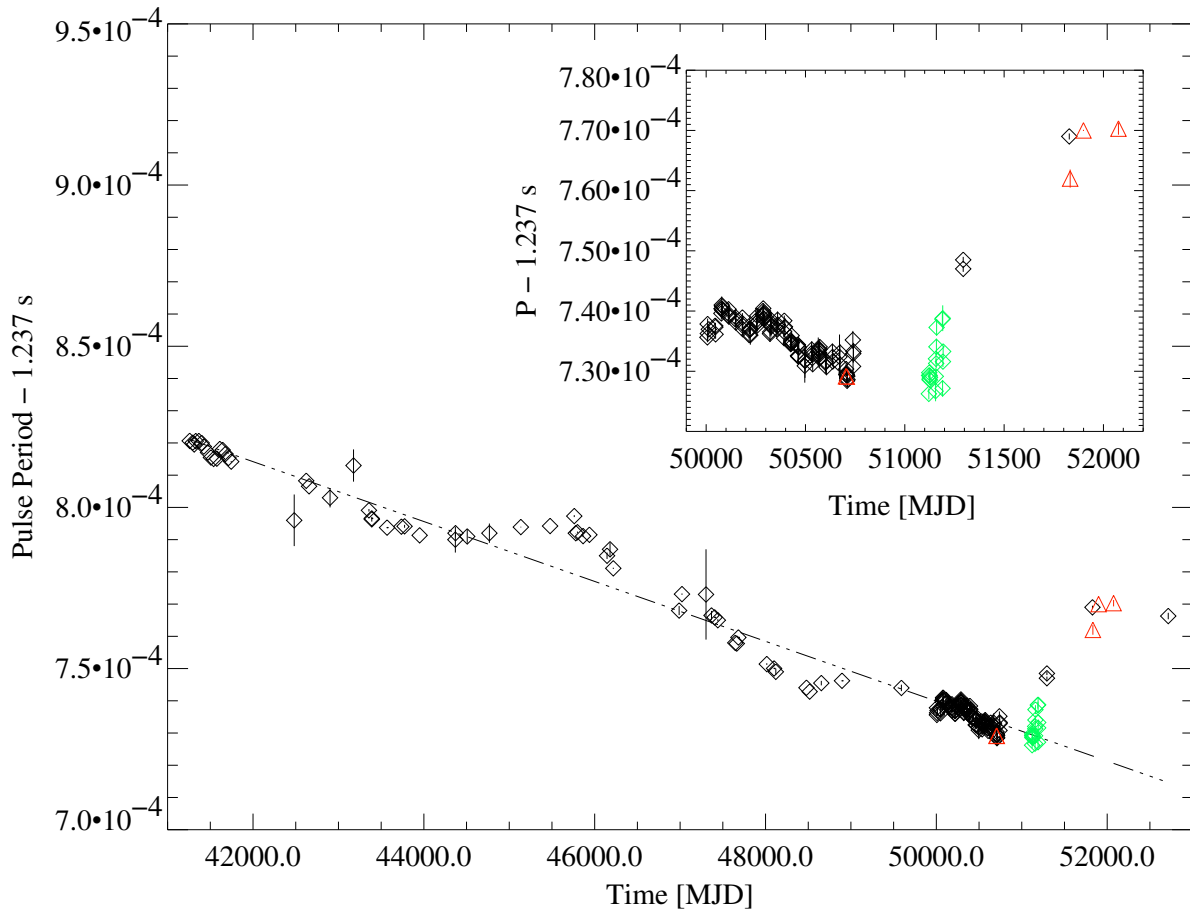
Figure 2.8: The history of the pulse period of the XRP Her X-1 since 1971. The long term spin-up behavior is clearly visible. For a more detailed explanation see section 6.2.2.

ray pulsars. Comparing the spin-up rate calculated from Eq. (2.10) to the observed spin-up rate of $\langle \dot{P} \rangle = -3.40 \pm 0.04 \times 10^{-6}\,\mathrm{s\,yr}^{-1}$ in Her X-1 shows that this theoretical model is in good agreement with the observation (see Fig. 2.8).

2.3.6   The Accretion Column

When the accreted matter passes the boundary layer, it is forced to follow the magnetic field lines. During this transition, the orbital motion in the accretion disk changes to a free fall flow and the gas stream is concentrated in an accretion funnel onto both magnetic poles of the neutron star. This small region ($A \approx 1\,\mathrm{km}^2$) is the main origin of the observed X-ray emission. The extreme physical conditions in the accretion funnel with magnetic field strengths up to 10^{13} Gauss, relativistic plasma velocities of $v \approx 0.6\,c$, and luminosities close to L_{Edd} make it hard to find a self-consistent model of the accretion column. Even for lower luminosity, $L \ll L_{\mathrm{Edd}}$ the problem does not simplify noticeable.

Although the detailed structure of the accretion funnel is still not known, several simplified theoretical models exist. For a neutron star with a dipole like magnetic field, two possible geometries are shown in Fig. 2.9 which follow the theory of Basko & Sunyaev (1976). For low accretion rates ($L \ll L_{\mathrm{Edd}}$) the results of their hydrodynamical simulations reveal that the infalling plasma
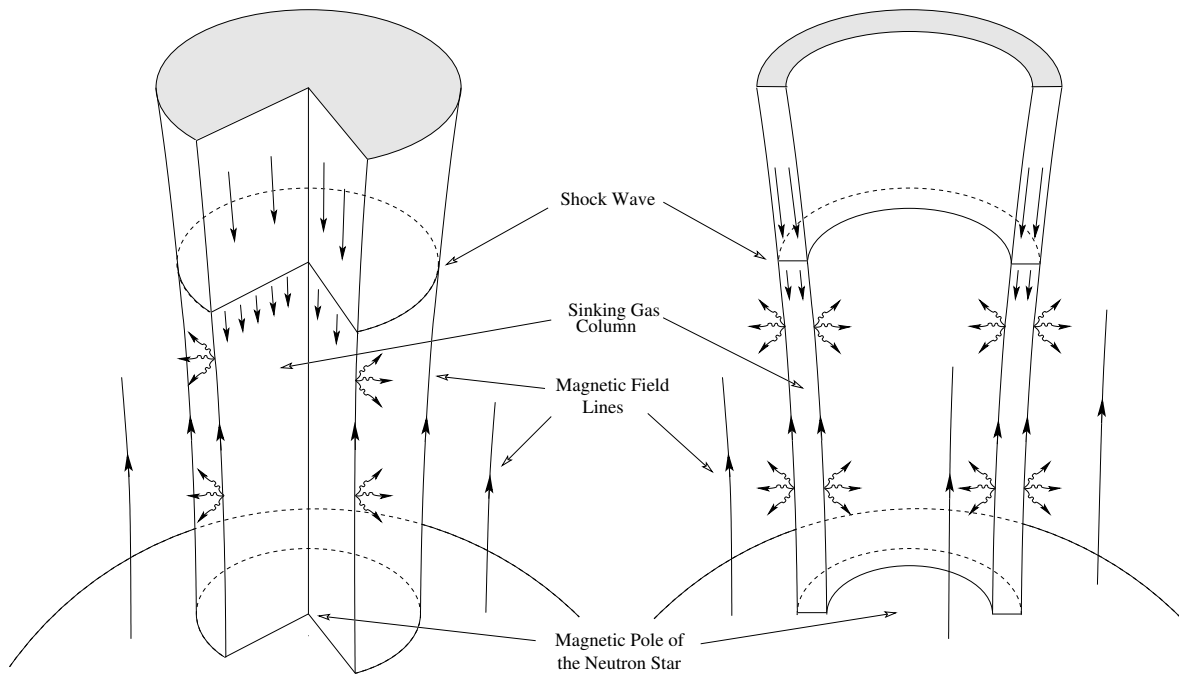
Figure 2.9: Left: Column like accretion geometry, resulting in a *fan beam* or *pencil beam* like emission characteristic depending on the accretion rate (see text for discussion). Right: Cylindric accretion geometry where plasma is accreted in a hollow, accretion funnel (after Basko & Sunyaev, 1976, Fig. 1).

passes a free-fall zone until it reaches almost the neutron star's surface. Close to the surface of the neutron star the plasma is decelerated by Coulomb interactions with electrons of the neutron star's atmosphere and due to inelastic scattering with protons. Following Brown & Bildsten (1998) the height of this accretion mound on the neutron star surface is of the order of $\approx$ 1.0–15.0 m. Under these conditions the emergent radiation pressure acting on the infalling plasma in the accretion column is negligible and the optical depth of the accreting plasma is low, giving rise of a *pencil beam* like emission characteristic: photons are escaping through the accretion funnel in vertical direction. For high accretion rates the radiation pressure is dominating and according to Basko & Sunyaev (1976) the plasma dissipates almost all of its kinetic energy by inverse Compton scattering in a radiative shock above the polar cap of the neutron star. Below the shock front the speed of the plasma is subsonic and the heated plasma is highly radiative (see left image of Fig. 2.9). The large optical depth within the shock reduces the photon flux above the shock in vertical direction to almost zero. Therefore photons are presumably emitted in horizontal direction towards the side of the accretion funnel resulting in a *fan beam* like emission characteristic. The elevation of the radiative shock front above the neutron star's pole depends on the accretion rate $\dot{M}$ and can range up to a few neutron star radii above the neutron star's surface.

Although, this model of the accretion funnel is very simplified, it gives a qualitative impression of the accretion process close to the neutron star's surface. It is controversially discussed whether low accretion rates cause a shock emerging in the accretion flow as well (Frank et al., 1995). In any case, the structure of the shock front, which is a discontinuity in fluid temperature, velocity, and density is still unclear. A mean free path of the ions in the free fall plasma of $\lambda \gtrsim 5 \times 10^9$ cm

(Frank et al., 1995) for a gas velocity $v \approx c/2$ and a neutron star radius $r \approx 10$ km, rules out a collisional shock for low accretion rates since the probability for collisions becomes negligible. Therefore, some kind of collisionless shock, where energy is dissipated without the influence of viscosity, must play an important role (Harding, 1994).

Chapter 3

Radiation Processes in X-ray Binaries

For interpreting the observed spectra of X-ray binaries it is essential to understand the underlying radiation processes. The apparent spectrum always is a superposition of several spectral components which originate in different emission regions of the binary system. For example, thermal blackbody radiation from accretion disk contributes to the observed spectrum and is often approximated by a simple blackbody or multi-color disk blackbody like shape (section 3.1). Cold or partially ionized material as present in the outer and cooler parts of the accretion disk or accretion disk corona can modify the observed spectrum by photoelectric absorption or fluorescent line emission. Due to the relativistic energies of electrons and high magnetic fields present in the accretion column close to the neutron star's surface, non-thermal emission processes like synchrotron radiation contribute significantly to the observed spectral flux (section 3.2). In addition the observable spectrum can be altered by cyclotron resonant scattering in the presence of a strong magnetic field or by Compton scattering from free electrons (section 3.3 and section 3.4).

In this chapter I summarize the radiation processes which are important for the following data analysis. It is not the intention of this work to fully accommodate for the complex physics of radiation transport in the accretion column or accretion disk. Instead the intention of this chapter is focused on radiation processes which are important for data analysis and the physical interpretation. Furthermore, the temporal influence of Compton scattering on beamed emission is investigated in section 3.5. In this section the theoretical background for the simulations of pulse profiles presented later during this work in section 8 is introduced. When not stated otherwise, the content of this chapter is based on the book of Rybicki & Lightman (1979).

3.1 Thermal – Blackbody Radiation

Blackbody radiation is one of the most important and fundamental radiation processes known. In general each object with a temperature $T \neq 0\,\mathrm{K}$ emits thermal radiation. For the idealized case, when the object is in thermodynamical equilibrium with its environment at all wavelengths, it radiates as a blackbody. In other words a blackbody is a perfect absorber and emitter of radiation. The shape of the observable spectrum emitted by a blackbody depends on its temperature T and follows Planck's law (see, e.g. Rybicki & Lightman, 1979):

$$B_\nu(T) = \frac{2h}{c^2} \frac{\nu^3}{\exp(h\nu/kT) - 1} \tag{3.1}$$

with the Boltzmann constant $k = 1.381 \times 10^{-15}\,\mathrm{erg\ K^{-1}}$ and the Planck constant $h = 6.626 \times 10^{-27}\,\mathrm{erg\ s}$. In Fig. 3.1 several blackbody spectra are shown for different temperatures. For the
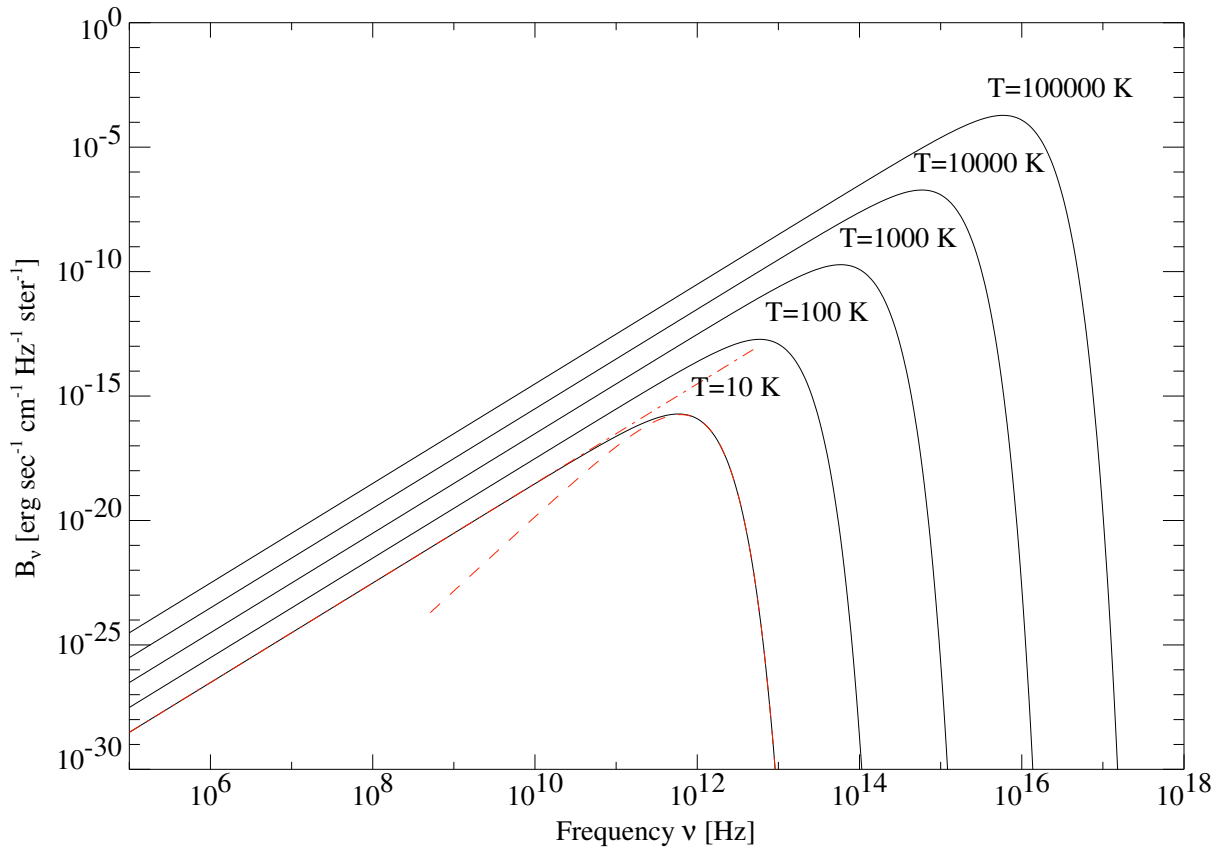
Figure 3.1: Spectrum of a blackbody for different temperatures T. The Rayleigh-Jeans and Wien's approximation are indicated as dash-dotted red and dashed red lines for the spectrum at $T = 10\,\text{K}$.

limit of low photon energies ($h\nu \ll kT$) Planck's law can be approximated by the Rayleigh-Jeans law, which is independent of Planck's constant:

$$B_\nu(T) \approx \frac{2\nu^2}{c^2}kT \tag{3.2}$$

The Rayleigh-Jeans law can also be derived using mere classical physics, ignoring quantum mechanical effects. If the Rayleigh-Jeans law is applied to high photon energies, which is equivalent to high frequency values ($h\nu \gg kT$), the total amount of emitted energy of the blackbody diverges (ultraviolet catastrophe). This is a direct consequence of the classical treatment, ignoring the quantum nature of photons. For the opposite case where the photon energy is large ($h\nu \gg kT$), Eq. (3.1) takes the simple form:

$$B_\nu(T) \approx \frac{2h\nu^3}{c^2}\exp\left(-\frac{h\nu}{kT}\right) \tag{3.3}$$

which is called Wien's law. Both approximations, Wien's law and the Rayleigh-Jeans law, of the quantum mechanical correct Planck Law are indicated in Fig. 3.1 as dash-dotted and dashed lines. According to Wien's law, $B_\nu(T)$ drops exponentially for large frequencies. The wavelength $\lambda_{\max}$ where the brightness of a blackbody has its maximum, linearly depends on the temperature of the blackbody and follows Wien's displacement law $\lambda_{\max}T = 2.9 \times 10^{-3}\,\text{mK}$.

In astrophysical sources Planck spectra can be observed whenever the emitting plasma is in thermodynamical equilibrium. As an example, Planck spectra can be used as approximation for

the emitted spectrum of accretion disks. Especially a spectrum superposed of several blackbody spectra with a temperature distribution $T(r) \propto r^{-3/4}$ is able to reproduce the observed spectra from thin accretion disks. For this work a simple blackbody spectrum is used to approximate emission from the accretion disk in Her X-1 (see section 7.3.1).

3.2   Cyclotron and Synchrotron Radiation

An electron which is bound to a magnetic field and which has a velocity component parallel to a magnetic field, moves along a helix like path about the magnetic field vector $\vec{B}$. The force thereby acting on the electron is the Lorentz force. According to classical electrodynamics an accelerated charged particle emits a narrow line of emission at the frequency (e.g. Ginzburg & Syrovatskii, 1965):

$$\nu_c = \frac{eB}{2\pi m_e c} = \frac{\omega_c}{2\pi} \tag{3.4}$$

where m_e is the electrons rest mass, e the electron charge, and ν_c is called cyclotron frequency. For non-uniform magnetic fields like in realistic astrophysical objects and because of the influence of Doppler-broadening the observed emission lines are no sharp delta peaks at frequency ν_c but slightly broadened lines. In the astrophysical more realistic case of a hot electron plasma, where the velocity of the electron can be close to the speed of light, the emission process requires full relativistic treatment. This leads to the relativistic analogon of cyclotron radiation which is called synchrotron radiation, named after relativistic particle accelerators used in nuclear physics. Then the orbit frequency of the electron scales $\propto 1/\gamma$ compared to the non-relativistic case. In the lab frame ν_s is given by:

$$\nu_s = \frac{eB}{2\pi\gamma m_e c} = \frac{\nu_c}{\gamma} \tag{3.5}$$

For cyclotron emission the emission characteristic of the electron has a dipole like $\cos^2\theta$ shape. In contrast to this, in the relativistic case the electron presumably radiates in forward direction. The resulting emission characteristics has a cone like shape in the direction of motion of the electron, which is a consequence of the Lorentz transformation from the electrons rest frame to the observes frame in the relativistic calculation (see Fig. 3.2). The opening angle of the emission cone is about $\Delta\theta \propto \gamma^{-1}$ and the radiation is strongest in the plane perpendicular to the magnetic field.

The corresponding single electron spectrum is no longer a single line, but is spread over a large frequency range. The spectrum of a large number of electrons emitting synchrotron radiation is a superposition of single electron spectra and has the shape of a power-law, under the assumption that the energy distribution of
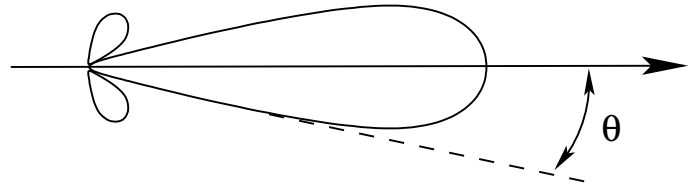

Figure 3.2: Emission characteristic of a relativistic electron emitting synchrotron radiation (after Rybicki & Lightman, 1979, Fig. 4.11).

the electron is non-thermal and follows a power-law distribution as well (Rybicki & Lightman, 1979). The energy range of the synchrotron spectrum is characterized by the magnetic field strength. For typical pulsars or isolated neutron stars, the magnetic field strength B is of the order of 10^8–10^{12} Gauss (Becker, 2002), implying that the observable spectrum covers the energy range from the radio to the X-ray band. As an example young pulsars like the Crab pulsar approximatively have a synchrotron spectrum. Spectra of X-ray binaries generally differ from pure synchrotron spectra. Especially at higher energies the observed spectra show an exponential drop

in the continuum flux, which is not compliant to a sole synchrotron spectrum (see section 7.3).

3.3   Cyclotron Resonant Scattering

For very strong magnetic fields, with a magnetic field strength $B \gtrsim 10^{12}$ Gauss, the radius of the helix of the moving electron in a magnetic field is close to the de Broglie wavelength of the electron and the influence of quantum mechanics becomes important (Mészáros & Nagel, 1985a). As a result, the energy of the electron perpendicular to the magnetic field is no longer continuous but is quantized into discrete energy levels, called Landau levels. The allowed electron energies perpendicular to the magnetic field are given by:

$$E_n = m_e c^2 \sqrt{1 + \left(\frac{p}{m_e c}\right)^2 + 2n \frac{B}{B_{\text{crit}}}} \tag{3.6}$$

where n is the principal quantum number which can be of integer value $n = 0, 1, 2, ...$ and p is the momentum of the electron parallel to the magnetic field (Harding & Daugherty, 1991; Harding, 1994). Considering the electron spin $s = \pm 1/2$ as well, the quantum number n can take the values $n = l + \frac{1}{2} + s$, with $l = 0, 1, 2, ...$ being integral numbers. For electrons in the ground level $n = 0$, the only allowed spin state is $s = -\frac{1}{2}$. All other energy eigenstates are degenerated twice with respect to the electron spin and possible spin values are $s \pm \frac{1}{2}$. The energy difference between two allowed eigenstates is called cyclotron energy E_{cyc} and can be approximated for $B \ll B_{\text{crit}}$ by:

$$E_{\text{cyc}} = E_{n+1} - E_n = \hbar \omega_c = \frac{e\hbar}{m_e} \cdot B \approx 11.6 \, \text{keV} \cdot B_{12} \tag{3.7}$$

with $B_{12} = B/10^{12}$ Gauss. According to Eq. (3.6) and Eq. (3.7) an electron in the ground state $n = 0$ can only be excited to an excited state $n > 0$ by photons which have an energy of integer multiples of nE_{cyc}. For plasma temperatures $kT \ll E_{\text{cyc}}$, the life time of the Landau levels is short compared to the time for collisional de-excitation. Thus electrons in an excited state $n \geq 1$ almost instantaneously return to ground state by emitting a resonant photon. This excitation-, de-excitation process is similar to a resonant scattering process, rather than to an absorption process (Harding & Daugherty, 1991). Consequently photons are scattered out of the line of sight and the resulting resonance line (cyclotron resonant scattering feature – CRSF) can be observed at the energy nE_{cyc} in the photon spectrum.

Eq. (3.6) holds as long as the magnetic field strength B is small compared to B_{crit}, where B_{crit} is the magnetic field strength where the energy of the electron equals $m_e c^2$ (Harding & Daugherty, 1991):

$$B_{\text{crit}} = \frac{m_e^2 c^2}{e\hbar} = 4.414 \times 10^{13} \, \text{Gauss} \tag{3.8}$$

For $B \approx B_{\text{crit}}$ relativistic corrections become important and the cyclotron energy further depends on the angle θ between the primary photon and the magnetic field axis. According to Harding & Daugherty (1991) the energy E_n of the electron eigenstates in the electron rest frame then is:

$$E_n = \frac{m_e c^2}{\sin^2 \theta} \left(\sqrt{1 + 2n \frac{B}{B_{\text{crit}}} \sin^2 \theta} - 1 \right) \tag{3.9}$$
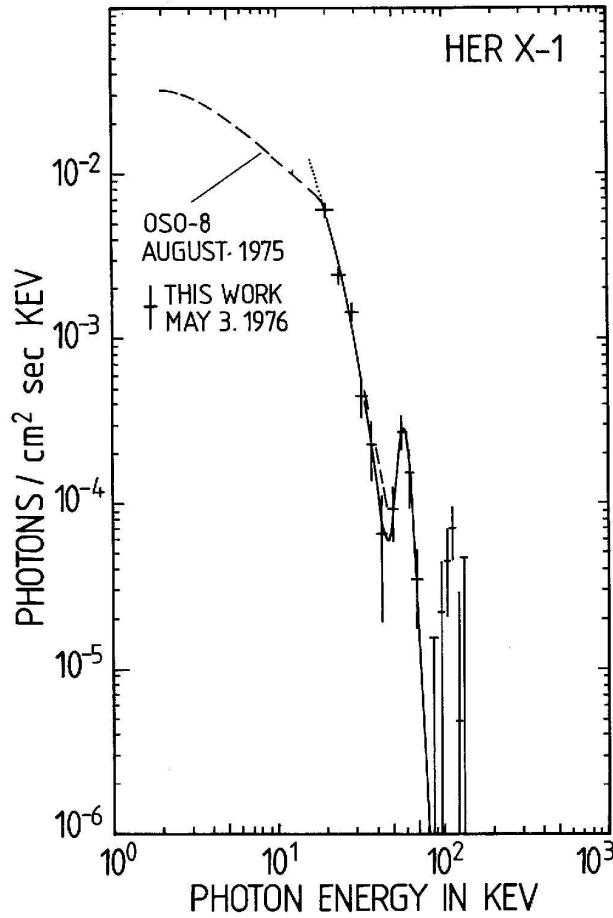
Figure 3.3: First observational evidence for a cyclotron resonant scattering feature (CRSF) observed in Her X-1 by Trümper et al. (1977).

From the relativistic calculation follows that the line shape of the CRSF is not a mere Lorentzian profile and extremely sensitive on the viewing angle with respect to the magnetic field. The magnetic field, and the temperature T of the electron plasma have influence on the line shape as well (e.g., Doppler broadening), but their weight is less important.

In X-ray binaries like Her X-1, the boundary conditions for cyclotron resonant scattering are given in the accretion column close to the neutron star's surface, where the magnetic field strength increase up to $B \gtrsim 10^{12}$ Gauss. There, the influence of gravity deep in the gravitational potential well of the neutron star cannot be neglected any more. Consequently the apparent energy of the CRSF E'_{cyc} measured by an observer will be gravitationally red-shifted. The intrinsic energy E_{cyc} then is higher compared to the apparent energy E'_{cyc} and can be calculated from:

$$E'_{\text{cyc}} = \frac{E_{\text{cyc}}}{1+z} = E_{\text{cyc}} \sqrt{1 - \frac{2GM_{\text{x}}}{Rc^2}} \qquad (3.10)$$

where M_{x} is the mass of the neutron star and R its radius. For typical X-ray binary pulsars the energy shift due to the gravitational field is of the order of 20–30 %, thus the expected energy for CRSFs is $E_{\text{cyc}} \approx 10$–50 keV. Using Eq. (3.7) and Eq. (3.10) leads to the simple relation between the intrinsic energy E_{cyc} and the magnetic field strength:

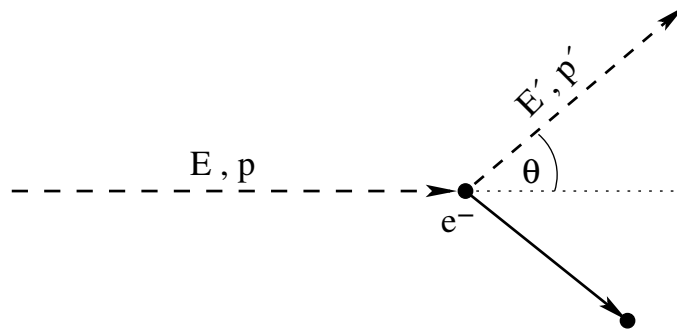$$E_{\text{cyc}} = 11.6 \,\text{keV} \cdot B_{12} \,(1+z) \qquad (3.11)$$

Figure 3.4: Schematic view of the Compton scattering process. An incident photon with energy E and momentum p is scattered by a free electron. After the scattering process, the electron has an energy E' and a momentum p'. For Thomson scattering the scattering process is elastic and the energy of the electron does not change ($E = E'$).

The first observational evidence for a CRSF in X-ray binaries systems and pulsars was reported by Trümper et al. (1977) following an observation of Her X-1/HZ Her in 1975. The spectrum of this observation is shown in Fig. 3.3. Up to now, CRSFs have been reported from 13 X-ray binary systems, including LMXB and HMXB systems. A recent study of CRSFs in accreting X-ray binary systems can be found in Coburn (2001). Although the line shape of a CRSF is complicated in detail, the energy of the line centroid is a direct link to the surface magnetic field strength of the neutron star, which can be determined via Eq. (3.7) when the energy of the CRSF is known from a spectral analysis (cf. section 7.3.3).

3.4   Thomson/Compton Scattering

The classical treatment of scattering of photons with incident photon energies $E \ll m_e c^2$ by stationary free electrons is called Thomson scattering after J. J. Thomson (1903). For this simplified case the scattering process can be assumed as elastic, because the rest mass energy of the electron is large compared to the photon energy. Thus while being scattered, the incident photon changes its direction and momentum but not its energy ($E = E'$). The differential cross section is then given by:

$$\frac{d\sigma_T}{d\Omega} = \frac{r_e^2}{2}(1 + \cos^2\theta) \tag{3.12}$$

where $r_e = e^2/m_e c^2$ is the classical electron radius. The shape of the differential cross section depending on θ follows a typical $\cos^2\theta$ distribution and the scattering process is symmetric with respect to the scattering angle θ. Furthermore the scattered radiation is polarized even if the incident photon is unpolarized. The total scattering cross section is a constant:

$$\sigma_T = \frac{8\pi}{3}r_e = 6.652 \times 10^{-29}\,\mathrm{m^2} = 0.6652\,\mathrm{barn} \tag{3.13}$$

As soon as the energy of the photon is close to the electrons rest mass energy $m_e c^2$, the energy transfer from the photon to the electron cannot be neglected any more. Then relativistic and quantum electrodynamical effects, like interaction of the spin and magnetic moment of the electron with the photon become important. This case of inelastic scattering is called Compton scattering and

the different cross section follows the shape given by the Klein-Nishina formula (Klein & Nishina, 1929):

$$\frac{d\sigma_{\text{KN}}}{d\Omega} = \frac{3}{16\pi}\sigma_{\text{T}}\left(\frac{E'}{E}\right)^2\left(\frac{E}{E'} + \frac{E'}{E} - \sin^2\theta\right) \tag{3.14}$$

and the total cross section:

$$\sigma_{\text{KN}} = \frac{3}{8}\sigma_{\text{T}}\frac{1}{\epsilon}\left\{\left[1 - \frac{2(\epsilon+1)}{\epsilon^2}\right]\ln(2\epsilon+1) + \frac{1}{2} + \frac{4}{\epsilon} - \frac{1}{2(2\epsilon+1)^2}\right\} \tag{3.15}$$

with $\epsilon = E/m_{\text{e}}c^2$. In the limit of $E = E'$ the Klein-Nishina formula reduces to the Thomson formula. As a consequence of general relativity the emission characteristic now changes depending on photon energy. Instead of a dipole like emission characteristic as for Thomson scattering, photons with incident energies $E > 100\,\text{keV}$ are preferentially scatted in forward direction. This effect is called relativistic beaming. The deviation of the total Thomson cross section relative to the total scattering cross section calculated from the Klein-Nishina formula is $\approx 1\,\%$ for photons with an energy of $\approx 3\,\text{keV}$ and $\approx 5\,\%$ for a photon energy of 15 keV. The energy loss per scattering event is:

$$E' = \frac{E}{1 + \frac{E}{m_{\text{e}}c^2}(1 - \cos\theta)} \Rightarrow \Delta\lambda = \frac{h}{m_{\text{e}}c}(1 - \cos\theta) \tag{3.16}$$

The basic assumption for the derivation of the Klein-Nishina cross section is a stationary and free electron. For electrons bound to an atom, the situation is different. According to a semi-classical approach similar to the one used to derive the cross section for Thomson scattering, the total cross section for photon scattering from a bound electron is (e.g. Lang, 1999):

$$\sigma = \frac{8\pi}{3}r_{\text{e}}^2\frac{\nu^4}{(\nu^2 - \nu_0^2)^2 + (\gamma\nu)^2} \tag{3.17}$$

Here ν_0 is the resonant frequency of the bound electron, which is treated as semi-classic harmonic oscillator. For the limit $\nu \ll \nu_0$ Eq. (3.17) simplifies to $\sigma_{\text{R}} \approx \sigma_{\text{T}}\left(\frac{\nu}{\nu_0}\right)^4$. This is the characteristic ν^4 dependency of the total cross section of Rayleigh scattering (see, e.g. Lang, 1999). A quantum mechanical correct calculation has to include the interaction of the photon with all electrons of the atom. This is generally done by introducing an atomic scattering factor $f(\nu,\theta)$. For forward scattering ($\theta = 0$) and long wavelengths ($\lambda \gg a_0$, where a_0 is the Bohr radius), $f^0(\nu)$ gives the deviation of the total scattering cross section from the classical Thomson cross section. In general the scattering factor is the mathematical description for the deviation of the scattering electric field of a multi-electron atom relative to that of a single free electron. The cross sections for scattering of photons from a multi-electron atom are then given by (Attwood, 2002):

$$\frac{d\sigma_{\text{R}}(\nu)}{d\Omega} = r_{\text{e}}^2\,|f^0(\nu)|^2\sin^2\theta \qquad \sigma_{\text{R}}(\nu) = \sigma_{\text{T}}\,|f^0(\nu)|^2 \tag{3.18}$$

with:

$$f^0(\nu) = \sum_s\frac{g_s\nu^2}{\nu^2 - \nu_s^2 + i\gamma\nu} \tag{3.19}$$

where g_s is the oscillator strength normalized according to $\sum_s g_s = Z$. Similar to Thomson scattering the energy transfer from the photon to the atom can be neglected since $h\nu \ll m_A c^2$. Furthermore, the scattering process can be assumed as elastic as long as $\nu \neq \nu_0$. However, in X-ray

astronomy scattering from bound electrons plays no important role, since the typical recoil energy of a 10 keV photon is of the order of 200 eV. This energy is larger than the typical ionization energy of an electron of the outer shell of an atom. Thus bound electrons scattered from X-ray photons in first approximation can be treated in the same way as free electrons. This assumption fails for electrons of the inner shells of atoms with high Z.

3.4.1   Inverse Compton Scattering – Comptonization

In the scattering process described above a photon is scattered from a *stationary* electron or a electron with *negligible kinetic energy*. During each scattering the photon looses energy which is transfered to the electron. The energy change of the photon $\Delta E/E$ per scattering averaged over all scattering angles θ is approximatively given by:

$$\frac{\Delta E}{E} \approx -\frac{E}{m_e c^2} \tag{3.20}$$

In hot electron plasmas like in accretion disks or accretion disk coronae the assumption of stationary electrons fails, because of the thermal motion of the electron plasma becomes important. Assuming a thermal velocity distribution (Maxwellian) of the electrons and the non-relativistic limit $h\nu \ll m_e c^2$, the energy transfer per scattering calculates as:

$$\frac{\Delta E}{E} \approx \frac{4kT_e - E}{m_e c^2} \tag{3.21}$$

where T_e is the temperature of the electron plasma (Rybicki & Lightman, 1979). For incident photon energies $E < kT_e$ the energy transfer to the photon is positive and the photon gains energy during scattering. As a consequence electrons in the hot plasma can be cooled very effectively because photons leaving the corona after being up scattered carry away energy. This is the inverse process to Compton scattering and thus called *inverse Compton* scattering or *Comptonization*.

Under real physical conditions a photon propagates though the scattering plasma and is scattered more than once. On its path through the cloud it follows a random walk like track. For a pure scattering plasma with non-relativistic electron energies, the mean number of scatterings can be calculated from random walk theory and is approximatively given by $n \approx \max(\tau, \tau^2)$. For each scattering event the energy of the photon changes according to Eq. (3.21). Since ΔE itself depends on the energy of the photon, it is a non-trivial problem to calculate the spectral distribution of photons after multiple Compton scatterings analytically, especially when the energy transfer to the photon is high. However, for the simplified situation of non-relativistic electrons which have a thermal energy distribution, the Kompaneets equation gives the spectral distribution of Compton scattered photons depending on time (Rybicki & Lightman, 1979):

$$\frac{\partial n}{\partial t_c} = \left(\frac{kT_e}{m_e c^2}\right)\frac{1}{x^2}\frac{\partial}{\partial x}\left[x^4\left(n + n^2 + \frac{\partial n}{\partial x}\right)\right] \tag{3.22}$$

where $t_c = (n_e \sigma_{\mathrm{T}} c)\, t$ is the time measured in units of the mean time between two scatterings. To derive the Kompaneets equation Comptonization is treated as a diffusion process, which is a valid assumption for large optical depths. To study Comptonization depending on different incident spectral distributions, the solution of the Kompaneets equation is required. This is generally done using Monte Carlo methods, since analytical solutions are hard or impossible to find. The resulting spectral distribution of scatted photons strongly depends on the incident photon spectrum and the
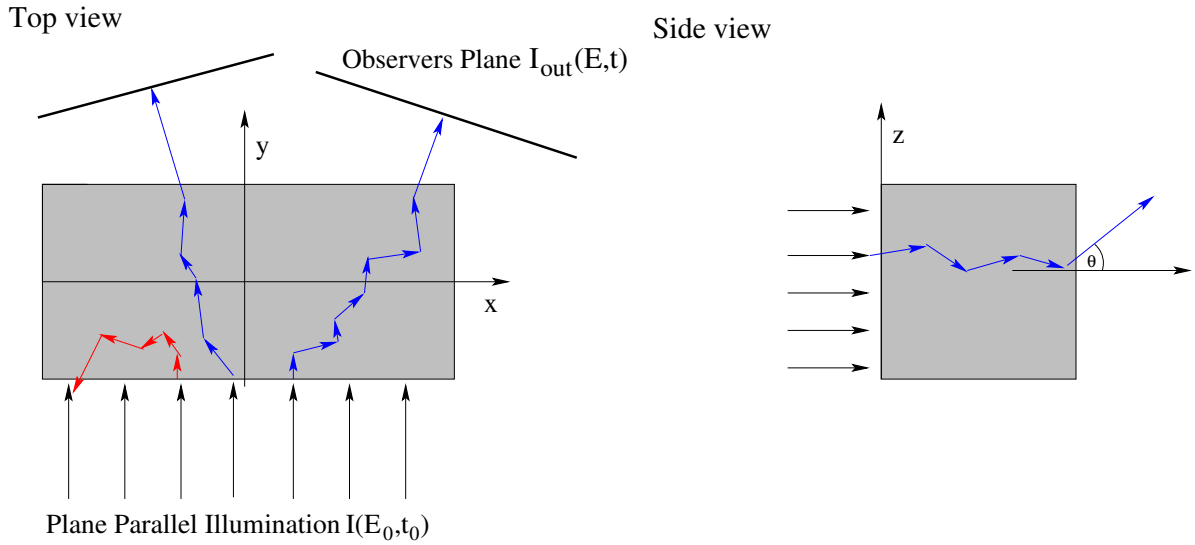
Figure 3.5: Schematic view of a slab geometry which is illuminated by a point source located at infinity. Note, in the left image the with of the slab in *x*-direction is infinite. The angle θ is the angle between the surface normal of the slab and the direction of the photon leaving the slab.

energy distribution of the electrons in the plasma. Extensive work on Comptonization spectra of accretion disk coronae of black hole candidates (e.g., for Cyg X-1) can be found in the PhD-Thesis of Wilms (1998) and references therein.

3.5   Temporal Consequences of Compton Scattering

Beneath the influence on the spectral distribution of the photons, Compton scattering affects the temporal distribution of the photons as well. When a photon with energy E_0 is emitted at time t_0, it will propagate and spread through the scattering cloud and finally leave the cloud at a time t. The time the photon needs to leave the cloud is called diffusion time $t_{\text{diff}} = t - t_0$ and depends on the path length the photon travels on its random walk track while crossing the cloud. If $l = d/\tau$ is the mean free path of the photon, then the mean diffusion time of the photon calculates as $\bar{t}_{\text{diff}} = nl/c \approx \tau d/c$, where n is the number of scatterings in an optically thin medium (Kylafis & Klimis, 1987). Therefore, it is obvious that photons which are scattered more frequently will stay longer in the cloud and lag photons which cross the medium directly. For photons crossing the medium without scattering, the diffusion time equals the light crossing time of the slab. In case the cloud is approximated by a plane-parallel slab geometry, the angle θ between the direction of the photon leaving the cloud and the surface normal is commonly referenced as $\mu = \cos\theta$ (cf. Fig. 3.5). If $I(E_0, t_0)$ is the intrinsic intensity of the source at a specific energy E_0, the intensity on observer located behind the Comptonization medium would observe can be calculated as:

$$I^{\infty}_{E_1,E_2}(\mu, t) = \int_{-\infty}^{t} G_{E_1,E_2}(\mu, E_0, t, t_0) I(E_0, t_0)\, dt_0 \tag{3.23}$$

where $G_{E_1,E_2}(\mu, E_0, t, t_0)$ is the Green's function. The Green's function gives the probability that a photon with an initial energy E_0 entering the cloud at time t_0, will leave the cloud under the angle μ after time t, with an energy between E_1 and E_2. First analytical approaches to determine the Green's function for Compton scattering are based on the fundamental work of Lightman et al.
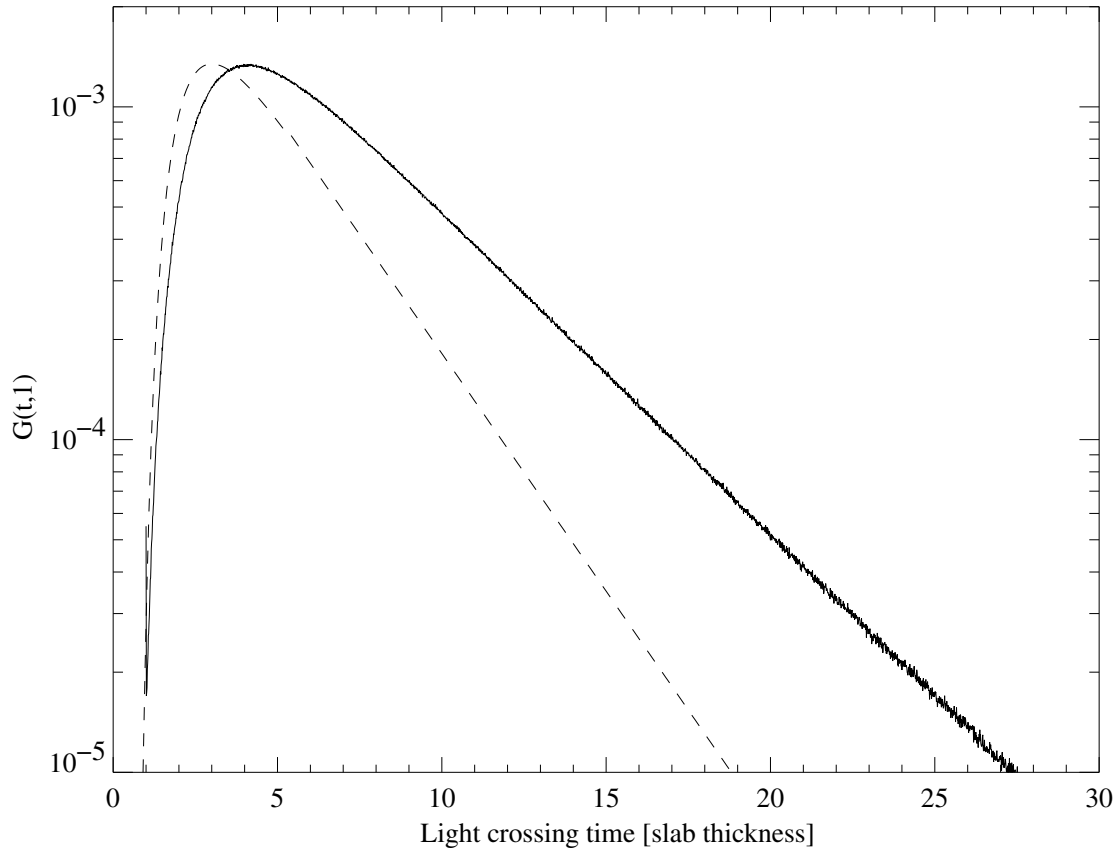
Figure 3.6: Comparison of the Green's function derived by Kylafis & Klimis (1987) (dashed line) and the Green's function calculated numerically by Monte Carlo simulation (solid line). For both the optical depth is set to $\tau = 10$. For a description of the Monte Carlo code and the simulations see chapter 8.

(1981). Their work is focused on spectral implications of Compton scattering by cold electrons and does not include the time dependency of the Green's function. They calculated $G(E, E_0)$ analytically for simple geometries, such as the diffusion of photons out of a spherical shell surrounding a central point source or a semi-finite slab geometry (see also Nowak et al., 1999b, for different applications). The first analytical work on time variable sources was done by Kylafis & Klimis (1987) and Brainerd & Lamb (1987). They assumed energy independent Thomson scattering and a point source located in the center of a spherical shell with a radius R, an uniform electron density, and temperature distribution. The resulting Green's function they found using the theory of Lightman et al. (1981) is:

$$G(t, t_0) = \begin{cases} \frac{\sqrt[3]{3}}{2\sqrt{\pi}} \frac{\Delta t}{(\tau a)^3} \sqrt{\frac{\Delta t}{\tau a}} \left(1 - \frac{2\Delta t}{3\tau a}\right) \exp(-\frac{3\tau a}{4\Delta t}), & \text{for } \Delta t/a < 0.5\tau; \\ \frac{2\pi^2}{3\tau a} \exp(-\frac{\pi^2 \Delta t}{3\tau a}), & \text{for } \Delta t/a > 0.5\tau; \end{cases} \tag{3.24}$$

where $a = R/c$. This Green's function is shown in Fig. 3.6 as dashed line for an optical depth of $\tau = 10$. For comparison a numerically calculated Green's function derived with the Monte Carlo code introduced later in section 8, gives a slightly broader distribution, implying that the photons spend more time in the cloud than predicted from the analytical solution. This is a consequence of uncertainties due to simplifications in the analytic theory. For an extensive discussion of this problem see Lightman et al. (1981) and Kylafis & Klimis (1987).
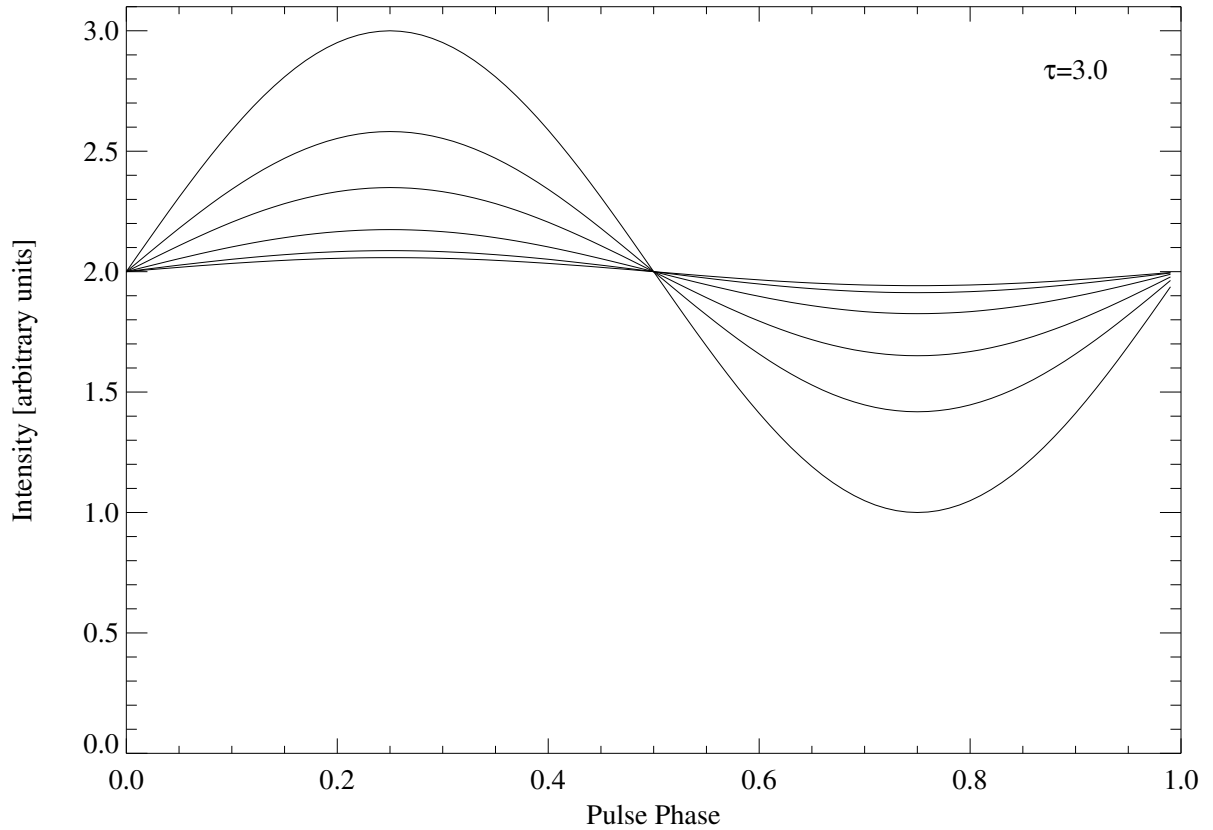
Figure 3.7: Sinusoidally modulated intensity modified by a scattering medium according to Eq. (3.26). The optical depth is set to $\tau = 3.0$. The radius of the sphere increases with decreasing pulsed amplitude. From top to bottom, the radius is: 0.3, 0.5, 1.0, 2.0, and 3.0 times the light crossing time of the sphere.

If the source in the center of the shell emits isotopically and its amplitude is sinusoidally modulated according to $I(t) = I_0(1 + a\cos(\omega t + \phi))$, the amplitude of modulation of the observed intensity will depend on the diffusion time of the photons and the geometric extension of the scattering medium. For small values of τ and thin geometries ($\omega\tau d/c \ll 1$), the observed intensity $I^\infty(t)$ using Eq. (3.23) and Eq. (3.24) calculates to:

$$I^\infty(t) = I_0 \left\{1 + a\cos[\omega(t - t_{\mathrm{diff}}) + \phi]\right\} \tag{3.25}$$

where ω is the initial modulation frequency of the source. Thus the observed intensity has the same time dependence as the original source (Kylafis & Klimis, 1987, Eq. 12) apart from an additional shift in modulation phase. The result is obvious when taking into account that the diffusion time of the photons is short compared to the period of the modulation and thus the photons can leave the slab before the source intensity changes. The result is different for the limit $\omega\tau d/c \gg 1$, which is the case, when the diffusion time is large compared to the modulation period of the source. Then the apparent intensity $I^\infty(t)$ is given by (Kylafis & Klimis, 1987):

$$I^\infty(t) = I_0 \left\{1 + a\frac{\pi^2}{3\omega\tau d/c}\sin[\omega(t - t_{\mathrm{diff}}) + \phi)]\right\} \tag{3.26}$$

As a consequence of the large diffusion time, the intensity profile of the source is "smeared out" and the amplitude of the modulation is reduced $\propto 1/(\tau d/c)$. As an example, the variation of modulated intensity according to Eq. (3.26) is shown in Fig. 3.7 for a fixed modulation frequency ω, an optical depth of $\tau = 3$, and a variable radius of the spherical shell. As can be seen from Fig. 3.7, the amount of pulsed amplitude decreases rapidly with increasing size of the sphere. In an analog way the intensity profile changes with increasing τ and constant radius of the sphere.

Astrophysical sources like accreting X-ray pulsars in general or the X-ray pulsar in Her X-1 are not expected to have an isotropic emission characteristic. They typically show *pencil* or narrow *fan beam* like emission as described in section 2.3.6 with complex modulation patterns, like e.g. multiple maxima and minima in intensity. For such sources the assumption of isotropic emission apparently breaks down.

However, for non-isotropic emission the effects of a scattering medium can be illustrated assuming an idealized rotating and point like source emitting a beam which has the shape of a δ-function. Assuming mere Thomson scattering, Brainerd & Lamb (1987) found that for such an emission characteristic, even for the limit $\omega \tau d/c \ll 1$, the amplitude of the oscillation reduces $\propto 1/(1+\tau)$ or even faster depending on the beam shape. This result is different from the results for an isotropic emitting source. The behavior can be understood from the shape of the differential scattering cross section of Thomson scattering, which has an isotropic angular distribution. Thus pointed emission is redistributed isotropically in all directions while passing a scattering medium. As a consequence the amplitude of the oscillation is reduced and the apparent pulse shape is broadened. Thereby the observable pulse shape strongly depends on the shape of the initial intensity profile. In general sharp and peaked emission profiles apparently have a *sinusoidal shape* after passing a scattering medium with an optical depth $\tau \gtrsim 2$. In other words, for a distant observer the apparent width of the beam increases due to scattering. Furthermore, for beamed emission compared to isotropic emission values of $\tau \gtrsim 5$ are sufficient to hide the oscillation *completely* from the observer. To summarize the analytical models presented so far, an optically thick scattering medium has two major effects on time variable and beamed emission:

- The amount of pulsed flux of a beamed, point like source is reduced, since the apparent width of the beam increases because of the isotropic angular distribution of Thomson scattering.

- For the case that the diffusion time t_{diff} of the photons is large compared to the period of the pulsation, the pulse signature is reduced because of loss of coherence between subsequent pulses.

3.5.1 Simulating Diffusion Time

For more complicated geometries and for different intrinsic spectral distributions, analytical methods are difficult to obtain and one has to resort to numerical solutions by using Monte Carlo simulations. Furthermore, for small optical depths the analytical results of Brainerd & Lamb (1987) and Kylafis & Klimis (1987) break down, since their analytical models are explicitly given for the limit of large optical depths. For a systematic study of the influence of a scattering medium on beamed emission I used a modified version of a linear Monte Carlo code developed at the IAAT to calculate $G_{E_1,E_2}(\mu, E_0, t, t_0)$. This code is based on the method of weights (Sobol, 1991, and references therein) and considers Compton scattering (using the Klein-Nishina cross section and relativistic scattering), photoelectric absorption from material of solar abundance using the cross sections of Verner et al. (1996), and fluorescent line emission (using the fluorescence yields of Mewe et al.,

1985, 1986; Kaastra & Mewe, 1993). The code was previously used to compute $G(t, t_0)$ for the case of a hot comptonizing plasma (Nowak et al., 1999a, 1998). A detailed introduction to the code and results for other applications can be found in, e.g., Wilms (1996), Dove et al. (1997), and Wilms (1998). To simplify matters for the simulations and the following discussion, I will concentrate on a scattering medium with uniform electron density and a semi-finite slab like geometry, similar to the geometry shown in Fig. 3.5. The extension of the slab in x-direction is infinite and the slab is illuminated by a point source located at infinity with an intensity $I(E_0, t_0)$, giving a plane-parallel illumination of the slab. To reduce the calculation time to a necessary minimum two cases were considered, a neutral and a fully ionized medium. Output of the simulation is the Green's function $G_{E_1, E_2}(\mu, E_0, t, t_0)$ as a function of N_H (the equivalent hydrogen column density in units of atoms/cm^2) or N_e, the thickness of the slab d, and the angle-dependent photon spectrum of photons leaving the slab. For a medium where only a fraction f is fully ionized, the total Green's function then is given by a superposition of the two single Green's functions according to:

$$G_{E_1, E_2}(\mu, E_0, t, t_0) = (1 - f) \, G_{\text{ion}}(t, t_0, E_1, E_2) + f \, G_n(t, t_0, E_1, E_2) \qquad (3.27)$$

For practical reasons, the diffusion time t_{diff} of the photons is normalized to the light crossing time of the slab, i.e., $t - t_0$ is measured in units of the light crossing time of the slab. Therefore, the Green's functions for different values of d can be obtained by simply rescaling the time. The spectral distribution of the incident photon spectrum follows a power-law distribution with exponential cut-off. This spectral shape is similar to the model spectrum used later in this work for the spectral analysis of the observed data presented in chapter 7. To achieve good counting statistics 10^7 photons for the neutral and the fully ionized case with $N_H, N_e \leq 3 \times 10^{25}$ cm^{-2} were propagated. For $N_H, N_e > 3 \times 10^{25}$ cm^{-2} the number of simulated photons had to be increased to 5×10^7 to reduce Poissonian noise. As an example, simulated Green's functions for different optical depth values corresponding to $N_e = 1.5 \times 10^{24}$ cm^{-2}, 3×10^{24} cm^{-2}, 7.5×10^{24} cm^{-2}, and 1.5×10^{25} cm^{-2} are shown in the top panel of Fig. 3.8 for the case of a fully ionized corona. The spectral distribution of the incident photons is shown by the small inlaid plot.

For small values of τ ($\tau < 5$) the Compton shot is dominated by photons crossing the slab in a direct way without being scattered from electrons. These photons are apparent from the peak at $t_{\text{diff}} = 1$. For $\tau > 1$ the number of scatterings per photon increases $\propto \tau^2$ and consequently the number of unscattered photons decreases rapidly, until for $\tau > 5$ the shot is dominated by photons scattered multiple times. Using Eq. (3.16) the energy loss per scattering event can be estimated for a 15 keV photon to $\Delta E \approx 0.44$ keV. This implies that, as soon as the mean number of scattering per photon increases above $\approx$ 15–20 ($\tau > 4$), photons of the energy range between 10–20 keV are redistributed to the energy band of 2–10 keV. This redistribution effect is the origin of the changing spectral shape with increasing optical depth visible in Fig. 3.8 (top panel). As a consequence the cut-off energy moves towards lower energies and a small bump at energies between 1–5 keV arises. For even larger $\tau > 10$ this bump slowly vanishes and the flux above 6 keV decreases rapidly. The overall spectral shape is then given by the left most spectrum shown in the top panel of Fig. 3.8. Considering a neutral medium, absorption plays the dominant role over the temporal effects of Compton scattering. For a neutral medium with an optical depth close to unity almost all flux below 10 keV is suppressed. At such optical depths the effects caused by diffusion time are negligible since the mean number of scatterings is close to unity. Thus, to achieve noticeable changes in beam shape a high fraction of ionized material is needed which is similar to a low value of f. On the other hand a high fraction of neutral material only weakly alters the beam shape but reduces the flux at low energies.
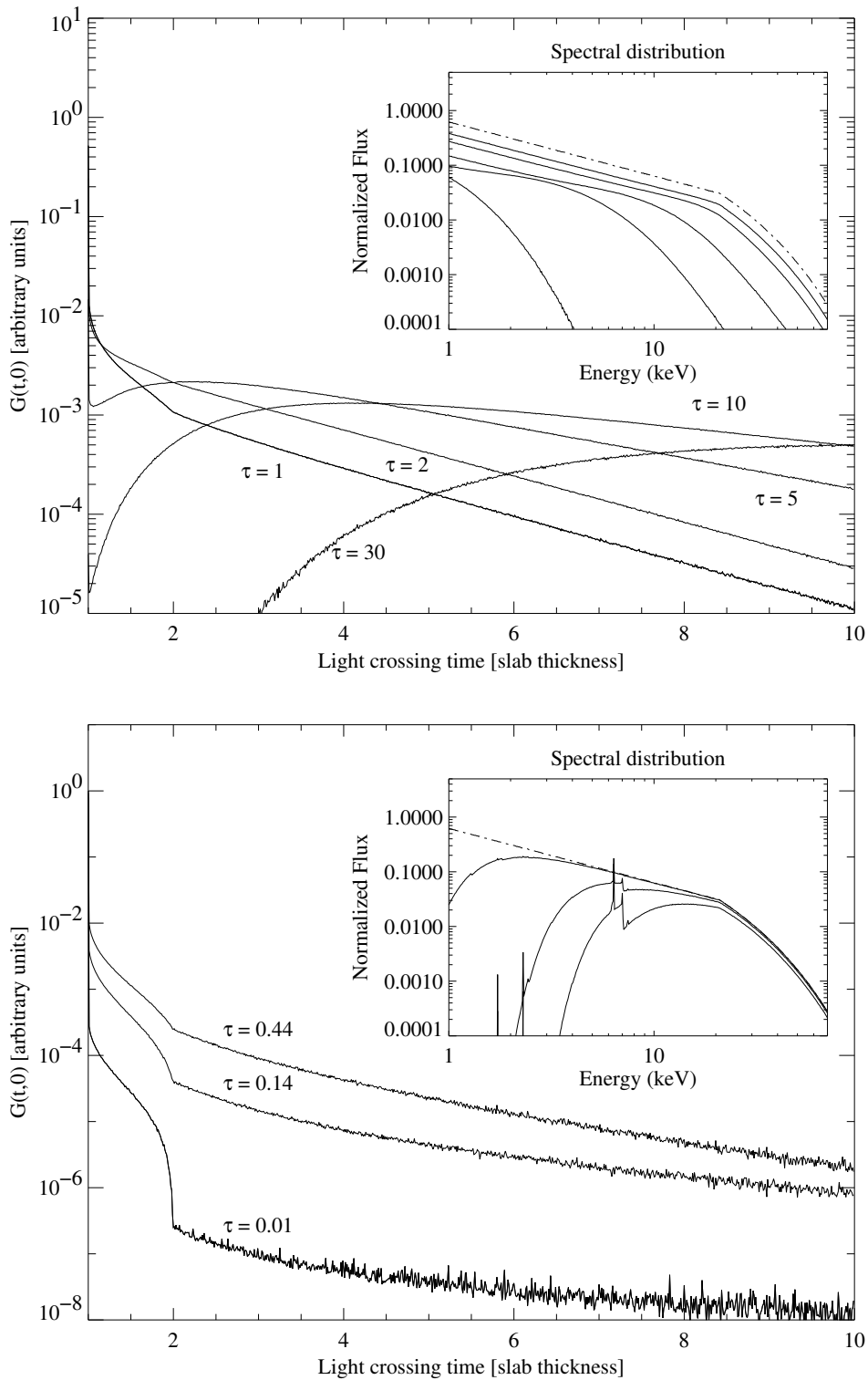
Figure 3.8: Compton shots for different values of τ and a fully ionized (top panel) and a neutral medium (bottom panel). In both cases the spectral distribution (inset plot) of the unscattered photons follows a power-law with exponential cut-off (dash dotted line). The spectra of scattered photons are shown as solid lines. The optical depth τ for the spectra increases from top to bottom. In the top panel the change in spectral shape due to down scattered photons is clearly visible with increasing τ. From the spectra in the lower panel fluorescent emission is apparent (e.g., the iron line at 6.4 keV or the nickel line at 7.5 keV).
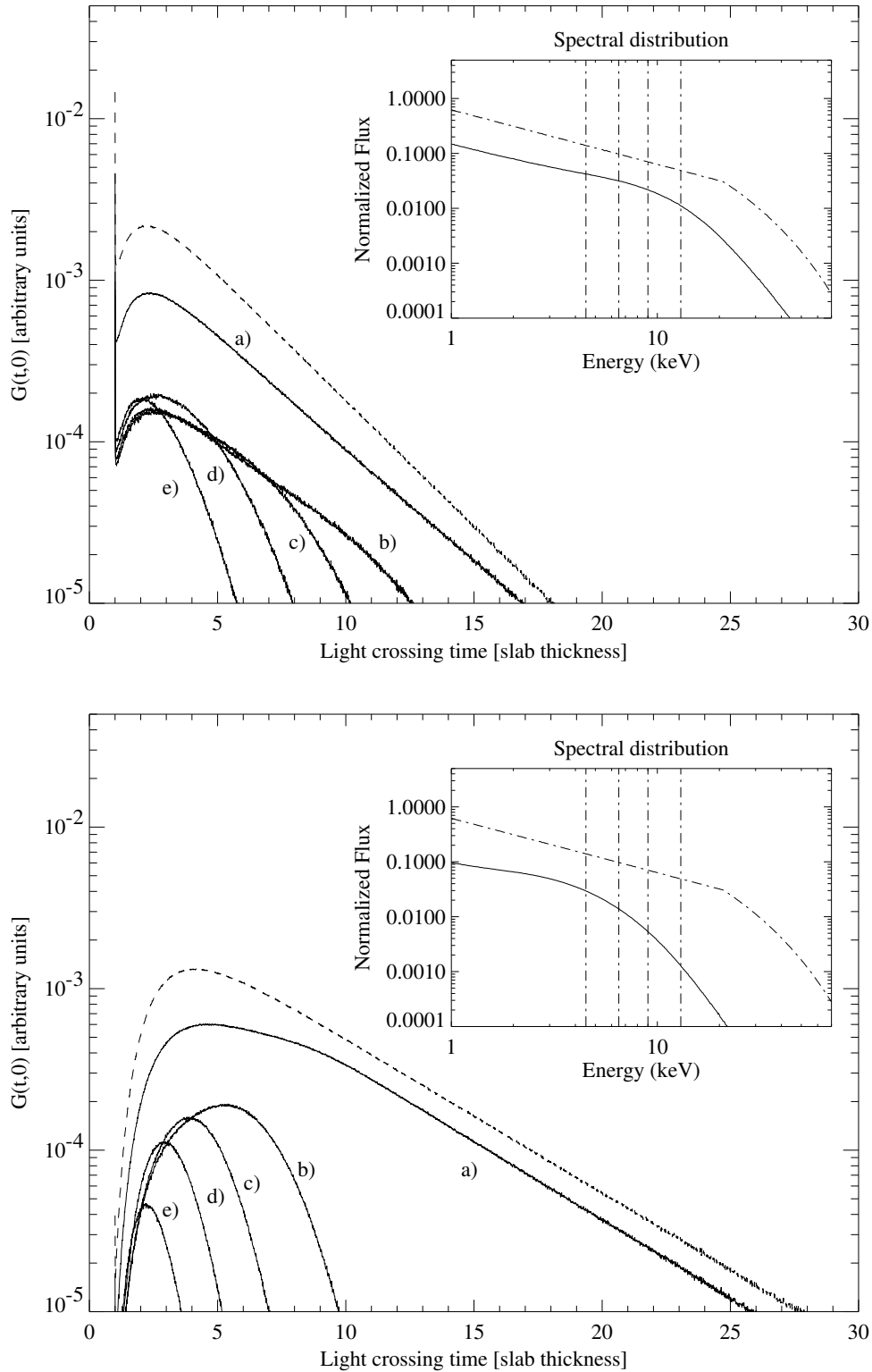
Figure 3.9: Energy dependence of $G_{\mathrm{ion}}(t, 0, E_1, E_2)$ for an optical depth of $\tau = 5$ (top panel) and $\tau = 10$ (bottom panel) assuming energy dependent Compton scattering. The labels mark shots for different energy bands: a) 0.5–4.5 keV, b) 4.5–6.5 keV, c) 6.5–9.0 keV, d) 9.0–13.0 keV, and e) 13.0–19.0 keV. The individual energy bands are marked in the inlaid spectra by vertical dash dotted lines. The integrated shot over all energy bands is drawn as dashed line.

3.5.2   Simulating Pulse Variation

If the Green's function $G_{E_1,E_2}(\mu, E_0, t, t_0)$ is known, the influence of a Comptonization medium on a modulated and beamed intensity distribution $I(t_0)$ such as the pulsed emission of an X-ray pulsar can be calculated from Eq. (3.23). To do so, $I(t_0)$ in Eq. (3.23) has to be substituted by the intensity depending on the pulse phase $I(p_0)$, the pulse profile respectively. Here $I(p_0)$ is the intrinsic pulse shape, depending on the pulsar rotational phase. Pulse variation can then be simulated depending on a variable thickness d of the slab, different optical depth values τ, and different ionization fractions f.

For a fully ionized medium with $\tau_e = 5.0$, the resulting modified pulse profiles are shown in Fig. 3.10. After subtracting the unpulsed flux the original and unmodified pulse profile is drawn in black. The thickness of the slab is indicated by the different colors of the smeared pulse profiles. For large optical depth values ($\tau > 3$), even a thin scattering layer ($d > 0.1$) is sufficient to completely hide pulsed emission from the observer. In addition, the pulse signature which has a detailed substructure is modified to an almost sinusoidal shape, even for small values of d. This makes it impossible to observe any detailed sub-structure of the pulse profile behind the scattering cloud, as e.g. the leading and trailing shoulder of the main pulse of the pulse profile of Her X-1 (cf. Fig. 6.4). For $\tau < 1.5$ the substructure of the pulse is still apparent, albeit not as distinct as in the unmodified pulse profile. Note, the shift in pulse phase of the maximum of the main pulse, which is clearly visible in the modified pulse profile for $\tau > 2.0$.
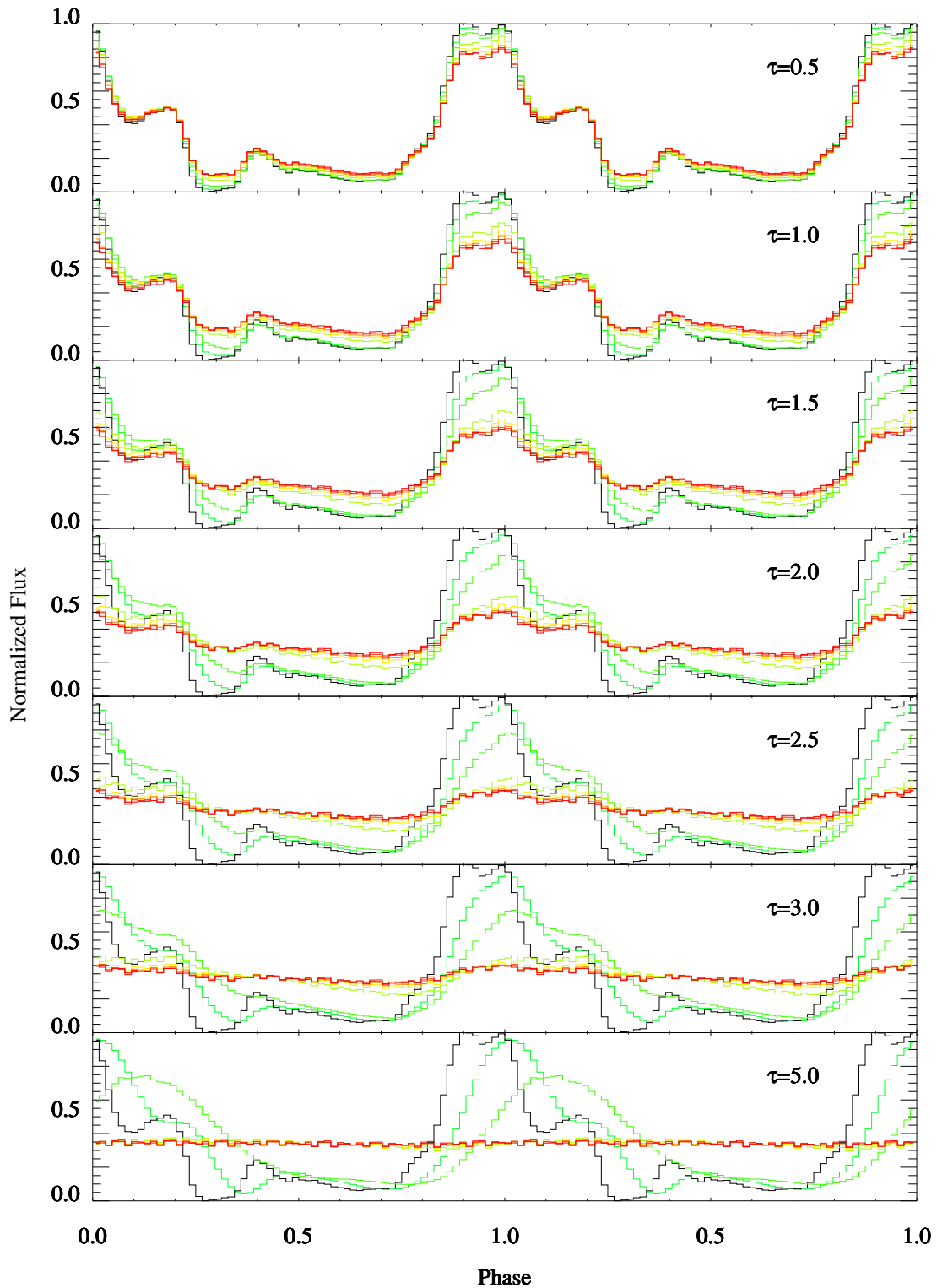
Figure 3.10: Her X-1 pulse profile of the turn-on observation modified by a fully ionized scattering medium. The pulse profile shown in black is the observed pulse profile of orbit 31 (cf. section 7.2.1). The optical depth varies from top to bottom from $\tau = 0.5$ to $\tau = 5.0$. In addition, for each optical depth value the thickness d of the scattering medium is set to 0.02, 0.05, 0.1, 0.2, 0.4, 0.6, 0.8, and 1.0 times (increasing thickness from green, to yellow, to red) the light crossing time of the slab.

Chapter 4

Data Analysis

The results presented in this thesis are based on data gained from observations with the Rossi X-ray Timing Explorer – *RXTE* (see chapter 5). The analysis of the observed X-ray spectra and light curve presented later in chapter 7 divides into two parts: a spectral and a temporal analysis. Section 4.1 gives a brief introduction to the analysis methods used for the spectral analysis of the data, while section 4.2 is focused on temporal analysis methods.

4.1   Spectral Analysis

The basic aim of a spectral analysis is to compare observed photon spectra of astrophysical objects to theoretical model spectra, with the intention to deduce physical parameters of the observed object from the data. The major problem in analyzing data of modern detectors is still their poor energy resolution (10–20 % FWHM), which makes an interpretation of the observed spectra difficult, in particular if the level of accuracy of the analysis has to be below 10 % systematic error to discriminate different theoretical models. To achieve this accuracy the response of the detector on a incident photon spectrum has to be known with high precision. Hence a good calibration of the detectors is essential, which generally is done on ground before launching the experiment, with the aid of known photon spectra such as, e.g., synchrotron spectra or line emission of X-ray tubes. The fundamental variable which characterizes the properties of a detector is the detector response function. Formally the response function gives the relation between the continuous incident photon spectrum $S(E)$ to the binned pulse height spectrum by the integral equation (Davis, 2001):

$$N_{\mathrm{pha}}(h) = \int_0^\infty R(h, E)\, S(E)\, dE \qquad (4.1)$$

where h is the pulse height channel of the detector, and $R(h, E)$ the detector response function. The response function itself is the product of the redistribution function and the effective area of the detector, which both depend on energy. The effective area characterizes the quantum efficiency, which is the probability that a photon with a specific energy can be detected. The redistribution function $R(h, E)$ gives the probability that a photon with a energy E ends up in a pulse height channel h. In general the response function is represented by a matrix (response matrix) instead of a continuous function and the integrals in Eq. (4.1) are replaced by sums. In X-ray detectors like proportional counters or scintillation detectors effects like, e.g., non-linearities of the gain (energy to pulse height conversion), the finite energy resolution, or effects of higher order like escape photons and the non-linearity of the light yield of scintillation counters lead to a response matrix with

non-diagonal elements. As an example the response matrix of the Proportional Counter Array of *RXTE* (*PCA*) is shown in Fig. 5.5. For the *PCA* the Xe-Kα escape peak is the main contribution which makes the response matrix non-diagonal. Generally such a response matrix can be inverted numerically but the calculation is numerically very unstable. Consequently Eq. (4.1) does not have a unique solution and the primary spectrum of the observed object can not be calculated directly from the observed pulse-height spectrum. This is the reason why spectral analysis in X-ray astronomy is based on a different approach. During the calibration of the detector the response matrix is determined with the best possible accuracy. Instead of computing the observed spectra with the inverted matrix of $R(h, E)$, the theoretical model spectra are folded with the detector response matrix and the resulting spectra are compared (fitted) to the observed spectra. This process is repeated, while varying the physical parameters of the model spectra, until the deviation between the model spectrum and the observed spectrum has a minimum. The physical parameter set of this model spectrum are called best-fit parameters. As estimate for the goodness of the fit the χ^2-statistics (Pearson-Statistics) is often used:

$$\chi^2 = \sum_{i=1}^{N} \frac{(c_{\mathrm{obs},i} - c_{\mathrm{mod},i})^2}{\sigma_i^2} \tag{4.2}$$

where $c_{\mathrm{obs},i} = N_i \cdot T_{\mathrm{life}}$ is the total amount of counts in energy bin i of the background corrected observed spectrum, with N_i being the count rate in bin i given in counts per second, and T_{life} the life time of the detector. $c_{\mathrm{mod},i}$ is the number of counts for each bin of the model spectrum, and σ_i^2 is the variance of the observed data in bin i. An essential condition for Eq. (4.2) to be valid is that $c_{\mathrm{obs},i}$ and $c_{\mathrm{mod},i}$ are both Poissonian distributed. Then the χ^2 distribution characterizes the dispersion of the observed spectrum to the model spectrum and σ_i can be estimated by $\sqrt{c_{\mathrm{obs},i}}$ (neglecting systematic errors). If the model spectrum is in ideal agreement with the observed spectrum the expected value for $\nu = N - n_{\mathrm{c}}$ degrees of freedom is $\chi^2 \approx \nu$, where n_{c} is the number of dependent parameters (parameters determined from the data, e.g. model parameters). It is convenient to use the *reduced chi-square* $\chi_\nu = \chi^2/\nu$ instead of χ^2, which has the expectation value of one (for a detailed introduction see, Lampton et al., 1976). Values of $\chi_\nu \gg 1$ imply a low probability that the model spectrum agrees with the observed data. On the other hand $\chi_\nu \ll 1$ is an indication that the uncertainties σ_i of the data are incorrect, e.g. by overestimating the systematic error budget. The goal of the fitting process is to find the set of parameters of the model spectrum which describe the observed spectrum best, which is equivalent to a minimum χ^2. Subsequently the statistical error for each parameter must be calculated for a given confidence interval. The confidence interval is generally set to 1σ which is equivalent to a 68.3 % probability (assuming Gaussian distribution) that the measured parameter value lies within the upper and lower limit given for the parameter. The probability can directly be deduced from the probability distribution function of the χ^2 distribution for each value of χ^2 (see Lampton et al., 1976; Bevington & Robinson, 1992). By varying the parameter of interest until $\Delta\chi^2$ reaches the limit of the confidence interval, the upper and lower limits for each parameter can be deduced.

For the analysis of the data off this thesis and the calculation of statistical uncertainties of the derived parameters the astronomical fitting package *XSPEC* was used (Arnaud & Dorman, 2002). All statistical uncertainties given are 1σ confidence levels with a $\Delta\chi^2 = 2.71$ for one parameter of interest.

4.2 Temporal Analysis

Besides the spectral information, a temporal analysis of the data can reveal additional important information on the observed object. As mentioned in section 2.1, the flux of accreting XRPs is periodically modulated and often shows aperiodic or quasi-periodic variability (QPO) in the X-ray or other wavelength bands (Belloni et al., 2002). The observed variability can give a direct link to physical parameters of, e.g., accretion processes close to the neutron star (which can be the origin of QPOs) (van der Klis, 1995) or the rotational period of a neutron star.

Generally a quantity c which depends on time is called a time series $c(t)$. In astronomical context, e.g., a light curve is a time series, which gives the observed count rate depending on time in units of counts per seconds. Common techniques to search for a periodic signal in light curves are based on the Discrete Fourier Transformation (DFT) or methods relying on counting statistics like folding the data modulo a trial period and grouping the data into discrete phase bins. Both techniques have advantages and disadvantages depending on the type of data they are applied to.

4.2.1 Fourier Techniques

For a light curve with equidistant samples (evenly sampled), i.e., $t_{i+1} - t_i = \Delta T = $ const., the Discrete Fourier Transformation (DFT) is given by:

$$f_j = \sum_{k=0}^{N-1} c_k \exp(2\pi i jk/N) \qquad (4.3)$$

where N is the number of samples. The corresponding periodogram is defined as:

$$P_j = A|f_j|^2 \qquad (4.4)$$

with A being the normalization factor of the periodogram. In literature various different normalizations exist e.g. the one proposed by Leahy (1987) has the advantage that the ensemble average power is 2 under the assumption that the noise of the light curve is Poissonian distributed. With this normalization $A = 2\Delta t^2/N_\gamma$, with N_γ being the total number of photons. An extensive introduction to this topic can be found in König (1997),Wilms (1998), Pottschmidt (2002), or Benlloch (2003). The frequency limit of a DFT is given by the sampling theorem and is called Nyquist frequency $\nu_N = 1/2\Delta t$. From the definition of the DFT in Eq. (4.3) it is obvious that Fourier methods are most sensitive on sinusoidally modulated signals, since for a distinct frequency ω, the periodogram show a narrow peak at P_j. The sensitivity for sharp and narrow peaks like those observed in X-ray astronomy is rather poor, because then the power in the periodogram is spread over a large range of frequencies. For observations distributed very non-uniform or data with gaps, there exist modifications of the classical DFT, e.g. the modified Lomb-Scargle periodogram (Scargle, 1982).

4.2.2 Epoch Folding

To search for non-harmonic oscillations in a light curve statistical methods are more suitable compared to Fourier methods (i.e., more sensitive) such as maximum entropy methods or analysis of variance (Schwarzenberg-Czerny, 1989). A very common technique used in X-ray astronomy is called "Epoch Folding". To use Epoch Folding to search for a signal modulated with a period P_0, one has to define a trial period interval $[P_{min}, P_{max}]$ divided into i period steps. Thereby, the

period P_0 is assumed to lie within the trial period interval $P_0 \in [P_{min}, P_{max}]$. For each trial period $P_i \in [P_{min}, P_{max}]$, the data is folded modulo P_i to a pulse profile with n pulse phase bins. If the trial period is not equal to the modulation period of the signal ($P_i \neq P_0$) or in the absence of any periodic signal the number of counts per phase bin is expected to be uniformly distributed (Poincaré-Theorem). Then the statistics

$$S = \sum_{j=0}^{n} \frac{(c_j - \langle c \rangle)^2}{\sigma_j^2} \tag{4.5}$$

takes the expectation value ≈ 1, where c_j is the count rate in counts per second in phase bin j, and $\langle c \rangle$ the mean count rate of the binned light curve with l time bins and a total integration time T:

$$\langle c \rangle = \sum_{m=0}^{l} \frac{c_m}{T} \tag{4.6}$$

For large count rates (Poisson limit) S is approximately χ_{n-1}^2 distributed with $\nu = n - 1$ degrees of freedom (Schwarzenberg-Czerny, 1989). In the presence of a periodic signal, the value of S takes its maximum value ($\chi_{max}^2 \gg \nu$) for $P_i = P_0$. The shape of the function $\chi^2(P_i)$ depends on the sampling of the data, on its length, and the pulse shape. For the simple case of an evenly sampled and continuous light curve (light curve with no gaps) which is sinusoidally modulated the shape of $\chi^2(P_i)$ can be calculated analytically to (Leahy, 1987):

$$S = S_{noise} + \frac{A^2 N_\gamma}{2} \frac{\sin^2(x)}{x^2} f(n) \tag{4.7}$$

where $f(n) = [1 - \pi^2/3n^2 + 2\pi^4/45n^4 - ...]$ and $x = T\pi\delta/P_i$. Here n is the number of bins in the folded light curve, A is the amplitude of the sinusoid, N_γ the total number of photons, T the total observation time, and $\delta = P_i/P_0 - 1$. Because of observational constraints, such as earth occultations in satellite based observations, data sets in most cases consist of short parts of typically several ksec length interrupted by irregular time gaps. For such light curve, the $\chi^2(P_i)$ distribution shows additional "beat" maxima symmetrically distributed around the main maximum of the track of $\chi^2(P_i)$ and deviates from a simple $\sin^2(x)/x^2$ like shape. The number and height of the beat maxima depends on the length of the gaps and the period of the signal (see Kunz, 1991).

One of the major drawbacks of Epoch Folding in contrast to Fourier methods is the lack of an analytical way to calculate significance levels or errors of the derived period for arbitrary pulse shapes. A very common approximation for σ_P is, to use the width of the central peak of the $\chi^2(P_i)$-distribution as an estimate of the uncertainty of the period:

$$\sigma_P = \frac{P_0^2}{T} \tag{4.8}$$

here T is the total observation time. Another relation is based on the assumption that a shift of one phase bin when folding the light curve to a pulse profile with k phase bins has an significant influence of the pulse shape. This assumption leads to the uncertainty estimate:

$$\sigma_P = \frac{P_0^2}{kT} \tag{4.9}$$

In most cases, Eq. (4.8) and Eq. (4.9) both overestimate the uncertainty since they only take into account the finite length of the observation time, but neglect effects due to counting statistics. For this reason a general way to estimate the uncertainties of the derived periods is desirable.

Leahy (1987) and Larsson (1996) suggested that the period uncertainty can be estimated by fitting analytic χ^2-functions to the $\chi(P_i)^2$ distribution derived from the data. Leahy (1987) used Eq. (4.7) to fit the χ^2 versus trial period distribution calculated from the data and found the following power-law relation for the error of the period (valid for 10 pulse phase bins):

$$\sigma_{\text{P}} = 0.71 \, (\chi_\nu^2 - 1)^{-0.63} \, \frac{P^2}{2T} \tag{4.10}$$

and for the uncertainty of the amplitude of the signal:

$$\sigma_{\text{A}} = 0.46 \, (\chi_\nu^2 - 1)^{-0.65} \, A \tag{4.11}$$

where χ_ν^2 is the reduced χ^2 value of the central peak of the $\chi^2(P_i)$ distribution. A major disadvantage of this method is that it is only applicable to sinusoidally shaped pulses.

Another approach, uses an analytical expression derived from power density spectra assuming a sinusoidally modulated signal to estimate the error of the period (Larsson, 1996). For the case of an evenly sampled light curve, σ_P is (Kovacs, 1981; Bloomfield, 1976):

$$\sigma_{\text{P}} = \frac{6\sigma_{\text{tot}}^2}{\pi^2 N A^2 T^2} \, P_0^4 \tag{4.12}$$

where N is the total number of bins in the light curve, A the amplitude of the sinusoid, T the total integration time, and σ_{tot} the standard deviation of the unfolded light curve. This equation can be generalized for arbitrary pulse shapes if the data is decomposed in its Fourier components:

$$\sigma_{\text{P}} = \frac{6\sigma_{\text{tot}}^2}{\pi^2 N T^2} \, \frac{P_0^4}{\sum_{k=1}^{m} k^2 A_k^2} \tag{4.13}$$

where A_k are the amplitudes of the Fourier series.

The remaining problem of this technique is that the Fourier amplitudes A_k have to be known for the observed light curve to be able to apply Eq. (4.13). These can be calculated in an iterative process from the data. In a first step an initial $\chi_0^2(P_i)$ distribution must be calculated from the data and the maximum of the distribution is used as a first period estimate P_{e} for the real period P_0. Subsequently, the observed data is folded to a pulse profile with P_{e}. To this pulse profile one has to apply a Fourier decomposition to derive the amplitudes A_k and the phase of each harmonic. The significance of each Fourier component is estimated (Priestley, 1981; Larsson, 1996, Eq. 8) and only those amplitudes above a pre-defined significance level are accepted for further analysis. This step is necessary to remove higher frequencies which do not contribute to the signal. Now, an analytic light curve with the same length and binning as the observed light curve can be calculated using the remaining A_k. From this analytic data a new $\chi_1^2(P_i)$ function can be deduced. Fitting $\chi_1^2(P_i)$ to the $\chi_0^2(P_i)$ values of the data gives a new period estimate P_{e}. This process is repeated until the pulse period stays constant, which is usually the case after 2–3 iterations. With the final set of Fourier amplitudes σ_{P} calculates from Eq. (4.13). This analysis procedure is applicable to data sets with gaps as long as the segments are evenly sampled and the length of the segments is of similar size. The errors deduced from Eq. (4.10) and Eq. (4.13) are generally smaller and better estimates of the real statistical error than the errors calculated from Eq. (4.8).

Generally, it is also possible to calculate the statistical error by mere Monte Carlo simulations which use the observed pulse profile to simulate light curves of the same length and with similar statistical fluctuations as the observed data. However, Monte Carlo and Epoch Folding methods compared to Fourier methods are much more time consuming with respect to CPU time, especially when comparing the first two methods with the Fast Fourier Transformation (FFT).

Chapter 5

The Rossi X-ray Timing Explorer

5.1 Introduction

The Rossi X-ray Timing Explorer (*RXTE*) was launched on 1995 December 30 from NASA's Kennedy Space Center with a Delta II rocket into a low-earth circular orbit with an altitude of 580 km. The orbit has an inclination of 23° and an orbital period of 90 min. With a gap of 15–30 min due to Earth occultation and South Atlantic Anomaly (SAA) passage the resulting time for observations is about 60–80 % of the orbital period. The instruments on *RXTE* cover an energy range from 2 to 250 keV and time scales ranging from microseconds to months. The primary mission goal of *RXTE* is "to study temporal and broad band spectral phenomena associated with stellar and galactic systems containing compact objects" (NASA, 1996).

On board of *RXTE* are two pointed instruments, the Proportional Counter array (*PCA*) and the High Energy X-ray Timing Experiment (*HEXTE*). While the *PCA* was developed at Goddard Space Flight

Figure 5.1: Schematic view of *RXTE* and its instrumentation, the five *PCA* modules, the two *HEXTE* clusters, and the *ASM* (Rothschild et al., 1998, Fig. 1).

Center (GSFC), *HEXTE* was built at the University of California, San Diego (UCSD). The third instrument is a wide field detector performing a scan of the sky about every 90 min, the All-Sky Monitor (*ASM*). The *ASM* is a contribution of the Massachusetts Institute of Technology (MIT). In the following sections I give a brief overview on the individual instruments and their technical characteristics, which are of importance for the further data analysis. Most of the content of this chapter is based on the "Appendix F: The XTE Technical Appendix" available at `http://rxte.gsfc.nasa.gov/docs/xte/appendix_f.html`. A detailed documentation of the *PCA* with respect to energy calibration and energy response can be found in Jahoda (1997) or Jahoda et al. (1997). An introduction to *HEXTE* is given in Rothschild et al. (1998) and to the *ASM* by Doty (1994) or Levine et al. (1996).
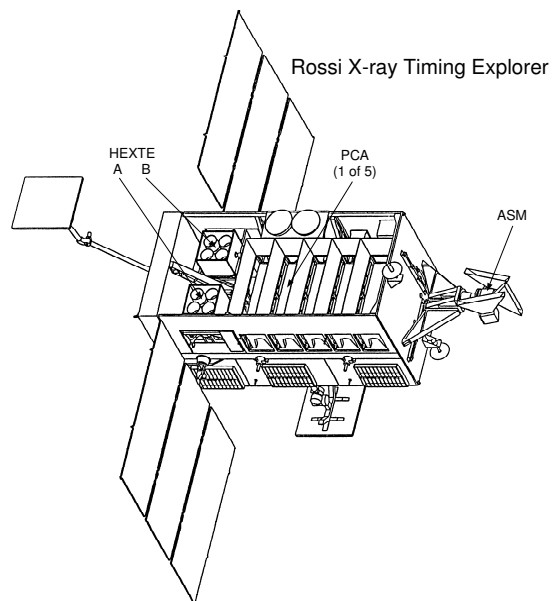
Table 5.1: *RXTE* instruments and their technical parameters (taken from Jahoda et al., 1997; Gruber et al., 1996; Blanco et al., 1997).

PCA

Detector	Xenon/Methane Proportional Counters
Energy range	2–60 keV
Energy resolution	18% at 6 keV
Effective area	3000 cm^2 at 6 keV
	6000 cm^2 at 10 keV
Sensitivity	0.1 mCrab
Temporal resolution	1 μs
Field of View	1° FWHM

HEXTE

Detector	NaI(Tl)/CsI(Na) Phoswich Scintillator Detectors
Energy range	15–250 keV
Energy resolution	18 % at 60 keV
Effective area	1200 cm^2 at 50 keV
	1100 cm^2 at 100 keV
Temporal resolution	10 μs
Field of View	1° FWHM
Source background dwell cycle	16 to 128 s
Gain variation	0.3 %

ASM

Detector	Position Sensitive Xenon Proportional Counter
Energy range	2–12 keV
Collecting area	3×30 cm^2
Sensitivity	0.1 mCrab
Temporal resolution	80 % of the sky, every 90 min
Field of View	$6° \times 90°$
Spatial resolution	$3' \times 15'$

5.2   The Proportional Counter Array – *PCA*

The *PCA* on board of *RXTE* consist of 5 identical, xenon/methane multi-anode Proportional Counter Units (*PCUs*), whereas each PCU can be operated independently. Table 5.1 gives a review of the technical specifications of the *PCA*, *HEXTE*, and *ASM* instruments. The design of the *PCA* (shown in Fig. 5.2) is similar to one of the *A-2 High Energy Detectors* (HED) flown on the *High Energy Astronomy Observatory* (HEAO-1) mission launched in 1977 (Jahoda et al., 1997; Jahoda, 1997).

5.2.1 Detector Principle

The detector of the *PCA* is based on the principle that X-ray photons interact with the detector gas by photo or Auger effect generating free electrons. These free electrons are accelerated in an electric field towards a detection anode. Due to the high electric field (≈ 1000 V), an avalanche process is induced. During this process, further secondary electrons are generated by collisional ionization, until the electron cloud reaches the detector anode. By the avalanche process the primary charge is amplified by several orders of magnitude (up to 10^6), until it is detected at the anode. For a certain range of electric field strength, the signal measured at the anode is directly proportional to the energy of the incident photon, therefore such a detector is called proportional counter. Generally inert gases such as argon, or xenon are used as detector gases.

In addition to secondary electrons, excitations of the gas atoms are created by collisional ionization during the electron multiplication process. The remaining excited detector gas atoms do not contribute to the electron avalanche process any more, but can emit photons instead. These photons additionally ionize the detector gas by photoelectric interactions, leading to a loss of proportionality between the primary energy of the incident photon and the signal measured at the anode of the proportional counter (Knoll, 2000). In a proportional counter this effect degrades the energy resolution and furthermore events induced by secondary photons can cause the gas discharge to spread along the anode causing dead time effects and reducing spatial resolution of position sensitive proportional counters. Methane molecules can suppress this process and act as so called *quench gas* by absorbing secondary photons without further ionization (Knoll, 2000). Therefore in the xenon chamber of the *PCA* a mixture of 90 % xenon and 10 % methane under a pressure of originally 1067 mbar is used as fill gas, instead of pure xenon.

A major disadvantage of using larger molecules like methane is their tendency of polymerization on the detector anode surface. As a result of such polymerization the *PCA* has shown occasional "breakdowns", characterized by an increased count rate on some detector layers in 1996 March (Jahoda et al., 1997). To prevent the detector from further degradation, the detector high voltage was reduced decreasing the gain of the detector by 35 %, as well. During the operational time of the *PCA* several more gain adjustments took place, resulting in different gain epochs. The start and end time of each epoch is given in Tab. 5.2. The observer has to take these gain epochs into account by generating specific response matrices for each observation and respective gain epoch during which the observation took place. For all data used for this work, Epoch 3 is the relevant

Table 5.2: Gain epochs for the *RXTE PCA* which are important for background correction. Note, only for the Faint background model Epoch 3 is divided into two parts Epoch 3a and Epoch 3b. This information is available on the *RXTE* home-page via `http://lheawww.gsfc.nasa.gov/users/craigm/pca-bkg/bkg-users.html`

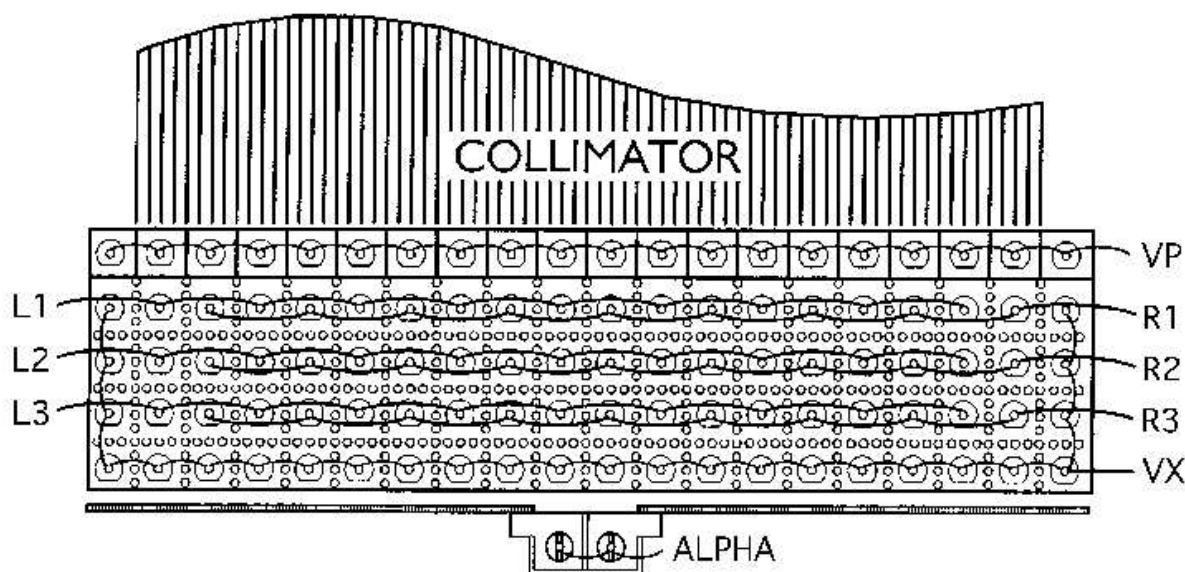| Epoch	Start Time	End time
Epoch 1	Launch	21 March 1996
Epoch 2	21 March 1996	15 Apr 1996
Epoch 3a	15 Apr 1996	09 Feb 1998
Epoch 3b	09 Feb 1998	22 Mar 1999
Epoch 4	22 Mar 1999	13 May 2000
Epoch 5	13 May 2000	present

Figure 5.2: Cross section through the *PCA* showing the collimator, the top most propane volume (VP), and the xenon chamber with three X-ray detecting layers L1-L3/R1-R3. The fourth xenon layer, the veto layer, is marked in this picture as VX. An alpha particle detector, housing the ^{241}Am calibration source, is mounted below the xenon chamber. The propane volume is closed to the front by a mylar entrance window. A second window separates the xenon and propane volume. For any further explanation see text (NASA, 1997).

gain epoch (see section 7.1).

5.2.2 Design of the *PCA*

The hexagonal beryllium copper collimator modules in front of each PCU provides a field of view (FOV) of 1° FWHM. Since each PCU is slightly offset relative to the others, the differing field of view (FOV) has to be taken into account in the detector response matrix as an additional collimator response (see section 5.2.6). Each PCU consists of two parts, a propane volume and the main xenon chamber. The propane volume mainly is used as electron veto shield to reduce background, while the xenon chamber is the main detection volume for source photons. The entrance window in front of each PCU is built of an aluminized mylar foil. An additional window separates the propane volume from the xenon chamber. Both windows restrict the low energy range of the *PCA* to photon energies > 2 keV.

The front most propane chamber (see Fig. 5.2) serves as an electron veto region and as an anti-coincidence shield, together with the the fourth anode layer in the xenon chamber and the outermost anodes of the xenon chamber. The anti-coincidence rates measured give an estimate of the detector internal background flux. Additional shielding is provided by the Beryllium/Copper plate on the rear side of each PCU. For calibration purposes an Americium-241 (^{241}Am) source is mounted on this plate below the xenon chamber. ^{241}Am is energetically unstable against spontaneous alpha particle emission with an energy of 5.49 MeV and 5.44 MeV. Simultaneously to the alpha particles, X-rays with an energy of 59.6 keV are emitted. The alpha particles are detected in a particle counter surrounding the ^{241}Am source. In a coincidence measurement with the X-rays detected in the xenon volume, the calibration events can be separated from X-rays originating in

astrophysical sources. The resulting calibration spectrum is continously used to monitor the offset and gain calibration which is needed for the channel-to-energy conversion during the data analysis. Because the efficiency of the coincidence measurement is about 80 %, a small amount of ^{241}Am induced X-rays contribute to the internal detector background and has to be taken into account in the background model of the *PCA* (see section 5.2.6).

Only the upper three of the four xenon layers of the *PCA* are used for X-ray photon detection. The first layer called top-layer is the most sensitive and thus will yield the best signal to noise ratio. Especially for faint sources with soft spectra it is of advantage to analyze the top-layer data separately during the data extraction process and the subsequent spectral analysis. For such sources the detection probability for photons is highest in the top-layer and consequently the other two layers do not contribute much to the overall detected count rate.

5.2.3   Timing

To study temporal behavior of X-ray sources the time of arrival of each detected photon has to be measured. The relative time of arrival for a photon event is tagged by the *Experiment Data System* (*EDS*) with an accuracy of $1\,\mu$s. This high accuracy is possible due to the stability of the on-board hardware clock, which is better than $10\,\mu$s over several hours (NASA, 1996).

The absolute photon arrival time of a photon is of importance when comparing data of *RXTE* with other satellite or ground based instruments (e.g., data from optical observatories). To determine the absolute detection time of a photon, signal travel times in the detector hardware and light travel time from satellite to Earth have to be taken into account. Auxiliary periodic effects due to Doppler effect caused by the orbital motion of the satellite, movement of the Earth on its orbit around the sun, and the rotation of the Earth itself have to be corrected as well. This cannot be done on board by the *EDS*, but later during the data extraction process with software tools like `fxbary` or `faxbary` (see section 7.1.1). Therefore the position and velocity of the satellite have to be known at any time during an observation. This information is available in "orbit" files, to be used as input for `fxbary` or `faxbary`.

The absolute timing capability of *RXTE* is validated in orbit to an accuracy of 1 ms, based on simultaneous X-ray and radio observations of young millisecond pulsars, such as PSR B1509–58 (Rots et al., 1998). Taking into account all necessary corrections, the photon arrival times can be measured to an absolute time within $8\,\mu$s accuracy for *PCA*, as well as for *HEXTE*. To maintain this high accuracy over a long time, the Mission Operation Center (MOC) performs several calibration observations of the spacecraft clock per day.

5.2.4   Experiment Data System – *EDS*

The Experiment Data System (*EDS*), built at the Massachusetts Institute of Technology, is responsible for a first pre-analysis and on-board processing of the *PCA* raw data. In addition it controls the pointing of the *ASM* and processing of the data at the same time (see section 5.4). Due to the large effective area of the instruments, the event rate can easily overcome the telemetry capabilites of the satellite. Therefore, prior to transmission, the large amount of *PCA* data has to be reduced, to match the average telemetry constraints of 40 kbps. For short intervals of about 30 minutes telemetry can be buffered by spacecraft memory, to prevent loss of data up to telemetry rates of ≈ 300 kbps (Jahoda et al., 1997).

The *EDS* offers 6 different data modes for the *PCA* which are operated by 6 independent event analyzers. Two additional event analyzers are responsible for the *ASM* data handling. All event

Table 5.3: Observational modes of the *PCA* used during the data analysis for this work.

Mode	Time Resolution [s]	# Energy Channels
Standard-2	16	129
E_250us_128M_0_1s	2.5×10^{-4}	128
B_16ms_16B_0_49_H	1.6×10^{-2}	49 channels binned to 16

analyzers operate in parallel and handle the data of all PCUs. Thus the final observational data contains the data of the same PCU processed by the *EDS* in different data modes. Each event analyzer offers seven basic data processing modes where two of the event analyzers always operate in the Standard-1 and Standard-2 mode. For this work data in Standard-2 mode, B_16ms_16B_0_49_H binned mode, and E_250us_128M_0_1s event mode data was used. The energy and time resolutions for these observation modes are shown in Tab. 5.3.

5.2.5   Detector Background

Generally the background signal of a detector in orbit consists of two components, the diffuse sky background and the internal detector background. The sky background is assumed to originate in very distant X-ray sources that cannot be spatially resolved (e.g. faint AGN) and contribute with constant flux to the overall background (Hasinger et al., 2000; Gilli et al., 2001). This background component is independent of the pointing direction or the position of the satellite. The source of internal detector background are particles and radiation interacting with the detector or the spacecraft itself. Since the particle and radiation density changes with the position of the spacecraft on its orbit, the internal detector background component depends on position and orientation of the satellite. Especially during South Atlantic Anomaly (SAA) passages this component increases dramatically.

In the case of the *PCA* the internal background component is modeled under the assumption that it changes on time scales < 16 s. In detail the model consists of three sub components which are combined to the overall internal background models (combined models), these are: a particle model, an activation model, and a cosmic X-ray background model. The particle model is based on direct background measurements on board, e.g. the count rate measured in the anti coincidence shield. The background flux is recorded in housekeeping data and shows a variation of a factor of 2.5 over a one satellite orbit NASA (1996). This background contribution mainly originates in the solar wind or particles captured by Earth's magnetic field in the SAA. The activation model considers secondary radiation from materials activated by particles or primary radiation. This activation model has a radioactive decay timescale of $t_{1/2} = 240$ min (Markwardt et al., 2002). The third contribution to the background model, the cosmic X-ray background, is approximated as a Bremsstrahlung spectrum. These sub components are included in the combined background models available for the observer, which are:

- The Faint combined model, including an activation model with $t_{1/2} = 240$ min, long term background variations, and a particle background model. This model is applicable for count rates < 40 cts s^{-1} PCU^{-1}.

- The SkyVLE combined model, based on direct background measurements of blank sky regions and two activation models with $t_{1/2} = 240$ min and $t_{1/2} = 24$ min. This model is applicable for count rates > 40 cts s^{-1} PCU^{-1}.
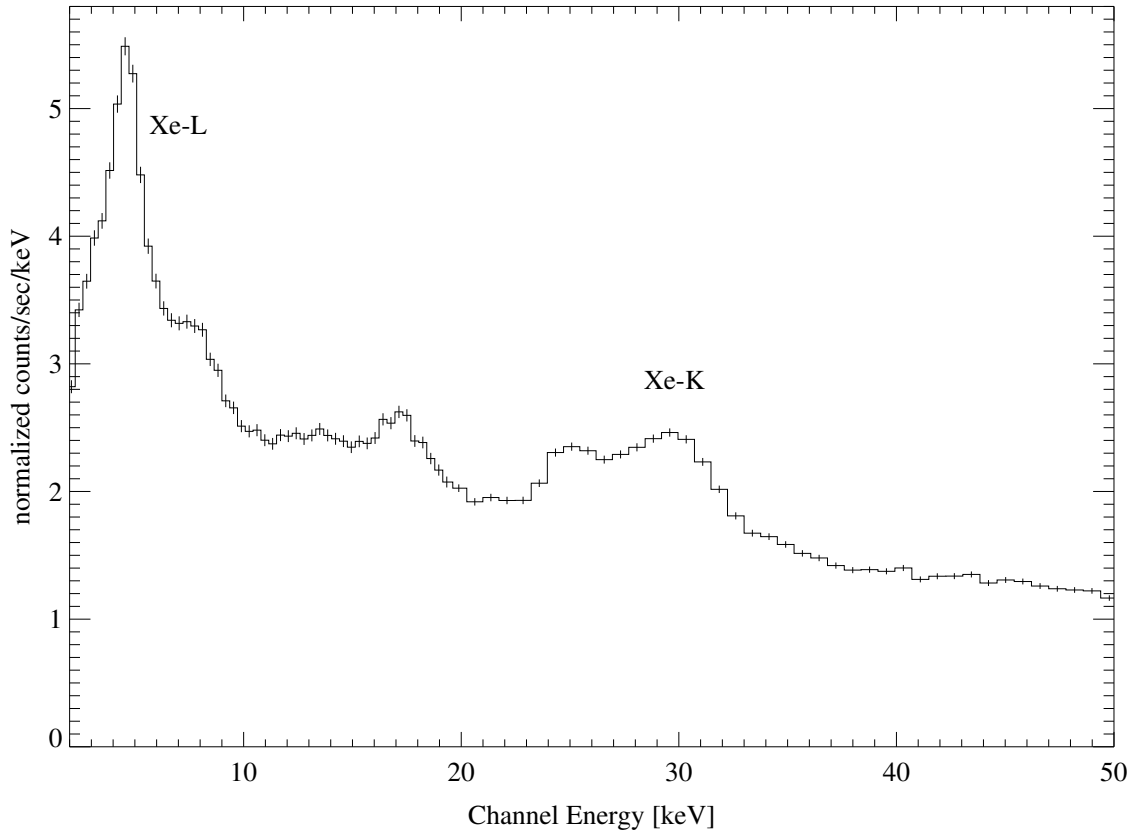
Figure 5.3: Background spectrum of the *PCA* in Standard-2 mode for the energy range 0–50 keV. This background spectrum was generated using the SkyVLE background model for orbit 30. The main contribution to the background is due to particle interaction with the spacecraft.

As an alternative method to estimate the total background, the observer can use periods during which the satellite moves to and from the target (slews), or times of Earth occultations. During these periods, the source object is not in the field of view or covered by the Earth. Thus the measured flux originates in the area surrounding the source, which is a good estimate for diffuse sky background as long there is no nearby source in the FOV. In contrast to the background model this method can only give estimates of background flux for the time before or close to an observation, whereas the background model can be used to get background estimates for any time of the observation. This is important for correcting the background in light curve, which cannot be done using slew observations or times of Earth occultations only. Therefore, especially for long observations, using the *PCA* background model is the better choice. A typical background spectrum generated for the observation in orbit 30, using the SkyVLE background model is shown in Fig. 5.3.

5.2.6   Energy Response and Effective Area

For the analysis and interpretation of X-ray spectra, the knowledge of the energy response of a detector on an incident spectrum is indispensable, since most of the systematic errors originate in uncertainties of the detector calibration and hence the response matrix. Generally the response matrix is determined on ground during calibration phase by comparing known X-ray line or continuum spectra with the response of the detector. In orbit calibration is verified and improved with
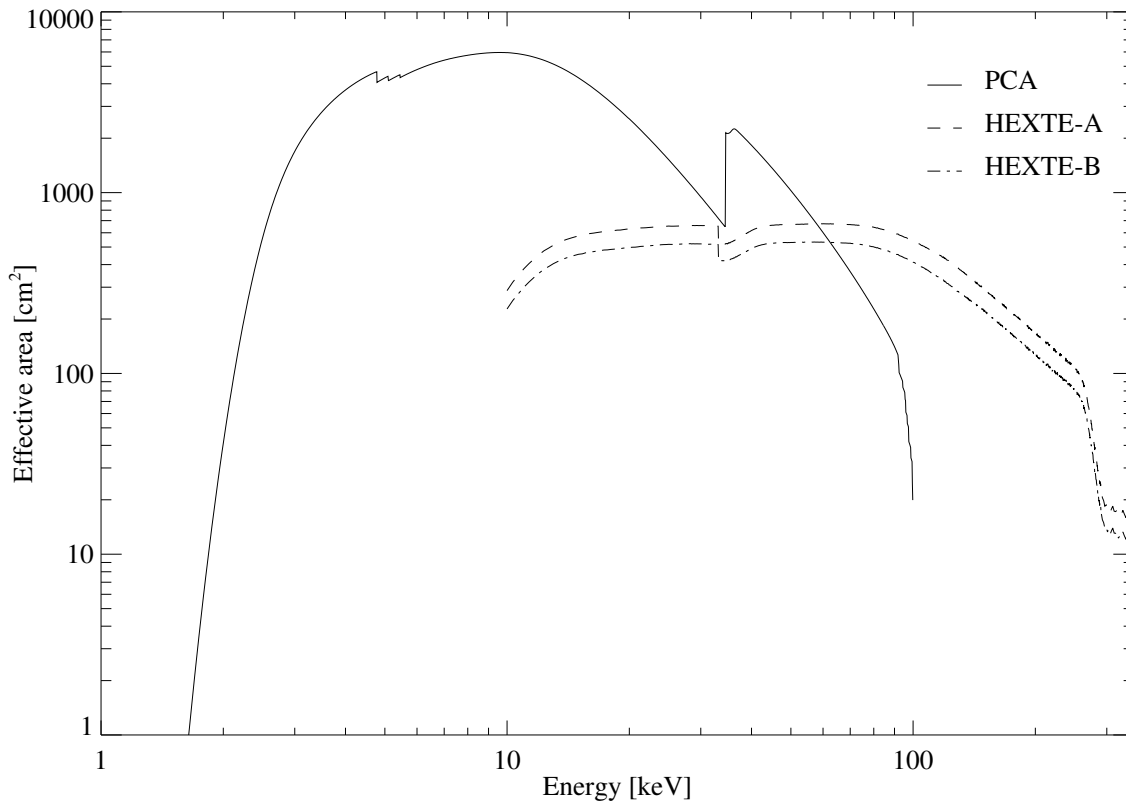
Figure 5.4: The effective area of the two pointed instruments of *RXTE*, the *PCA* and *HEXTE*. For *HEXTE* the effective area of each cluster is shown separately, whereas for the *PCA* the overall effective area of PCU 0–4 is shown.

so called standard sources like the Crab pulsar or supernova remnants, which have well known continuum or line spectra. Most difficulties for the calibration arise close to absorption edges of detector materials like the xenon gas in proportional counters, where the photoelectric absorption cross section shows sudden increases (Wilms, 1998). As a consequence, the systematic uncertainties of the detector response matrix are largest around absorption edges.

As a further parameter, the gain of the detector, i.e. the channel to energy conversion factor, contributes to the response matrix. Since during the last years the detector high voltage was changed several times (see section 5.2.1), the gain was consequently changed, too. In addition, polymerization effects on the detector anode lead to long term variations of the gain. To take these effects into account, time dependent response matrices for different gain epochs exist (see Tab. 5.2). Furthermore the response of the *PCA* depends slightly on the pointing direction of the satellite, because of the influence of the collimator. The collimator shows an offset between different PCUs giving a slightly different FOV for each PCU. Therefore for each observation a response matrix has to be generated. This can be done by using the software tool `pcarmf` which is included in the HEASOFT 5.1 software package.

In Fig. 5.4 the total effective area of all PCUs of the *PCA* and the effective area of the *HEXTE* clusters A and B are shown. The useful energy range for *PCA* lies within 2–50 keV. For $E < 2$ keV absorption effects in the mylar entrance window of the *PCA* and around the Xe-K (34.6 keV) and Xe-L absorption edges ($\approx$ 5 keV) jumps in the photoelectric absorption cross section reduce the
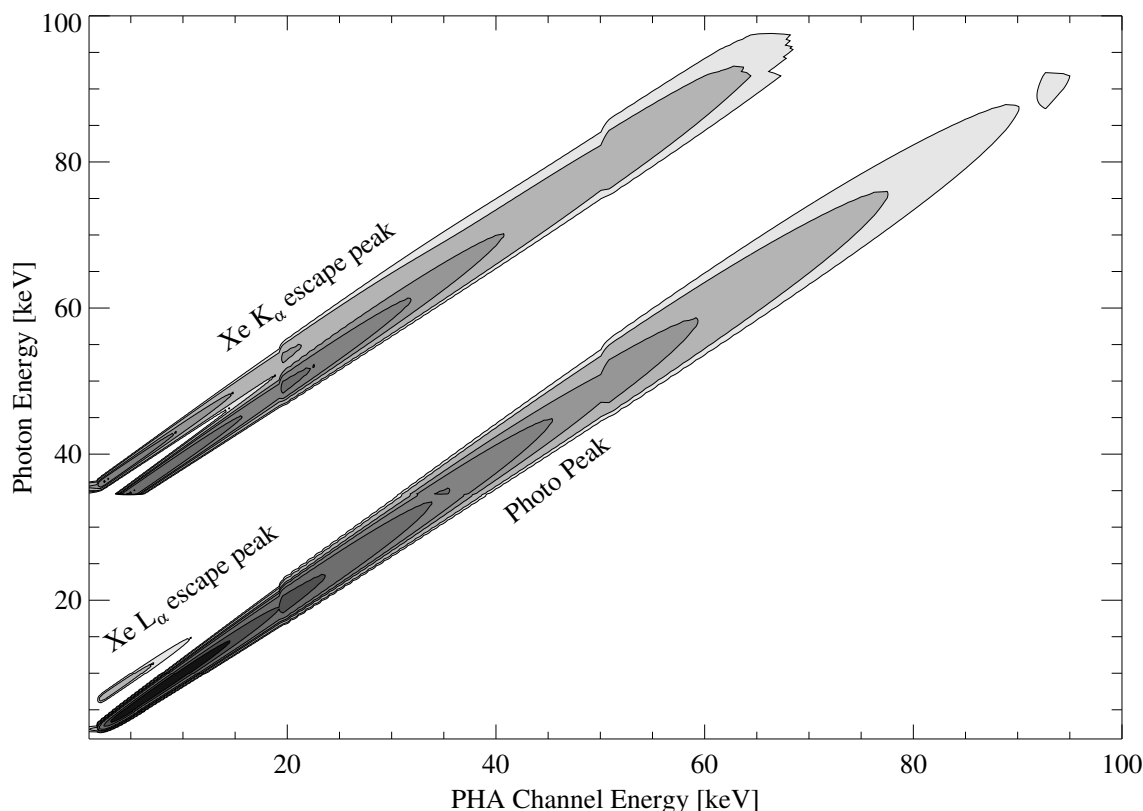
Figure 5.5: Contour plot of the response matrix of the *PCA* for PCU 0–4. Note that the grey scale is non-linear. Diagonal as well as the non-diagonal contributions due to Xe-Kα (29.5 keV) and Xe-Lα (4.1 keV) escape photons, are clearly visible.

total effective area. Between 10 and 90 keV the effective area mirrors the absorption cross section for photoelectric absorption.

In general, the energy response of a proportional counter is linear over a large energy range, which is clearly visible in Fig. 5.5 as a diagonal line. This linear distribution is caused by $\approx$ 86 % of the photons interacting with the xenon detector gas by K-shell absorption and is called photo peak. The remaining 14 % are preferentially absorbed in the L- and M- shell of xenon. The width of the photo peak directly gives the energy resolution of the detector. Nevertheless there is an additional small contribution to the response function by photons of Xe-Kα and Xe-Lα fluorescent emission which are emitted after a K shell absorption. Some of these photons can leave the detector volume when the absorption process took place close to a border of the detector volume. Consequently the apparent measured energy of the incident photon is reduced by the energy of these photons and appear as second peak called escape peak close to the photo peak at $\approx$ 5 keV and $\approx$ 40 keV. According to this response function, an incident photon with an energy of 40 keV contributes with a certain probability to the measured spectrum at 40 keV and at $\approx$ 10 keV. This effect will be of importance later in section 8 for simulating pulse profiles.

5.3 The High Energy X-ray Timing Experiment – *HEXTE*

The *HEXTE* detector consists of two independent clusters of 4 NaI(TL)/CsI(Na) phoswich scintillator/photomultiplier detectors, each covering an energy range from 15–250 keV (see Tab. 5.1). The two clusters are named cluster A and B. The thallium doted NaI scintillator crystals are used as the primary detection volumes, while the CsI crystals are used as light guide in between the photomultipliers and the NaI crystal (Gruber et al., 1996; Blanco et al., 1997).

5.3.1 Detector Principle

The *HEXTE* detector is based on the scintillation effect in solid state crystals like NaI and CsI. During a scintillation process a incident X-ray photon or charged particle generates a number of electron hole pairs by exciting electrons from the valence to the conduction band of a NaI or CsI crystals. In a pure crystal the efficiency of emitting photons by a de-excitation process of electrons from the conduction band back to the valence band is very poor. To improve the efficiency, the scintillation crystal is doted with impurities like Tl. The Tl atoms modify the energy band structure of the scintillation crystal and acts as "activator" (Knoll, 2000). As a result additional allowed energy states exists in the doted crystal within the forbidden band, which energetically lies between the valence and conduction band of a pure NaI or CsI crystal. In such a doted crystal a positive hole, generated by an incident X-ray photon or charged particle, can drift to an activator cell (Tl) and ionize it. The free electrons in the valence band can now neutralize the thallium ions leaving them in an excited configuration. The de-excitation of the thallium occurs by emission of an optical scintillation photon in the range of 350–500 nm. The population and depopulation process of the luminescent states in the scintillator material takes a finite time, called decay time. This decay time depends on the detector material and has a characteristic value of $0.2\,\mu$s for NaI(Tl) and $0.46\,\mu$s for CsI(Na) (Knoll, 2000). The resulting light yield of the scintillation process is directly proportional to the energy of the incident photon, except for energies < 30 keV where a weak non-proportionality for NaI exists (see Knoll, 2000).

Between the NaI(Tl) crystal and the photomultiplier tube a CsI(Na) crystal is mounted which is used for background rejection and additionally acts as light guide, see Fig. 5.7. The photomultiplier converts the scintillation light into charge which can be measured by the detector electronics. Since not only photons originating in an astronomical source cause events but also charged particles, a sophisticated scheme of background rejection is needed. Therefore, the four detectors of each cluster are surrounded by plastic scintillators. They are used together with the CsI crystal as an active anti-coincidence shielding. All charged particles initiating events in the CsI and the plastic anti-coincidence shield are recognized as background events and thus can be rejected by the detector electronics. This also includes events initiated in the NaI and CsI, as well as events detected in the CsI, only. Events which occurred in the NaI only can be distinguished from events recognized in the CsI or both crystals by rise-time discrimination. The rise time of the signal measured by the photomultiplier is different for NaI and CsI because of the differing decay times for both materials. Such a detector scheme is know as phoswich detector.

In front of each of the phoswich detector modules a hexagonal collimator is mounted, build of a mixture of 95 % lead and 5 % antimony. It is collimating the infalling source light with respect to the NaI crystal and reduces the stray light. In addition it is used as the housing for the gain control detector which continously monitors the gain of the detector by the aid of an [241]Am source in an analog way as for the *PCA*.
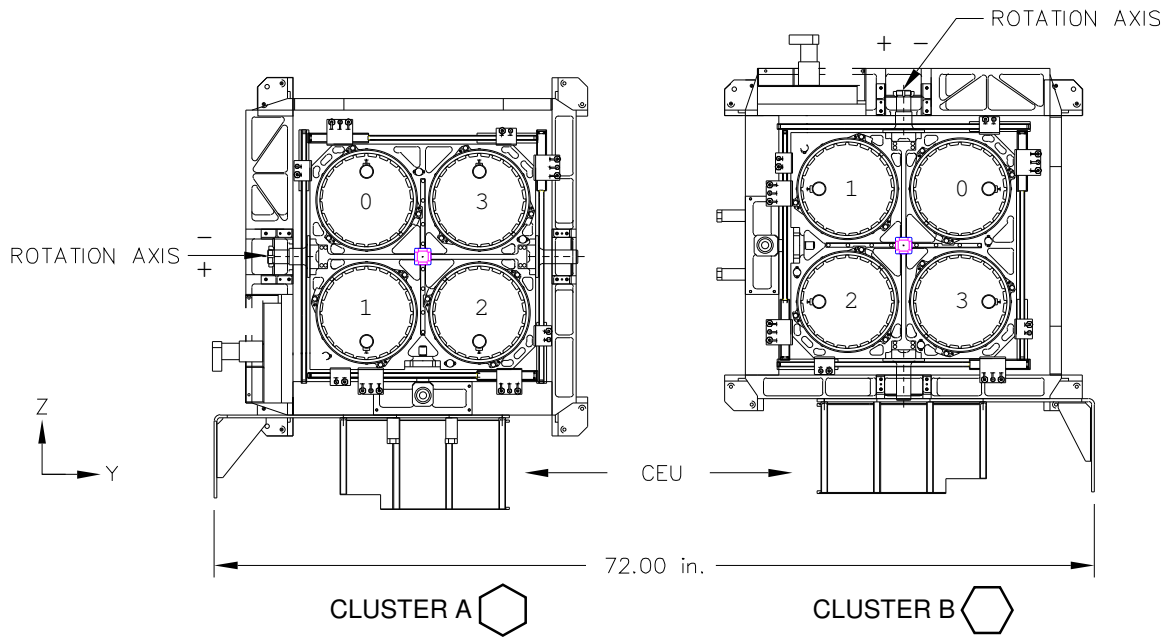
Figure 5.6: Top view of the two *HEXTE* clusters A and B. Each cluster contains 4 phoswich detectors of the type shown in Fig. 5.7. The rotation axis of the two clusters are perpendicular to each other (Blanco et al., 1997).
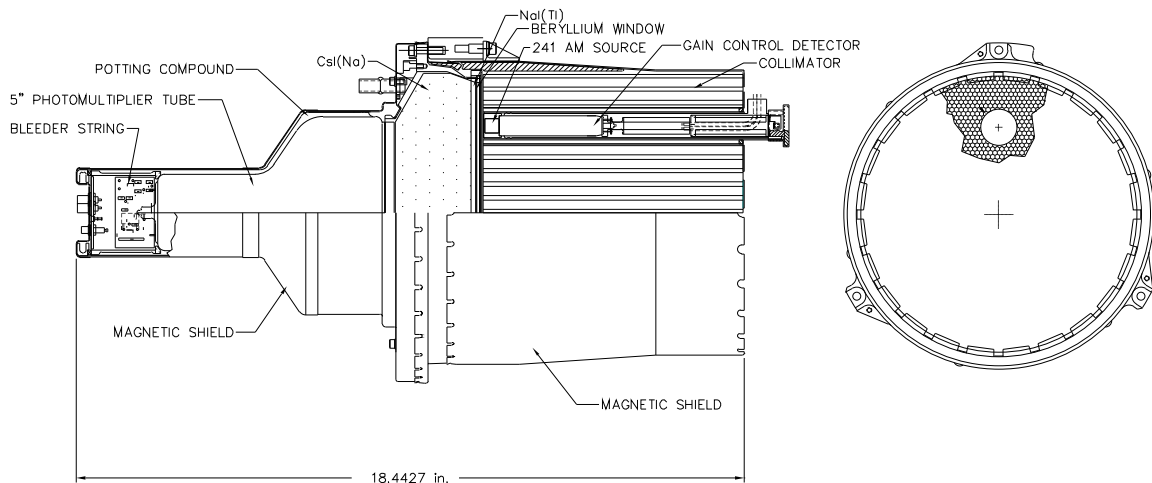

Figure 5.7: Schematic view of a single *HEXTE* phoswich detector module. Left image: Side view of a detector module. From right to left, the collimator, the beryllium window, the CsI light guiding crystal, and the photomultiplier tube is shown. The whole device is surrounded by a magnetic shield, protecting the detector against external magnetic fields. Right image: Front view of the collimator module, showing the housing of the ^{241}Am calibration source and of the gain control detector (Blanco et al., 1997).
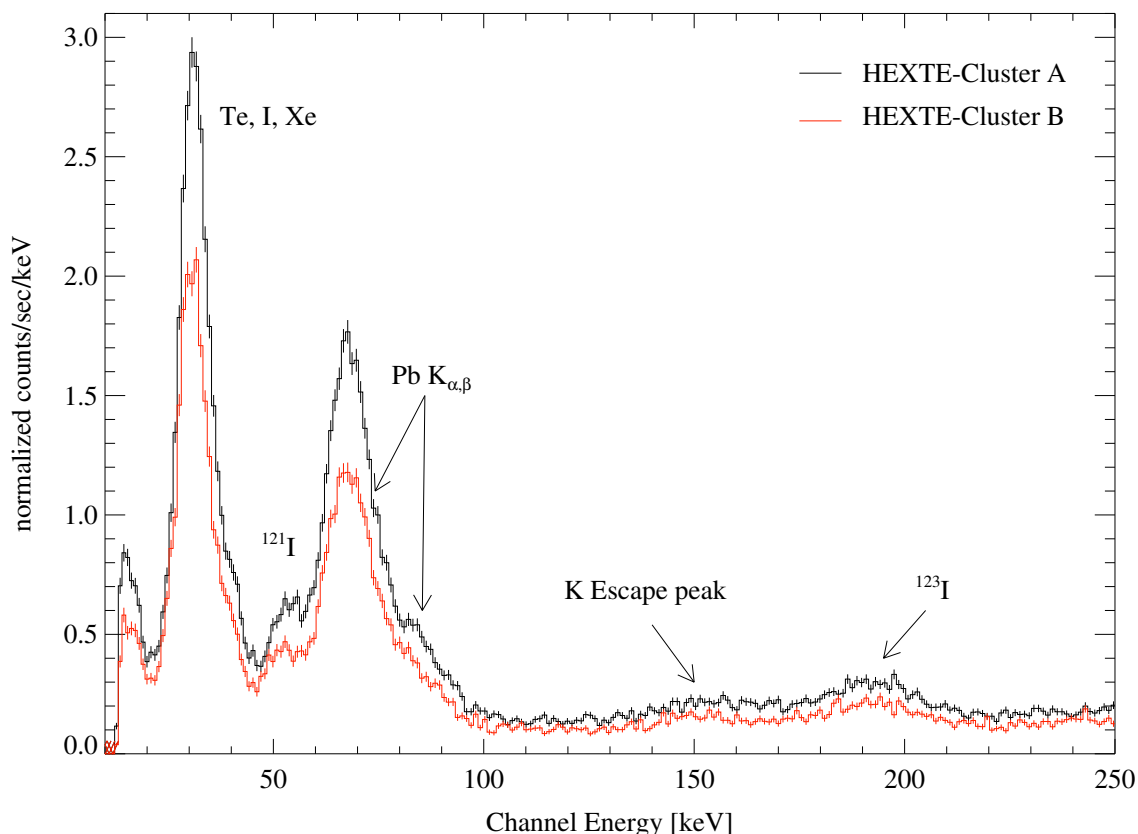
Figure 5.8: Background spectrum of both clusters *HEXTE* A and B. The effective integration time was ≈ 0.8 ksec for each cluster. The observed line features can be identified with: line emission from Te, I and Xe at 30 keV, line emission of ^{123}I at 190 keV, ^{123}I at 455 keV, and iodine lines at 30 keV; $K_{\alpha,\beta}$ fluorescent emission of the lead collimator at 74.2 keV and 85.4 keV; K escape lines from ^{123}I emission at 190 keV (R. Rothschild, priv. comm.).

5.3.2 Detector Background

Contrary to the *PCA* the diffuse sky background is measured directly during *HEXTE* observations. During an observation each cluster periodically moves from "off-source" to "on-source" position, this process is called rocking. Thereby the two clusters are moved orthogonal to each other, two times per rocking cycle to off-source and on-source position, thus providing 4 background measurements with a duration of 32 s per full rocking cycle. These measurements can be used later during the data analysis for correcting the diffuse sky background.

Furthermore the particle background is monitored using the count rate detected in the active anti-coincidence shielding and the flux measured with an additional particle detector. This particle detector monitors the ambient particle flux of each cluster which is of importance mainly during SAA passages. With the signal of of both, the particle detector and the anti-coincidence shield, the power of the photomultiplier tubes is controlled, as otherwise the anodes of the photomultipliers can be damaged by too high anode currents during times of high particle flux. Using the active plastic anti-coincidence shielding surrounding the detectors and additional rise-time discrimination, the internal detector background of *HEXTE* is reduced to a level $< 100 \, \text{cts} \, \text{s}^{-1}$.

Fig. 5.8 shows a background spectrum for both *HEXTE* clusters A and B for the turn-on ob-
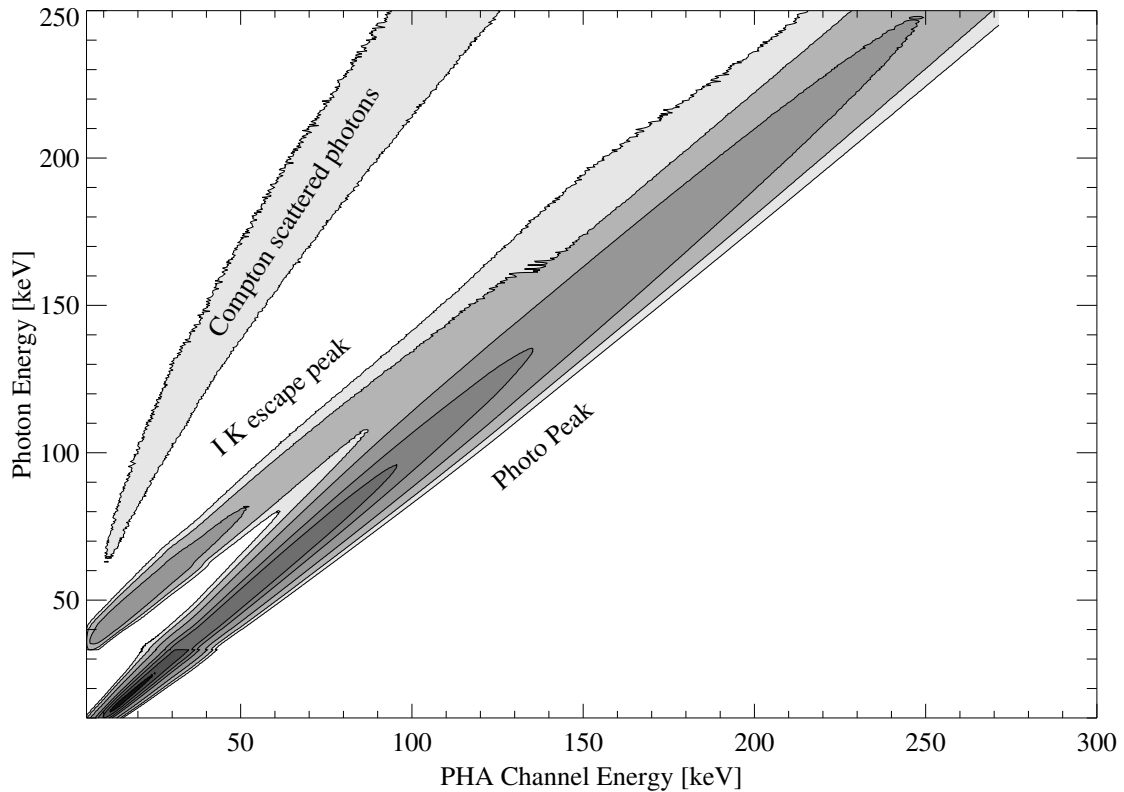
Figure 5.9: Contour plot of the response matrix of *HEXTE* cluster A showing the photon energy to detector channel energy conversion. The response function is dominated by the diagonal photo peak and additional terms due to escape photons and Compton scattered photons. Note that the grey scale is non-linear.

servation of orbit 30 (see Fig. 7.1), which has an effective integration time of 0.8 ksec. The most prominent contribution to the overall background are the line emission due to activation of detector material, like the lead collimator, and the contribution by spallation products.

5.3.3   Energy Response and Effective Area

The effective area of the *HEXTE* clusters A and B shown in Fig. 5.4 is characterized by the efficiency of the scintillation process, absorption in the detector window, and partial energy loss due to in the NaI scintillation crystal Compton scattered events which are detected in the CsI crystal anti-coincidence shield and rejected. An image of the response function for *HEXTE* is shown in Fig. 5.9. It displays the almost linear relationship between incident photon energy and detector channel energy. The broadening of the diagonal photo-peak towards higher energies leads to a decreasing energy resolution. The slightly offset second band is due to NaI K-escape photons which reduce the apparent energy by 33 keV. Further non-diagonal contributions arise in partial energy loss events caused by Compton scattered photons or in the CsI back scattered photons. An additional and important point for spectral analysis is the fact that the absolute flux measured by *HEXTE* differs from the flux measured by *PCA* by $\approx 10\,\%$. This has to be taken into account by a normalization factor during spectral fitting. A more detailed overview on the calibration status of *HEXTE* can be found in Rothschild et al. (1998).
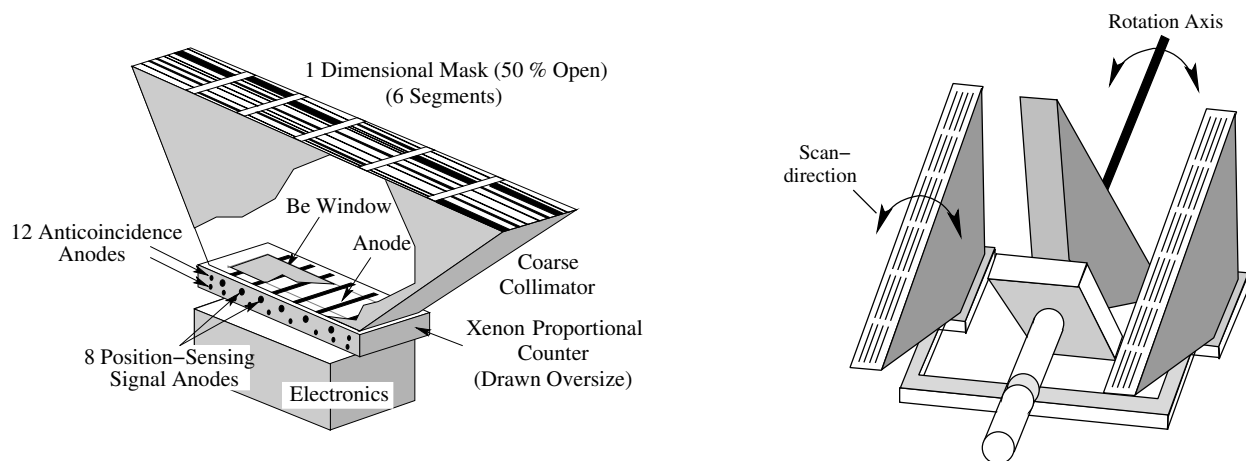
Figure 5.10: Cross section of the All Sky Monitor. Left: A single *ASM* module with a shadow mask, the position sensitive xenon proportional counter with beryllium entrance window, and the electronic devices needed for signal processing. Right: The assembly of the three *ASM* cameras on the satellite structure. The three modules can be operated and rotated independently (Levine et al., 1996).

5.4 The All Sky Monitor – *ASM*

The All-Sky Monitor (*ASM*) is a contribution by the Massachusetts Institute of Technology (MIT), and consists of three identical Scanning Shadow Cameras (SSC). Each camera covers an energy range from 2 up to 10 keV and has an active area of $\approx 30\,\mathrm{cm}^2$. The filed of view of the *ASM* covers $6° \times 90°$ of the sky with a spatial resolution of $3' \times 15'$ (Doty, 1994; Levine et al., 1996). The major scientific objectives of the *ASM* can be summarized as follows:

- Studying the long term behavior of selected bright sources with a time resolution of about 1.5 h.

- Studying short term variability of selected bright sources on time scales of ≈ 0.1 s.

- Performing a continuous scan of the whole sky, to find possible target of opportunities (TOOs), like X-ray transients or other periodic phenomena in X-ray sources.

- Detection of new, so far unknown X-ray sources.

To fulfill these objectives, the *ASM* scans the sky each satellite orbit (≈ 90 min). During each scan the sky up to 80 % of the sky is covered and 50 selected bright sources, plus additional 25 weaker sources are monitored on a time scale of 1.5 h and 1 day. For each source, trigger limits for the source flux are set, to identify possible target of opportunities. To study short term variations of bursts or pulsating bright sources like Her X-1, count rate data of each detector is binned to 0.1 s light curves. The data is stored in an archive, analyzed with a standard procedure, and made available for public access. This is a very good fundamental data base to study long time behavior of known X-ray sources (Benlloch, 2003).

In each of the three SSCs a position sensitive proportional counters (PSPC) is mounted as detector. All SSCs can be rotated independently by motors. The structure and the assembly of the *ASM* follows the design shown in Fig. 5.10. The SSCs are based on the principle that an X-ray source located at infinity produces a shadow image of the slit mask on the entrance window of

the PSPC. By analyzing the displacement and the intensity distribution of the shadow patterns, the position and the flux of the X-ray source can be reconstructed (Doty, 1994). The data of the *ASM* are accumulated in single series of exposures, called dwells. For the duration of each dwell, the position of the SSC is kept fixed.

After receiving the *ASM* data, the MIT performs a near real time analysis, to determine the source intensities and positions. A cross check with existing source catalogs enables them to identify so far unknown sources or any change in source flux of already know sources. In case of a detection of any kind of "interesting" incident, a TOO observation can be triggered by the GSFC on decision of the principle investigator. This enables the controllers to react on short time scales and in a very flexible way on any kind of occasion on the X-ray sky. For this work *ASM* data was used only for comparison to the light curve derived from *PCA* data (see Fig. 7.1).

Chapter 6

Hercules X-1/HZ Her

6.1 Introduction

The history of Her X-1/HZ Her started in 1936, when the system was discovered and classified as an irregular variable star (Hoffmeister, 1941). Since Tananbaum et al. (1972) identified Her X-1 as an X-ray source during an observation with *UHURU*, Her X-1 has puzzled astrophysicists with its variety of spectral and temporal phenomena. Most of the properties of the system are qualitatively understood, but in detail still unexplained. The system shows strong variability on short and long time scales, as well as over a wide spectral range, from the optical to the X-rays.

The binary system consists of a 1.5 $M_\odot$ neutron star and its 2.3 $M_\odot$ optical companion HZ Her. Both components rotate in a P_{orb} = 1.7 d long, near circular orbit ($e < 1.3 \times 10^{-4}$) with a projected orbital radius of $a \cdot \sin i$ = 13.19 ls = 0.026 AU around their common center of mass (Still et al., 2001; Stelzer et al., 1997). Due to the high inclination of about 83° the observer sees the system almost edge-on and periodical eclipses of Her X-1 by HZ Her are observable in all wavelength bands. Since HZ Her fills its Roche Lobe, mass transfer via the inner Lagrangian point L_1 can occur, resulting in an accretion disk surrounding the neutron star (see section 2.3.1). For an overview on the system parameters see Tab. 6.1.

In the following sections I give an introduction to the observable properties of the binary system Her X-1/HZ Her and its accretion disk. A detailed introduction to Her X-1/HZ Her can be found in the literature, e.g. in Kunz (1996b) or Scott (1993). In the first section 6.2 I concentrate on temporal properties observable in the X-ray energy band and their underlying physical mechanisms, section 6.3 summarizes the optical variability of Her X-1/HZ Her, and in section 6.4 the main focus lies on the spectral characteristics of the system.

6.2 X-ray Variability

6.2.1 The 35^d cycle

General The averaged 35^d X-ray light curve of Her X-1 shows a strong modulation in X-ray intensity and has a characteristic shape, with two maxima called *main-on* and *short-on* (see Fig. 6.2). The main-on, during which the maximum X-ray intensity can be observed, is followed by a 2–3 d lasting rapid drop of intensity called *turn-off*.

The second ≈ 7–8 d long maximum, called *short-on* or *short-state*, starts around 35^d phase ϕ_{35} = 0.6. The flux during the short-on has a maximum level of 10–20 % of the main-on intensity.

Table 6.1: Parameters of the binary system Her X-1/HZ Her

System – Her X-1/HZ Her

Rectascension	$\alpha(2000)$	$16^{\mathrm{h}}\,57'\,50\rlap{.}{''}5$	
Declination	$\delta(2000)$	$+35°\,20'\,52''$	
Optical B Magnitude	m_{B}	13.0	Kukarkin et al. (1971)
Distance	D	$6.6 \pm 0.4\,\mathrm{kpc}$	Reynolds et al. (1997)
Binary Orbital Period	P_{orb}	1.7003(3) d	Still et al. (2001)
Proj. Orbital Radius	$a \cdot \sin i$	13.1902(9) s	Still et al. (2001)
Superior Conjunction	$T_{\pi/2}$	51004.729581(9)	Still et al. (2001)
Change of Orbital Period	$\dot{P}_{\mathrm{orb}}$	$-1.33(7) \times 10^{-8}\,\mathrm{d\,yr^{-1}}$	Still et al. (2001)
Orbit Inclination	i	$83(4)°$	Dennerl (1991)
Eccentricity	e	$< 1.3 \times 10^{-4}$	Kunz (1996b)
Large Semi Major Axis	a	22 lts	Kunz (1996b)

Neutron Star – Her X-1

Mass	M_{x}	$1.5 \pm 0.3\,M_{\odot}$	Reynolds et al. (1997)
Spin Period (MJD 50708.1985)	P_{spin}	1.23772910(3) s	this work
Magnetic Field Strength	B	$4.1 \times 10^{12}\,\mathrm{G}$	this work
Magnetic Moment	μ	$3 \times 10^{30}\,\mathrm{G\,cm^3}$	Kunz (1996b)
Radius of Magnetosphere	R_{mag}	$\approx 3000\,\mathrm{km}$	Deeter et al. (1998)
Mass Transfer rate [1]	$\dot{M}_{\mathrm{acc}}$	$(1.29\text{–}8.34) \times 10^{-8}\,M_{\odot}\,\mathrm{yr^{-1}}$	Stelzer (1997)

Optical Companion – HZ Her

Mass	M_{opt}	$2.3 \pm 0.3\,M_{\odot}$	Reynolds et al. (1997)
Radius	R_{opt}	$4.2 \pm 0.2\,R_{\odot}$	Reynolds et al. (1997)
Spectral Type		B3–B4/F	Reynolds et al. (1997)
Photospheric Temp. (unheated side)	T	$8100 \pm 240\,\mathrm{K}$	Cheng et al. (1995)
Photospheric Temp. (heated side)	T	$15000\text{–}20000\,\mathrm{K}$	Ketsaris et al. (2001)

Accretion Disk

Mean Precession Period	P_{pre}	$34.875 \pm 0.002\,\mathrm{d}$	Ketsaris et al. (2001)
Inclination	i_{disk}	$28°$	Howarth & Wilson (1983)
Inner Radius	$R_{\mathrm{disk,in}}$	$10^8\,\mathrm{cm}$	Horn (1992)
Outer Radius	$R_{\mathrm{disk,out}}$	$2 \times 10^{11}\,\mathrm{cm}$	Cheng et al. (1995)
Temperature inner edge	$T_{\mathrm{disk,in}}$	$1.0 \times 10^4\,\mathrm{K}$	Cheng et al. (1995)
Temperature outer edge	$T_{\mathrm{disk,out}}$	$9.5 \times 10^6\,\mathrm{K}$	Cheng et al. (1995)

[1] The mass accretion rates given are derived from $\dot{P}_{\mathrm{orb}}$ and are depending on the accretion model used. The values given are lower and upper limits for the coronal wind model of Schandl & Meyer (1994).
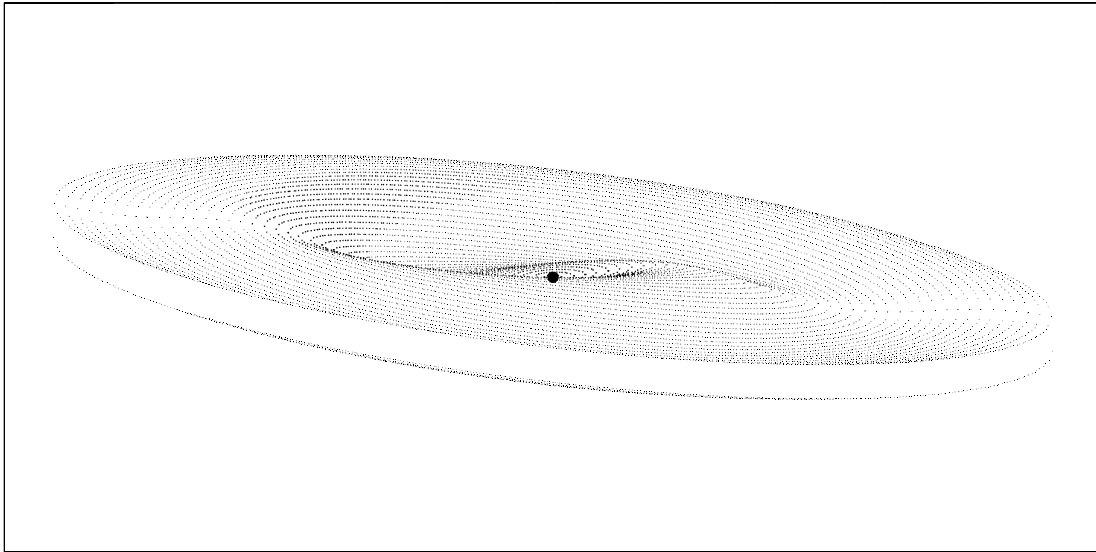
Figure 6.1: A tilted and warped accretion disk similar to the accretion disk in Her X-1. The neutron star is located in the center of the disk. The warp is clearly visible close to the inner edge of the disk (Schandl & Meyer, 1994).

Both time ranges, the steady increase in flux at the beginning of the main-on and before the short-on are called *turn-on*. During 35$^{\rm d}$ phase 0.4–0.6 and 0.85–1.0, the *low-states*, almost no flux and only weak pulsations from the neutron star can be detected, which is interpreted as scattered radiation of an accretion disk corona (Becker et al., 1977; Mihara et al., 1991; Coburn et al., 2000).

The beginning of a 35$^{\rm d}$ cycle, $\phi_{35} = 0$, is defined throughout of this work as the time during the turn-on when the X-ray flux reaches 10 % of the maximum main-on flux. The duration of successive 35$^{\rm d}$ cycles does not follow a strict periodic law with a mean precession period of $P_{\rm disk} = 34.875$ d (see Tab. 6.1). It shows a variation between 20.0 ×, 20.5 ×, or 21.0 × the duration of a binary orbital period. This behavior was modeled by Staubert et al. (1983) using a random walk model which can describe the deviation from a constant mean precession period. Furthermore, the turn-on to the main-on presumably occur at fixed binary orbital phases $\phi_{\rm orb} \approx 0.3$ or ≈ 0.7.

Warped and Tilted Accretion Disk The 35$^{\rm d}$ modulation is one of the best evidences for a tilted, warped, and counter orbital precessing accretion disk in X-ray binaries. An image of such a disk geometry is shown in Fig. 6.1. The neutron star is located in the center of the disk and is not visible at this scale. Due to the inclination of the accretion disk, parts of the disk periodically cover the central neutron star for about 60 % of the 35$^{\rm d}$ cycle, causing the intensity variation shown in the top panel of Fig. 6.2. The lower panel of Fig. 6.2 (Scott et al., 2000) shows the projected inner and outer edge of the disk as seen from an observer on the neutron star. The times of main-on, short-on, and low-state are indicated by solid vertical lines and are roughly aligned with the intensity plot in the top panel for clarity. The dashed horizontal line marks the position of the observer, which is not at elevation of 0° but slightly below. In this geometry, the turn-ons to the main-on and short-on are attributed to the outer rim of the accretion disk opening the line of sight to the central neutron star. During the decline phases at the end of main- and short-on the inner parts of the disk start to cover the neutron star again. This disk model is contrary to the model proposed by Schandl & Meyer (1994) which explains the turn-on to the short-on by the influence of the inner edge of the accretion disk.
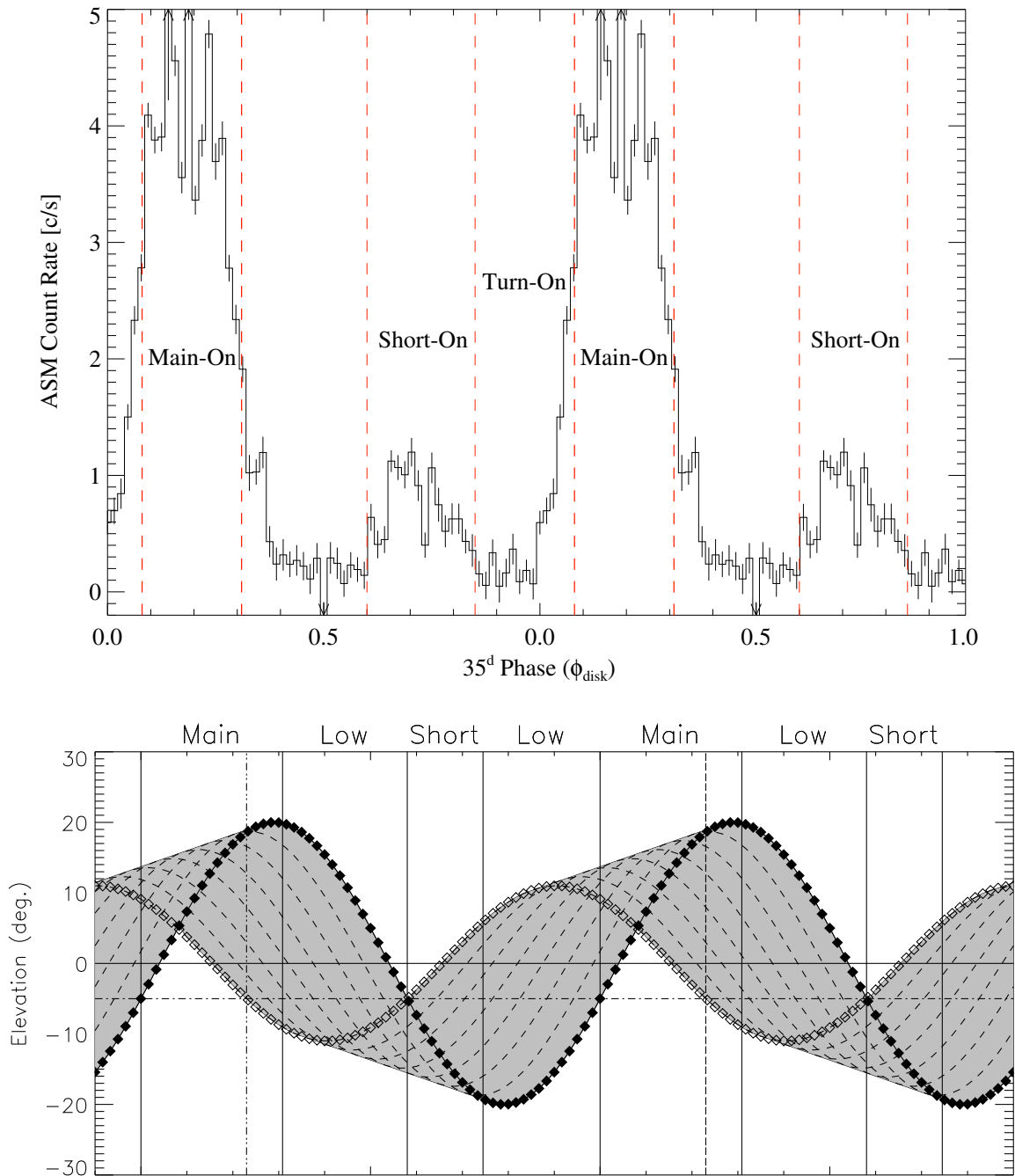
Figure 6.2: Top panel: The 35^d variation of the X-ray intensity of Her X-1 observed with *RXTE ASM*. Only data belonging to 21.0 · ϕ_{orb} long precession cycles are used to fold a mean 35^d light curve. Vertical lines mark different phases during the 35^d cycle: the main-on, short-on, and turn-on to the main-on are indicated. Bottom panel: The accretion disk rim as seen from an observer on the neutron star. The filled diamonds mark the outer edge of the disk, empty diamonds the inner edge. The lower image is taken from Scott et al. (2000). For further explanation see text.

As Schandl et al. (1997) and Maloney & Begelman (1997) show, a warped shape of an accretion disk may either be caused by radiation pressure or by radiation driven coronal winds. When the X-ray beam from the neutron star periodically sweeps over the optically thick accretion disk surface, it causes a momentum on the disk by the radiation pressure of reemitted photons. Since the disk is inclined, the illumination of the disk surface is not axial-symmetric and the resulting torques can be the origin of the observed warp (e.g., Pringle, 1996, 1997; Maloney & Begelman, 1997).

In another model discussed by Schandl et al. (1997), torques perpendicular to the surface of the accretion disk emerge from matter leaving the disk due to an coronal accretion disk wind. The wind itself is caused by X-rays from neutron star emission, irradiating and Compton heating the disk surface, which leads to the formation of a hot corona covering the accretion disk. The velocity of the gas in the outer parts of such a corona can exceed the escape velocity of the gravitational potential resulting in mass loss, which in extreme cases can be of the order of the mass accretion rate of the neutron star. Extensive theoretical work on accretion disk coronae and coronal winds can be found in, e.g., Begelman et al. (1983), Begelman & McKee (1983), or Maloney & Begelman (1997).

The underlying "clock" driving the retrograde precession of the disk at a very stable precession period of 35 d is still unclear and controversially discussed. Precession caused by tidal forces in the gravitational field of the binary system or a freely precessing neutron star are possible scenarios under discussion (Trümper et al., 1986; Ketsaris et al., 2001). The stability of the 35$^{\mathrm{d}}$ cycle over several decades makes pure tidal precession unlikely. In Ketsaris et al. (2001) we presented a model in which a freely precessing neutron star coupling via its magnetosphere to the inner accretion disk is the "central clock" of the 35$^{\mathrm{d}}$ cycle. Together with theoretical considerations, the periodic behavior of pre-eclipse dips strongly supports the model of an accretion disk which is precessing in retrograde direction relative to the orbital motion.

The shadow cast by the accretion disk onto HZ Her periodically obscures the X-ray heated side of the companion resulting in asymmetric illumination. This causes that the accretion stream does not lie within the orbital plane but rather has a velocity component perpendicular to the orbital plane. The impact of such a non-coplanar accretion stream on the outer parts of the disk results in a torque perpendicular to the orbital plane which can be the origin of the tilt of the disk (Shakura et al., 1999; Ketsaris et al., 2001).

Dips   In addition to the regular modulation of X-ray intensity described in section 6.2.1, sudden decreases in X-ray flux (dips) can be observed during the 35$^{\mathrm{d}}$ cycle. During these dips the intensity drops very rapidly, within a few seconds by a factor of 3–4 and shows strong variability on timescales of minutes. This dipping phenomena has been subject of many systematic studies, e.g., Stelzer et al. (1999), Shakura et al. (1999), or Leahy (1997). The dips can be categorized into two types: pre-eclipse dips and anomalous dips. Pre-eclipse dips are only observed up to several binary orbits after turn-on to the main-on and short-on at binary orbital phases ϕ_{orb} = 0.6–0.9 (Shakura et al., 1999). The pre-eclipse dips occur with a period of P_{dip} = 1.65 d which is slightly smaller compared to the orbital period. Therefore successive pre-eclipse dips "move" towards earlier ϕ_{orb} during a 35$^{\mathrm{d}}$ precession cycle. The regular period P_{dip} can be understood in terms of a beat frequency between the orbital period and the disk precession period $1/P_{\mathrm{dip}} = 1/P_{\mathrm{disk}} + 1/P_{\mathrm{orb}}$.

Anomalous dips preferentially occur at ϕ_{orb} = 0.45–0.65 and not later than one binary orbital period after turn-on. They do not obey a strict periodicity like pre-eclipse dips but rather occur randomly.

Both types of dips have in common that the observed spectra are heavily affected by photoelec-
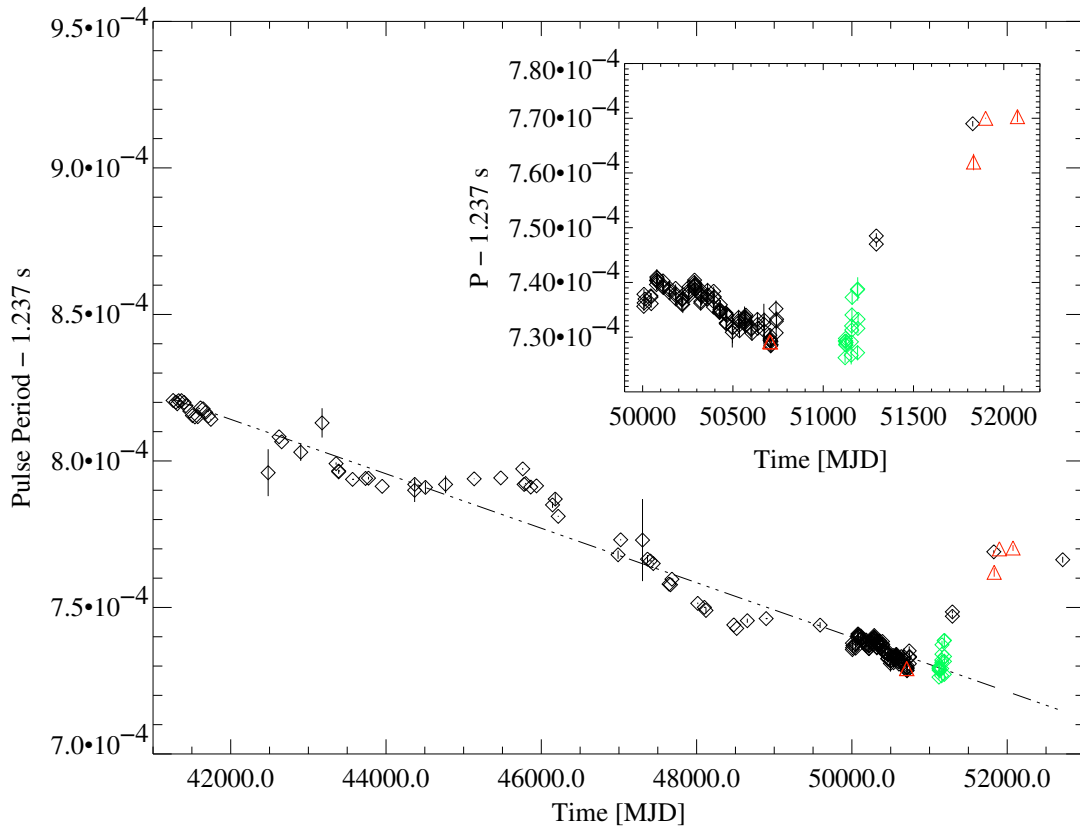
Figure 6.3: The history of the pulse period of Her X-1 from 1971 November 3 till 2001 June 16. The pulse period shows two extended spin-down phases: the rapid spin-down phase recently observed after return form the anomalous low state close to MJD 51000 and a spin-down phase starting at MJD 45000. Triangles mark pulse periods determined for this work in collaboration with P. Risse (IAAT) and the dashed line a linear fit to the period data giving the $\dot{P}$ as mentioned in the text.

tric absorption (see Stelzer et al., 1999, for a detailed analysis of spectral evolution during dips). Thus the origin of both types of dips is related to cold or mildly ionized material crossing the line of sight to the neutron star. In the model presented by Shakura et al. (1999), a non-coplanar accretion stream (see section 6.2.1) intersecting the line of sight to the observer is the origin of pre-eclipse dips. The process underlying the anomalous dips is more complex. Since the outer accretion disk parts perform a wobbling motion (secular precession) in the tidal field of the binary system, the outer edge of the disk can occult the neutron star, which causes anomalous dips (Shakura et al., 1999).

6.2.2   1.23 s Pulsations from the Neutron Star

On shorter time scales, X-ray intensity observed from Her X-1 shows periodic behavior with a period of $P_{1.23} \approx 1.23$ s, called pulse period. This variation has its origin in the rotation of the neutron star itself and is attributed to the rotational period of the neutron star. A history of the pulse period measured since 1971 is shown in Fig. 6.3. The observed pulse period is decreasing with time with $\langle \dot{P} \rangle = -3.40 \pm 0.04 \times 10^{-6}$ s yr^{-1}. This corresponds to a spin-up of the neutron star
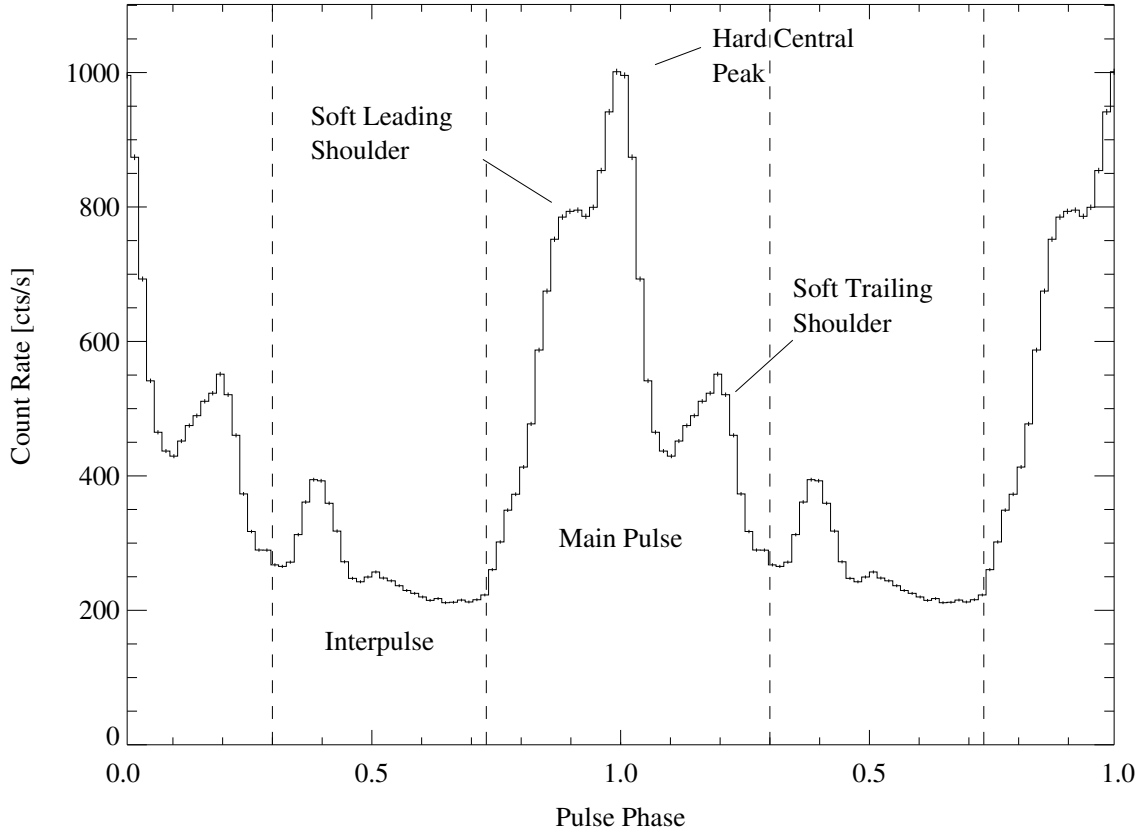
Figure 6.4: Typical 1.23 s pulse profile observed at the beginning of the main-on of the 35^{d} cycle, in the energy range of 9–13 keV. Note the complex structure of the main pulse and interpulse.

due to angular momentum transfer by mass accretion from the secondary star. $\langle \dot{P} \rangle$ was derived by a linear fit to data shown in Fig. 6.3, ignoring the data of the recent spin-down phase observed later than MJD 51000.

The mean X-ray intensity versus neutron star rotation phase is called pulse profile and is shown in Fig. 6.4 over two neutron star rotation phases. This pulse profile was observed during the main-on in the energy range 9.0–13 keV. The nomenclature used for the different peaks of the pulse profile is similar to the one in Deeter et al. (1998) and will be used throughout this work for clarity. The maximum intensity is named "hard central peak" and is most prominent in the energy band $9.0\,\mathrm{keV} < E < 20\,\mathrm{keV}$. The amount of pulsed flux in the two shoulders, "soft leading shoulder" and "soft trailing shoulder", relative to the central peak is increasing with decreasing energy. In between two successive main pulses a "interpulse" is apparent at pulse phase ≈ 0.4 with a maximum intensity of about 40 % of the main pulse intensity.

The shape of the pulse profile, the width of the peaks, and the ratio of pulsed flux to non-pulsed flux show strong variation with ϕ_{35} and energy (see, e.g., Soong et al., 1990a). As an example the dependence on the 35^{d} cycle and energy of the pulse profile is shown in Fig. 6.5 for two energy bands, 1.0–4.6 keV and 9.3–14.0 keV. At the beginning of the main-on during the first $\approx 6\,\mathrm{d}$, changes in the profile are relatively small. Close to the end of the main-on the flux in the soft leading shoulder drops. This event was observed by several authors and described as a narrowing of the hard central peak at the end of main-on (e.g., Joss et al., 1978; Gruber et al.,
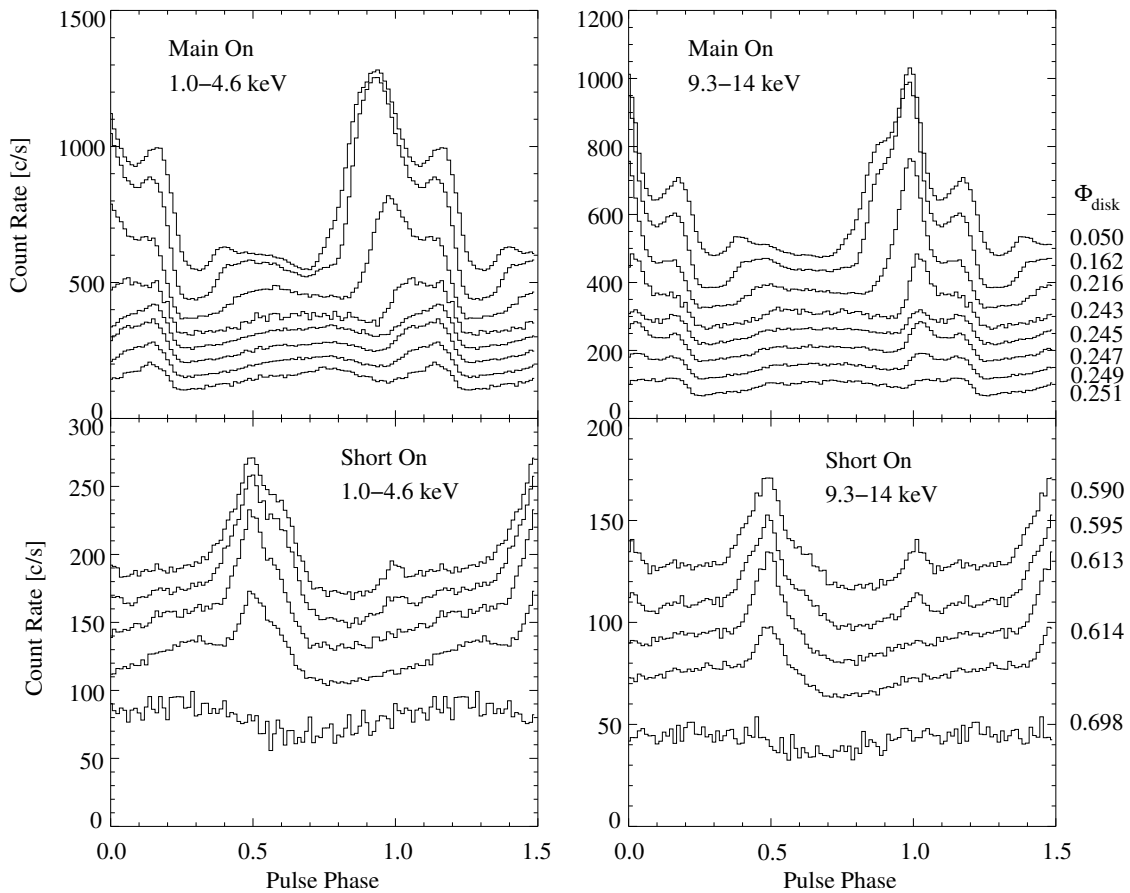
Figure 6.5: Changes in shape and flux of the pulse profile during the main-on and short-on of the 35^d cycle, observed in 1989 April with *Ginga*. Shown are pulse profiles in two energy bands 1.0–4.6 keV (left panel) and 9.3–14.0 keV (right panel). The 35^d phase of the accretion disk (ϕ_{35}) is indicated for each pulse profile on the right side for both, the right and left panel (after Fig. 6 of Scott et al., 2000).

1980; Kahabka, 1989; Soong et al., 1990a, and references therein). Finally, the intensity of the hard central peak decreases very rapidly until no pulsations can be detected about 10–12 d after turn-on. The remaining residual flux has an almost sinusoidal pulse shape which disappears at the end of the main-on (cf. pulse profiles shown in Fig. 6.5 for $\phi_{35} = 0.251$). In addition, the gap at pulse phase around 0.2–0.3 gets deeper and wider while the interpulse disappears.

During the short-on the overall flux in the pulse profile is about 30 % of the main-on flux and the interpulse is dominating the pulse profile. While the small hard central peak is visible at the beginning of short-on only, the interpulse declines more slowly until pulse phase 0.7, where the flux in the interpulse starts to vanish rapidly. At the end of the short-on, only a small amount of residual pulsed flux is detectable, which shows a quasi-sinusoidal pulse shape shifted by 180° in phase relative to the main-on sinusoidal component, see lower panel of Fig. 6.5. This phenomenological pulse evolution was observed with several instruments and shows a systematical pattern depending on ϕ_{35} (Scott, 1993; Kunz, 1996a; Deeter et al., 1998; Blum, 2000, and references therein). Furthermore, the pulse shape observed at fixed ϕ_{35} is very stable on time scales of years. An interpretation of the pulse evolution is given in section 7.2.4.
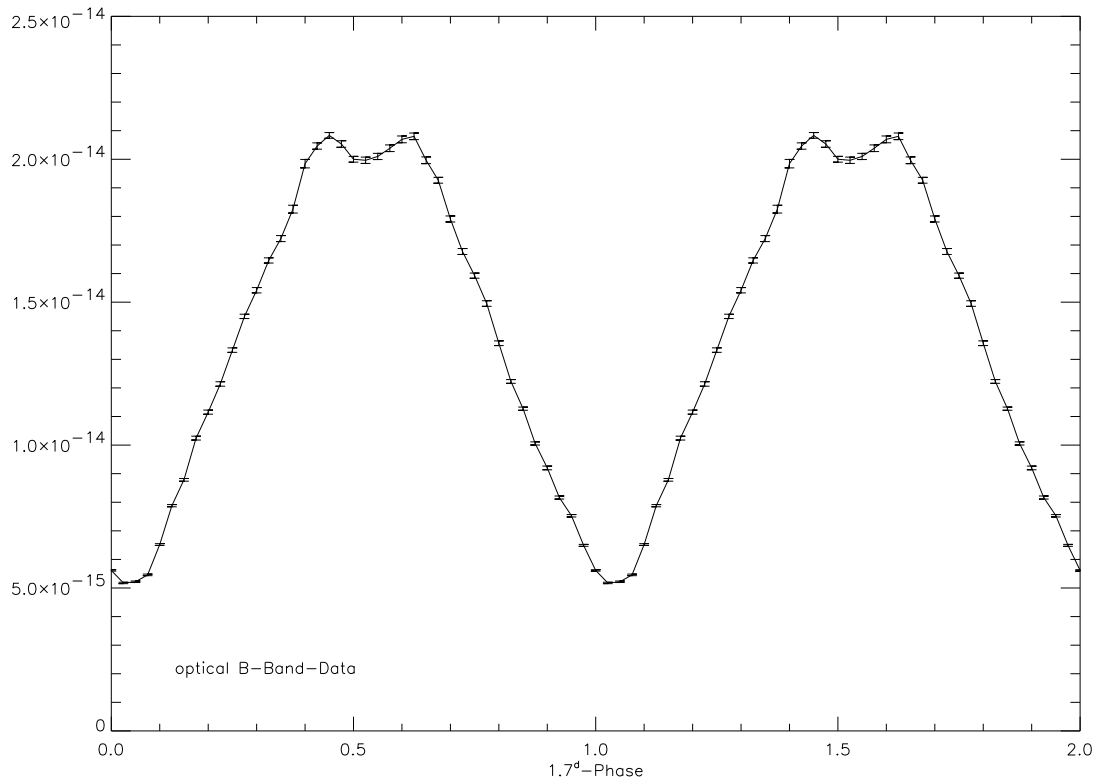
Figure 6.6: Orbital light curve in the optical B-band, folded with a mean $P_{orb} \approx 1.7$ d and averaged over all 35 d phases. The data base covers ≈ 26 years. The drop in intensity at $\phi_{orb} = 0.5$ is due to the accretion disk shadowing parts of the X-ray heated side of the secondary HZ Her (Risse, 2003).

6.3 Optical Variability

Shortly after the discovery of Her X-1 by Tananbaum et al. (1972), first indication for its optical counterpart HZ Her was published by Liller (1972) in an IAU circular. Only a few weeks later, Bahcall & Bahcall (1972) reported on orbital modulation of the optical light curve of HZ Her between $m_B = 13.2$–14.7, and almost at the same time 1.24 s pulsations were observed by Davidsen et al. (1972). Altogether, based on these observations HZ Her was identified as the optical companion of Her X-1.

6.3.1 Orbital Light Curve

In the optical band, the observable flux of Her X-1/HZ Her originates mainly in two sources: *direct* optical emission from HZ Her, and *reprocessed* X-rays from the X-ray heated side of HZ Her or the accretion disk. HZ Her dominates the optical emission with about 68 % of the total flux. The remaining 32 % of the flux originates in blackbody emission from the X-ray heated accretion disk, which has a temperature of $T \approx 10^4$ K at the inner disk boundary and $T \approx 10^7$ K close to the disk rim (Cheng et al., 1995). Almost 50 % of the hard X-ray flux irradiating the parts of HZ Her pointing towards the neutron star is reprocessed to optical wavelengths (Howarth & Wilson, 1983).
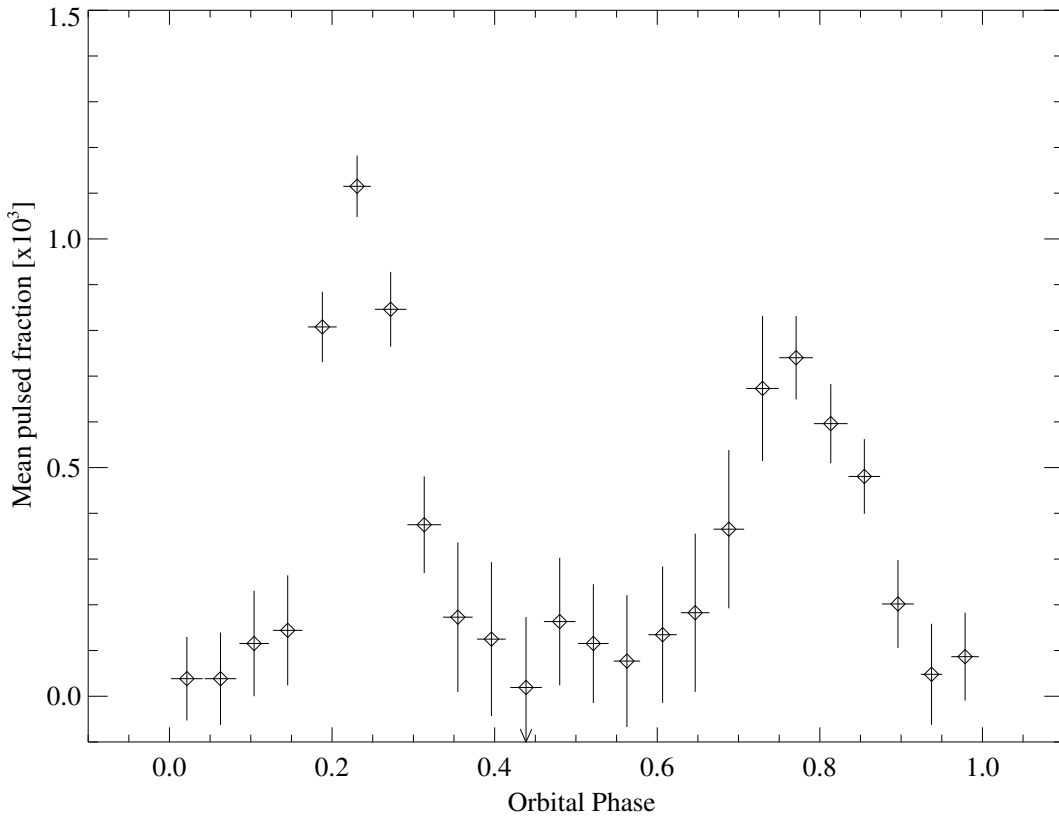
Figure 6.7: Pulsed fraction versus orbital phase for optical pulsations with a period of P_spin. Optical pulsations are most prominent around orbital phases $\phi_\mathrm{orb} = 0.2$ and $\phi_\mathrm{orb} = 0.8$ (Figure from Middleditch & Nelson, 1976).

As a result of such strong X-ray heating, the spectral type of HZ Her changes between a B3–B6 and a late A type star depending on ϕ_orb, corresponding to a mean photospheric temperature of 8100 K and 15000–20000 K (Reynolds et al., 1997). Thus the observable flux and the photospheric temperature are expected to have a maximum around $\phi_\mathrm{orb} \approx 0.5$, when the X-ray heated side of Her X-1/HZ Her is visible for the observer. Fig. 6.6 shows a optical B-band orbital light curve of Her X-1/HZ Her averaged over all disk precession phases. The data for this light curve covers more than 26 years (Risse, 2003). Because of the distorted, non-spherical shape of HZ Her in the Roche potential of the binary system, the orbital light curve has a non-sinusoidal shape. Since the inclination of the accretion disk is quite large ($i_\mathrm{disk} = 28°$), the disk shadows a substantial part of the surface of HZ Her from X-ray emission of the neutron star. Furthermore, the size of the projected disk shadow changes with disk precession phase ϕ_{35}, causing a measurable change in the orbital light curve of Her X-1/HZ Her which is clearly visible in Fig. 6.6 as a drop in intensity around $\phi_\mathrm{orb} = 0.5$. The amount of change in intensity systematically depends on ϕ_{35}. Using light curve synthesis models including accretion disk and stellar atmosphere models, the orbital light curve can be used to determine system parameters like the dimension of the accretion disk, the temperature of the secondary, or the distance of the system (Howarth & Wilson, 1983).
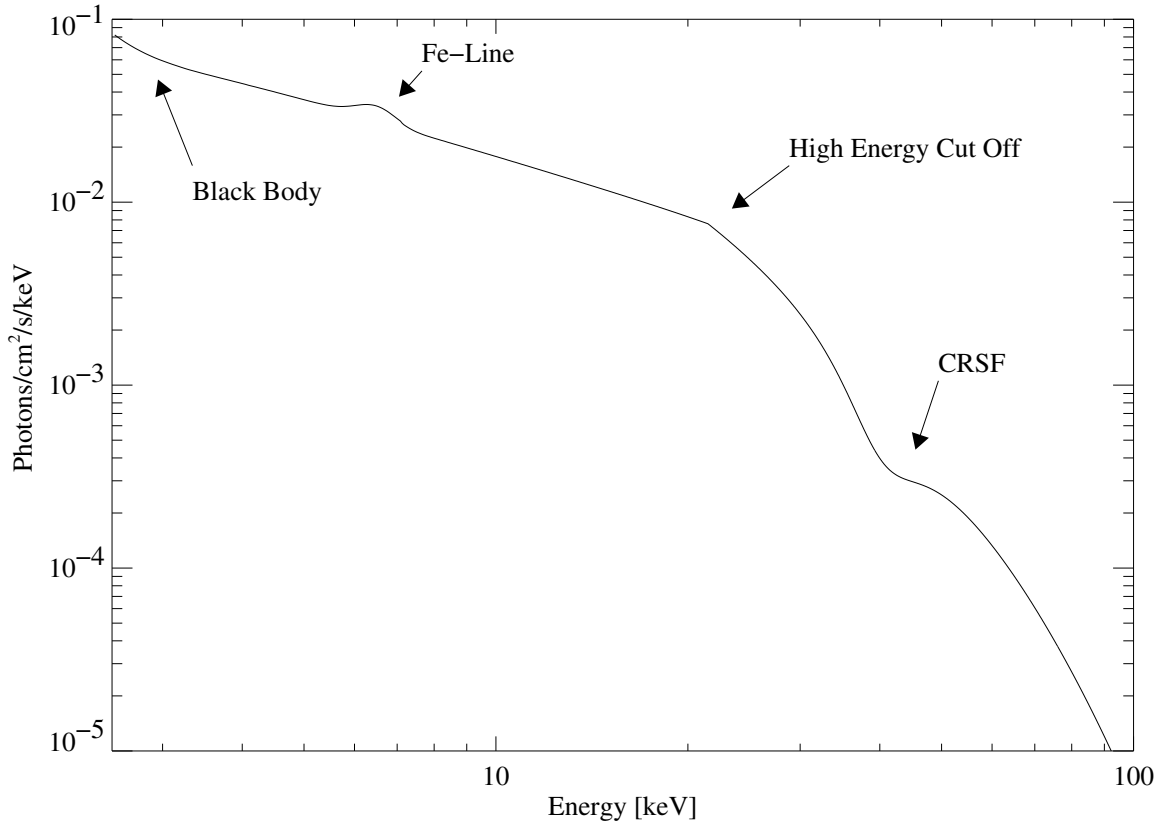
Figure 6.8: Phase averaged main-on spectrum of Her X-1 in the energy range 2.0–100 keV. The components contributing to the overall spectrum are indicated by arrows. For a more detailed description see text.

6.3.2 Short Time Variability

Pulsations with periods equal to the neutron star's spin period P_{spin} cannot only be observed in X-rays but in optical wavelengths as well. The amount of pulsed flux is largest around orbital phases $\phi_{\mathrm{orb}} = 0.2$ and $\phi_{\mathrm{orb}} = 0.8$ (see Fig. 6.7). Middleditch (1983) and Middleditch & Nelson (1976) show that the optical pulsations mainly originate in reprocessed X-rays. The reprocessing sites are located in the lobe of HZ Her and outer parts of the accretion disk or the accretion stream. In the millihertz regime, Boroson et al. (2000) and O'Brien & Horne (2001) found evidence for quasi-periodic oscillations (QPO) with frequencies of 35 mHz in the optical and 45 mHz in the UV.

6.4 The Spectrum of Her X-1

The time averaged main-on continuum spectrum of Her X-1 has the shape of a typical X-ray binary pulsar spectrum. Between 1 and 10 keV it can be well described by a power-law with a photon-index of $\alpha \approx 0.95$–1.0. At higher energies, $E > 20$ keV, the flux rapidly drops, similar to an exponential cut-off with a cut-off energy of $E_{\mathrm{cut}} \approx 20$ keV and $E_{\mathrm{fold}} \approx 14$ keV (White et al., 1983). The exact shape of the cut-off is still uncertain. Several theoretical models like anisotropic Thomson scattering in a strong magnetic field (Boldt et al., 1976), Comptonization or the influence of cyclotron resonant scattering in combination with Comptonization exist (Mészáros & Nagel,
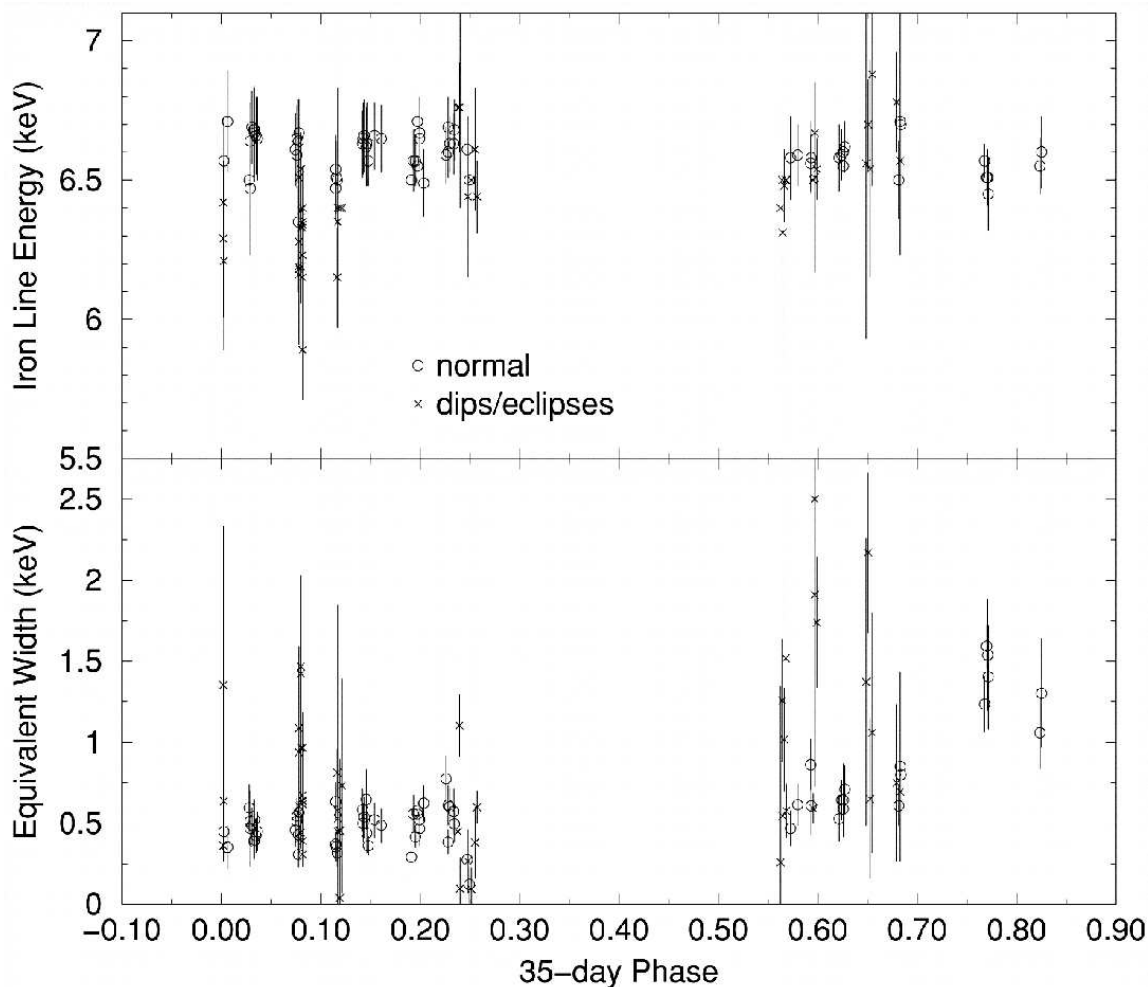
Figure 6.9: The equivalent width and energy of the Fe line depending on ϕ_{35}. The spectral model used to fit the observed data is similar to the partial covering model used in section 7.3.1 in this work (for further details on the spectral analysis see Leahy, 2001).

1985a,b). But none of the models can reproduce the lack of flux above 20 keV in Her X-1 and other X-ray pulsars. Towards lower energies $E < 1$ keV thermal blackbody emission contributes significantly to the spectrum with $kT_{BB} \approx 0.1$ keV. This component was first observed by Shulman et al. (1975) and is generally interpreted as thermal emission from the inner parts of the accretion disk or matter close to the neutron star's magnetosphere (e.g., McCray et al., 1982; DalFiume et al., 1998; Endo et al., 2000). In addition to the continuum flux, line emission contributes to the overall spectrum; at ≈ 6.5 keV a broad Fe Kα emission line, and Fe L emission at ≈ 0.9 keV. Both, the Fe L and Fe Kα line, show strong flux correlation over the pulse phase with the amount of flux observed in the blackbody component. This indicates that both, line emission and blackbody emission, originate in the same emission region (Oosterbroek et al., 1997). At ≈ 39 keV a cyclotron resonant scattering feature (CRSF) was observed for the first time by Trümper et al. (1978). The depth and shape of the CRSF strongly depends on pulse phase and is most prominent around the maximum of the hard central peak (Fig. 6.4). The energy of the line centroid of the CRSF is a direct indicator for the magnetic field strength of the neutron star, for which Kunz et al. (1996) found a value of $B = 3 \times 10^{12}$ Gauss. A systematic study of CRSFs was recently published by Gruber et al. (2001) and Coburn (2001).
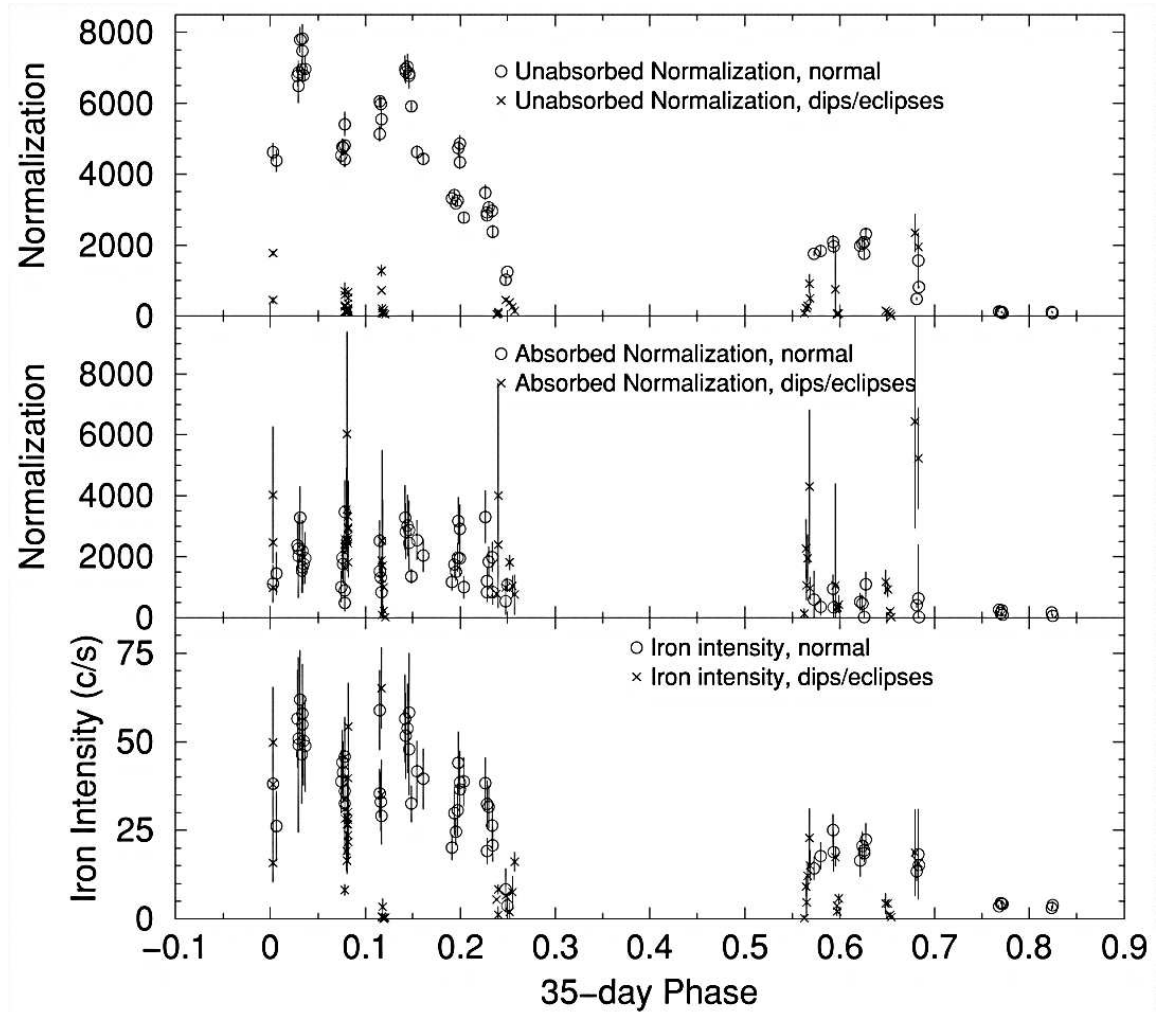
Figure 6.10: The Fe line intensity, the normalization of a absorbed spectral component, and the normalization of an unabsorbed spectral component depending on ϕ_{35}, using the same spectral model as for Fig. 6.9 (Leahy, 2001).

During the 35^{d} cycle this canonical spectrum is modified mainly by the influence of the accretion disk and an accretion disk corona, except during dips which have another physical origin as described earlier and are not taken into account in the remainder of this thesis. A spectral analysis for the time of the dips is given by Stelzer et al. (1999). Leahy (2001) tried to establish a consistent image of the spectral evolution during the 35^{d} cycle based on a spectral model composed of two components: an absorbed spectral component plus an additional unabsorbed spectral component. For a description of the spectral model see Leahy (2001) or section 7.3.1, where a similar spectral model is introduced. Especially during the turn-on to the main-on and short-on photoelectric absorption increases and dominates the spectrum with $N_{\mathrm{H}} \approx 10^{24}\,\mathrm{cm}^{-2}$ (cf. section 7.3), while during all other times the unabsorbed spectral component is dominant (see Fig. 6.10). The origin of the absorbed component is generally attributed to cold material of the accretion disk covering the line of sight to the emission region on the neutron star. The power-law index is consistent with a constant value of $\alpha \approx 1.0$ throughout the 35^{d} cycle, except during the short-on where the spectrum is significantly harder with $\alpha \approx 0.8$ (Leahy, 2001).

While the equivalent width of the iron emission line is stable at $EW = 490\,\mathrm{eV}$ for the time of

the main-on, it increases during short-on and low-states up to $\approx$ 660 eV (see Fig. 6.9). Several authors reported a variability of the Fe line energy in the range of 6.4–6.7 keV during the past. Due to, the low energy resolution of earlier instruments this phenomenon could not be studied in detail. Endo et al. (2000) recently found evidence for two line components at 6.41 ± 0.04 keV and 6.73 ± 0.05 keV (Fexxv) in observations with *Ginga*. Since these two lines contribute to the total Fe line flux observed in Her X-1, a change in relative intensity can explain the observed energy variability observed with instruments with a lower energy resolution. They interpreted the 6.41 keV line as fluorescent emission from the inner edge of the accretion disk. For 6.73 keV photons they derived a corresponding radius of $r = 10^8$–10^{10} cm for the emission region, which has to be located closer to the outer parts of the accretion disk with higher temperatures, e.g. in an accretion disk corona.

Chapter 7

The Her X-1 Turn-On Observation

On 1997 September 13–16, a complete turn-on of Her X-1 was observed in a three day long monitoring observation with the Rossi X-ray Timing Explorer (*RXTE*). An overview of this observation is shown in Fig. 7.1. Beneath the light curve measured with the *RXTE PCA*, data from the *RXTE ASM* and *CGRO BATSE* are shown for the same time range. During the turn-on the mean count rate steadily increases from almost zero flux to $\approx 2000 \, \mathrm{cts \, s^{-1}}$ at the end of the turn-on. Around JD 2450706.0 an eclipse due to the secondary HZ Her took place. Furthermore, two dips were detected: pre-eclipse dips around JD 2450705.8 and an anomalous dip around JD 2450705.3. While the end of the main-on has been the subject of previous *Ginga* observations Deeter et al. (1998), observational data on spectral and temporal evolution during turn-on have been rare. Due to *RXTE*s large effective area and high time resolution, this observation allows a better systematic study of the temporal and spectral behavior during a turn-on compared to earlier observations of Becker et al. (1977) or Giacconi et al. (1973). The total observation consists of 32 individual satellite pointings with an effective observation time of 81.5 ksec, interrupted by Earth occultations. The numbers in Fig. 7.1 mark individual *RXTE* orbits (pointings) and are referenced in the further discussion as, e.g., orbit 05 for the 6th pointing or observation. A list of observing times, mean count rate, and effective exposure times is given in Tab. A.1. During the observation all five *RXTE* PCUs were operating, therefore all count rates given throughout this work are total count rates of all PCUs.

In the following, I will give an overview on the data extraction procedure and the screening criteria applied to the data which are necessary before a detailed temporal and spectral analysis can be performed. In section 7.2 I will concentrate on temporal analysis with main emphasis on the pulse profile and emission geometry, followed by a spectral analysis of the pulse phase averaged spectrum in section 7.3. A geometric model which can explain the observed spectral and temporal properties will be introduced in section 7.4.

7.1 Data Extraction and Preparation

In a first step, before extracting light curve and spectra, the raw data has to be screened for background contamination and data quality. Therefore good-time intervals (GTI) have to be defined. These time intervals indicate periods of observation times which are accepted as "good" and are further taken into account during the analysis process. Criteria for selecting good-time intervals are the detector background flux, the source elevation, and times of SAA passage. An indicator for the low energy internal detector background contamination of the *PCA* is the housekeeping value called electron-ratio. This parameter indicates the amount of the internal detector background flux
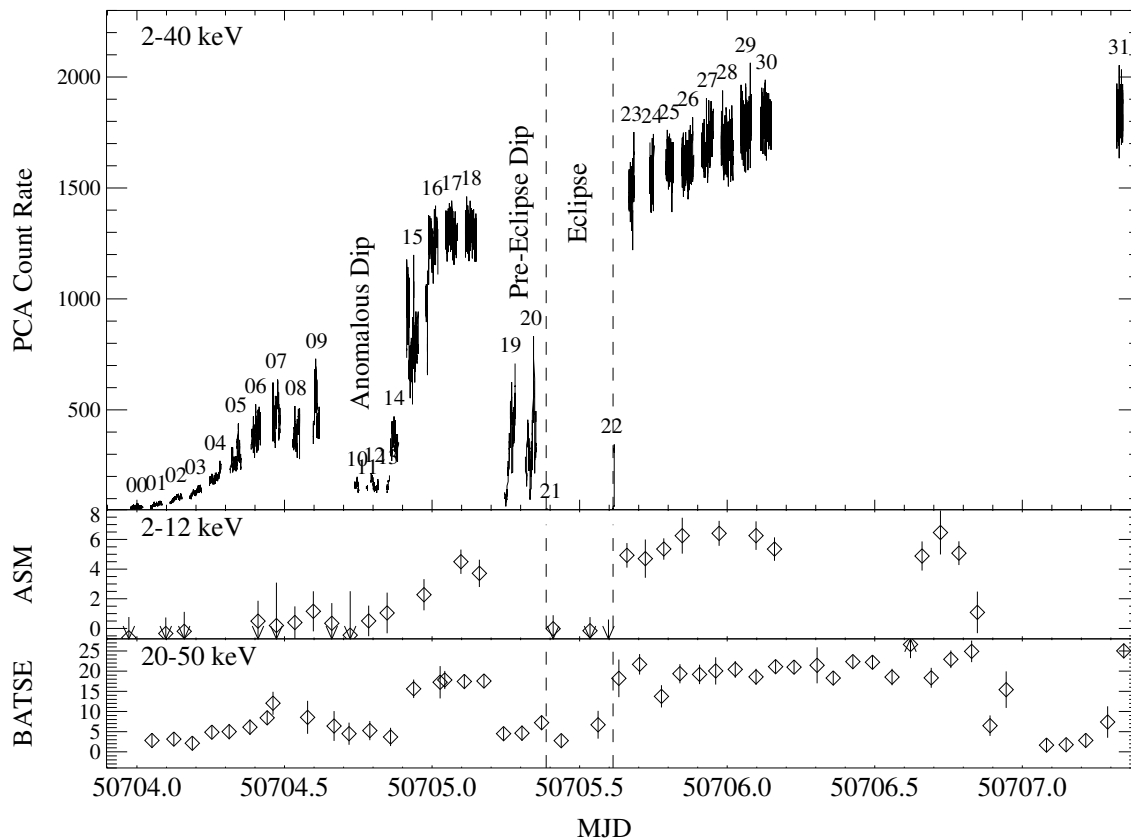
Figure 7.1: From top to bottom: *RXTE PCA*, *RXTE ASM*, and CGRO *BATSE* count rates for the time of the turn-on. The time resolution for *PCA* data is 16 s, for *ASM* 90 min and 100 min for *BATSE*, respectively. The beginning and the end of the time of the eclipse by HZ Her are marked by vertical dashed lines. The numbers identify individual *RXTE* orbits starting with orbit 00 up to orbit 31.

caused by charged particles, like electrons trapped in the Earth's magnetosphere (section 5.2.5). To minimize the background, an electron-ratio < 0.1 was chosen during data extraction. Since the Earth's atmosphere absorbs low energy X-rays, time periods with a source elevation relative to the Earth's limb $< 10°$ were rejected. Especially during SAA passages the background increases dramatically. For this reason, times 30 min before and after the SAA passage were excluded of the data analysis as well. Subsequently the data were divided into single *RXTE* pointings (orbits), labeled with numbers 00–31 in Fig. 7.1.

Based on these GTIs, *PCA* source and background spectra as well as source light curve were extracted for each orbit using `standard2f` mode data. For the selection of the appropriate background model of the *PCA* the count rate was taken into account. For *PCA* count rates $\leq 40 \, \text{cts s}^{-1}$ the *PCA* Faint background model was used according to the recommendation given in the *PCA* documentation (NASA, 1997). This is of importance for observations at the beginning of the turn-on and times of the dips and eclipse when the signal to noise ratio is low. All other observations are corrected using the SkyVLE background model. The resulting light curve for data in `standard2f` mode is shown in the top panel of Fig. 7.1. Furthermore, during the spectral analysis only *PCA* data with $3 \, \text{keV} \leq E \leq 18 \, \text{keV}$ was used.

For spectral analysis of data with energies $E > 18 \, \text{keV}$ *HEXTE* source and background spectra

were extracted. Since the *HEXTE* background is measured directly by rocking (see section 5.3.2), the background spectra can be extracted using off-source data. As detector response matrices for spectral analysis of *PCA* data the newest available V 7.1 was used and for *HEXTE* data the response matrix version V 8.4.2.

An accurate temporal analysis of the 1.23 s pulsations emerging from Her X-1 requires a time resolution $\ll 16$ s as available in `standard2f` mode. Hence, additional light curves using *PCA* raw data in `EA1_B_16ms_16B_0_49_H` mode, were generated with a time binning of 32 ms and 16 ms based on the same GTI as for low time resolution *PCA* light curve. This mode offers an intrinsic time resolution of 16 ms. To obtain energy resolved light curves for all orbits, 5 energy bands were selected: 0–4.5 keV, 4.5–6.5 keV, 6.5–9.0 keV, 9.0–13.0 keV, and 13.0–19.0 keV, and light curves generated for each energy band.

7.1.1 Barycentric Correction

Before the temporal behavior of Her X-1 can be studied in detail, the effects of orbital motion of the satellite and the motion of the Earth on the photon arrival time have to be corrected. Both cause a periodic modulation of photon arrival times because of Doppler effect. This can be corrected for by transforming the photon arrival times from the on-board time system of the satellite to the barycenter of the solar system. This time system is called Barycentric Dynamical Time. To do so, the position of the satellite and its velocity components, as well as the velocity of the Earth relative to the barycenter, have to be known at any time during the observation with high accuracy. For *RXTE* the barycentric correction can be applied to a light curve using the tools `fxbary` or `faxbary`. For an absolute time measurement additional constant time delays, like signal travel times to and from ground stations or signal delays in the detector electronics are considered by these tools as well. The absolute time accuracy that can be achieved after applying all corrections is 8 μs (Rots et al., 1998).

7.1.2 Binary Orbital Motion

In an analog way, the motion of the binary system around its common center of mass causes a modulation of the photon arrival times due to the Doppler effect. If the orbital period P_{orb}, the projected orbital separation $a/c \cdot \sin i$, the eccentricity of the orbit e, and the reference orbital phase $T_{\frac{\pi}{2}}$ are known, then the photon arrival times can be corrected for this effect. Since the eccentricity

Table 7.1: Orbital parameters of the binary system Her X-1/HZ Her. These parameters are used for correcting light curve with respect to binary orbital motion. The values are taken from Stelzer et al. (1997).

Parameter	Value
$T_{\frac{\pi}{2}}$	43804.519980(14) MJD
P_{orb}	1.700167720(10) d
$\dot{P}_{\mathrm{orb}}$	$-2.5 \pm 0.27 \times 10^{-8}$ d yr^{-1}
$\frac{a}{c} \cdot \sin i$	13.1831(3) lts
e	0
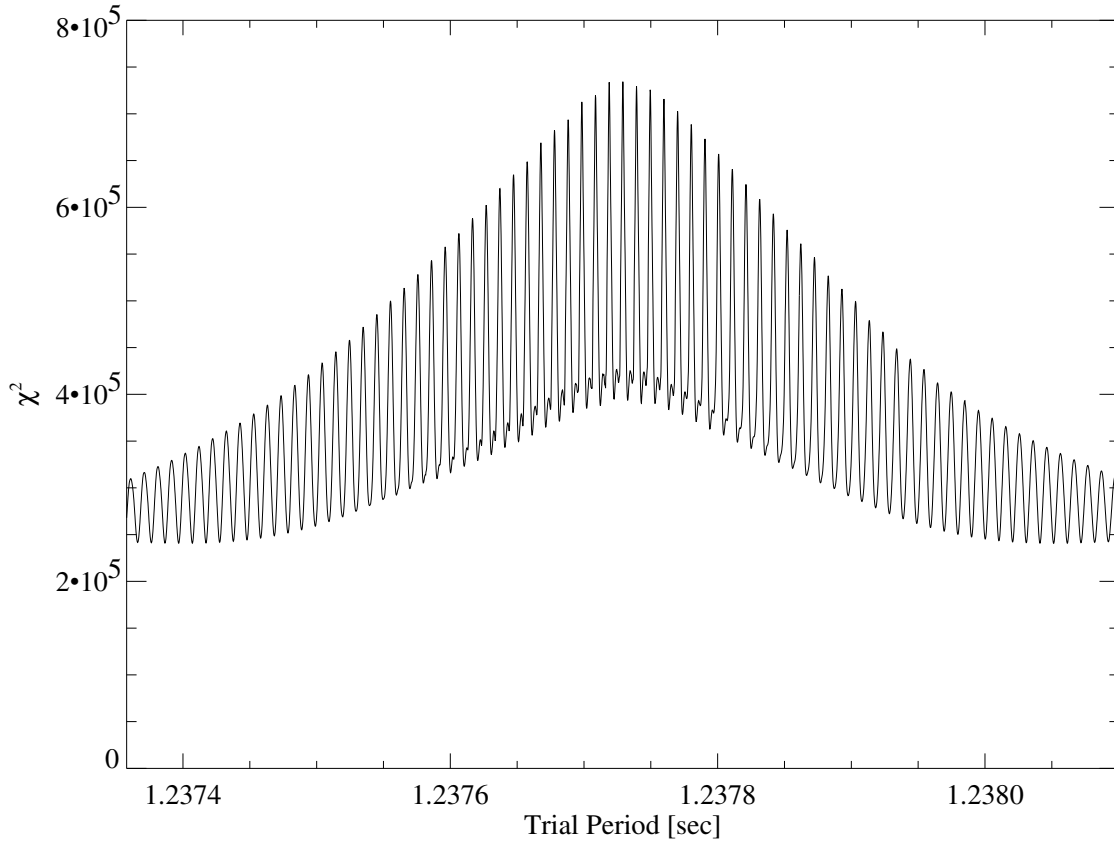
Figure 7.2: χ^2 distribution of the search for the neutron star's spin period. The *x*-axis gives the trial period and the *y*-axis the corresponding χ^2 value. The best period estimate corresponds to the central peak with the maximum χ^2 value which is surrounded symmetrically to the left and right by additional beat maxima from gaps in the observed light curve.

of the orbit of Her X-1/HZ Her is very small ($e < 1.3 \times 10^{-4}$), the simplified case of a circular orbit can be assumed, where the photon arrival times are modulated sinusoidally according to:

$$t_{\mathrm{CM}} = t_{\mathrm{obs}} - \frac{a}{c} \cdot \sin i \cdot \cos\left(2\pi \, \Phi(t_{\mathrm{obs}})\right) \qquad (7.1)$$

here, t_{obs} is the observed photon arrival time and t_{CM} the photon arrival times relative to the center of mass of the binary system. The actual orbital phase $\Phi(t_{\mathrm{obs}})$ can be calculated as follows:

$$\Phi(t_{\mathrm{obs}}) = \frac{t_{\mathrm{obs}} - T_{\frac{\pi}{2}}}{P_{\mathrm{orb}}} - \frac{1}{2} \cdot \frac{\dot{P}_{\mathrm{orb}}\,(t_{\mathrm{obs}} - T_{\frac{\pi}{2}})^2}{P_{\mathrm{orb}}^2} \qquad (7.2)$$

To correct the light curve of the turn-on observations, the photon arrival times of each light curve were transformed to t_{CM} by applying Eq. (7.1). Since the orbital phase $\Phi(t_{\mathrm{obs}})$ itself depends on time, this correction has to be done iteratively. The orbital parameters used, are those derived by Stelzer et al. (1997) and given in Tab. 7.1.

7.1.3 Determination of the Pulse Period

To determine the spin period of the neutron star, data with the best signal to noise ration were binned to light curves with a bin size of 0.98 ms with a total observation time of 152167 s. All light curves were background subtracted and the photon arrival times were corrected for binary orbital motion and transformed to the solar systems barycentre. Finally a period search by epoch folding as described in section 4.2.2 was performed. The resulting χ^2 values plotted versus the trial period is shown in Fig. 7.2. By fitting a Gaussian profile to the central peak of the χ^2 distribution the pulse period can be determined from the position of the maximum of the Gaussian to $P_{\text{spin}} = 1.23772910$ s (MJD 50708.19855). According to Eq. (4.9) the error of the pulse period is $\sigma_P = \pm 1.5 \times 10^{-7}$ s, if the pulse profile is folded into 64 phase bins. Following the method of Larsson (1996) the error is $\sigma_p = 3 \times 10^{-8}$ s (after Eq. 4.13).

7.2 Variation of the Pulse Profile

As described in section 6.2.2, the shape of the pulse profile changes substantially during the 35^{d} cycle. While variations during the main-on, short-on, and turn-off have been the subject of many studies (e.g. Scott et al., 1997; Joss et al., 1978; Scott, 1993), a detailed analysis of the pulse profile during the turn-on to the main-on is still missing. To do so, light curves of all energy bands and orbits with a time resolution of 16 ms were folded with the pulse period P_{spin}. For folding the light curve, the photons have to be sorted into distinct phase intervals (phase bins) modulo the pulse period. To maintain a good counting statistics 64 phase bins were chosen, giving a sampling time of ~ 20 ms per phase bin. After background subtraction, the unpulsed flux was determined as the minimum flux in each pulse profile. Subsequently, the unpulsed flux was subtracted and the remaining pulse normalized to unity relative to the maximum flux in each energy band. Finally the flux maximum was shifted to pulse phase zero in each profile. The resulting pulse profiles are shown in Fig. 7.4 and Fig. 7.5 for all orbits and the five energy bands mentioned. For clarity the pulse profiles are plotted over two pulse phases and the vertical dashed line marks pulse phase zero. In addition, the pulsed fraction is calculated for each orbit and energy band. The pulsed fraction is defined as:

$$F_{\text{pulsed}} = \frac{\langle F \rangle - F_{\text{min}}}{\langle F \rangle} = 1 - \frac{F_{\text{min}}}{\langle F \rangle} \qquad (7.3)$$

where F_{min} is the minimum and $\langle F \rangle$ the mean count rate observed. F_{pulsed} gives the percentage of pulsed flux versus unpulsed flux. Since Poisson noise complicates an accurate determination of F_{min}, the pulse profiles have to be smoothed. This was done for observations during earlier phases of the turn-on where noise dominates the pulse profile (orbits 00–06, the times of the dips around orbits 10–14 and orbits 19–20, and the time shortly before and after the eclipse, orbits 21–22).

7.2.1 Time Dependence

The time dependence of the pulse profile is shown in Fig. 7.4 and 7.5 for the time of the turn-on. At the beginning of the turn-on (see Fig. 7.4, orbits 00–03) all energy bands are affected by strong noise. The pulse profiles show almost sinusoidal pulse shapes which are similar to the profiles observed at the beginning and later phases of low-state (Deeter et al., 1998; Scott et al., 2000). Later on, during orbit 04–09, only lower energy channels ($E = 0$–6.5 keV) are affected by low signal to noise ratio, while at higher energies ($E > 6.5$ keV) the pulse signature becomes more and more pronounced. This indicates that during these times photoelectric absorption and scattering
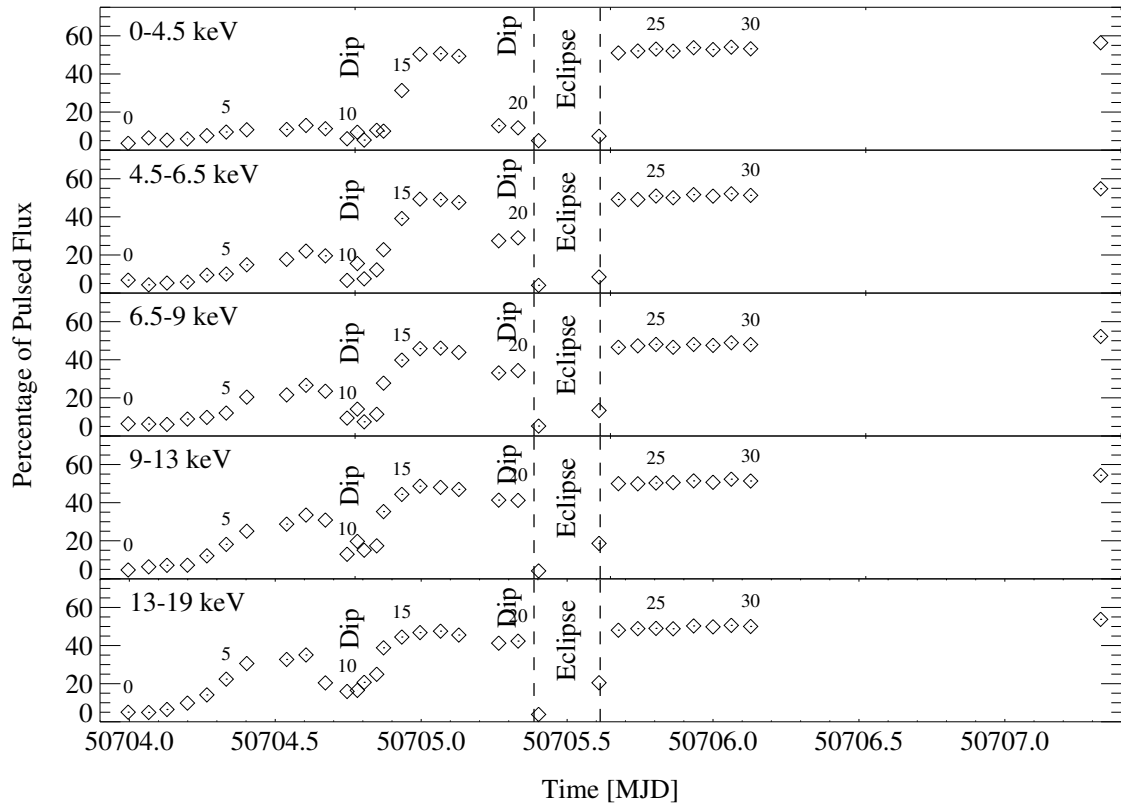
Figure 7.3: Energy dependent pulsed fraction for the time of the turn-on. The uncertainties shown are 1σ uncertainties. For a discussion see text.

in an optical thick medium are the dominant processes (cf. section 3.5). For the time of the anomalous dip (orbit 10–13) the pulse profile shows a similar shape as during the beginning of the turn-on. The amplitude of the sinusoid at lower energies, however, is smaller compared to those of orbit 03–05 and especially for orbits 10 and 11 where no pulsations can be detected below 6.5 keV. During the eclipse (orbit 21) no pulsed flux can be detected. After orbit 23 the pulse shape stays constant.

To summarize, in contrast to the turn-off of the main-on or later phases during the short-on the *intrinsic* pulse shape does not change significantly over the time of the turn-on. This result is in agreement with earlier findings of, e.g., Gruber et al. (1980), Bai (1981), Trümper et al. (1986), or Deeter et al. (1998). In other words, the pulse profile observed at the beginning of the turn-on can be interpreted as the main-on pulse profile, which is modified by the influence of photoelectric absorption and scattering.

The amount of pulsed flux relative to unpulsed flux is shown in Fig. 7.3 for the same energy bands and time. It is clearly visible that F_{pulsed} increases more rapidly in the high energy bands. At lower energies, the pulsed flux is suppressed towards the beginning of the turn-on. This is similar to the situation observed during egress of the anomalous dip, where the pulsed flux increases faster at higher energies. At the end of the turn-on, after orbit 23, the pulsed fraction is almost constant.
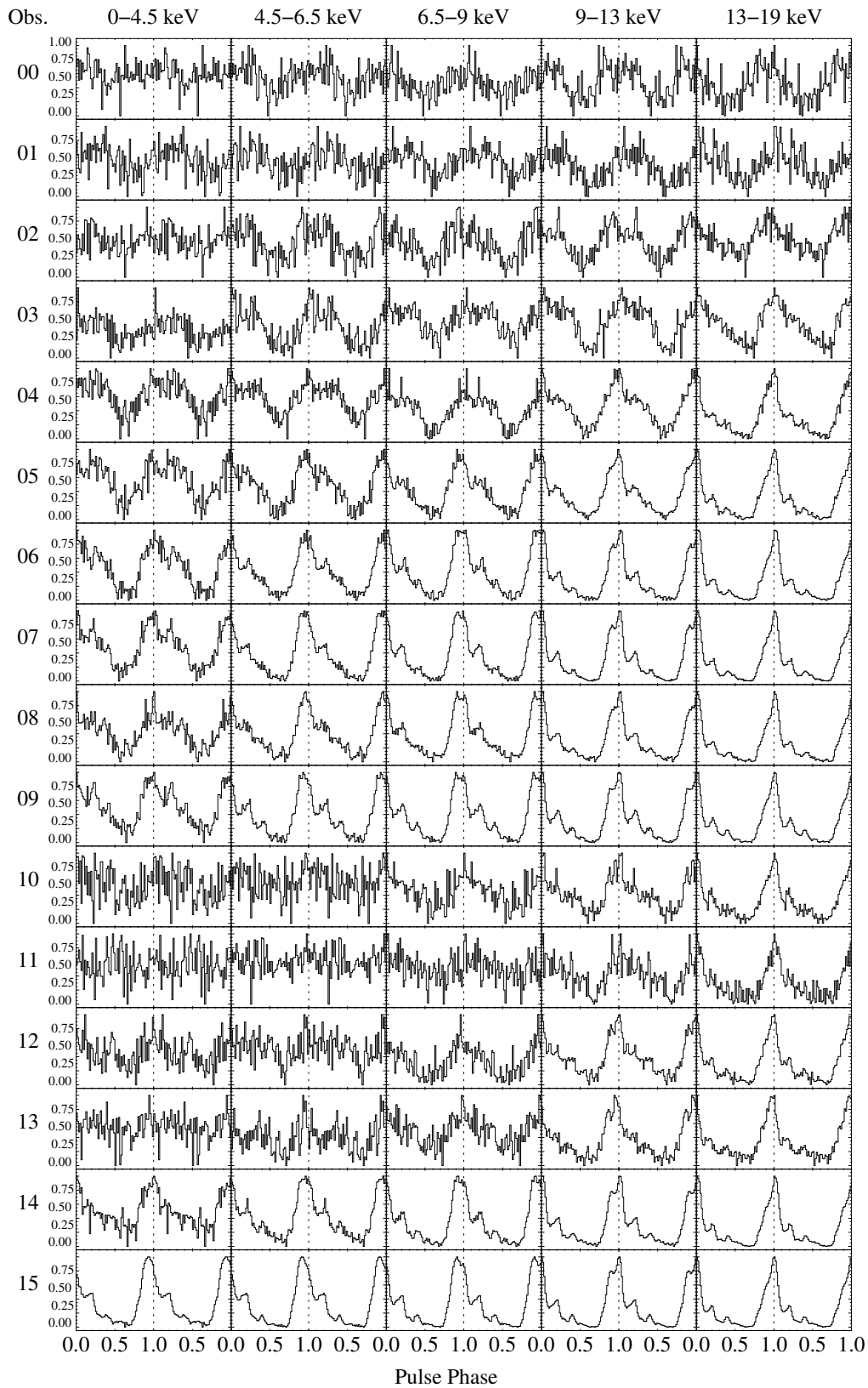
Figure 7.4: Evolution of the pulse profile for orbit 00–15. All profiles are normalized to unity at the maximum of the main pulse, after subtraction of the off-pulse constant flux. Phase 0 is defined as the maximum of the main pulse in the energy band of 13–19 keV.
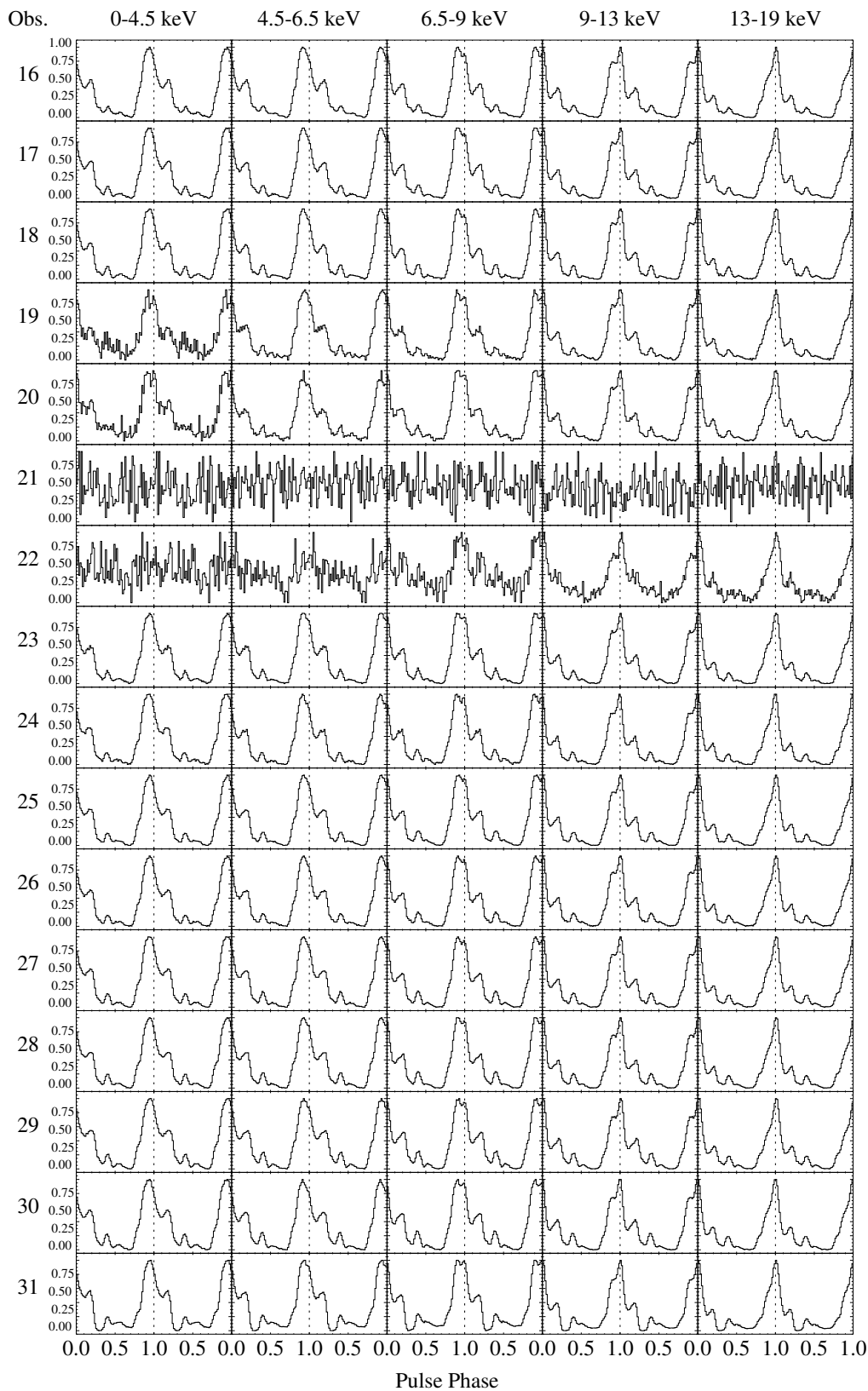
Figure 7.5: Evolution of the pulse profile for orbit 16–31. All profiles are treated in the same way as described for Fig. 7.4.
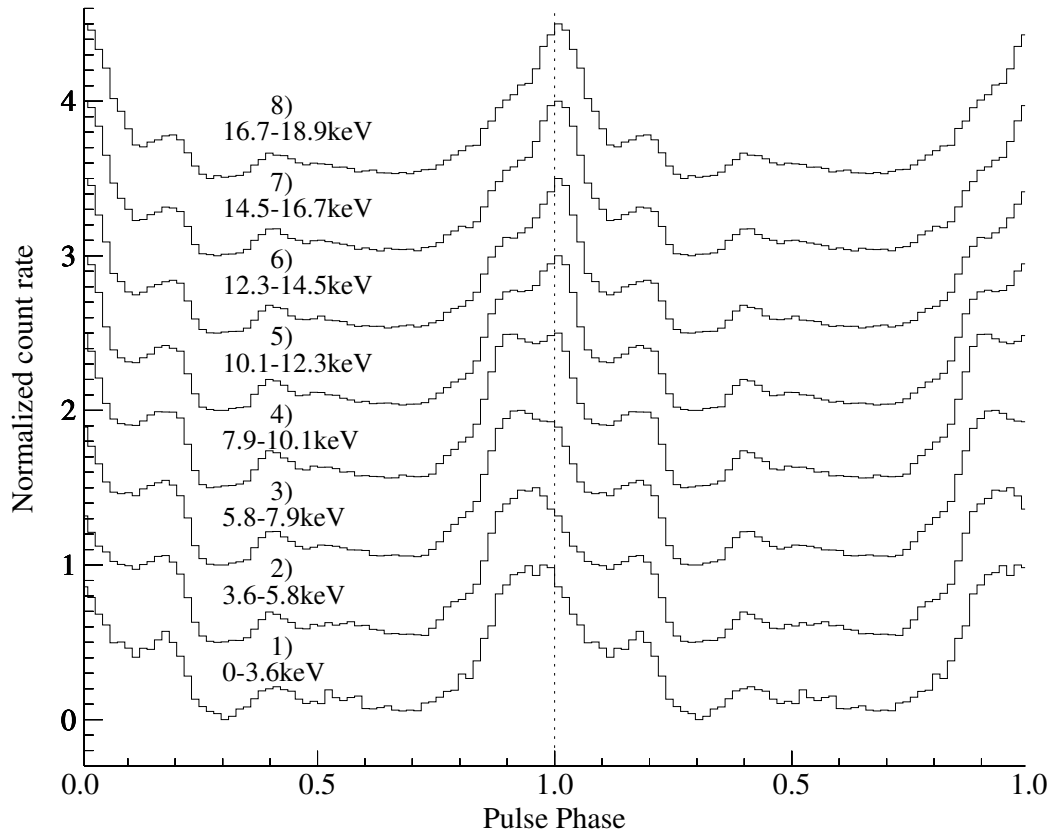
Figure 7.6: The energy dependence of the pulse profile illustrated using the profile observed in orbit 31. All pulse profiles shown are normalized to unity and each profile, except the profile of the energy range 0–3.6 keV, is shifted by 0.5 in the *y*-direction relative to the previous profile. Note the double peaked structure of the hard central peak close to pulse phase 1.0.

7.2.2 Energy Dependence

It is known from various observations that the shape of the pulse profile changes with energy (e.g., Soong et al., 1990a; Scott et al., 2000, and references therein). Fig. 7.6 shows energy dependent pulse profiles observed in orbit 31. All pulse profiles shown are treated in the same way as described for Fig. 7.4. For clarity an offset of 0.5 in *y*-direction is added to each pulse profile, except the pulse profile labeled with (1).

The most obvious change visible in Fig. 7.6 is the increasing amount of flux in the soft leading shoulder with decreasing energy. This leads to a double peaked structure around the hard central peak in the energy band 7.9–10.1 keV. Towards lower energies the interpulse peak shows a double peaked structure which is most prominent in the energy range of 0–3.6 keV. In parallel, the gap between the hard central peak an the soft trailing shoulder is more distinct at low energies and the flux in the soft trailing shoulder relative to the hard central peak is slightly increasing with decreasing energy. This behavior confirms recent findings of Scott et al. (2000) and is consistent with earlier observations of, e.g., Soong et al. (1990a).
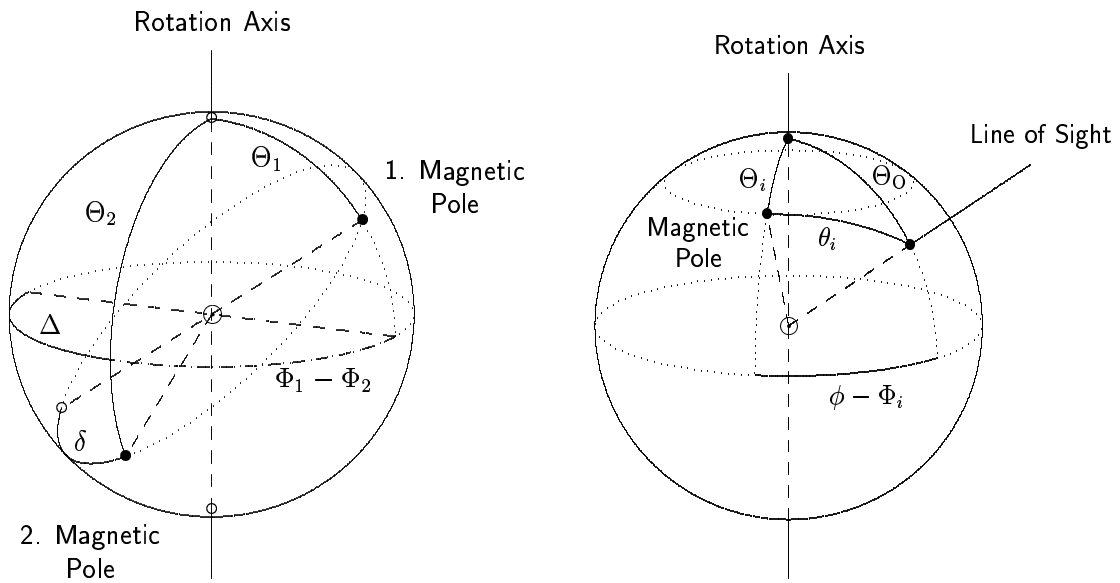
Figure 7.7: Left: Schematic view of the neutron star surface and the two magnetic poles. δ marks the offset angle between the first and second magnetic pole which causes the asymmetry observed in the pulse profile. Θ_1, Θ_2 and Φ_1, Φ_2 are the polar and azimuthal position angles of the magnetic poles. Right: Position of the emission region relative to the magnetic pole and line of sight of the observer. The viewing angle θ_i depends on rotational phase or pulse phase ϕ, respectively (Fig. 3.1 and 3.2, Blum, 2000).

7.2.3 Emission Geometry

In case the neutron star is directly visible for the observer (e.g., during main-on), a pulse profile represents the superposed flux emerging from both neutron star poles (hot spots) and the accretion column depending on the neutron star's rotational phase. The intrinsic emission characteristic of each neutron star pole is a function of several parameters, such as the geometry of the emission region, which is affected by the structure of the accretion column. In addition, the magnetic field structure, and energy and angle dependent emission processes like resonant cyclotron scattering or Compton scattering are key parameters in understanding the structure of the emission geometry and consequently the observable pulse profile and its time and energy dependence. In general the emission characteristic can be described as a *pencil beam* or *fan beam* characteristic, or a superposition of both. Since the accretion disk partially covers the neutron star, only parts of the emission region are visible for a distant observer at a certain time which further complicates the situation. However, the current theoretical understanding of the emission geometry and processes involved is not good enough, to give a satisfying self-consistent explanation of the pulse profile and its evolution.

A mere geometric interpretation of the pulse shape can be given, using the method of Blum & Kraus (2000). This approach is independent of any kind of emission model. It permits to determine the beam pattern of the magnetic poles, which is the flux $f(\theta_i)$ measured by a distant observer depending on the angle θ_i between the direction of observation and the magnetic field axis. This method allows to decompose the pulse profile into its contributions from the two poles, taking into account effects like relativistic light bending in the gravitational field of the neutron star. Such a decomposition is applicable under the assumption that the pulse profile $f(\phi)$ of a single pole is axial symmetric with respect to rotational phase ϕ: $f(\Phi - \phi) = f(\Phi + \phi)$. The asymmetry of
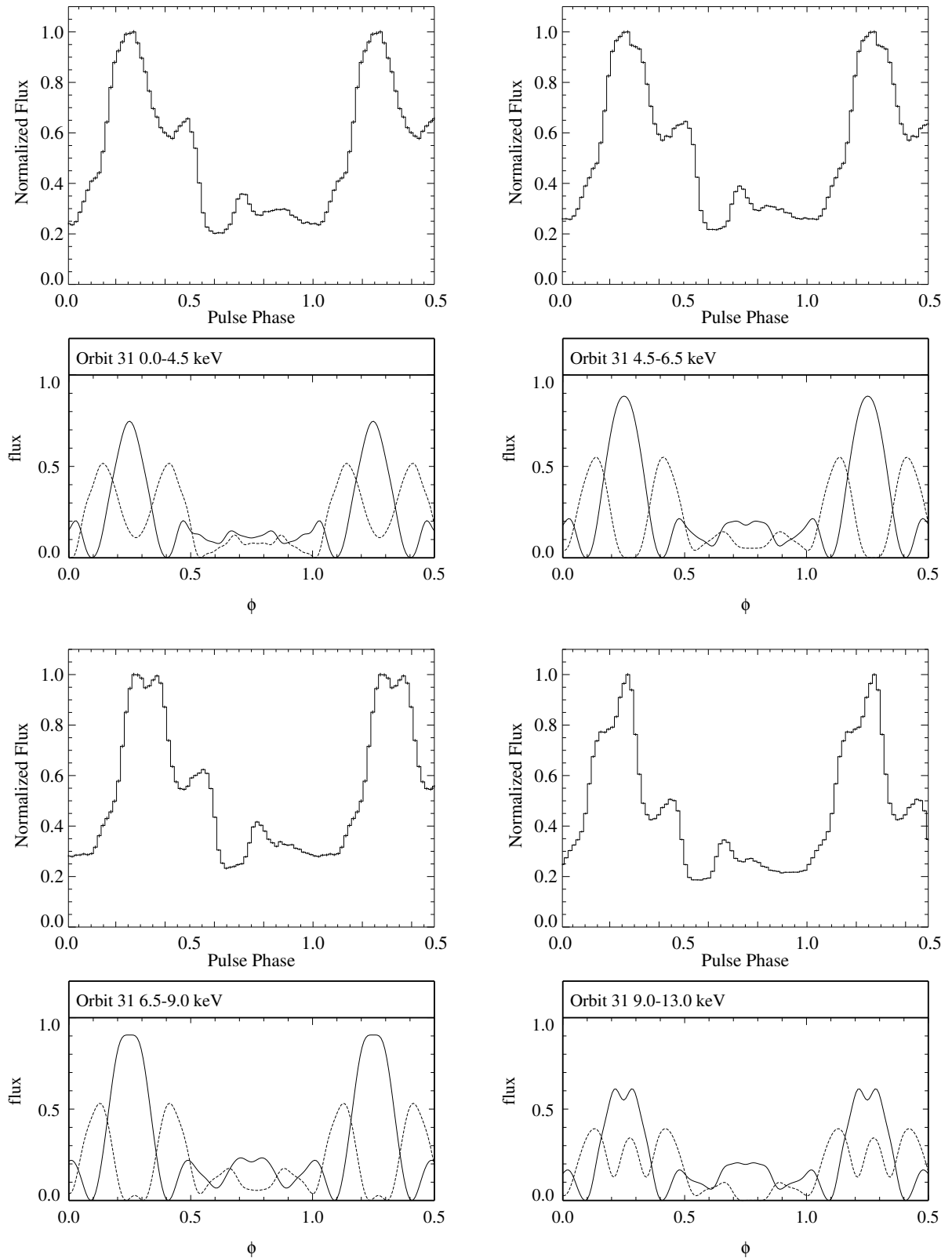
Figure 7.8: Decomposition of the observed pulse profile of orbit 31 into two single pole contributions. The results for the following energy ranges are shown, top left and right panel: 2.0–4.5 keV and 4.5–6.5 keV, bottom left and right panel: 6.5–9.0 keV and 9.0–13.0 keV. For each energy range the observed pulse profile and the decomposition in single pole contributions is shown. The dashed and solid lines represent the contributions of the two poles.
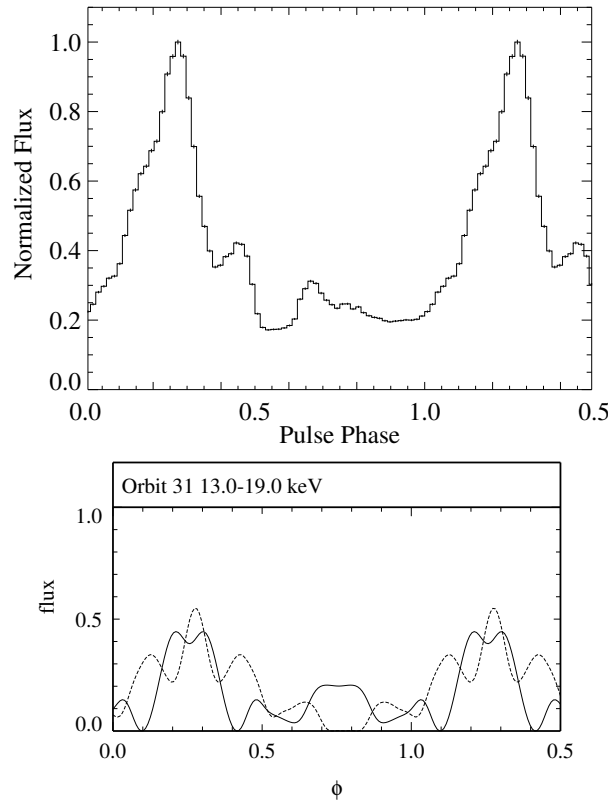
Figure 7.9: The same as Fig. 7.8 for the energy range: 13.0–19.0 keV.

the observed pulse profile is then caused by a non-antipodal location of the magnetic poles with an offset angle δ (see Fig. 7.7).

A decomposition of the pulse profile of the turn-on observation was applied to energy dependent pulse profiles of orbit 31 (in collaboration with S. Blum) to determine the flux contributions of the two poles and the angular dependence of the emission characteristic (Kuster et al., 2001b). The resulting decomposition and the corresponding observed pulse profiles are shown in Fig. 7.8 and Fig. 7.9. For an inclination $i = 83°$ of the binary system Her X-1/HZ Her the analysis yields $\theta_1 = 18°$ and $\theta_2 = 159°$, and an offset angle of $\delta \lesssim 5°$. This result indicates that the magnetic field configuration of Her X-1 only slightly deviates from an ideal dipole like geometry.

According to this decomposition, the peak which is most pronounced in low energy bands around phase 0.25 (see Fig 7.8) can be interpreted as the *pencil beam* contribution of one pole, while the double peaked structure consisting of peaks at phases 0.1 and 0.4 is caused by a *fan beam* component of the opposite pole. Comparing these results with the corresponding observed pulse profiles, the *pencil beam* component can be directly attributed to the hard central peak and the *fan beam* component to the soft leading and trailing shoulder of the observed pulse profile. In contrast to this, the interpulse contains flux contribution from both poles. Since the flux contribution of the peak at phase 0.25 decreases with increasing energy, the flux observed in the soft leading and trailing shoulder relative to the hard central peak changes in the same manner. Therefore the hard central peak will become broader towards lower energies.

A more detailed explanation and the theoretical background of the pulse decomposition method can be found in Blum & Kraus (2000) and Blum (2000). Additional results for Her X-1 in general and for the turn-on observation are presented in these publications, too.

7.2.4 $35^{\rm d}$ **Dependence**

Several authors tried to interpret the change in pulse shape depending on ϕ_{35} described in section 6.2.2 in terms of a geometric interpretation, where a warped and twisted accretion disk periodically covers the line of sight of the observer to the emission regions on the neutron star poles. Earlier and more simple geometric models like the one presented by Bai (1981) cannot explain the complex changes of the pulse profile in all details. Therefore more complex models are needed.

Since the scale hight of the inner accretion disk rim is comparable to the diameter of the neutron star, emission from the two poles is affected differently in time when parts of the inner disk parts start to obscure the neutron star. In terms of the pulse decomposition model this means that, e.g., the flux in the first peak of the *fan beam* component at phase 0.1 is expected to change differently in time compared to the flux in the *pencil beam* component at phase 0.25, since both originate from different poles (see Fig. 7.8). Furthermore, even the intensity of the two peaks of the *fan beam* at pulse phase 0.1 and 0.4 can change differently in time, when assuming that those are caused by an *extended* and *ring*-like emission region close to one pole. Then parts of this ring can be covered by the disk while another part is still visible and consequently the apparent intensity variation of the peaks at pulse phase 0.1 and 0.4 of the pulse decompositions shown in Fig. 7.8 will be asymmetric. Such a geometric model can explain the observed asymmetric changes of the pulse profile shown in Fig. 6.5, where the soft leading shoulder disappears first at the end of main-on before the soft trailing shoulder. This interpretation is similar to the recently published model of Scott et al. (2000), which can reproduce the pulse evolution in many details. The model relies on a very complex and empirical emission geometry composed of *fan* and *pencil beam* like emission regions located close to both neutron star poles. Additional flux contributions arise from radiation scattered by material being accreted and located above the neutron star poles close to the magnetosphere.

The situation during turn-on is different. Assuming that the turn-on is caused by the influence of the outer accretion disk rim slowly freeing the line of sight to the neutron star, the density gradient in the material is much smaller as compared to the inner disk rim. Furthermore, the size of the covering region is much larger compared to the X-ray emission regions on the neutron star. Consequently, the neutron star can be assumed as a point like source. In this case radiation emerging from both poles experiences the same absorption and the pulse shape does not change appreciably, as is indeed observed during turn-on (see Fig. 7.4 and 7.5).

7.3   **Spectral Evolution**

As Davison & Fabian (1977), Parmar et al. (1980), or Becker et al. (1977) have shown, a combination of direct, scattered, and absorbed photons is observed during early phases of the turn-on. The *PCA* spectra of selected orbits shown in Fig. 7.10 qualitatively confirm these findings. During the first orbits 00–15 the low energy spectrum ($E < 8.0\,{\rm keV}$) is heavily absorbed and the iron emission line at 6.4 keV is pronounced. As a consequence, a spectral model is needed which combines an absorbed and scattered, and an unaffected spectral continuum model in order to describe the observed data consistently over the time of the turn-on. Before introducing the spectral model used for the analysis in detail, the analytical description of the continuum flux has to be motivated.

Unfortunately, there are still no self consistent theoretical models existing which can reproduce the shape of the continuum spectrum in X-ray binaries in general. As a consequence, phenomenological models have to be used for fitting the spectra. It was shown in section 6.4 that the observed
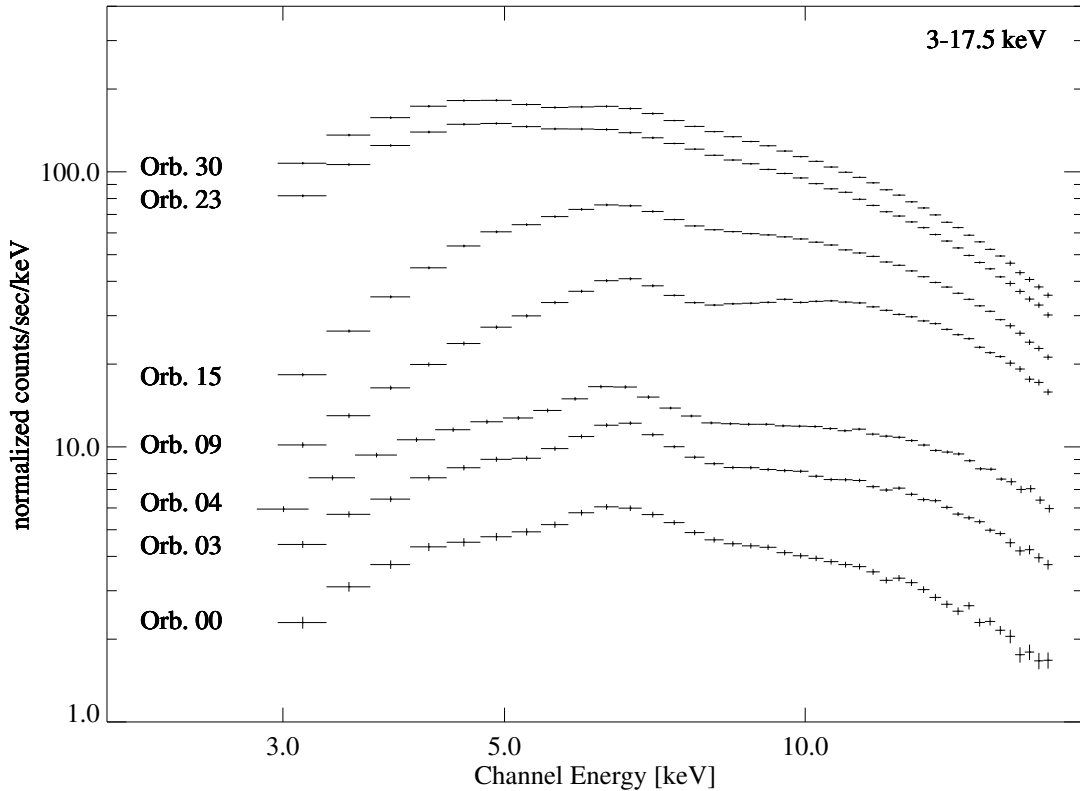
Figure 7.10: *PCA* spectra of selected orbits in the energy range of 3–17.5 keV. The influence of photoelectric absorption below ≈ 7 keV and Fe fluorescent emission at 6.4 keV is clearly visible.

spectrum of Her X-1 follows the shape of a power-law with an exponential drop in flux above ≈ 20 keV. During the past, several analytical models which can reproduce this spectral shape with different accuracy have been proposed. The standard models generally used, are a power-law with high energy cut-off (`highecut`), a power-law with a Fermi-Dirac cut-off (`fdcut`), or a combination of two power-laws with opposite signs and an exponential cut-off (`npex`). A short introduction to these models and their analytical description is given in the manual of the XSPEC package (Arnaud & Dorman, 2002) or in Kretschmar (1996) and Kreykenbohm (2003). A general problem which arises when using the `highecut` model is its discontinuity around the cut-off energy E_{cut} which causes a sudden break in the model spectrum. Since observed spectra from X-ray binaries do not show such a break, the use of this model can result in unphysical residuals during a spectral fit for energies close to E_{cut} (Kretschmar, 1996). This problem and further aspects are discussed in detail by Kreykenbohm (1997) and can be avoided using, e.g., the `fdcut` or `npex` models which both have a continuous and smooth shape. Nevertheless these two models have other disadvantages. Especially when using the `fdcut` model the folding energy E_{fold} and the cut-off energy E_{cut} show large uncertainties when fitting spectra of Her X-1 (Stelzer, 1997). Spectral fits using the `npex` model have problems in determining an accurate N_{H} of absorbed spectra. For low values of N_{H} the curvature of the spectrum at $E < 10$ keV can either be modeled by variation in photon indices and E_{fold} of the `npex` model or by changing N_{H} of the absorption model. For the analysis of the turn-on observation a spectral model has to be found which reduces systematic effects to a minimum. In the following section I will introduce the complex spectral model used to fit the observed spectra during the turn-on, before presenting the results of the analysis.

7.3.1   Spectral Model for the Turn-On

For the analysis of the turn-on data, the `highecut` model was used as a continuum model (f_{highe}), because it can reproduce the observed data best with respect to determining accurate values of N_{H} (see also the discussion in Stelzer, 1997). As further components a cyclotron line feature at $\approx 39\,\mathrm{keV}$ using the analytical model of Mihara et al. (1990) (f_{cyc}), and a Gaussian emission line at $\approx 6.4\,\mathrm{keV}$ (f_{Fe}) has to be added. For orbits 15 and later an additional blackbody component with $kT = 0.19\,\mathrm{keV}$ (f_{BB}) improves the χ^2_{red} of the fit noticeably (DalFiume et al., 1998). These components represent a basic spectral model called *Primary spectrum*, which can well reproduce the shape of observed spectra of Her X-1 during the main-on.

For the turn-on the spectral model has to be expanded, because the influence of photoelectric absorption at the beginning of the turn-on has to be taken into account. This can be done by introducing an energy dependent multiplicative factor $a(E)$, which accounts for Thomson scattering and photoelectric absorption (see Eq. 7.4). A second component, which is identical to the primary spectrum, accounts for unaffected radiation. Such a spectral model is called a *partial covering model* and is given analytically by:

$$\frac{dN(E)}{dE} \;=\; B \cdot (1 + a(E)) \cdot \underbrace{(f_0(E) + f_{\mathrm{BB}}(E) + f_{\mathrm{Fe}}(E))}_{\text{Primary Spectrum}} \tag{7.4}$$

with

$$a(E) \;=\; \underbrace{e^{-N_e \sigma_{\mathrm{T}}}}_{\text{Thomson-Scattering}} \cdot\; C \;\cdot\; \underbrace{e^{-N_e \sigma_{\mathrm{bf}}}}_{\text{Absorption}} \tag{7.5}$$

and

$$f_0(E) \;=\; f_{\mathrm{power}}(E) \,\cdot\, f_{\mathrm{highecut}}(E) \,\cdot\, f_{\mathrm{cyc}}(E) \tag{7.6}$$

where $dN(E)/dE$ is the differential photon flux in units of photons $\mathrm{cm}^{-2}\,\mathrm{s}^{-1}\,\mathrm{keV}^{-1}$, the constant C gives the ratio between absorbed and scattered radiation, and the unaffected primary spectrum, the normalization factor B accounts for the difference in absolute flux measured in *PCA* and *HEXTE* (section 5.3.3) and is needed when fitting data of both instruments simultaneously, σ_{T} is the Thomson cross section, and the bound-free absorption cross sections, σ_{bf}, are those used in the `phabs` model of XSPEC. Especially for large N_{H}, using the standard Morrison & McCammon (1983) absorptivity (the `wabs` model of XSPEC) does result in unphysical residuals, which may be caused by weak absorption edges that are not taken into account for in the `wabs` model. Using the cross sections of Bałucińska-Church & McCammon (1992) (the `phabs` model of XSPEC) removes this problem. However, the resulting N_{H} values are smaller than those inferred from the `wabs` model. For the fitting, the absorption and scattering part in equation 7.5 uses the same N_{H}. During the remainder of this work the unaffected model component will be called MC I and the second component, influenced by absorption and Thomson scattering, will be referenced as MC II.

A physical and geometric interpretation of this spectral model is schematically shown in Fig. 7.11. Photons directly reaching the observer, indicated as solid line and marked with A, contribute to the primary and unaffected spectrum (MC I). Photons absorbed in cold material and partially scattered out of the line of sight are associated with beam B. These photons contributes to the flux of the spectral model component MC II. Using such a spectral model, it is possible to separate MC I from MC II during the fit process of the model spectrum to the observed spectrum (beam A and beam
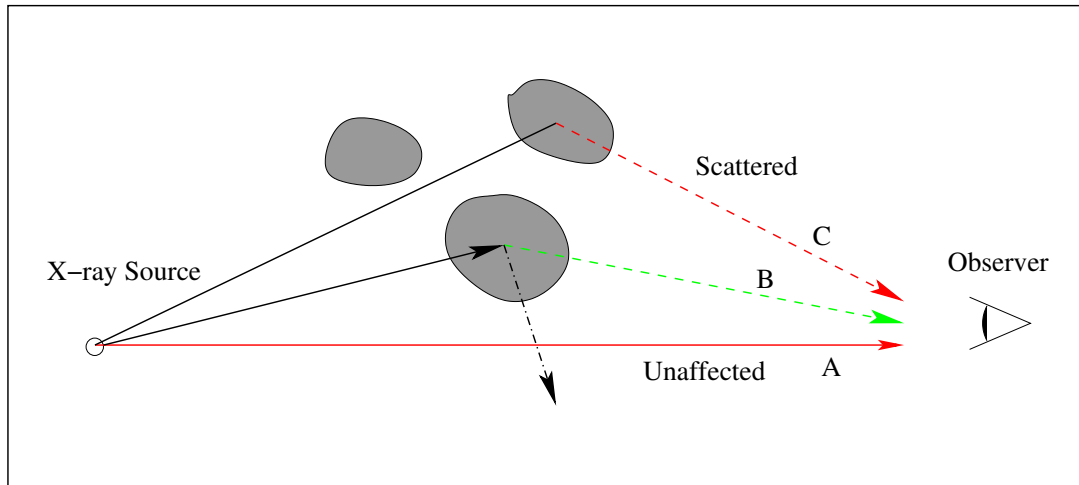
Figure 7.11: Schematically illustration of a partial-covering model. Three components contribute to the overall spectrum, unaffected direct radiation (solid line, beam A), and radiation absorbed in cold material and further reduced in flux by Thomson scattering (dashed line, beam B). Beam C corresponds to photons scattered into the line of sight.

B respectively) from the overall observed spectrum because of their different spectral shape. In contrast, flux scattered into the line of sight (beam C) has the same spectral shape as the MC I, since Thomson scattering is energy independent in first order approximation. Consequently these photons will contribute to the flux of the model component MC I and cannot be separated from the overall spectrum by a mere spectral analysis.

7.3.2   Evolution of Spectral Parameters

Using this spectral model all 32 spectra over the turn-on were fitted in a first iteration with all fit parameters free except the power-law index α which was kept fix at 1.068. This value is equal to the mean value obtained from the analysis with α set free, of the data of orbit 15–31. Further it is consistent with results of earlier observations (e.g. Stelzer, 1997). As an example the resulting fit for orbit 15 is shown in Fig. 7.12 with residuals shown in the lower panel. The $\chi^2_{\rm red}$ of 0.92 for this fit indicates that the model spectrum is an acceptable description of the observed data. The results of all fits are given in Tab. A.2 and Tab. A.3 in the appendix.

Parameter	Value
α	1.068
$E_{\rm cut}$	21.5 keV
$E_{\rm fold}$	14.10 keV
$E_{\rm cyc}$	39.9 keV
$\sigma_{\rm cyc}$	5.1 keV

Table 7.2: Parameters kept fixed for the fitting of the spectra over the time of the turn-on .

This analysis reveals that the folding energy $E_{\rm fold}$, $E_{\rm cut}$, $E_{\rm cyc}$, $\sigma_{\rm cyc}$, and $\sigma_{\rm Fe}$ show no significant variation over the duration of the turn-on (see Fig. 7.14). Note that the drop in $E_{\rm cut}$ observed during the beginning of the turn-on (panel (c) in Fig. 7.13) is due to low counting statistics above 20 keV, which prevents an accurate determination of $E_{\rm cut}$ and $E_{\rm fold}$ for these times. The constant C shows strong correlation with $A_{\rm power}$ for observations later than orbit 16, since for low values of $N_{\rm H}$, C in Eq. (7.5) simply acts as further normalization factor.

To prevent this effect, a value of $C = 1.0$ was used for observations later than orbit 16. In a second iteration, the parameters given in Tab. 7.2 are kept fix for the further analysis to their mean values shown. Leaving these values fixed allows to determine the variation of the remaining free parameters.

Figure 7.12: Simultaneous fit to *PCA* and *HEXTE* A and B spectra of orbit 15 in the energy range of 3–17.5 keV for *PCA* and 16.5–100 keV for *HEXTE* A and B. As spectral model a partial covering model is used as described in the text. The χ^2_{red} for this fit is 0.92 with 101 degrees of freedom (dof).

The results of the second iteration are shown in Fig. 7.14. Assuming a simple geometrical model of the turn-on where the outer edge of the accretion disk opens the line of sight to the central neutron star, the neutral column density N_{H} is expected to gradually decrease when the flux increases. The behavior of observed N_{H} is contrary to this simple model. Panel (a) of Fig. 7.14 shows the evolution of the neutral column density, N_{H}, deduced from the spectra. It is apparent that N_{H} increases during the beginning of the turn-on. This evolution goes in parallel to the amount of scattered and absorbed radiation, shown in Fig. 7.14 panel (b), which increases until orbit 09 and afterwards starts to decline. Only later on (later than orbit 05), N_{H} mirrors the count rate indicating that photoelectric absorption is the cause for the changing amount of flux (cf. Fig. 7.1 and panel (c)). After orbit 16, N_{H} becomes untraceable. Note that the turning point in the progression of C, which lies between orbit 04 and 05, matches almost exactly the maximum in N_{H}. The normalization of the iron emission line, A_{line}, and of the power-law, A_{power}, reproduce the progression of the count rate (cf. Fig. 7.1).

For comparison, the galactic neutral column density N_{H} in the direction of Her X-1 is $N_{\mathrm{H}} = 1.79 \times 10^{20} \, \mathrm{cm}^{-2}$. This is an interpolated value of N_{H} using the program nh of the HEASOFT 5.1 package. The data base used by this software goes back to the interstellar atomic hydrogen map of Dickey & Lockman (1990), which is derived from measurements of hydrogen Lyman-α and 21 cm line emission.
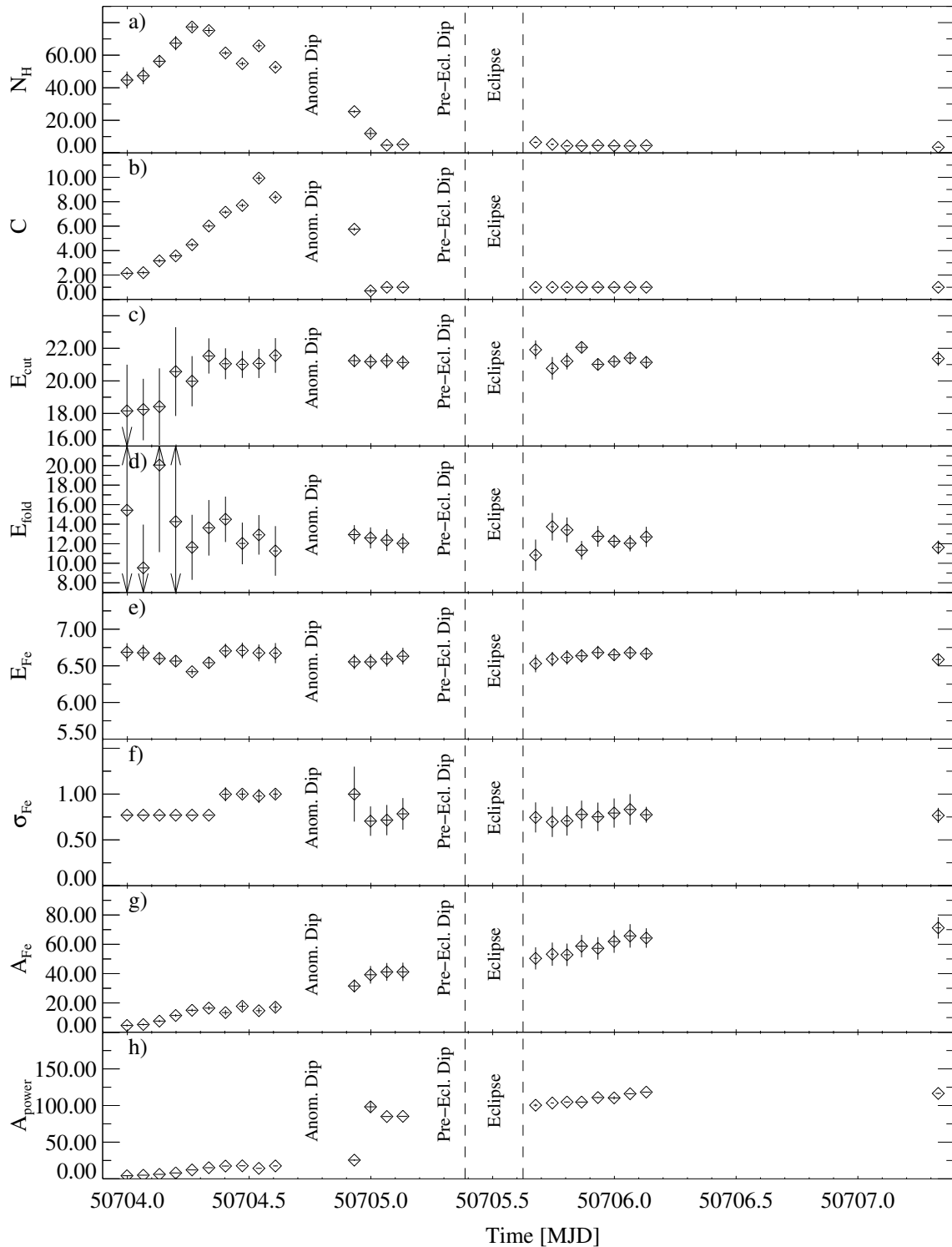
Figure 7.13: Evolution of the spectral parameters for orbits 00–31 of the turn-on: (a) N_H ($\times 10^{22}\,\mathrm{cm}^{-2}$), (b) Ratio C between the flux in the scattered and absorbed spectral component, and the primary spectrum, (c) cut-off energy E_{cut} (keV), (d) folding energy E_{fold} (keV), (e) Energy of Gaussian emission line E_{Fe} (keV), (f) width of the Gaussian emission line σ_{Fe} (keV), (g) normalization of the Gaussian emission line ($\times 10^{-4}$ photons $\mathrm{keV}^{-1}\,\mathrm{cm}^{-2}\,\mathrm{s}^{-1}$ at 1 keV). The uncertainties shown are 1σ confidence levels ($\Delta\chi^2 = 2.71$).
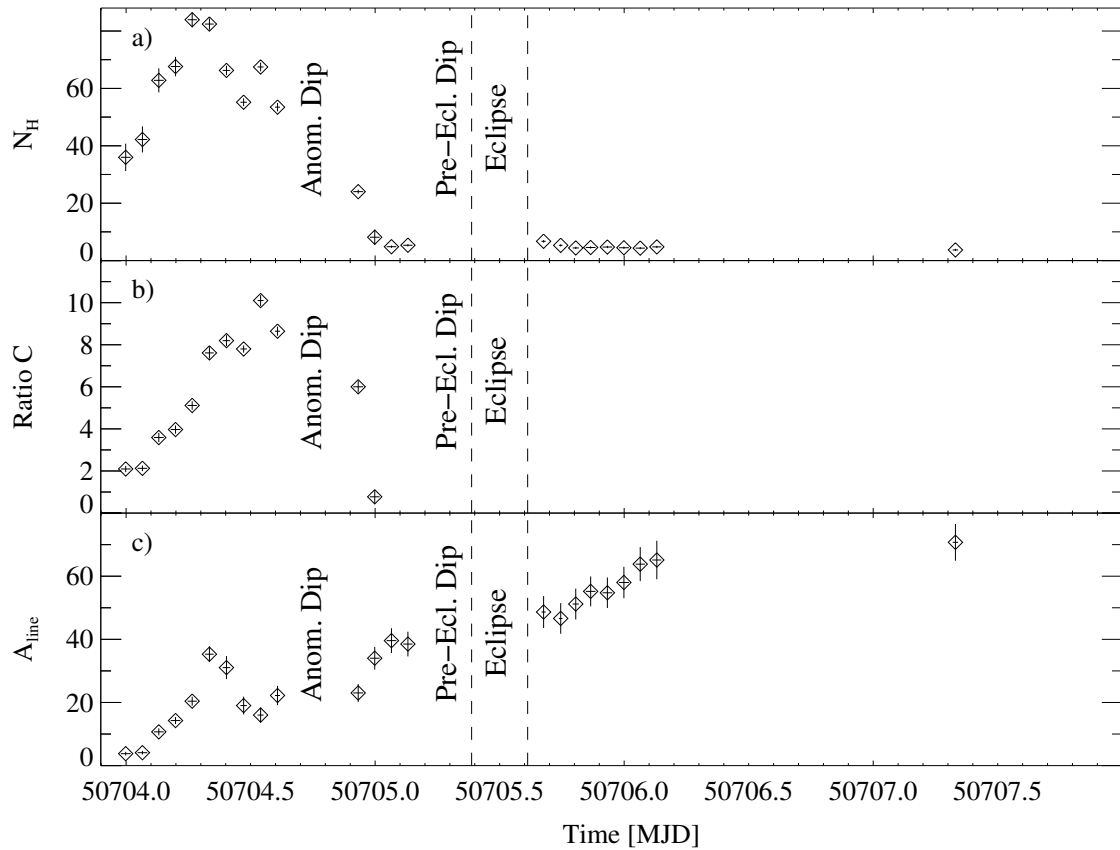
Figure 7.14: Evolution of the spectral parameters after keeping the parameters given in Tab. 7.2 fix during the fitting process. From top to bottom: (a) N_{H} ($\times 10^{22}\,\mathrm{cm}^{-2}$), (b) ratio C between the absorbed and scattered spectral component, and an unaffected, direct component, and (c) normalization of the iron line A_{line} ($\times 10^{-4}$ photons keV^{-1} cm^{-2} s^{-1} in the line). The uncertainties given are $\pm 1\,\sigma$ confidence levels.

7.3.3 The Magnetic Field Strength of the Neutron Star

As shown in section 3.3, the magnetic field strength of the neutron star is directly related to the energy of the line centroid E_{cyc} of a CRSF. An accurate determination of the line centroid energy of a CRSF crucially depends on a "good" analytical description of the spectral continuum flux and needs pulse phase resolved spectroscopy. In Kunz (1996b) various continuum models are critically analyzed with respect to an accurate determination of E_{cyc} in Her X-1. Since a comparison of different spectral continuum models and phase resolved spectroscopy is beyond the scope of this work, I used the spectral model introduced in section 7.3.1 to determine E_{cyc} from phase averaged spectra. For the analysis only data with high signal to noise ratio above an energy of $E > 20\,\mathrm{keV}$ is used, which is the data of the observations of orbit 24 and later. The mean energy found for the CRSF is $E_{\mathrm{cyc}} = 39.9 \pm 0.9\,\mathrm{keV}$. Using this value and Eq. (3.7) the resulting magnetic field strength for Her X-1 is $B = 4.10 \times 10^{12}$ Gauss, which is in a good agreement with the result of, e.g., Gruber et al. (2001).
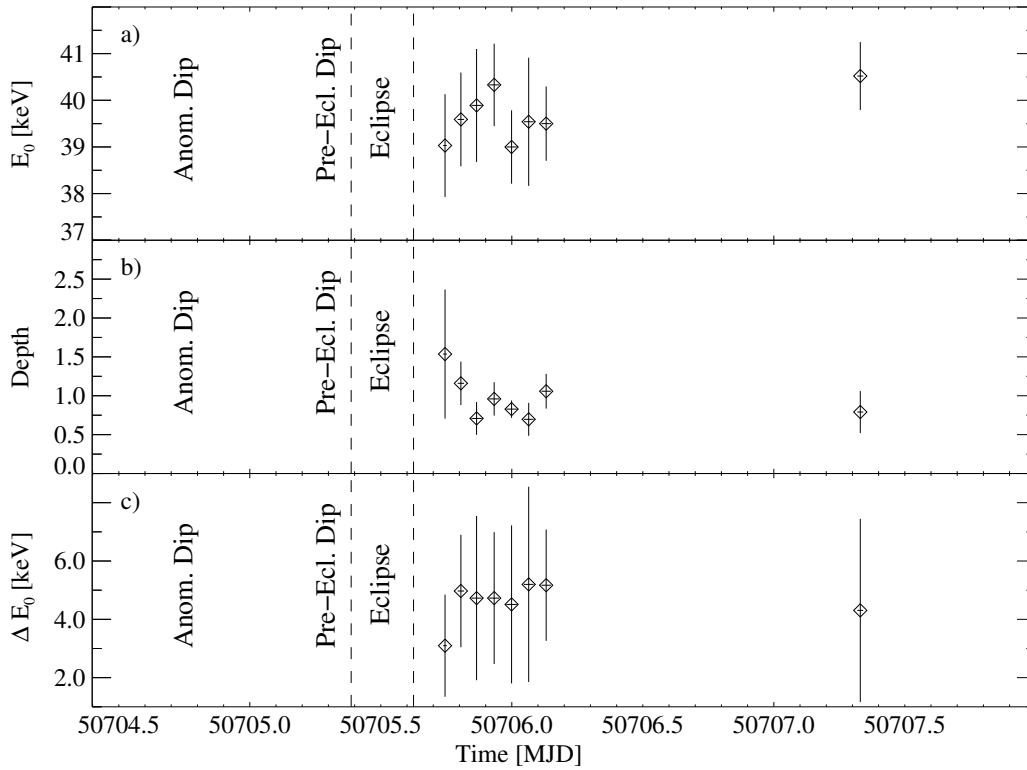
Figure 7.15: The cyclotron resonant scattering feature in Her X-1. From top to bottom: The energy of the line centroid E_{cyc}, the the width of the line ΔE_{cyc} ($\equiv 1/2 \cdot$ FWHM), and the depth of the line.

7.4   Geometric Model of the Turn-On

To interpret the results of the spectral and temporal analysis, it is essential to understand the geometric situation during the turn-on. A physically more realistic model compared to a simple absorption model takes into account the influence of a hot accretion disk corona located above and below the accretion disk. Such a geometric model is schematically shown in the left panel of Fig. 7.16. The position of the accretion disk, the disk corona, and the location of the observer is given for different times of the turn-on. The observed *PCA* spectra corresponding to the phases of the turn-on and the unfolded spectral model components are shown in the right panel for $3 \leq E \leq 12\,$keV. The individual components of the spectral model are shown separately. The observed spectrum is plotted as solid line, the model component MC I as dotted line, the absorbed and scattered model component MC II as dashed line, and the iron emission line is marked by a dash dotted line. For the orbits 17 and 27, the additional blackbody component is partially visible at energies $< 4\,$keV.

At the beginning of the turn-on, Thomson scattered radiation from the corona, which is partially observed in absorption, dominates the apparent spectrum. The top most image "Beginning of turn-on" illustrates the orientation of the disk and the location of the observer relative to the disk for this time. Photons following beam A, marked by a dashed line, are scattered in the corona and partially absorbed in the disk rim (beam C). The direct view to the neutron star at this time is still blocked and photons following beam B cannot reach the observer. The corresponding spectra are those observed in orbits 00 and 04. Apparently the spectral model component MC I dominates the observed spectral flux and only a small fraction of absorbed flux can be detected. As a result, the
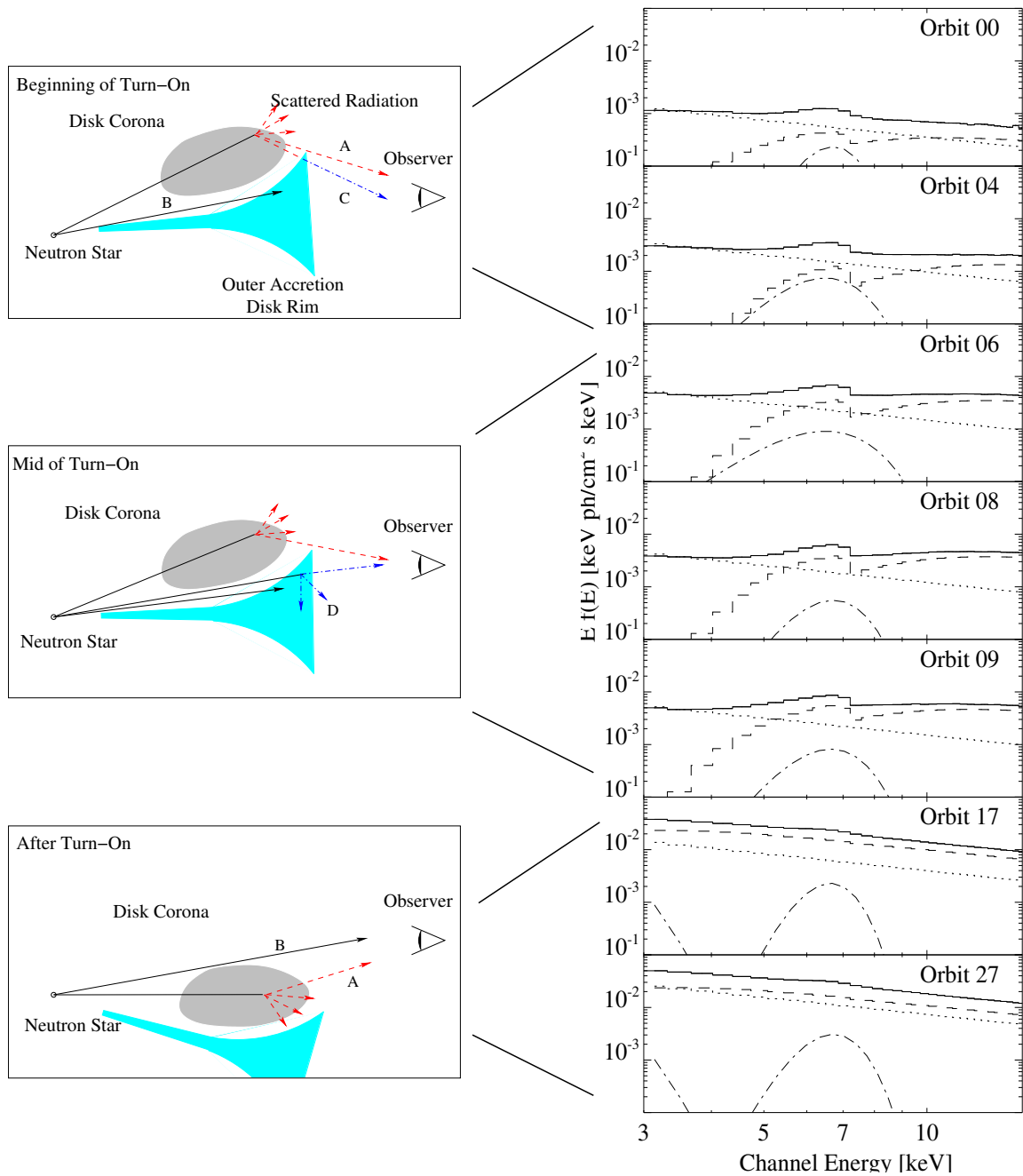
Figure 7.16: Left panel: Schematic view of the outer accretion disk rim, the accretion disk corona, and the neutron star for subsequent times during the turn-on. The location of the observer is indicated on the right side. Note, the images are not to scale. Right panel: Unfolded *PCA* spectra and the components of the spectral model for selected orbits. The following components are shown: solid line – the observed spectrum, dotted line – spectral model component MC I, dashed line – spectral model component MC II, and dash dotted line – iron line emission and blackbody component.

total observed spectrum, which is the sum of all model components, shows only a weak signature of absorption and small values of N_H are measured.

Since the disk moves downwards, the parts visible of the corona increase and therefore the flux in MC I. In parallel, the apparent absorbed flux increases as well, because the disk becomes more and more transparent for photons scattered in the corona (beam C). Around the mid of the turn-on, the outer disk rim starts to become optically thin for photons directly coming from the neutron star following beam D ("Mid of turn-on"). As a consequence the flux in component MC II (the ratio C in Fig. 7.14) rises more rapidly compared to the flux of MC I. Since component MC II determines the curvature of the total observable spectrum, N_H apparently raises. Now MC II further gains in influence, until it dominates the spectrum, which takes place right after the turning point in the track of N_H shown in panel a) of Fig. 7.14.

Shortly before the anomalous dip the apparent N_H rapidly starts to decrease, while the disk opens the view to the neutron star. Both components MC I and MC II are now indistinguishable (orbit 17 and later) because photoelectric absorption becomes negligible. At lower energies the flux of the blackbody component starts to rise slowly after orbit 15. Based on the interpretation of Cheng et al. (1995), this indicates that more and more photons from the inner parts of the accretion disk close to the neutron star reach the observer. Finally, at the end of the turn-on, the neutron star is directly visible when the main-on starts.

7.4.1   The Spectral Model Compared to the Geometric Model

As shown in the sections before, the spectral behavior during the turn-on can be described by a combination of an unaffected direct spectral component (MC I) and an absorbed and scattered spectral component (MC II). For this analysis a simplified partial covering model was used as spectral model to fit the observed data. Using a physically more realistic model which treats scattered, absorbed, and direct flux separately we can distinguish at least four components contributing to the overall spectrum which are (see Fig. 7.16):

- Beam A: An indirect component representing radiation scattered into the line of sight, i.e., the primary spectrum as modified by scattering.

- Beam B: A direct component representing the unaffected primary spectrum.

- Beam C: An indirect component, representing the primary spectrum modified by photoelectric absorption.

- Beam D: An Indirect component representing radiation scattered out of the line of sight, i.e., the primary spectrum as modified by scattering.

In this model, photons following beam A contribute to the flux which originates in photons scattered in the corona into the line of sight of the observer. This component is unknown and cannot be determined from the observed data with a mere spectral analysis. The contributions of beam C and beam D can be associated with the spectral model component MC II. The direct component beam B is equivalent to the model component MC I in the partial covering model.

Unfortunately, using a partial covering spectral model, which treats scattering separately, it is not possible to observationally separate beam B and beam A from the overall spectrum. The reason lies within the nature of Thomson scattering which is independent of energy. Thus Thomson scattering acts as a further normalization factor during the spectral fitting as explained in section 7.3.2 and

prevents to determine the underlying amount of N_e by spectral analysis. In the following chapter an attempt is made to combine the analysis of the pulse shape and the spectral analysis to determine N_e in an independent way.

Chapter 8

Combined Temporal and Spectral Analysis

8.1   Introduction

So far, a separate spectral analysis and a temporal analysis has been considered to gain information on the physical parameters of the outer parts of the accretion disk and an accretion disk corona. While the spectral analysis has a quantitative character giving physical parameter values depending on time, the temporal analysis was interpreted qualitatively only (the energy dependent changes in pulse shape). The interpretation of the results lead to a phenomenological model of the turn-on. Following this approach, it is not possible to get more information on the scattering medium which is supposed to be an accretion disk corona. As outlined in section 7.2, the shape of the observable pulse profile changes significantly and the pulsed signature is steadily "washed out" towards the beginning of the turn-on. This can be understood following the theoretical models presented in section 3.5 as the influence of a Compton scattering medium and photoelectric absorption, which both are apparent from the spectral analysis. The underlying physical parameters are the N_H of the absorbing material, and the N_e of the scattering medium, respectively. Since the shape of the pulse profile changes in a characteristic way after passing through a scattering medium, the observed pulse profile can be used to derive N_e of the underlying scattering plasma. To do so, the shape of the pulse profile is simulated depending on N_e, N_H, and the size of the scattering region using an observed "template" pulse profile. Subsequently, these simulated pulse profiles are compared to the observed pulse profiles to derive N_e and the size of the scattering region. In this chapter I will introduce the analysis method used, which combines both the spectral analysis and the results of the temporal analysis. Finally the results are presented in section 8.2, followed by a discussion in chapter 9.

8.2   Simulating Pulse Variation

To simulate the pulse variation observed during the turn-on of Her X-1 shown in Fig. 7.4 and 7.5, the Green's function $G_{E_1,E_2}(\mu, E_0, t, t_0)$ is needed. Furthermore, the intrinsic emission characteristic of the neutron star of Her X-1, represented by the pulse profile, has to be known. Since the main-on is attributed to the time when the neutron star of Her X-1 is directly visible to the observer, it is a good approximation that the pulse shape seen at the end of the turn-on (beginning of the main-on) is not or only weakly affected by matter in the accretion disk or accretion disk corona. This is also apparent from the pulse decomposition which gives similar results for the emission geometry of the two neutron star poles at the end of the turn-on and during the main-on. In addition, it is well

known that the pulse shape observed during the main-on is stable even over long time periods, like years (Scott et al., 2000). For these reasons, the pulse profile observed during, e.g., orbit 30 can be used as an approximation for the intrinsic pulse shape and as a "template" pulse profile, to investigate the effects of a scattering and absorbing corona on the pulse shape depending on N_e, N_H, the size, and geometry of the scattering region. Comparing simulated pulse profiles directly to observed pulse profiles, while keeping all physical parameters variable would fail, since the number of degrees of freedom is too large. Using the results for N_H from the spectral analysis reduces the number of free parameters and allows to fit observed versus simulated pulse profiles.

To do so, the Green's function $G_{E_1,E_2}(\mu, E_0, t, t_0)$ was calculated for five energy ranges similar to those used for the temporal analysis of the pulse profile in section 7.2.2 for two cases:

1. $G_n(t, t_0, E_1, E_2)$ for a neutral corona, with N_H taken from the spectral analysis shown in Tab. A.3 for each single orbit.

2. $G_{ion}(t, t_0, E_1, E_2)$ for a fully ionized corona with $1.0 \times 10^{22}\,\text{cm}^{-2} \leq N_e \leq 9.5 \times 10^{25}\,\text{cm}^{-2}$.

The spectral distribution of the incident photons for the simulations follows a power-law with high energy cut-off for both cases. The output of the simulations is beneath the Green's function, the spectral distribution of the photons leaving the slab. Comparing Eq. (3.27) with the partial covering model used for spectral modeling (see Eq. 7.4) reveals that the Green's function G_{ion} corresponds to the spectral model component MC I and G_n to the spectral model component MC II. Consequently using G_n with the respective N_H for each orbit derived from the spectral analysis and variable G_{ion} depending on N_e, the pulse profiles an observer located at infinity would see can be simulated by applying Eq. (3.23) to the "template" pulse profile. Because the time scale of the simulated Green's functions is normalized to the thickness of the slab geometry d, different values of d can be achieved by simply rescaling the time. For the analysis, d was chosen between 0.1 and 6 light seconds, appropriate for the dimension of the accretion disk in Her X-1 with $R_{disk,in} \approx 1.0 \times 10^8\,\text{cm}$ and $R_{disk,out} \approx 2.0 \times 10^{11}\,\text{cm}$ (Cheng et al., 1995). Since the output of the Monte Carlo simulation is a Green's function with arbitrary normalization, the Green's function needs to be normalized properly to the observed photon flux in each spectral energy band. From the spectral fitting of the partial covering model to the observed spectra, the parameters of the spectral model components MC I and MC II are known. By integrating the differential photon flux of the model spectra over the specific energy bands, the total flux per energy range can be calculated. Using the integrated photon flux both Green's functions, G_n and G_{ion}, can be normalized to the observed flux according to:

$$\int_{t_0}^{t_1} \int_0^{\infty} R(h, E) N_{ph}(E, t)\, dE\, dt = \int_{-\infty}^{t} G_{E_1,E_2}(t, t')\, dt \tag{8.1}$$

where $N_{ph(E)}$ is the differential photon flux and $R(h, E)$ the detector response matrix. Assuming that the pulse profile is normalized to unity

$$\int_0^1 I_{E_1,E_2}(p)\, dp = 1 \tag{8.2}$$

where p is the the pulse phase, the total Green's function $G_{E_1,E_2}(\mu, E_0, t, t_0)$ calculates from Eq. (3.27).

In Fig. 8.1 the resulting total $G_{E_1,E_2}(E_0, t, t_0)$ for one specific optical depth $\tau_e = 5.0$ is shown, using the spectral model of orbit 09 ($\tau_n \approx 0.3$) for normalization. The bottom panel of Fig. 8.1 gives the corresponding pulse profiles for different τ_e after folding the template profile with $G_{E_1,E_2}(E_0, t, t_0)$. The template profile used is the same as the one shown in the top panel of Fig. 8.2. The Green's
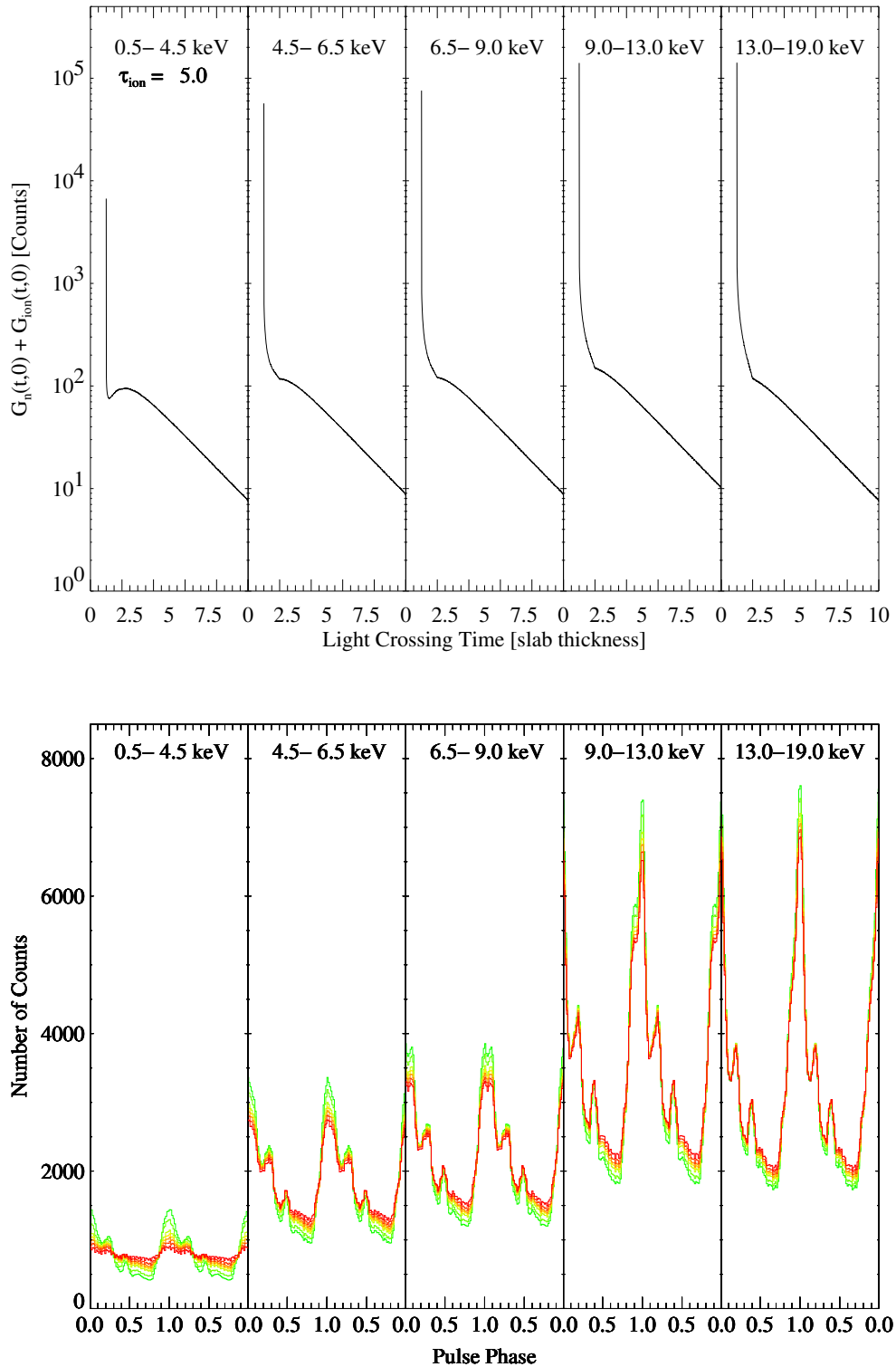
Figure 8.1: Top panel: Simulated Green's function $G_{E_1,E_2}(E_0, t, t_0)$ for orbit 09 and five different energy bands. For each energy band the total Green's function is calculated according to Eq. (3.27), with $\tau_n \approx 0.3$ and $\tau_e = 5.0$. All Green's functions are normalized to the spectral model flux derived from the spectral analysis. Bottom Panel: Corresponding simulated pulse profiles for different values of $\tau_e = 0.5, 1.5, 2.0, 2.5, 3.0,$ and 5.0 (increasing τ_e from green, to yellow, to red). The observed pulse profiles are shown in the top panel of Fig. 8.2.
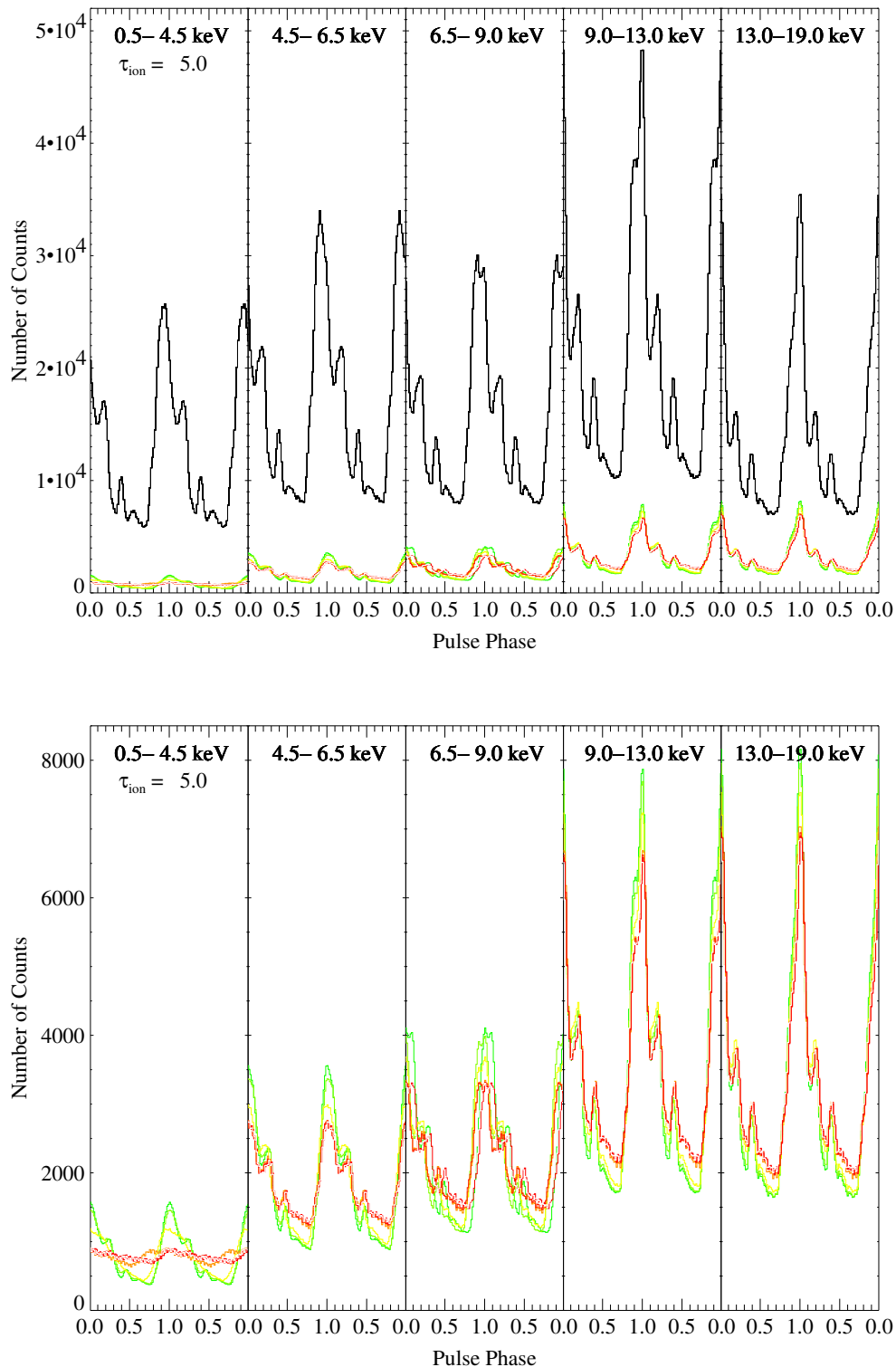
Figure 8.2: Top panel: Simulated pulse profiles for different values of the thickness *d* of the slab. The pulse profile plotted in black $I_{t_0}(t)$ represents the intrinsic intensity distribution (template pulse profile). The colored pulse profiles are the resulting simulated pulse profiles for $\tau_e = 5$ and $\tau_n \approx 0.3$. For any further explanation see text. Bottom panel: Enlarged plot of the simulated pulse profiles of the top panel. The thickness of the slab increases with the change in color from green, yellow to red ($d = 0.01$–0.6).
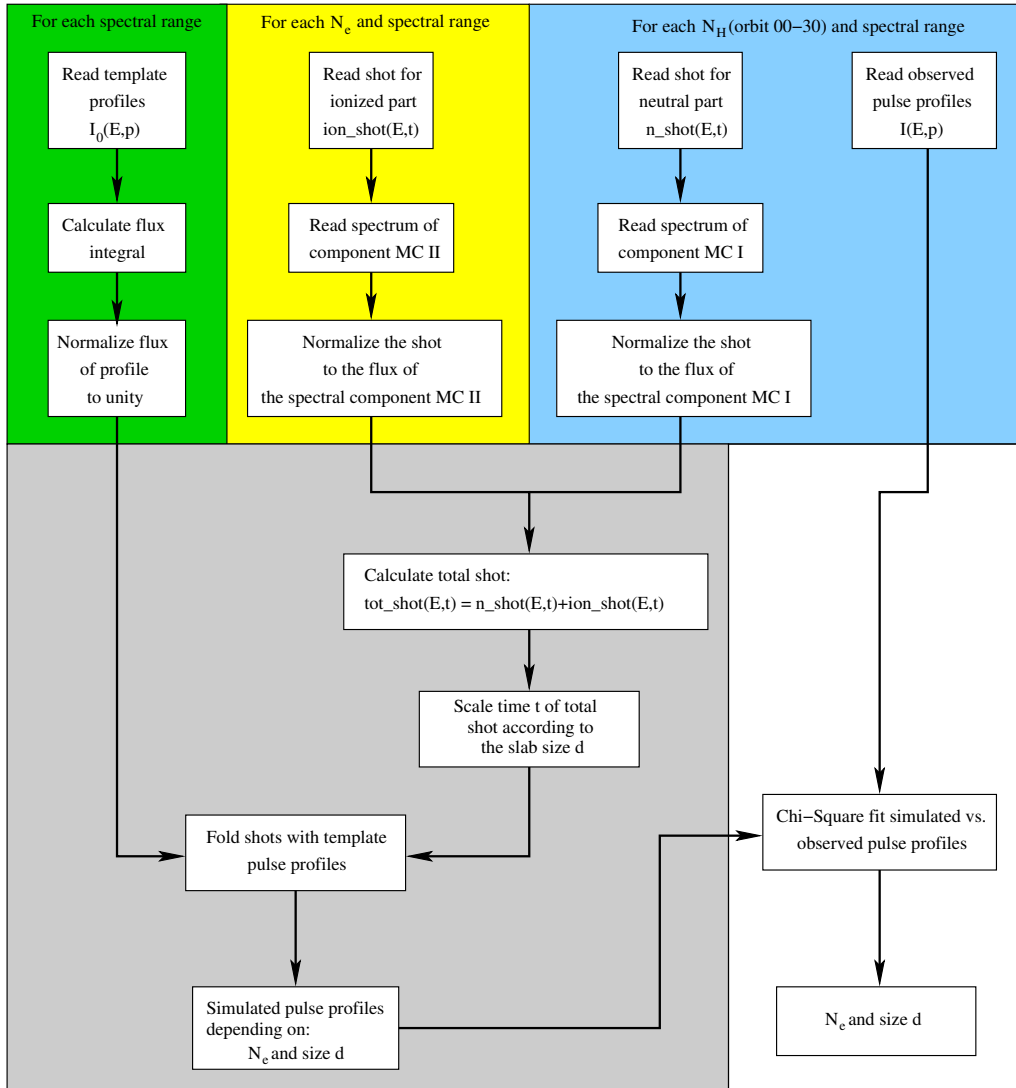
Figure 8.3: Schematic view of the pulse profile simulation code. For a detailed explanation see text.

functions given in the top panel of Fig. 8.1 show a strong peak at low diffusion times (diffusion time close to unity) in all energy bands which is typical for photons crossing the scattering medium directly. This strong peak is predominantly caused by photons of the spectral model component MC II which pass a medium of small optical depth ($\tau_{\mathrm{n}} \approx 0.3$). The tail towards higher diffusion times visible from the track of $G_{E_1,E_2}(E_0, t, t_0)$ solely comes from scattered photons contributed by the ionized spectral component MC I. These photons are the origin for the "smearing" of the pulse profile. From this plot it is obvious that the total Green's function is dominated by photons of the model component MC II at high energies while the contribution of model component MC I is significant only in the low energy bands ($E < 6.5\,\mathrm{keV}$). For earlier times during the turn-on (increasing N_{H}) the relative contribution of MC I at low energies starts to become more important since absorption reduces the flux contribution of G_{n}. This energy dependence is also apparent from the shape of the simulated pulse profiles shown in the bottom panel of Fig. 8.1. In the low energy band up to 4.5 keV the pulses are washed out (the pulsed fraction is reduced), while at higher energies this effect is very weak. Furthermore, the flux in low energy bands is reduced due to
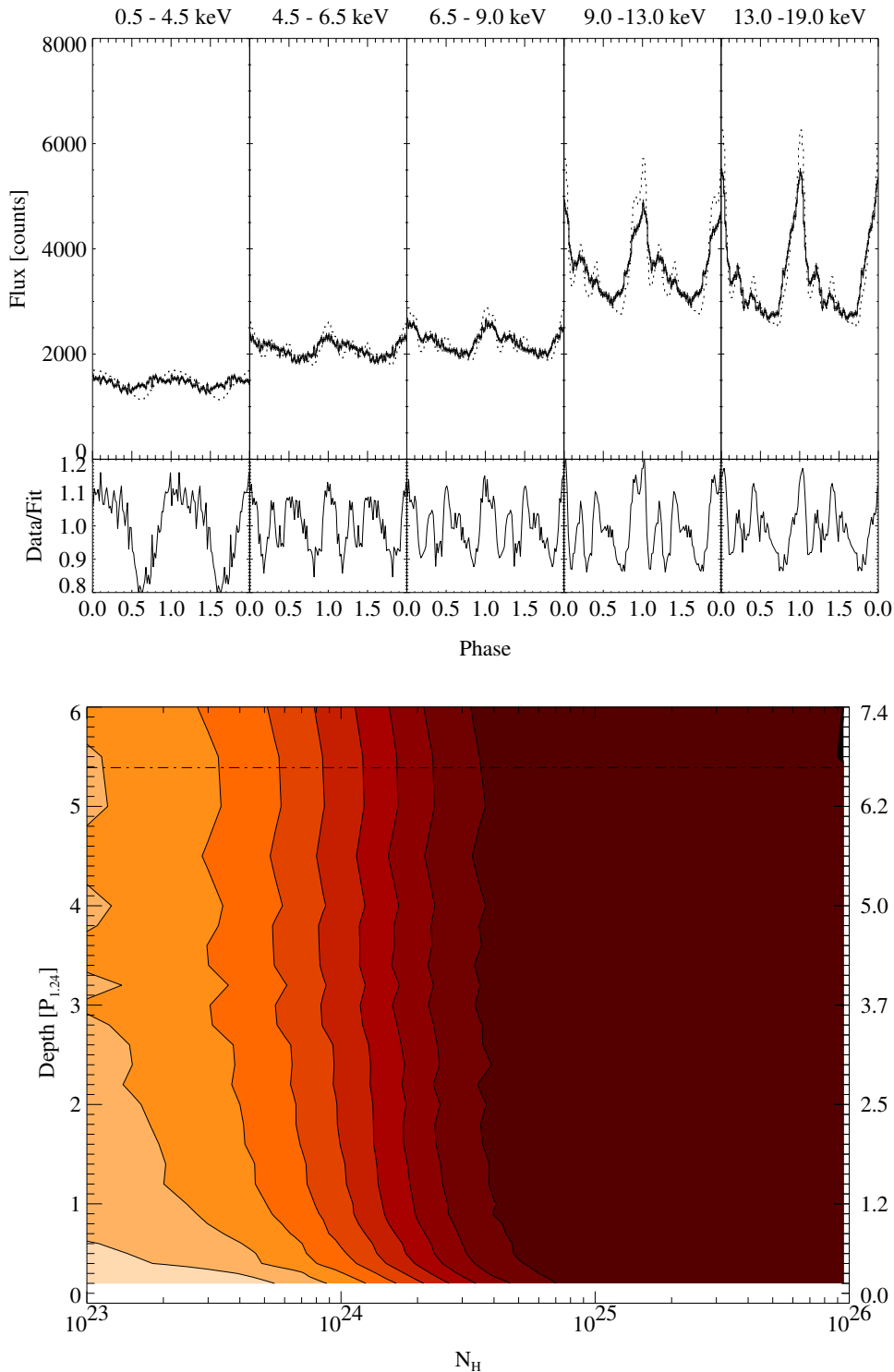
Figure 8.4: Top panel: Result of a fit of *simulated* to *observed* pulse profiles for the observation of orbit 05. The observed pulse profile is plotted as solid line, while the simulated and fitted pulse profile is plotted as dashed red line. The residuals of the fit are plotted below. Bottom panel: Thickness of the scattering medium d versus the optical depth given in units of N_e are shown as χ^2 contour plot. The darkest red area corresponds to a 1σ confidence level. The dash-dotted horizontal line marks the distance of the outer accretion disk rim from the neutron star.
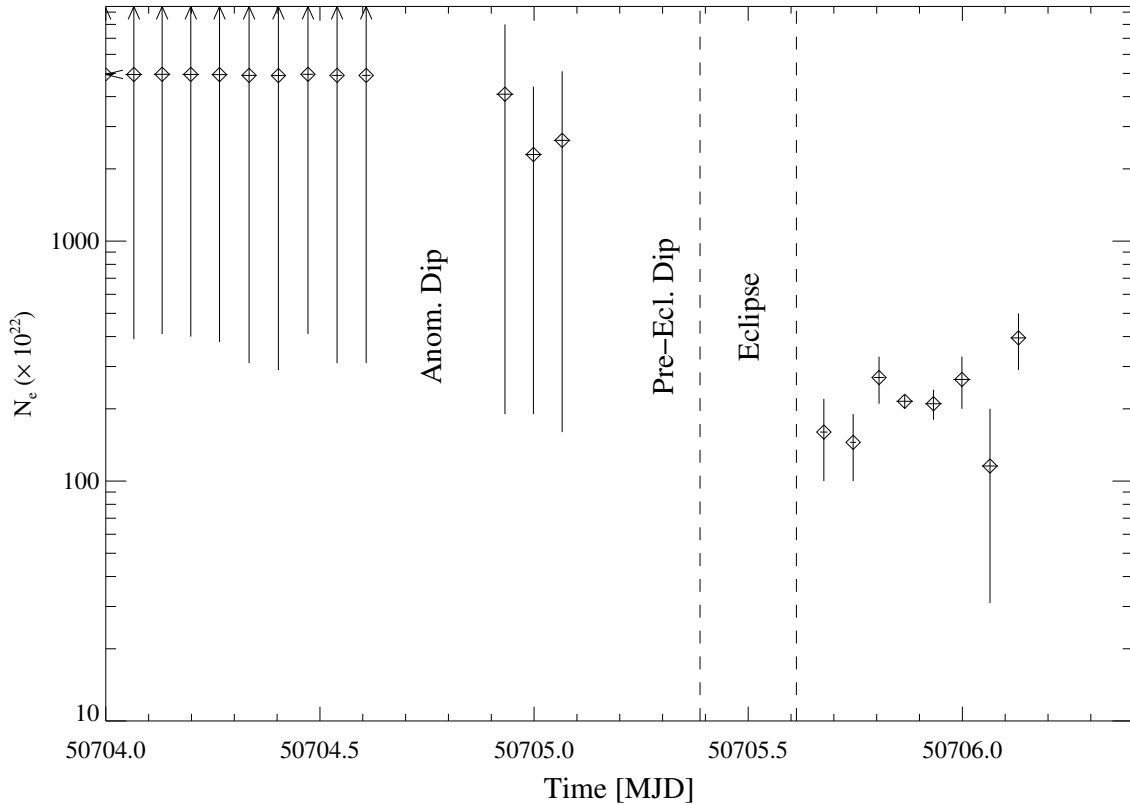
Figure 8.5: Time dependence of N_e derived by fitting simulated to observed pulse profiles. The upper and lower limits are 1σ confidence levels.

absorption. The influence of the thickness d of the scattering region on the simulated pulse profiles is shown in Fig. 8.2. In the top panel the template pulse profile together with the simulated profiles are given. An enlarged plot of the simulated profiles is shown in the panel below. Similar to the pulses shown in Fig. 8.1, lower energies are affected stronger by different values of d for similar reasons as for the τ_e dependency, the flux of model component MC I accounts for the smearing of the pulse profiles and dominates at low energies.

8.2.1 Pulse Fitting

Following the procedure schematically shown in Fig. 8.3, pulse profiles were simulated for all values of N_H given in Tab. A.3 and their flux normalized for all observations of the turn-on. The normalization was calculated according to Eq. (8.1) from the spectral model components MC I and MC II. Finally, a χ^2 minimization fit of *simulated* to *observed* pulse profiles was performed for each single *RXTE* orbit. Thereby the different energy ranges where fitted simultaneously. This procedure allows to determine N_e, and d as well as their uncertainties. As an example the results of orbit 05 are shown in Fig. 8.4. In the top panel the simulated profile (dashed line) and the observed data (solid line) are shown, as well as the residuals of the fit. The corresponding χ^2 contour plot is given in the panel below, with 1σ confidence contours shown as the darkest red area and the dimension of the accretion disk, indicated by a dash-dotted horizontal line.

The results for orbit 05 indicate that qualitatively the simulated pulse profiles can well repro-

duce the observed pulses in all energy bands. From the residuals it is apparent that there are still deviations between simulated and observed profiles which are most prominent in the lowest energy band and at higher energies $E > 9$ keV. In these energy bands, the flux in the hard central peak and the soft leading shoulder are overestimated by the simulation, as well as the flux in the interpulse. The integrated absolute flux in each energy band is reproduced with an accuracy $\lesssim 10\%$. This deviation is due to the fact that the spectral distribution of the incident photons for the simulations does not fully accommodate for all spectral features of the observed spectra, e.g., the CRSF is neglected in the simulations. In addition the iron line is supposed to be a blend of at least two separate lines originating from different regions of the accretion disk and material with different degree of ionization (see section 6.4). This is not taken into account during the spectral fitting and during the simulations and therefore the simulated flux close to the iron line is expected to be underestimated. Because of the redistribution effect of the response matrix of the *PCA* and the energy loss due to multiple scatterings the flux at lower energies < 6.5 keV is affected by these uncertainties as well.

From the χ^2 contour plot in Fig. 8.4 and from the results presented in the appendix B it is apparent that for the observations during early times of the turn-on no unique solution for the dimension of the scattering region could be found. For observations later than orbit 17 the χ^2 contours give an upper limit of ≈ 0.8–1.0 light seconds for the extension of the scattering region, which is close to the inner edge of the accretion disk.

Nevertheless, it is possible to calculate lower 1σ confidence limits for N_e for the beginning of the turn-on. Fig. 8.5 shows the resulting evolution of N_e over the time of the turn-on. Close to the end of the turn-on N_e varies between 100–300×10^{22} cm^{-2}. For this time the track of N_e is still consistent with a constant value. In contrast to the track of N_H shown in Fig. 7.14 there is no clear evidence for a systematic trend in the track of N_e.

Chapter 9

Discussion

The results presented in this work strongly support the existence of an accretion disk corona in Her X-1. This conclusion is in agreement with earlier findings of, e.g., Becker et al. (1977) who observed a turn-on for the first time and proposed a corona covering the accretion disk to explain the observed spectra. On the basis of data observed with *RXTE* it was possible to investigate a full turn-on of Her X-1 with high spectral and temporal resolution in the energy band of 2–100 keV.

Phase Averaged Turn-On Spectrum and Spectral Evolution   The phase averaged continuum spectrum at the end of the turn-on and the beginning of the main-on is well described by a standard spectral model for accreting X-ray pulsars, a phenomenological power-law spectrum with an exponential cut-off. Nevertheless, this spectral model deviates slightly from the observed spectra due to its discontinuity close to the cut-off energy, which is a well known effect. A cyclotron scattering feature is clearly apparent from the observed spectra towards the end of the turn-on, with no indication for a second harmonic. For all other observations the counting statistics in the higher energy bands was too low to investigate the CRSF in more detail.

Using a partial covering model is necessary to fit the observed spectra during the turn-on, using the standard spectral model would fail. In particular for the early times of the turn-on a two component spectral model is essential. From the spectral analysis I show that the track of N_{H} is in contradiction to a simple geometric model of an accretion disk which slowly opens the line of sight to the neutron star.

Emission Characteristic and Pulse Evolution   The decomposition of the pulse profile indicates two main contributions to the observed pulse profile, a *fan beam* and a *pencil beam* component. The relative contribution of these components to the observed pulse profiles changes with energy. At higher energies *pencil beam* like emission dominates over the *fan beam* contribution. The decomposition further supports the idea that the emission characteristic does not change between the end of the turn-on and the main-on in the 35$^{\mathrm{d}}$ cycle, consequently the "intrinsic" pulse profile does not change. Especially at the beginning of the turn-on the pulse profiles are heavily affected by Thomson scattering and photoelectric absorption. These two processes lead to a sinusoidal pulse shape in the early orbits. The pulse period of Her X-1 confirms the spin-up of the neutron star, which recently changed to a spin-down after the anomalous low-state of Her X-1.

Turn-On Model and Pulse Simulation   A geometric model which includes an accretion disk corona composed of fully or partially ionized material is the most simple explanation for the ob-
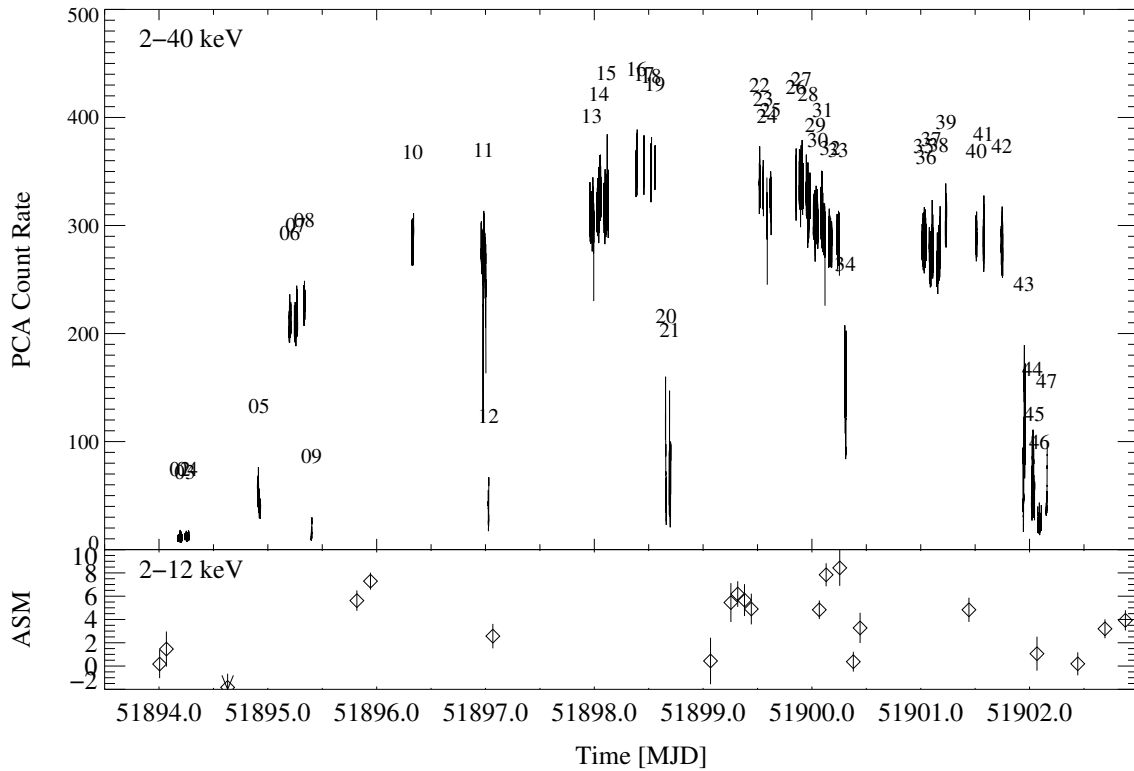
Figure 9.1: From top to bottom: *RXTE PCA* and *RXTE ASM* count rates. The time resolution for *PCA* data is 16 s, and 90 min for *ASM*. The numbers identify individual *RXTE* orbits starting with orbit 00 up to orbit 47

served unexpected behavior of N_{H} during the turn-on. This corona must be located close to the outer accretion disk rim and must be partially visible to the observer. Then, the spectral variations and temporal variations of the pulse profile can be explained by the geometric model presented.

By simulating the temporal signature of such a corona, an attempt was made to derive physical parameters for the corona from the change in shape and flux of the observed energy resolved pulse profiles. The results of the simulations support the idea of the geometric turn-on model and the observed pulse shape can well be reproduced, apart from the very early times during the turn-on where counting statistics is low. The absolute flux derived by the simulations in all energy bands is accurate to $\lesssim 10\,\%$.

Outlook On 2000 December 16 a second turn-on of Her X-1 was observed with *RXTE*. This 8 d long observation covers the turn-on and a full main-on. A quick-look analysis of the data gives similar results as the analysis of the 1997 turn-on. The *RXTE PCA* light curve together with *ASM* data for this turn-on is shown in Fig. 9.1. Recent observations of Her X-1 with the transmission gratings of *Chandra* will allow more accurate diagnostics of the accretion disk and its corona, like plasma density and temperature (Burwitz et al., 2001; Jimenez-Garate et al., 2003).

The pulse simulation can be improved in many ways. So far a fixed grid is used to fit simulated versus observed pulse profiles. Using interpolation methods would improved the fitting results noticeably. As mentioned in the theory section of this thesis, the absolute phase of the pulse profile changes when passing a scattering medium. This effect can be seen from the observed profiles but is not taken into account yet during simulation and fitting. As is apparent from Fig. 3.8 the spectral

shape changes with increasing τ_e when assuming energy dependent Compton scattering instead of Thomson scattering. This is not included in the *cabs* spectral model of the *XSPEC* package which was used for the fitting of the observed spectra. An implementation of a Compton scattering model is necessary since an optical depth of $\tau = 3$–5 is a typical range were the pulse "smearing" is most prominent, in this range changes in spectral shape are already significant and cannot be neglected any more.

References

Arnaud K., Dorman B., 2002, Xspec, An X-ray Spectral Fitting Package, User's Guide for version 11.2.x, Technical report, HEASARC – Laboratory for High Energy Astrophysics – NASA/GSFC available at `http://heasarc.gsfc.nasa.gov/docs/xanadu/xspec/manual/manual.html`

Attwood D., 2002, Soft X-rays and Extreme Ultraviolet Radiation, available at `http://coe.berkeley.edu/ast/sxreuv/`

Bahcall J.N., Bahcall N.A., 1972, Astrophys. J., Lett. 178, L1

Bai T., 1981, Astrophys. J. 243, 244

Balbus S.A., Hawley J.F., 1991, Astrophys. J. 376, 214

Balbus S.A., Hawley J.F., 1998, Rev. Mod. Phys. 70, 1

Bałucińska-Church M., McCammon D., 1992, Astrophys. J. 400, 699

Basko M.M., Sunyaev R.A., 1976, Mon. Not. R. Astron. Soc. 175, 395

Becker R.H., Boldt E.A., Holt S.S., et al., 1977, Astrophys. J. 214, 879

Becker W., 2002, X-ray Emission Properties of Pulsars and Isolated Neutron Stars, Habilitationsschrift, LMU München

Begelman M.C., McKee C.F., 1983, Astrophys. J. 271, 89

Begelman M.C., McKee C.F., Shields G.A., 1983, Astrophys. J. 271, 70

Belloni T., Psaltis D., van der Klis M., 2002, Astrophys. J. 572, 392

Benlloch S., 2003, Long-term X-ray variability of Active Galactic Nuclei and X-ray Binaries, Dissertation, Eberhard-Karls-Universität Tübingen

Bevington P.R., Robinson D.K., 1992, Data Reduction and Error Analysis for the Physical Sciences, McGraw-Hill, New York, 2nd edition

Blanco P.R., Rothschild R.E., the HEXTE team 1997, The High Energy X-Ray Timing Experiment (HEXTE), Center for Astrophysics & Space Science, University of California, San Diego

Bloomfield P., 1976, Fourier Analyis of time series: An introduction, John Wiley & Sons, New York

Blum S., 2000, Analyse der Pulseprofile von Hercules X-1 und anderer binarärer Röntgenpulsare, Dissertation, Eberhard-Karls-Universität Tübingen

Blum S., Kraus U., 2000, Astrophys. J. 529, 968

Boldt E.A., Holt S.S., Rothschild R.E., Serlemitsos P.J., 1976, Astron. Astrophys. 50, 161

Boroson B., O'Brien K., Horne K., et al., 2000, Astrophys. J. 545, 399

Brainerd J., Lamb F.K., 1987, Astrophys. J. 317, L33

Brown E.F., Bildsten L., 1998, Astrophys. J. 496, 915

Burwitz V., Dennerl K., Predehl P., Stelzer B., 2001, In: Two Years of Science with Chandra,

Abstracts from the Symposium held in Washington, DC, 5-7 September, 2001.

Chandrasekhar S., 1960, Proc. Natl. Acad. Sci. 46, 253

Chandrasekhar S., 1961, Hydrodynamic and hydromagnetic stability, International Series of Monographs on Physics, Oxford: Clarendon, 1961

Cheng F.H., Vrtilek S.D., Raymond J.C., 1995, Astrophys. J. 452, 825

Coburn W., 2001, A study of Magnetic Fields of Accreting X-ray Pulsars with the Rossi X-ray Timing Explorer, Dissertation, University of California, San Diego

Coburn W., Heindl W.A., Wilms J., et al., 2000, Astrophys. J. 543, 351

DalFiume D., Orlandini M., Cusumano G., et al., 1998, Astron. Astrophys. in press

Davidsen A., Henry J.P., Middleditch J., Smith H.E., 1972, Astrophys. J., Lett. 177, L97

Davidson K., Ostriker J.P., 1973, Astrophys. J. 179, 585

Davis J.E., 2001, Astrophys. J. 548, 1010

Davison P.J.N., Fabian A.C., 1977, Mon. Not. R. Astron. Soc. 178, 1P

Deeter J.E., Scott D.M., Boynton P.E., et al., 1998, Astrophys. J. 502, 802

Dennerl K., 1991, A comparative examination of LMC X-4 and Her X-1 X-ray double star systems, Dissertation, LMU München

Dermer C.D., Strickman M.S., Kurfess J.D., (eds.) 1997, Proc. 4th Compton Symposium, AIP Conf. Proc. 410, AIP, Woodbury

Dickey J.M., Lockman F.J., 1990, ARA&A 28, 215

Doty J., 1994, The All Sky Monitor for the X-ray Timing Experiment

Dove J.B., Wilms J., Begelman M.C., 1997, Astrophys. J. 487, 747

Endo T., Nagase F., Mihara T., 2000, Publ. Astron. Soc. Jpn. 52, 223

Forman W., Jones C.A., Liller W., 1972, Astrophys. J., Lett. 177, L103

Frank J., King A., Raine D., 1995, Accretion Power in Astrophysics, Cambridge Astrophysics Series, Cambridge University Press, The Edinburgh Building, Cambridge CB2 2RU, UK, second edition

Ghosh P., Lamb F.K., 1979a, Astrophys. J. 232, 259

Ghosh P., Lamb F.K., 1979b, Astrophys. J. 234, 296

Ghosh P., Pethick C.J., Lamb F.K., 1977, Astrophys. J. 217, 578

Giacconi R., Gursky H., Kellogg E., et al., 1973, Astrophys. J. 184, 227

Giacconi R., Gursky H., Kellogg E., et al., 1971, Astrophys. J., Lett. 167, L67

Giacconi R., Gursky H., Paolini F.R., Rossi B.B., 1962, Phys. Rev. Lett. 9, 439

Gilli R., Salvati M., Hasinger G., 2001, Astron. Astrophys. 366, 407

Ginzburg V.L., Syrovatskii S.I., 1965, ARA&A 3, 297

Gruber D.E., Blanco P.R., Heindl W.A., et al., 1996, Astron. Astrophys. Suppl. Ser. 641–644

Gruber D.E., Heindl W.A., Rothschild R.E., et al., 2001, Astrophys. J. 562, 499

Gruber D.E., Matteson J.L., Nolan P.L., et al., 1980, Astrophys. J., Lett. 240, L127

Gursky H., Giacconi R., Gorenstein P., et al., 1966, Astrophys. J. 146, 310

Harding A.K., 1994, in Holt & Day (1994), p. 429

Harding A.K., Daugherty J.K., 1991, Astrophys. J. 374, 687

Hasinger G., Lehmann I., Schmidt M., et al., 2000, New Astronomy Review 44, 497

Hawley J.F., 2000, Astrophys. J. 528, 462

Hawley J.F., Balbus S.A., 1991, Astrophys. J. 376, 223

Hawley J.F., Balbus S.A., 1995, Publications of the Astronomical Society of Australia 12, 159

Hawley J.F., Balbus S.A., Stone J.M., 2001, Astrophys. J., Lett. 554, L49

Hoffmeister C., 1941, in Kl. Verein. Beob. Bull., No. 24

Holt S.S., Day C.S., (eds.) 1994, The Evolution of X-Ray Binaries, AIP Conf. Proc. 308, AIP, Washington

Horn S., 1992, Dissertation, LMU München

Howarth I.D., Wilson B., 1983, Mon. Not. R. Astron. Soc. 202, 347

Iben I.J., 1991, Astrophys. J., Suppl. Ser. 76, 55

Jahoda K., 1997, Recent Progress in Callibration of the RXTE Proportional Counter Array, Technical report, NASA GSFC

Jahoda K., Swank J.H., Giles A.B., et al., 1997, In: Siegmund O.H. (ed.) EUV, X-Ray, and Gamma-Ray Instrumentation for Astronomy VII. Proceedings of SPIE 2808, SPIE, Bellingham, WA, p.59

Jimenez-Garate M.A., Liedahl D.A., Raymond J.C., Hailey C.J., 2003, AAS/High Energy Astrophysics Division 35, 0

Jones C., Forman W., 1976, Astrophys. J. 209, L131

Joss P.C., Fechner W.B., Forman W., Jones C., 1978, Astrophys. J. 225, 994

Kaastra J.S., Mewe R., 1993, Astron. Astrophys. Suppl. Ser. 97, 443

Kahabka P., 1987, Der 35-Tage Zyklus von Hercules X-1, Dissertation, Tech. Univ. München, (1987)

Kahabka P., 1989, In: Two Topics in X-Ray Astronomy, Volume 1: X Ray Binaries. Volume 2: AGN and the X Ray Background., p.447

Ketsaris N., Kuster M., Postnov K., et al., 2001, In: Hot points in Astrophysics.

Klein O., Nishina Y., 1929, Z. Physik 52, 853

Knoll G.F., 2000, Radiation detection and measurement, New York, John Wiley & Sons, Inc., 605 Third Avenue, New York, NY 10158-0012, 3rd edition

König M., 1997, Zeitvariabilität in Aktiven Galaxien, Dissertation, Eberhard-Karls-Universität Tübingen

Kopal Z., 1959, Close Binary Systems, Chapmann & Hall Ltd., London

Kovacs G., 1981, Astrophys. Space. Sci. 78, 175

Kretschmar P., 1996, Hochenergieröntgenspektren der akkretierenden Röntgenpulsare Vela X-1 und A 0535+26, Dissertation, Eberhard-Karls-Universität Tübingen

Kreykenbohm I., 1997, Beobachtungen von Vela X-1 mit RXTE., Diplomarbeit, Eberhard-Karls-Universität Tübingen, Institut für Astronomie und Astrophysik

Kreykenbohm I., 2003, X-ray spectra of highly magnetized neutron stars in X-ray binary systems, Dissertation, Eberhard-Karls-Universität Tübingen

Kukarkin B.V., Kholopov P.N., Pskovsky Y.P., et al., 1971, In: General Catalogue of Variable Stars, 3rd ed. (1971)., p. 0

Kunz M., 1991, Analyse von MIR-HEXE Beobachtungen: Pulsation und Energiespektrum des Röngendoppelsterns SMC X-1 im Energiebereich 20-80 keV., Diplomarbeit, Anstronomisches Institut der Universität Tübingen

Kunz M., 1996a, Astron. Astrophys. Suppl. Ser. 120, C231

Kunz M., 1996b, HEXE-Beobachtungen des Röntgenpulsars Her X-1, Dissertation, Eberhard-Karls-Universität Tübingen

Kunz M., Kendziorra E., Kretschmar P., et al., 1996, Astron. Astrophys. Suppl. Ser. 120, C233

Kuster M., Wilms J., Blum S., et al., 1999, Astrophys. Lett. Comm. 38, 161

Kuster M., Wilms J., Blum S., et al., 2001a, In: White N.E., Malaguti G., Palumbo G.G. (eds.) X-ray Astronomy: Stellar Endpoints, AGN and the Diffuse X-ray Background. AIP Conf. Proc., AIP Conf. Proc., New York, p.706

Kuster M., Wilms J., Staubert R., et al., 2001b, In: Gimenez A., Reglero V., Winkler C. (eds.) Exploring the Gamma-Ray Universe. ESA SP 459, ESA Publications Division, Noordwijk, p.309

Kylafis N.D., Klimis G.S., 1987, Astrophys. J. 323, 678

Lampton M., Margon B., Bowyer S., 1976, Astrophys. J. 208, 177

Lang K.R., 1999, Astrophysical Formulae, Vol. 1, Springer-Verlag, Berlin, 3rd edition

Larsson S., 1996, Astron. Astrophys. Suppl. Ser. 117, 197

Leahy D.A., 1987, Astron. Astrophys. 180, 275

Leahy D.A., 1995, Astron. Astrophys. Suppl. Ser. 113, 21

Leahy D.A., 1997, Mon. Not. R. Astron. Soc. 287, 622

Leahy D.A., 2000, Mon. Not. R. Astron. Soc. 315, 735

Leahy D.A., 2001, Astrophys. J. 547, 449

Leahy D.A., Yoshida A., Matsuoka M., 1994, Astrophys. J. 434, 341

Levine A.M., Bradt H., Cui W., et al., 1996, Astrophys. J., Lett. 469, L33

Lewin W.H.G., van Paradijs J., van den Heuvel E.P.J., (eds.) 1995, X-Ray Binaries, Cambridge Astrophysics Series 26, Cambridge Univ. Press, Cambridge

Lightman A.P., Lamb D.Q., Rybicki G.B., 1981, Astrophys. J. 248, 738

Liller W., 1972, IAU Circular, No. 2415

Lipunov V.M., 1982, Astrophys. Space. Sci. 82, 343

Liu Q.Z., van Paradijs J., van den Heuvel E.P.J., 2000, Astron. Astrophys. Suppl. Ser. 147, 25

Liu Q.Z., van Paradijs J., van den Heuvel E.P.J., 2001, Astron. Astrophys. 368, 1021

Makishima K., Maejima Y., Mitsuda K., et al., 1986, Astrophys. J. 308, 635

Maloney P., Begelman M.C., 1997, Astrophys. J. 491, L43

Markwardt C., Jahoda K., D. S., et al., 2002, Practical Advice for Users of New RXTE PCA Background Models, Technical report, University of Maryland, Goddard Space Flight Center available at http://lheawww.gsfc.nasa.gov/users/craigm/pca-bkg/bkg-users.html

McCray R., Shull J., Boynton P., et al., 1982, Astrophys. J. 262, 301

Mészáros P., Nagel W., 1985a, Astrophys. J. 298, 147

Mészáros P., Nagel W., 1985b, Astrophys. J. 299, 138

Mewe R., Gronenschild E.H.B.M., van den Oord G.H.J., 1985, Astron. Astrophys. Suppl. Ser. 62, 197

Mewe R., Lemen J.R., van der Oord G.H.J., 1986, Astron. Astrophys. Suppl. Ser. 65, 511

Middleditch J., 1983, Astrophys. J. 275, 278

Middleditch J., Nelson J., 1976, Astrophys. J. 208, 567

Mihara T., Makishima K., Ohashi T., et al., 1990, Nature 346, 250

Mihara T., Ohashi T., Makishima K., et al., 1991, Publ. Astron. Soc. Jpn. 43, 501

Miller K.A., Stone J.M., 2000, Astrophys. J. 534, 398

Miller M.C., 2000, Astrophys. J. 537, 342

Mitsuda K., Inoue H., Koyama K., et al., 1984, Publ. Astron. Soc. Jpn. 36, 741

Morrison R., McCammon D., 1983, Astrophys. J. 270, 119

Morton D.C., 1964, Astrophys. J. 140, 460

Nagase F., 1989, Publ. Astron. Soc. Jpn. 41, 1

NASA 1996, Rossi X-ray Timing Explorer Guest Observer Program, Cycle 2, Technical Report NRA 96-RXTE-02, Office of Space Science, NASA, Washington, DC

NASA 1997, Rossi X-ray Timing Explorer Guest Observer Program, Cycle 3, Technical Report NRA 97-OSS-09, NASA Office of Space Science, Washington, DC

Nowak M.A., Dove J.B., Vaughan B.A., et al., 1998, In: Scarsi L., Bradt H., Giommi P., Fiore F. (eds.) The Active X-Ray Sky: Results from Beppo-SAX and RXTE. Nucl. Phys. B, Proc. Suppl., Elsevier, Amsterdam, p.302

Nowak M.A., Vaughan B.A., Wilms J., et al., 1999a, Astrophys. J. 510, 874

Nowak M.A., Wilms J., Vaughan B.A., et al., 1999b, Astrophys. J. 515, 726

O'Brien K., Horne K., 2001, In: Boffin H., Steeghs D., Cuypers J. (eds.) Astrotomography, Indirect Imaging Methods in Observational Astronomy, Vol. 573. Lecture Notes in Physics, Springer, New York, Heidelberg, p. 416

Oosterbroek T., Parmar A., Martin D., Lammers U., 1997, Astron. Astrophys. 327, 215

Oosterbroek T., Parmar A.N., Fiume D.D., et al., 1999, Astron. Astrophys. in press

Oosterbroek T., Parmar A.N., Orlandini M., et al., 2001, Astron. Astrophys. 375, 922

Padmanabhan T., 2001, Theoretical Astrophysiscs Volume II: Stars and Stellar Systems, Vol. 2, Cambridge University Press, The Edinburgh Building, Cambridge CG2 2RU, UK, 1st edition

Parmar A., 1994, in Holt & Day (1994), p.415

Parmar A.N., Pietsch W., McKechnie S., et al., 1985, Nature 313, 119

Parmar A.N., Sanford P.W., Fabian A.C., 1980, Mon. Not. R. Astron. Soc. 192, 311

Parmar A.N., White N.E., Giommi P., Gottwald M., 1986, Astrophys. J. 308, 199

Petterson J.A., 1975, Astrophys. J. 201, L61

Petterson J.A., 1977, Astrophys. J. 218, 783

Petterson J.A., 1991, Astrophys. J. 378, 696

Pottschmidt K., 2002, Accretion Disk Weather of Black Hole X-Ray Binaries - The Case of Cygnus X-1, Dissertation, Eberhard-Karls-Universität Tübingen

Pravdo S.H., 1976, Hercules X-1: Spectral variability of an X-ray pulsar in a stellar binary system, Dissertation, National Aeronautics and Space Administration. Goddard Space Flight Center, Greenbelt, MD.

Pravdo S.H., Bussard R.W., White N.E., 1979, Mon. Not. R. Astron. Soc. 188, 5P

Prendergast K.H., Burbidge G.R., 1968, Astrophys. J., Lett. 151, L83

Priestley M.B., 1981, Spectral Analysis of Time Series, Academic Press London

Pringle J., 1997, Mon. Not. R. Astron. Soc. 292, 136

Pringle J.E., 1996, Mon. Not. R. Astron. Soc. 281, 357

Pringle J.E., Rees M.J., 1972, Astron. Astrophys. 21, 1

Rappaport S., Joss P.C., 1977, Nature 266, 683

Reynolds A.P., Quaintrell H., Still M.D., et al., 1997, Mon. Not. R. Astron. Soc. 288, 43

Risse P.M., 2003, Temporale und spektrale Untersuchungen des Röntgendoppelsternsystems Her X-1/HZ Herculis, Dissertation, Eberhard-Karls-Universität Tübingen

Rothschild R.E., Blanco P.R., Gruber D.E., et al., 1998, Astrophys. J. 496

Rots A.H., Jahoda K., Macomb D.J., et al., 1998, Astrophys. J. 501, 749

Rybicki G.B., Lightman A.P., 1979, Radiative Processes in Astrophysics, A Wiley-Interscience Publication, New York

Salpeter E.E., 1964, Astrophys. J. 140, 796

Sandage A., Osmer P., Giacconi R., et al., 1966, Astrophys. J. 146, 316

Scargle J.D., 1982, Astrophys. J. 263, 835

Schandl S., 1996, Astron. Astrophys. 307, 95

Schandl S., Meyer F., 1994, Astron. Astrophys. 289, 149

Schandl S., Staubert R., König M., 1997, In: AIP Conf. Proc. 410: Proceedings of the Fourth Compton Symposium., p. 763

Schwarzenberg-Czerny A., 1989, Mon. Not. R. Astron. Soc. 241, 153

Scott D.M., 1993, The 35-day pulse evolution cycle of HER X-1, Dissertation, University of Washington

Scott D.M., Leahy D.A., 1999, Astrophys. J. 510, 974

Scott D.M., Leahy D.A., Wilson R.B., 2000, Astrophys. J. 539, 392

Scott D.M., Wilson R.B., Finger M.H., Leahy D.A., 1997, in Dermer et al. (1997), p.748

Shakura N.I., Ketsaris N.A., Prokhorov M.E., Postnov K.A., 1998a, Mon. Not. R. Astron. Soc. 300, 992

Shakura N.I., Postnov K.A., Prokhorov M.E., 1998b, Astron. Astrophys. 331, L37

Shakura N.I., Prokhorov M.E., Postnov K.A., Ketsaris N.A., 1999, Astron. Astrophys. 348, 917

Shakura N.I., Sunyaev R.A., 1973, Astron. Astrophys. 23, 337

Shklovsky I.S., 1967, Astrophys. J., Lett. 148, L1

Shulman S., Friedman H., Fritz G., et al., 1975, Astrophys. J., Lett. 199, L101

Sobol I.M., 1991, Die Monte Carlo Methode, Deutscher Verlag der Wissenschaften, Berlin, 4. edition engl. transl.: The Monte Carlo Method, Chicago: Univ. Chicago Press, 1974

Soong Y., Gruber D.E., Peterson L., Rothschild R.E., 1990a, Astrophys. J. 348, 634

Soong Y., Gruber D.E., Peterson L.E., Rothschild R.E., 1990b, Astrophys. J. 348, 641

Soong Y., Gruber D.E., Rothschild R.E., 1987, Astrophys. J., Lett. 319, L77

Staubert R., Bezler M., Kendziorra E., 1983, Astron. Astrophys. 117, 215

Stelzer B., 1997, Beobachtungen von Her X-1 mit RXTE., Diplomarbeit, Eberhard-Karls-Universität Tübingen

Stelzer B., Staubert R., Wilms J., et al., 1997, in Dermer et al. (1997), p.753

Stelzer B., Wilms J., Staubert R., et al., 1999, Astron. Astrophys. 342, 736

Still M., O'Brien K., Horne K., et al., 2001, Astrophys. J. 553, 776

Still M.D., Quaintrell H., Roche P.D., Reynolds A.P., 1997, Mon. Not. R. Astron. Soc. 292, 52

Tananbaum H., Gursky H., Kellogg E.M., et al., 1972, Astrophys. J. 174, L143

Thomson J.J., 1903, Conduction of electricity through gases, Cambridge University Press, 1969 edition

Trümper J., Kahabka P., Ögelman H., et al., 1986, Astrophys. J. 300, L63

Trümper J., Pietsch W., Reppin C., et al., 1977, Anals of the New York Academy of Science 302, 538

Trümper J., Pietsch W., Reppin C., et al., 1978, Astrophys. J. 219, L105

van der Klis M., 1995, in Lewin et al. (1995), p.252

Verner D.A., Ferland G.J., Korista K.T., Yakovlev D.G., 1996, Astrophys. J. 465, 487

Voges W., Kahabka P., Ögelman H., et al., 1985, Space Sci. Rev. 40, 339

White N.E., Swank J.H., Holt S.S., 1983, Astrophys. J. 270, 711

Wilms J., 1996, Reprozessierung von Röntgenstrahlung in galaktischen und extragalaktischen Röntgenquellen., Diplomarbeit, Eberhard-Karls-Universität Tübingen

Wilms J., 1998, X-Rays from Galactic Black Holes: Theory and Observation, Dissertation, Eberhard-Karls-Universität Tübingen

Zel'dovich Y.B., Guseynov O.H., 1966, Astrophys. J. 144, 840

Appendix A

Results of the spectral analysis

This appendix contains an overview of the observations of the Her X-1 turn-on in Tab. A.1. The observation date, the exposure time, and the mean count rate are given for each *RXTE* orbit. Tab. A.2 gives best fit parameters which are the results of fitting the model spectrum presented in section 7.3.1 to the observed data. All uncertainties are on the joint 68 % confidence level. Tab. A.3 on page 126 summarizes the best fit parameters keeping the parameters given in Tab. 7.2 fixed during the fitting process.

Table A.1: Observing log of the Turn-On observations of Her X-1.

Obs.	Date [MJD]	Exposure [sec]	Count Rate [counts s^{-1}]
00	50703.979	3300	62.1 ± 0.2
01	50703.979	3400	73.3 ± 0.3
02	50703.979	3300	100.0 ± 0.3
03	50703.979	3300	130.0 ± 0.3
04	50703.979	3200	195.4 ± 0.3
05	50704.312	3000	280.8 ± 0.4
06	50704.312	2600	402.7 ± 0.5
07	50704.452	2300	469.2 ± 0.5
08	50704.452	2100	395.0 ± 0.5
09	50704.452	1700	501.7 ± 0.6
10	50704.727	1200	158.8 ± 0.5
11	50704.727	300	148.7 ± 1.0
12	50704.727	2100	160.6 ± 0.4
13	50704.727	700	156.7 ± 0.7
14	50704.860	2100	358.4 ± 0.5
15	50704.860	3400	813.6 ± 0.5
16	50704.860	3300	1197.0 ± 0.6
17	50705.045	3400	1298.1 ± 0.7
18	50705.045	3200	1293.7 ± 0.7
19	50705.045	3100	325.6 ± 0.4
20	50705.312	3000	329.3 ± 0.4
21	50705.381	2700	34.9 ± 0.3
22	50705.591	1800	73.2 ± 0.4
23	50705.659	1500	1494.1 ± 1.1
24	50705.726	1200	1568.2 ± 1.2
25	50705.793	2100	1607.3 ± 0.9
26	50705.793	3300	1612.5 ± 0.7
27	50705.793	3400	1697.5 ± 0.7
28	50705.793	3400	1699.1 ± 0.7
29	50705.793	3100	1787.7 ± 0.8
30	50706.096	3100	1810.4 ± 0.8
31	50707.313	1900	1828.2 ± 1.0

Exposure times shown are rounded to the closest 100 sec. The count rate is background subtracted.

Table A.2: Results of the spectral fitting to the Her X-1 turn-on data with all parameters set free, except the parameters where no errors are given for.

Obs.	N_H 10^{22}cm^2	C	A_{PL} 10^{-3}	E_{cut} keV	E_{fold} keV	E_{Fe} keV	σ_{Fe} keV	A_{Line} 10^{-4}	E_{cyc} keV	σ_{cyc} keV	τ_{cyc}	χ^2/dof
00	$44.73^{+3.17}_{-7.24}$	$2.14^{+0.14}_{-0.13}$	$4.2^{+0.2}_{-0.2}$	$18.16^{+3.46}_{-2.21}$	$15.4^{+16.6}_{-7.4}$	$6.69^{+0.11}_{-0.14}$	0.77	$4.6^{+0.8}_{-0.7}$	39.7	5.10	$0.50^{+2.58}_{-0.50}$	$77.3/103$
01	$47.34^{+6.14}_{-4.28}$	$2.19^{+0.15}_{-0.12}$	$5.0^{+0.2}_{-0.2}$	$18.24^{+2.21}_{-1.57}$	$9.5^{+5.6}_{-3.3}$	$6.68^{+0.11}_{-0.11}$	0.77	$5.3^{+0.7}_{-0.7}$	39.7	5.10	$0.00^{+2.09}_{-0.00}$	$102.4/103$
02	$56.26^{+4.13}_{-3.65}$	$3.16^{+0.16}_{-0.15}$	$6.1^{+0.2}_{-0.2}$	$18.42^{+3.01}_{-1.69}$	$20.0^{+10.3}_{-7.5}$	$6.60^{+0.09}_{-0.09}$	0.77	$7.6^{+0.8}_{-0.8}$	39.7	5.10	$1.31^{+1.38}_{-1.19}$	$163.7/103$
03	$67.38^{+1.07}_{-7.67}$	$3.57^{+0.16}_{-0.15}$	$8.1^{+0.2}_{-0.2}$	$20.57^{+2.76}_{-2.69}$	$14.3^{+8.8}_{-7.7}$	$6.57^{+0.07}_{-0.07}$	0.77	$11.4^{+0.9}_{-0.9}$	39.7	5.10	$1.61^{+1.71}_{-1.61}$	$134.5/103$
04	$77.35^{+1.81}_{-2.96}$	$4.49^{+0.14}_{-0.15}$	$12.2^{+0.2}_{-0.2}$	$19.98^{+1.45}_{-1.63}$	$11.6^{+3.9}_{-2.8}$	$6.42^{+0.06}_{-0.02}$	0.77	$15.0^{+1.1}_{-1.0}$	39.7	5.10	$0.46^{+0.82}_{-0.46}$	$165.3/103$
05	$75.17^{+1.62}_{-2.39}$	$6.01^{+0.14}_{-0.17}$	$15.2^{+0.2}_{-0.2}$	$21.53^{+1.08}_{-1.08}$	$13.6^{+2.8}_{-2.8}$	$6.54^{+0.07}_{-0.08}$	0.77	$16.5^{+1.4}_{-1.3}$	39.7	5.10	$0.91^{+0.56}_{-0.56}$	$198.9/103$
06	$61.37^{+1.46}_{-1.23}$	$7.15^{+0.13}_{-0.15}$	$17.4^{+0.3}_{-0.3}$	$21.05^{+0.92}_{-0.98}$	$14.5^{+2.4}_{-2.2}$	$6.70^{+0.10}_{-0.10}$	$1.00^{+0.13}_{-0.02}$	$13.4^{+1.8}_{-1.8}$	39.7	5.10	$1.25^{+0.52}_{-0.47}$	$142.7/103$
07	$54.84^{+1.35}_{-1.26}$	$7.70^{+0.17}_{-0.16}$	$17.7^{+0.4}_{-0.4}$	$21.01^{+0.78}_{-0.88}$	$12.0^{+2.2}_{-2.0}$	$6.71^{+0.09}_{-0.12}$	$1.00^{+0.00}_{-0.09}$	$17.7^{+2.7}_{-3.0}$	39.7	5.10	$0.41^{+0.51}_{-0.41}$	$122.2/102$
08	$65.75^{+2.77}_{-0.80}$	$9.94^{+0.31}_{-0.15}$	$14.3^{+0.3}_{-0.3}$	$21.07^{+0.86}_{-0.93}$	$12.9^{+2.2}_{-1.9}$	$6.68^{+0.12}_{-0.11}$	$0.98^{+0.13}_{-0.02}$	$14.7^{+2.3}_{-1.7}$	39.7	5.10	$0.69^{+0.46}_{-0.40}$	$119.8/102$
09	$52.66^{+1.27}_{-1.39}$	$8.37^{+0.17}_{-0.21}$	$17.6^{+0.4}_{-0.4}$	$21.56^{+1.04}_{-1.10}$	$11.3^{+2.6}_{-2.5}$	$6.67^{+0.13}_{-0.15}$	$1.00^{+0.00}_{-0.10}$	$17.1^{+3.0}_{-3.0}$	39.7	5.10	$0.77^{+0.67}_{-0.68}$	$135.1/102$
15	$25.36^{+0.70}_{-0.94}$	$5.75^{+0.13}_{-0.13}$	$25.5^{+0.8}_{-1.4}$	$21.24^{+0.39}_{-0.41}$	$12.9^{+1.0}_{-1.0}$	$6.55^{+0.10}_{-0.10}$	$1.00^{+0.00}_{-0.60}$	$31.6^{+4.2}_{-4.6}$	39.7	5.10	$1.02^{+0.22}_{-0.22}$	$108.2/101$
16	$11.91^{+2.30}_{-2.32}$	$0.70^{+0.25}_{-0.10}$	$98.3^{+1.5}_{-14.2}$	$21.18^{+0.46}_{-0.47}$	$12.6^{+1.1}_{-1.1}$	$6.55^{+0.10}_{-0.11}$	$0.71^{+0.18}_{-0.14}$	$39.2^{+6.8}_{-5.2}$	39.7	5.10	$0.80^{+0.25}_{-0.24}$	$93.1/101$
17	$4.74^{+0.42}_{-0.48}$	1.00	$85.0^{+0.4}_{-0.4}$	$21.24^{+0.46}_{-0.48}$	$12.4^{+1.1}_{-1.1}$	$6.60^{+0.11}_{-0.11}$	$0.72^{+0.18}_{-0.15}$	$41.2^{+6.6}_{-5.5}$	39.7	5.10	$0.77^{+0.26}_{-0.26}$	$98.9/102$
18	$5.17^{+0.45}_{-0.46}$	1.00	$85.3^{+0.4}_{-0.4}$	$21.13^{+0.43}_{-0.44}$	$12.0^{+1.0}_{-1.0}$	$6.63^{+0.11}_{-0.12}$	$0.78^{+0.18}_{-0.16}$	$41.2^{+6.8}_{-5.7}$	39.7	5.10	$0.76^{+0.25}_{-0.25}$	$84.4/102$
23	$6.49^{+0.37}_{-0.50}$	1.00	$100.5^{+3.2}_{-0.4}$	$21.91^{+0.58}_{-0.57}$	$10.8^{+2.2}_{-1.3}$	$6.53^{+0.11}_{-0.13}$	$0.75^{+0.19}_{-0.13}$	$50.4^{+8.3}_{-6.9}$	$40.6^{+0.8}_{-0.9}$	5.10	$2.39^{+3.92}_{-1.41}$	$108.7/101$
24	$5.23^{+0.48}_{-0.38}$	1.00	$103.5^{+0.7}_{-0.5}$	$20.77^{+0.67}_{-0.71}$	$13.7^{+1.6}_{-1.3}$	$6.59^{+0.09}_{-0.10}$	$0.70^{+0.18}_{-0.15}$	$53.3^{+8.7}_{-7.1}$	$39.2^{+1.1}_{-1.0}$	$3.34^{+1.90}_{-1.45}$	$1.48^{+0.96}_{-0.45}$	$122.7/100$
25	$4.30^{+0.43}_{-0.38}$	1.00	$104.8^{+0.7}_{-0.5}$	$21.21^{+0.53}_{-0.48}$	$13.4^{+1.5}_{-1.1}$	$6.62^{+0.09}_{-0.10}$	$0.71^{+0.17}_{-0.15}$	$52.8^{+8.1}_{-7.2}$	$39.7^{+1.0}_{-0.9}$	$5.37^{+2.13}_{-1.50}$	$1.16^{+0.27}_{-0.24}$	$117.7/100$
26	$4.31^{+0.40}_{-0.38}$	1.00	$104.7^{+0.6}_{-0.4}$	$22.06^{+0.38}_{-0.34}$	$11.3^{+1.1}_{-0.9}$	$6.64^{+0.08}_{-0.10}$	$0.78^{+0.17}_{-0.13}$	$58.8^{+8.6}_{-6.7}$	$40.0^{+1.2}_{-1.2}$	$5.18^{+2.85}_{-2.32}$	$0.71^{+0.20}_{-0.17}$	$106.6/100$
27	$4.58^{+0.41}_{-0.39}$	1.00	$110.9^{+0.7}_{-0.5}$	$21.01^{+0.35}_{-0.36}$	$12.8^{+1.3}_{-0.9}$	$6.68^{+0.09}_{-0.10}$	$0.75^{+0.17}_{-0.14}$	$57.2^{+8.4}_{-7.0}$	$40.4^{+0.9}_{-0.9}$	$5.16^{+2.33}_{-1.69}$	$0.95^{+0.19}_{-0.17}$	$110.9/100$
28	$4.36^{+0.36}_{-0.35}$	1.00	$110.5^{+3.9}_{-0.7}$	$21.19^{+0.29}_{-0.29}$	$12.2^{+0.8}_{-0.6}$	$6.65^{+0.08}_{-0.09}$	$0.79^{+0.17}_{-0.15}$	$61.9^{+7.9}_{-7.5}$	$39.1^{+0.8}_{-0.8}$	$4.70^{+1.81}_{-1.33}$	$0.83^{+0.16}_{-0.15}$	$114.6/100$
29	$4.24^{+0.36}_{-0.31}$	1.00	$116.1^{+0.7}_{-0.7}$	$21.40^{+0.33}_{-0.31}$	$12.1^{+1.0}_{-0.6}$	$6.68^{+0.08}_{-0.10}$	$0.83^{+0.18}_{-0.16}$	$65.8^{+7.8}_{-8.2}$	$39.7^{+1.0}_{-1.0}$	$5.59^{+3.31}_{-1.55}$	$0.71^{+0.14}_{-0.13}$	$114.5/100$
30	$4.55^{+0.34}_{-0.41}$	1.00	$118.3^{+0.7}_{-0.5}$	$21.14^{+0.39}_{-0.37}$	$12.7^{+1.2}_{-0.9}$	$6.67^{+0.08}_{-0.08}$	$0.77^{+0.03}_{-0.15}$	$64.3^{+6.4}_{-6.9}$	$39.5^{+0.7}_{-0.7}$	$5.25^{+1.92}_{-1.48}$	$1.05^{+0.20}_{-0.19}$	$119.7/100$
31	$3.48^{+0.37}_{-0.37}$	1.00	$116.6^{+0.5}_{-0.4}$	$21.37^{+0.44}_{-0.46}$	$11.6^{+0.7}_{-0.7}$	$6.59^{+0.07}_{-0.08}$	$0.77^{+0.03}_{-0.13}$	$71.2^{+7.1}_{-7.5}$	$40.5^{+0.7}_{-0.7}$	$1.00^{+6.25}_{-0.00}$	$1.97^{+0.99}_{-1.39}$	$95.8/100$

N_H: Hydrogen column density, C: Ratio of scattered to absorbed radiation, A_{PL}: Power law normalization (photons keV^{-1} cm^{-2} s^{-1} at 1 keV), A_{Line}: Line normalization (photons cm^{-2} s^{-1} in the line), E_{cut}: Cut-off energy (keV), E_{fold}: Folding energy (keV), E_{Fe}: Gaussian line energy (keV), σ_{Fe}: Width of the Gaussian line (keV), A_{Line}: Line normalization, E_{cyc}: Cyclotron line energy (keV), σ_{cyc}: Width of the cyclotron line (keV), τ_{cyc}: Depth of the cyclotron line. Uncertainties are at 90 % confidence level for one interesting parameter ($\Delta\chi^2 = 2.71$).

Table A.3: Results of the spectral fitting to the Her X-1 turn-on data for the following parameters: N_{H}, C, A_{PL}, and A_{Line}.

Obs.	N_{H} $10^{22}\mathrm{cm}^2$	C	A_{PL} 10^{-3}	A_{Line} 10^{-4}	χ^2/dof
00	$35.98^{+7.60}_{-1.93}$	$2.10^{+0.16}_{-0.15}$	$4.2^{+0.2}_{-0.2}$	$3.8^{+0.6}_{-0.6}$	83.9/108
01	$42.20^{+6.44}_{-2.63}$	$2.13^{+0.14}_{-0.13}$	$4.9^{+0.2}_{-0.2}$	$4.1^{+0.6}_{-0.6}$	112.4/108
02	$62.80^{+4.71}_{-3.65}$	$3.59^{+0.23}_{-0.21}$	$6.1^{+0.2}_{-0.2}$	$10.7^{+1.1}_{-1.1}$	162.3/108
03	$67.61^{+4.17}_{-2.60}$	$3.97^{+0.20}_{-0.19}$	$8.0^{+0.2}_{-0.2}$	$14.3^{+1.1}_{-1.1}$	131.1/108
04	$83.92^{+0.33}_{-4.83}$	$5.11^{+0.21}_{-0.19}$	$11.8^{+0.2}_{-0.2}$	$20.4^{+1.4}_{-1.4}$	151.1/108
05	$82.43^{+1.91}_{-2.03}$	$7.61^{+0.28}_{-0.28}$	$13.9^{+0.3}_{-0.3}$	$35.3^{+2.5}_{-2.5}$	115.5/108
06	$66.27^{+1.65}_{-1.65}$	$8.19^{+0.26}_{-0.25}$	$16.6^{+0.3}_{-0.3}$	$31.0^{+3.6}_{-3.7}$	130.4/108
07	$55.18^{+1.14}_{-1.57}$	$7.80^{+0.18}_{-0.17}$	$17.7^{+0.3}_{-0.4}$	$19.0^{+2.8}_{-2.8}$	138.9/108
08	$67.47^{+0.74}_{-2.29}$	$10.10^{+0.25}_{-0.26}$	$14.2^{+0.3}_{-0.3}$	$16.0^{+2.5}_{-2.5}$	135.3/108
09	$53.46^{+1.84}_{-1.09}$	$8.64^{+0.22}_{-0.21}$	$17.5^{+0.1}_{-0.4}$	$22.2^{+2.3}_{-3.8}$	154.4/108
15	$24.02^{+0.81}_{-0.52}$	$6.00^{+0.30}_{-0.24}$	$24.4^{+1.0}_{-1.1}$	$23.0^{+2.8}_{-2.8}$	145.7/107
16	$8.13^{+4.50}_{-0.90}$	$0.77^{+0.50}_{-0.10}$	$94.0^{+1.0}_{-2.2}$	$34.0^{+3.7}_{-3.4}$	128.7/107
17	$4.84^{+0.37}_{-0.44}$	$1.00^{+0.00}_{-0.00}$	$85.5^{+0.4}_{-0.4}$	$39.6^{+3.9}_{-3.9}$	135.6/108
18	$5.34^{+0.43}_{-0.41}$	$1.00^{+0.00}_{-0.00}$	$85.9^{+0.4}_{-0.4}$	$38.5^{+3.9}_{-3.9}$	105.6/108
23	$6.72^{+0.54}_{-0.35}$	$1.00^{+0.00}_{-0.00}$	$101.3^{+0.6}_{-0.5}$	$48.7^{+5.1}_{-5.0}$	121.9/108
24	$5.30^{+0.43}_{-0.31}$	$1.00^{+0.00}_{-0.00}$	$104.2^{+0.6}_{-0.5}$	$46.6^{+4.9}_{-4.8}$	144.1/108
25	$4.41^{+0.40}_{-0.38}$	$1.00^{+0.00}_{-0.00}$	$105.2^{+4.1}_{-0.4}$	$51.2^{+4.9}_{-4.9}$	137.4/108
26	$4.55^{+0.35}_{-0.42}$	$1.00^{+0.00}_{-0.00}$	$105.4^{+0.5}_{-0.4}$	$55.2^{+4.7}_{-4.7}$	129.3/108
27	$4.72^{+0.35}_{-0.42}$	$1.00^{+0.00}_{-0.00}$	$111.4^{+0.5}_{-0.4}$	$54.8^{+4.8}_{-4.8}$	134.8/108
28	$4.47^{+0.37}_{-0.39}$	$1.00^{+0.00}_{-0.00}$	$111.2^{+0.5}_{-0.5}$	$58.0^{+5.0}_{-5.0}$	140.9/108
29	$4.33^{+0.36}_{-0.40}$	$1.00^{+0.00}_{-0.00}$	$116.6^{+0.5}_{-0.5}$	$63.8^{+5.4}_{-5.4}$	173.8/108
30	$4.75^{+0.35}_{-0.43}$	$1.00^{+0.00}_{-0.00}$	$156.7^{+17.1}_{-14.1}$	$65.1^{+6.4}_{-5.8}$	150.2/108
31	$3.70^{+0.40}_{-0.38}$	$1.00^{+0.00}_{-0.00}$	$117.4^{+0.6}_{-0.5}$	$70.7^{+5.8}_{-5.8}$	102.9/108

N_{H}: Hydrogen column density C: Ratio of scattered to absorbed radiation A_{PL}: Power law normalization (photons $\mathrm{keV^{-1}\,cm^{-2}\,s^{-1}}$ at 1 keV). A_{Line}: Line normalization (photons $\mathrm{cm^{-2}\,s^{-1}}$ in the line), the following parameters were fixed: the Gaussian line was fixed at 6.45 keV with a width σ of 0.45 keV, the cut off energy E_{cut} at 21.5 keV, the folding energy E_{fold} at 14.1 keV, the power law index α at 1.068, and the cyclotron energy E_{cycle} at 39.4 keV. Uncertainties are at 90% confidence level for one interesting parameter ($\Delta\chi^2 = 2.71$).

Appendix B

Results of the pulse simulations

On the following pages the results of the pulse simulations and the fitting of simulated to observed pulse profiles are presented. For each *RXTE* orbit the observed pulse profile is shown in 5 different energy bands. The best-fit simulated pulse profiles are plotted on top of the observed profiles as dashed lines. The residuals, i.e., the observed pulse profiles divided by the best-fit profile, are indicated below.

For each orbit the thickness of the scattering medium d versus the optical depth in units of N_e are shown as χ^2 contour plot. These data was derived during the fitting process, by calculating the χ^2 of the fit for each N_e and size d combination. The darkest red area corresponds to a 1σ confidence level. From these areas 1σ upper and lower limits were calculated for N_e.

Orbit 00
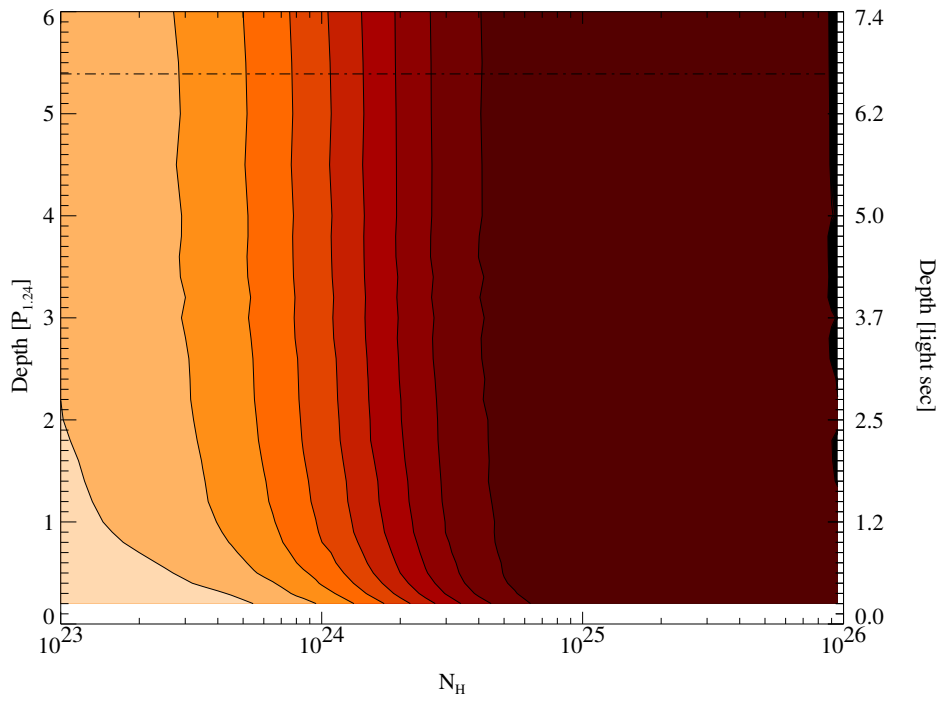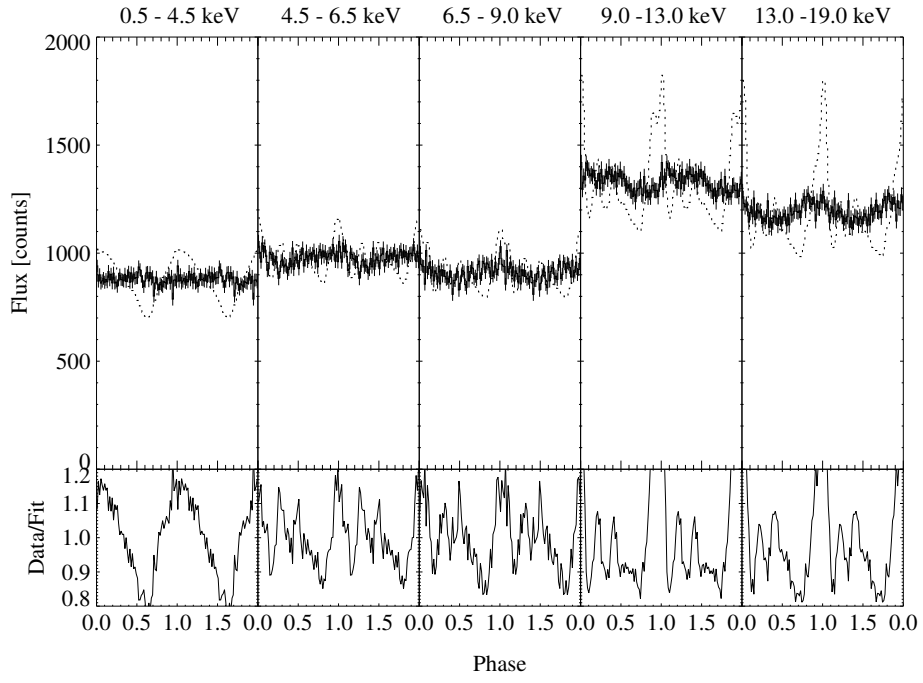
Figure B.1: Limits for N_e: $4.0 \times 10^{24} < N_e < 9.5 \times 10^{25}$ cm^{-2}

Orbit 01

| 0.5 - 4.5 keV | 4.5 - 6.5 keV | 6.5 - 9.0 keV | 9.0 -13.0 keV | 13.0 -19.0 keV |
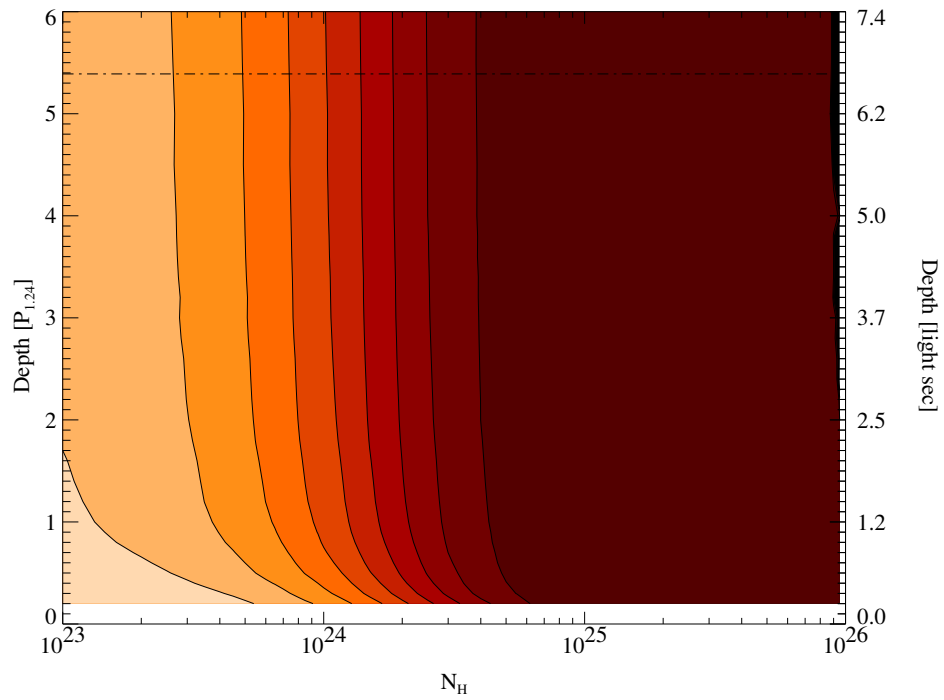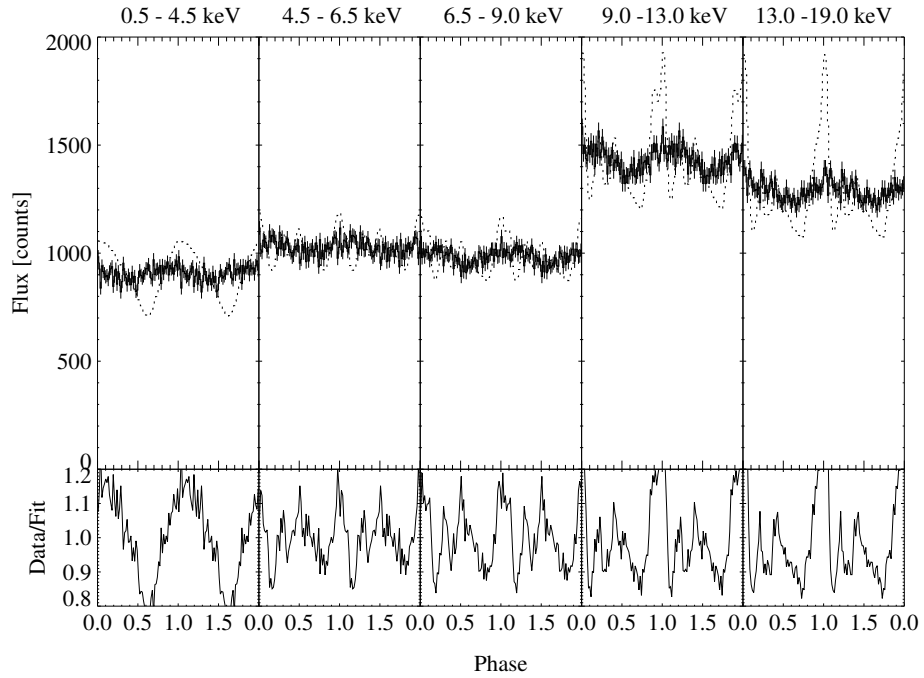
Figure B.2: Limits for N_e: $3.9 \times 10^{24} < N_e < 9.5 \times 10^{25}$ cm^{-2}

Orbit 02
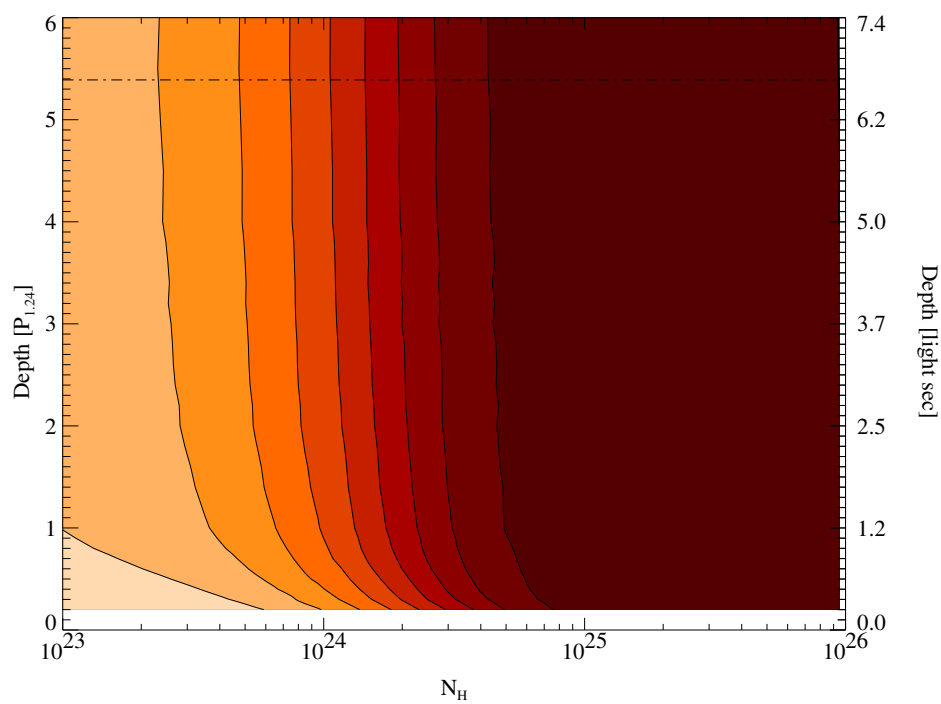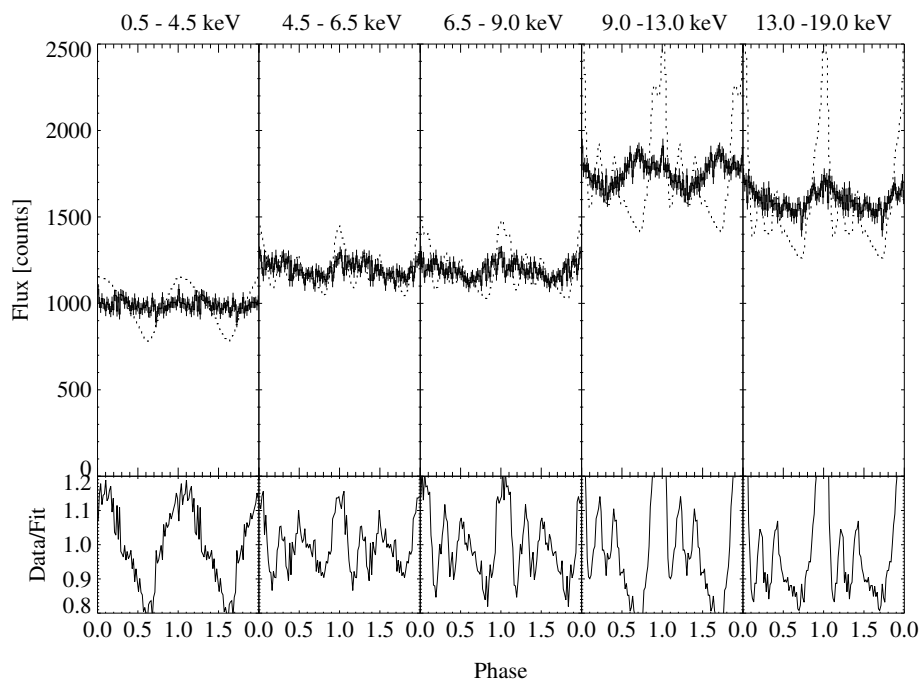
Figure B.3: Limits for N_{e}: $4.1 \times 10^{24} < N_{\mathrm{e}} < 9.5 \times 10^{25}$ cm^{-2}

Orbit 03
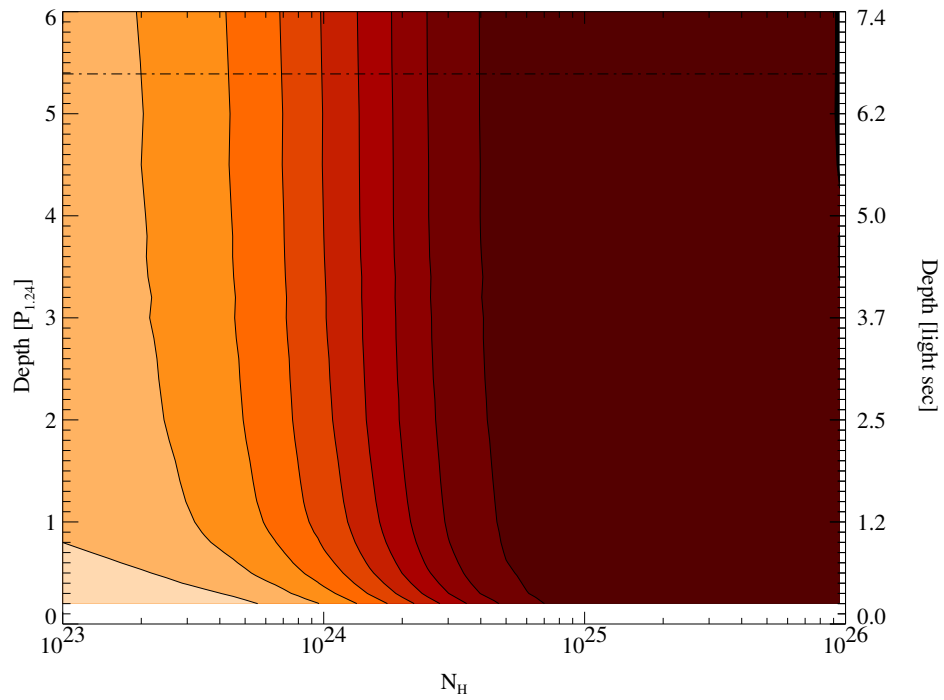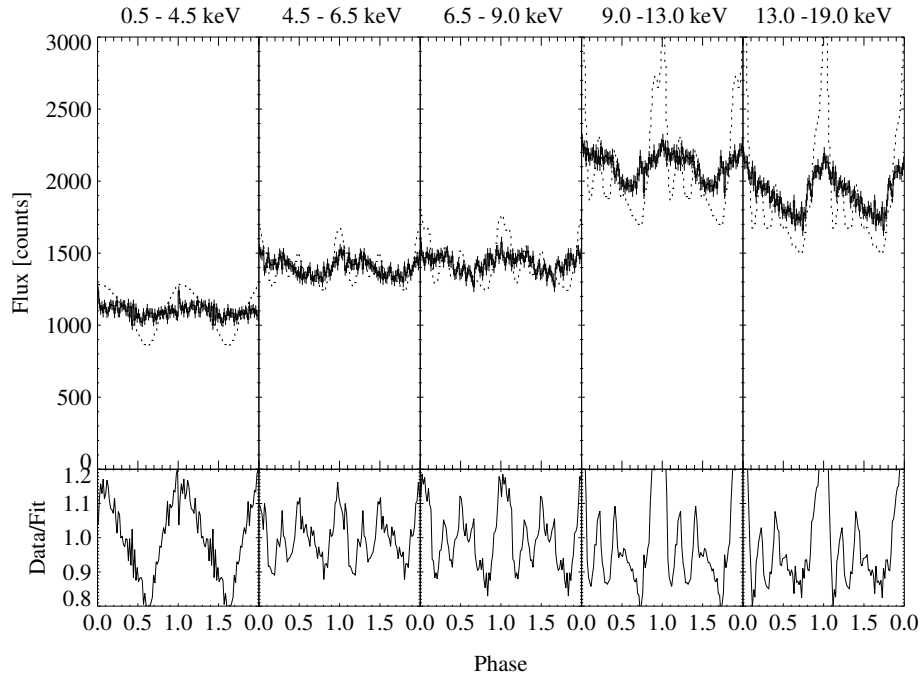
Figure B.4: Limits for N_e: $4.0 \times 10^{24} < N_e < 9.5 \times 10^{25}$ cm^{-2}

Orbit 04
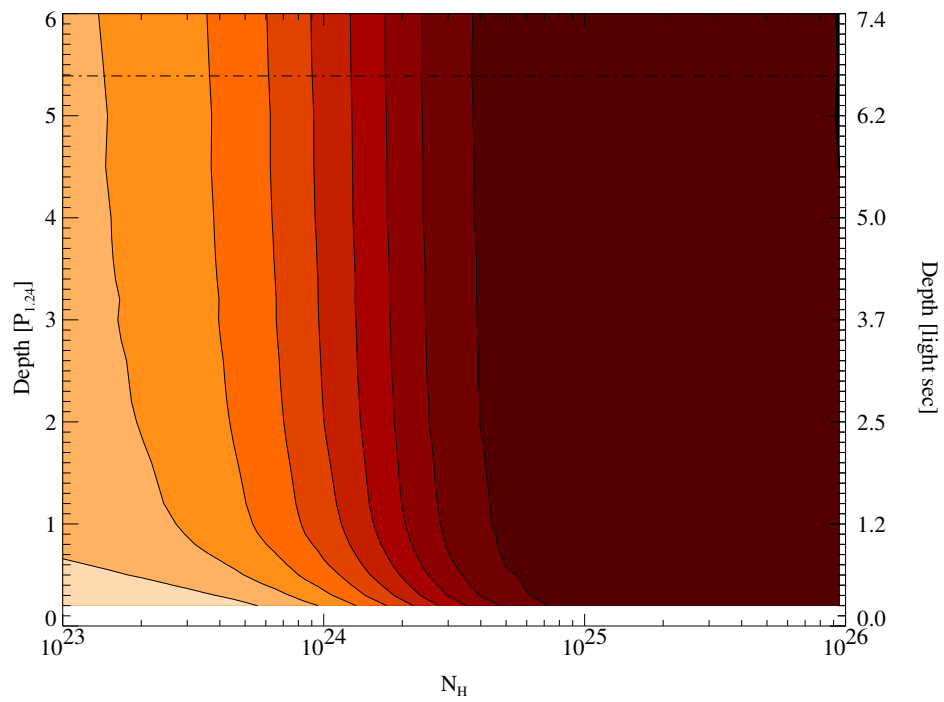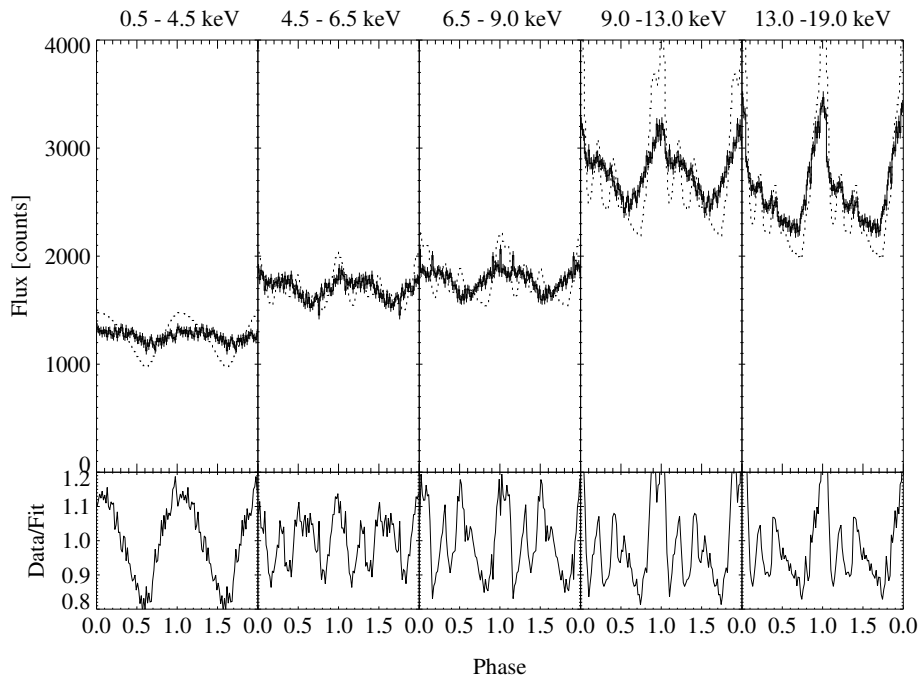
Figure B.5: Limits for N_e: $3.8 \times 10^{24} < N_e < 9.5 \times 10^{25}$ cm^{-2}

Orbit 05
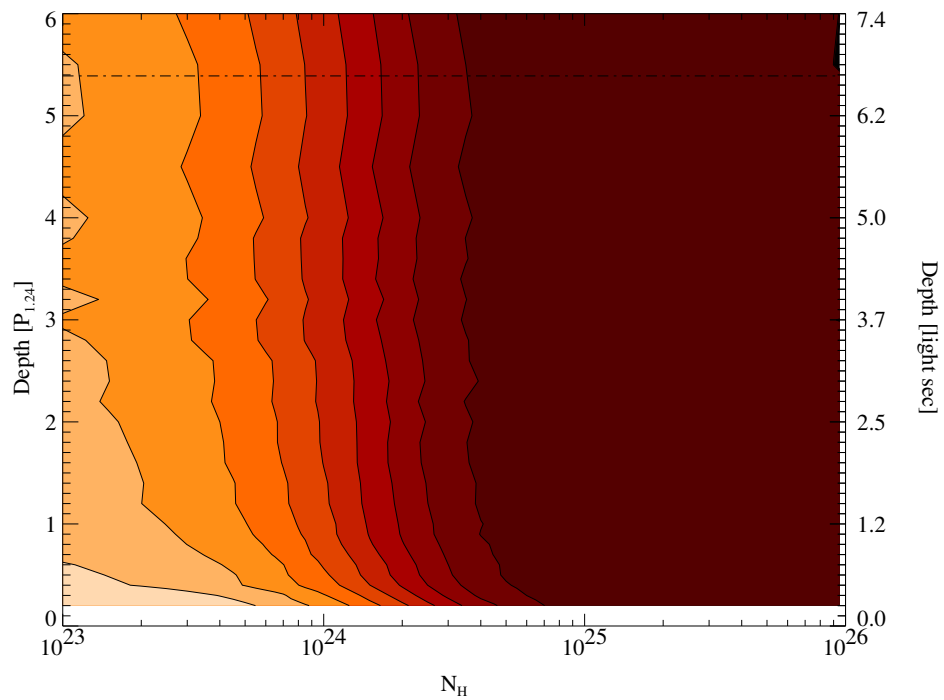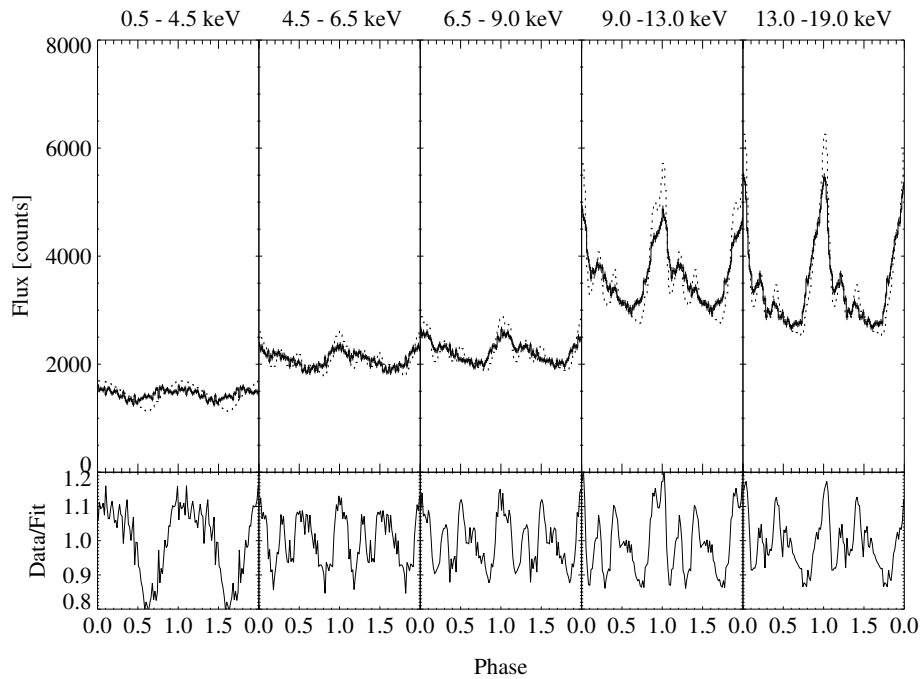
Figure B.6: Limits for N_e: $3.1 \times 10^{24} < N_e < 9.5 \times 10^{25}$ cm^{-2}

Orbit 06
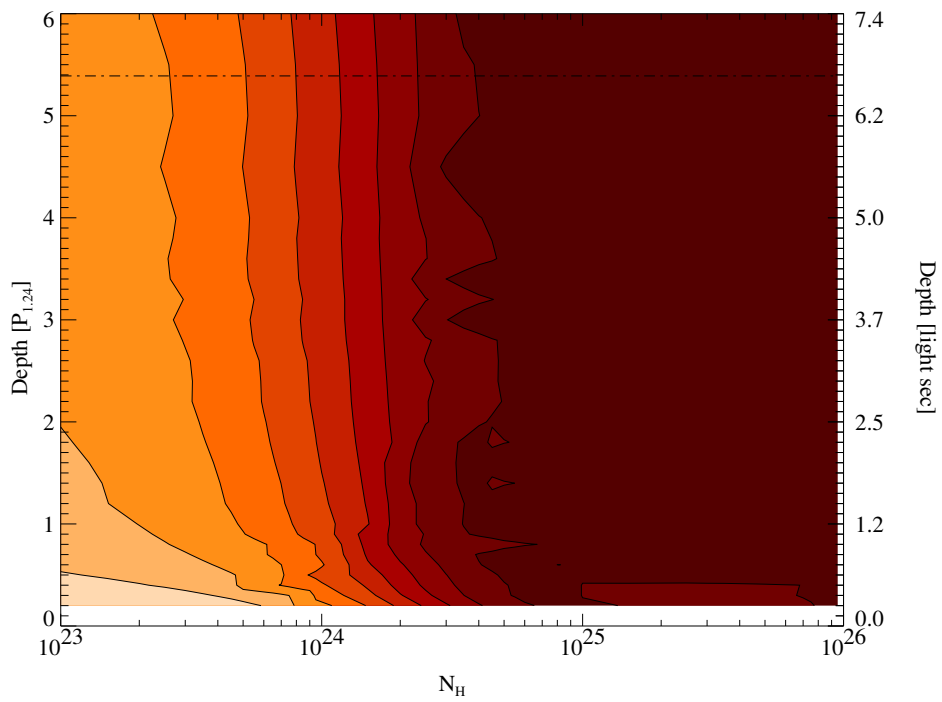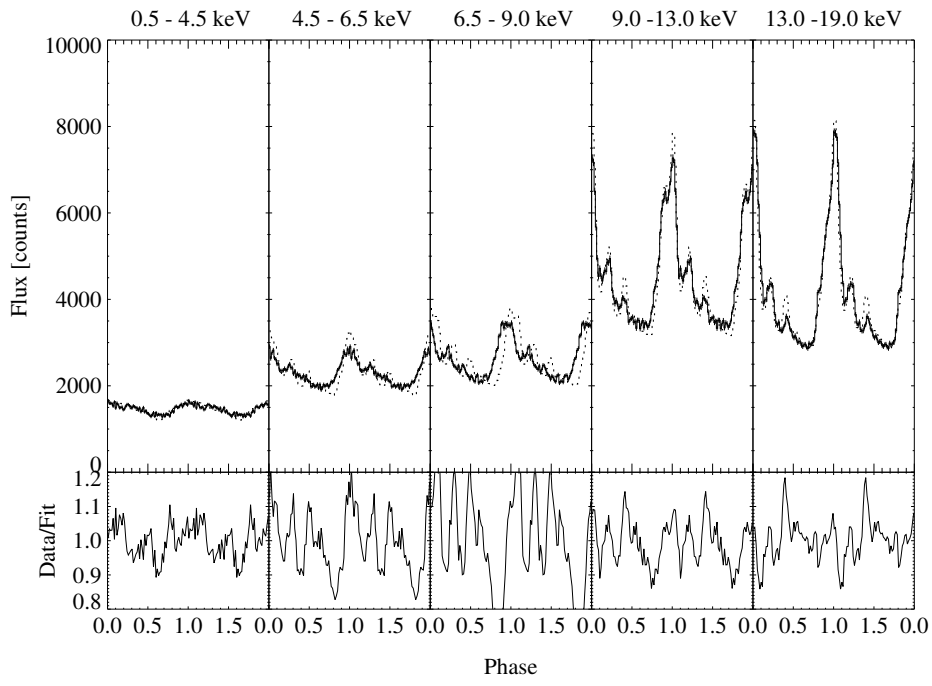
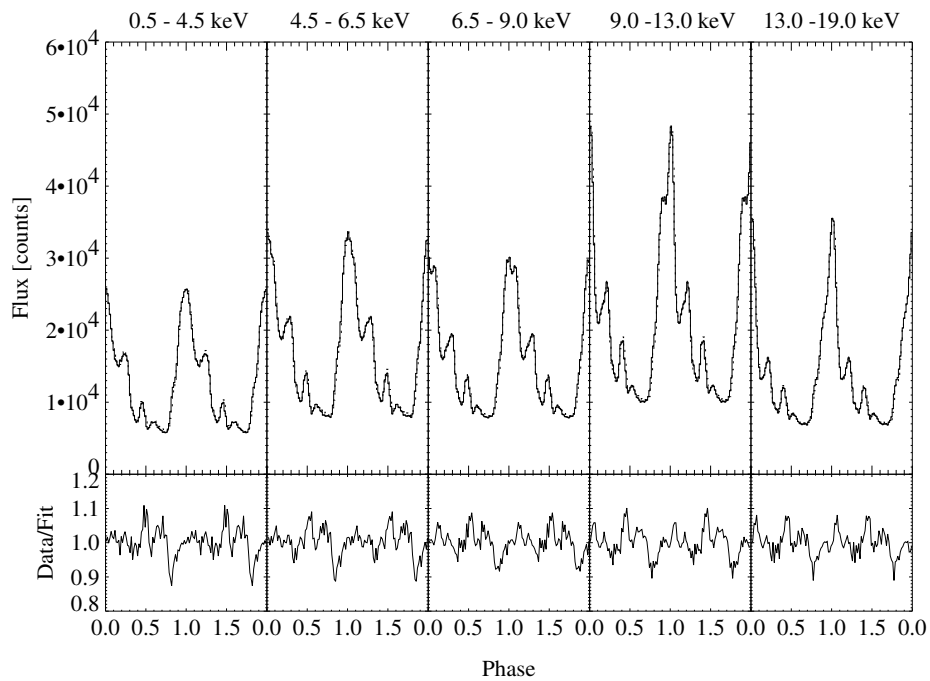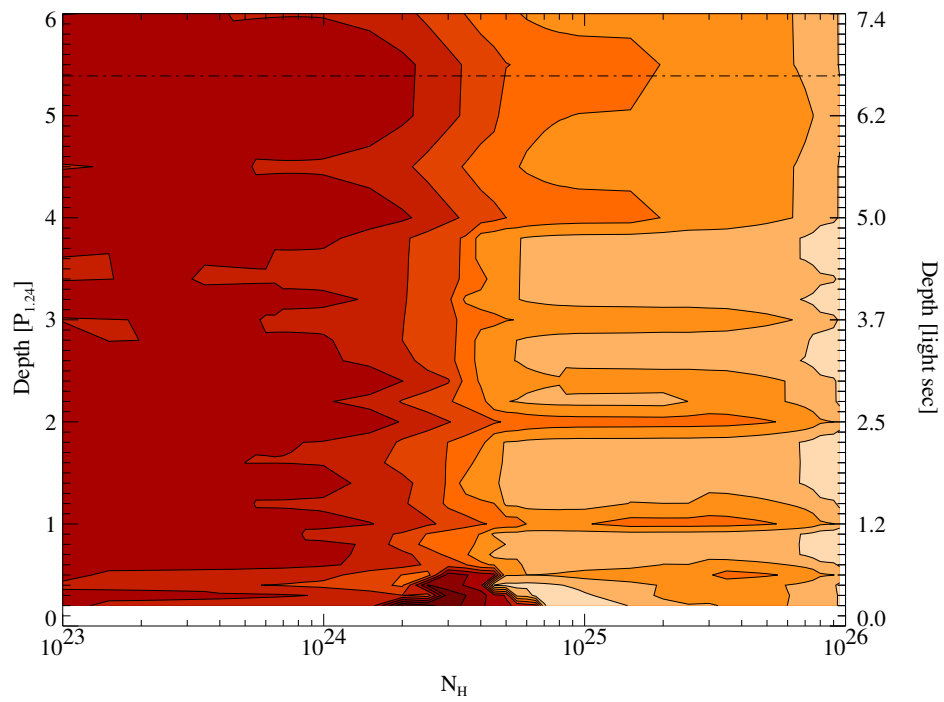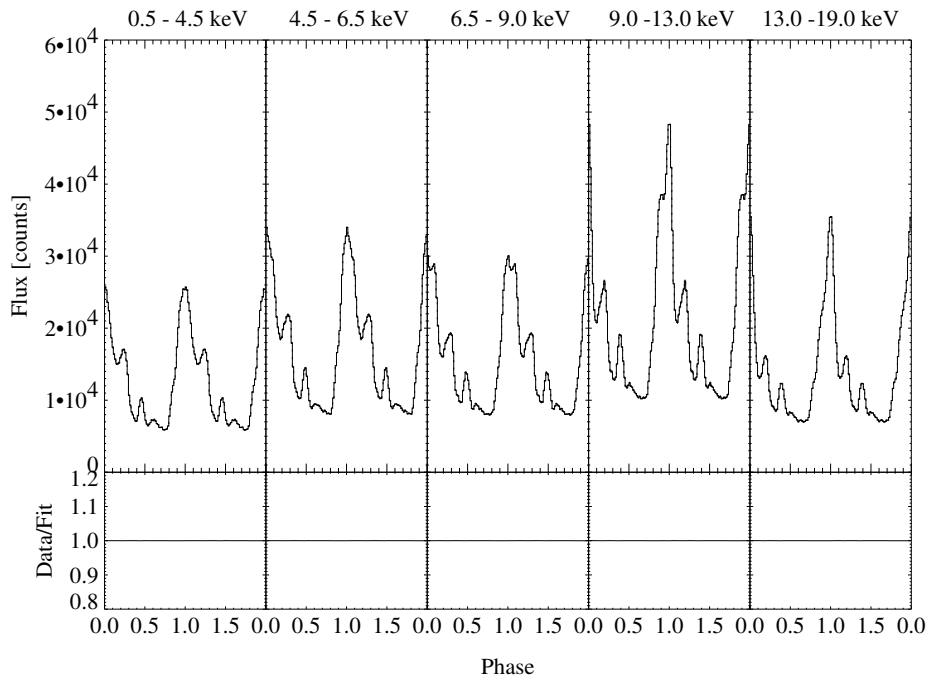

Figure B.7: Limits for N_e: $2.9 \times 10^{24} < N_e < 9.5 \times 10^{25}$ cm^{-2}

Orbit 07
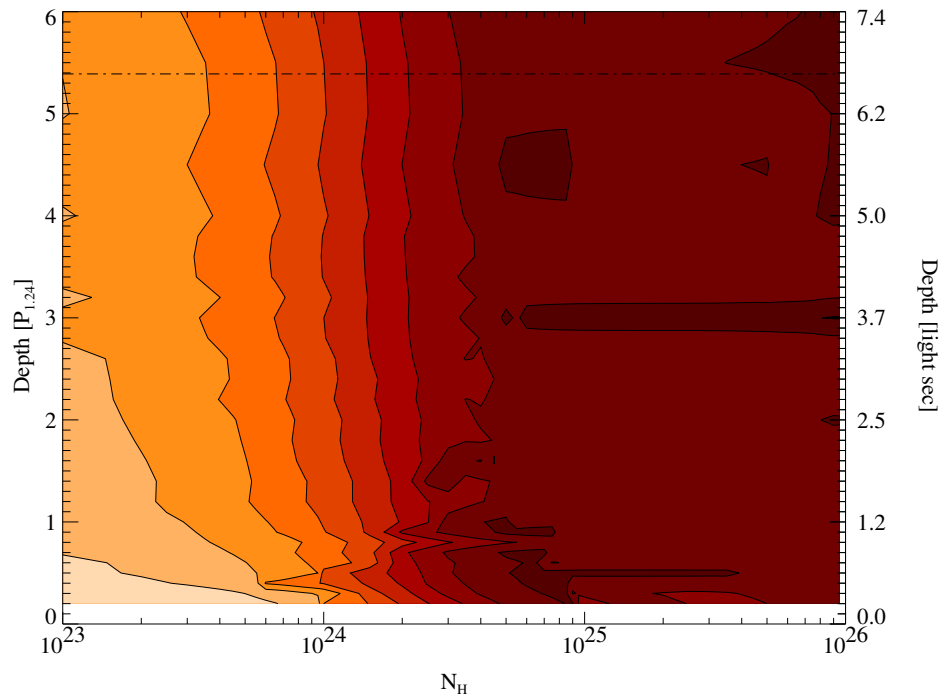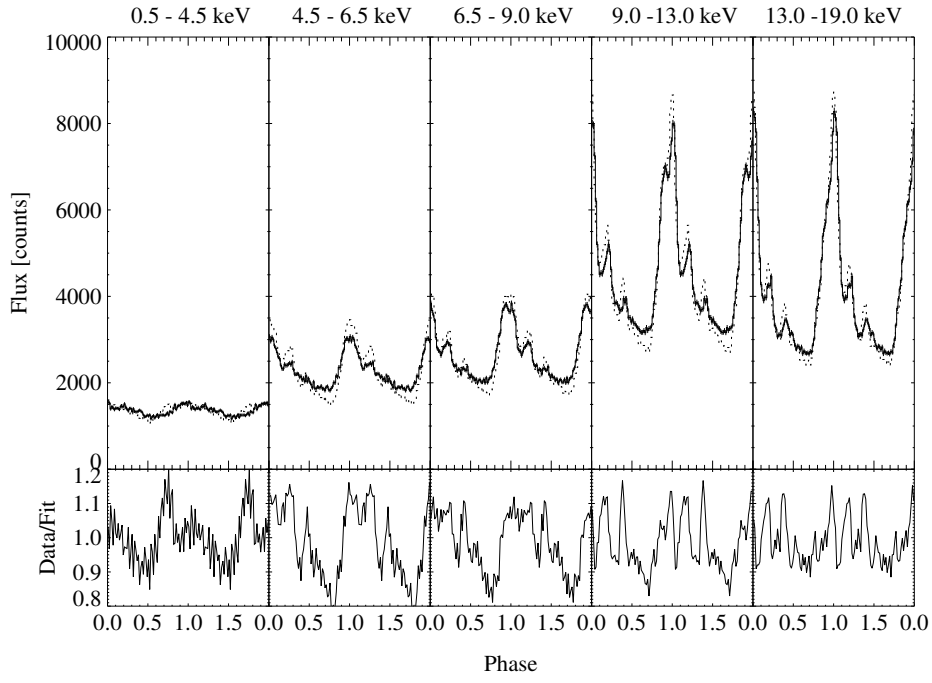
Figure B.8: Limits for N_e: $4.1 \times 10^{24} < N_e < 9.5 \times 10^{25}$ cm^{-2}

Orbit 08
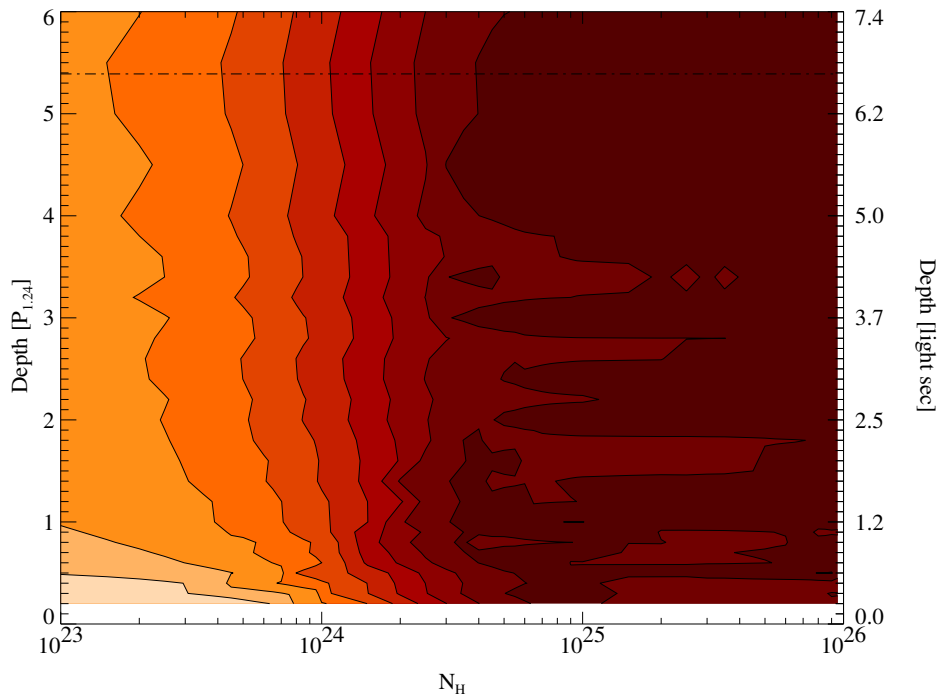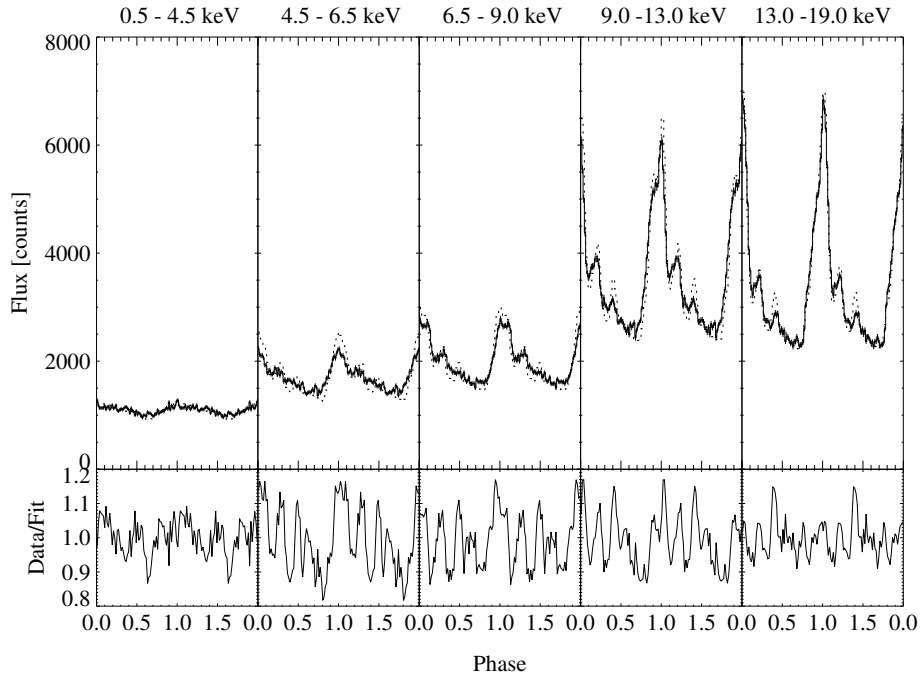
Figure B.9: Limits for N_e: $3.1 \times 10^{24} < N_e < 9.5 \times 10^{25}$ cm^{-2}

Orbit 09
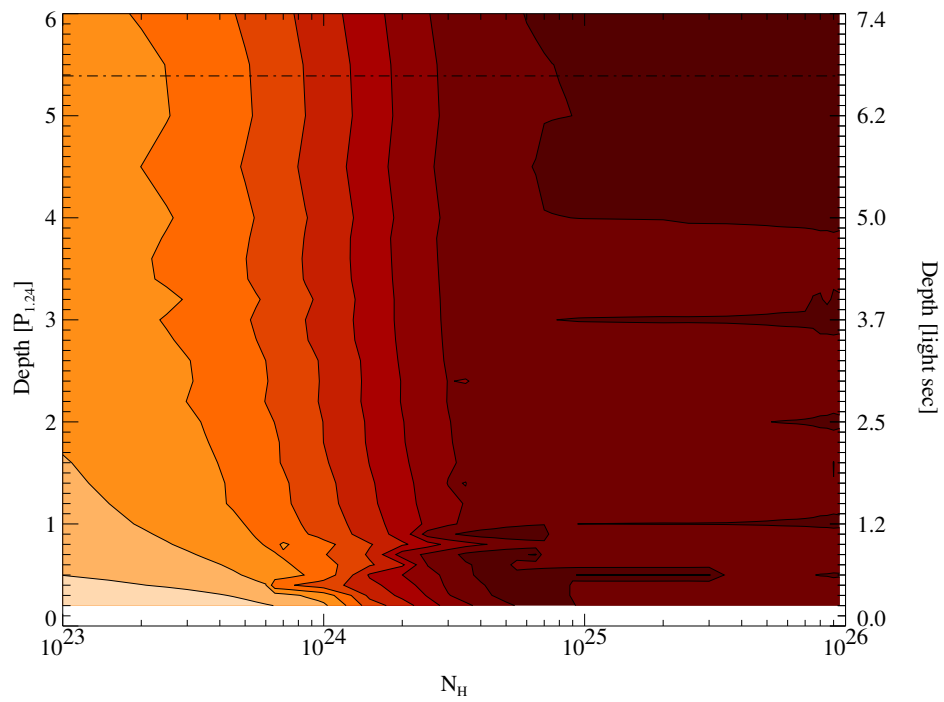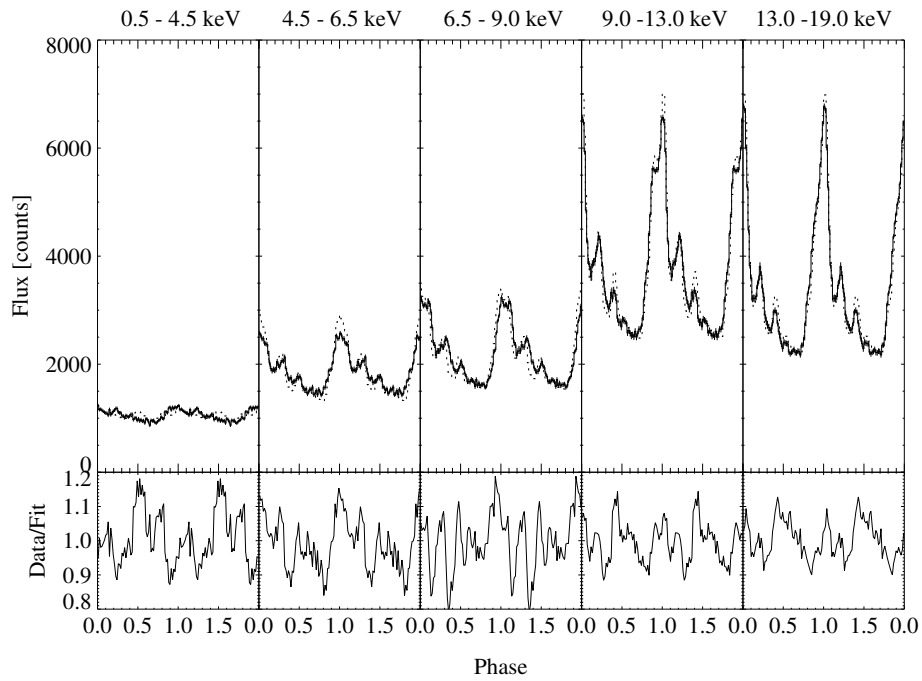
Figure B.10: Limits for N_e: $3.1 \times 10^{24} < N_e < 9.5 \times 10^{25}$ cm^{-2}

Orbit 15
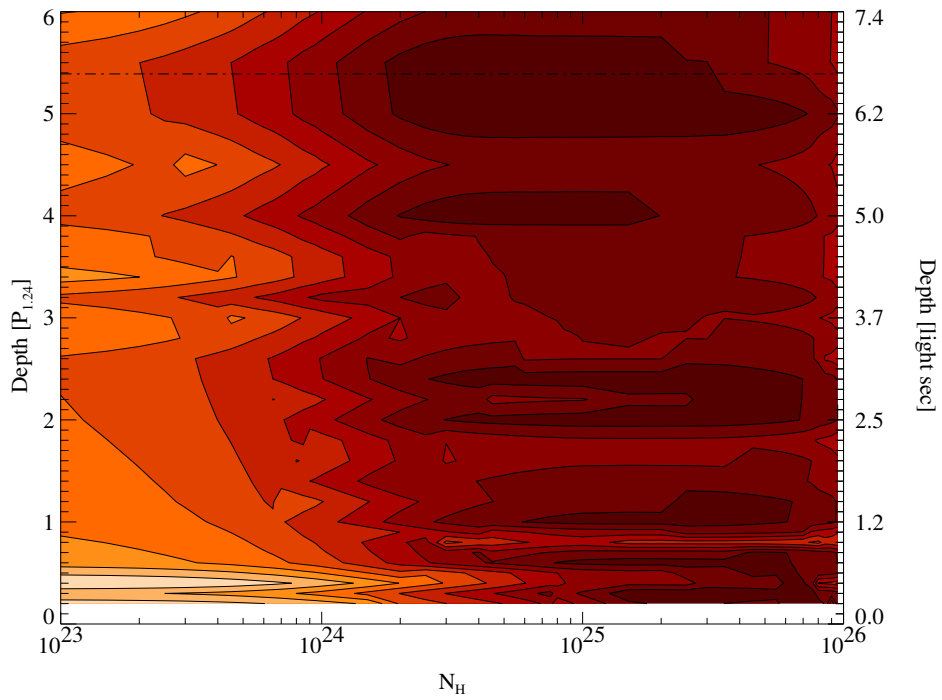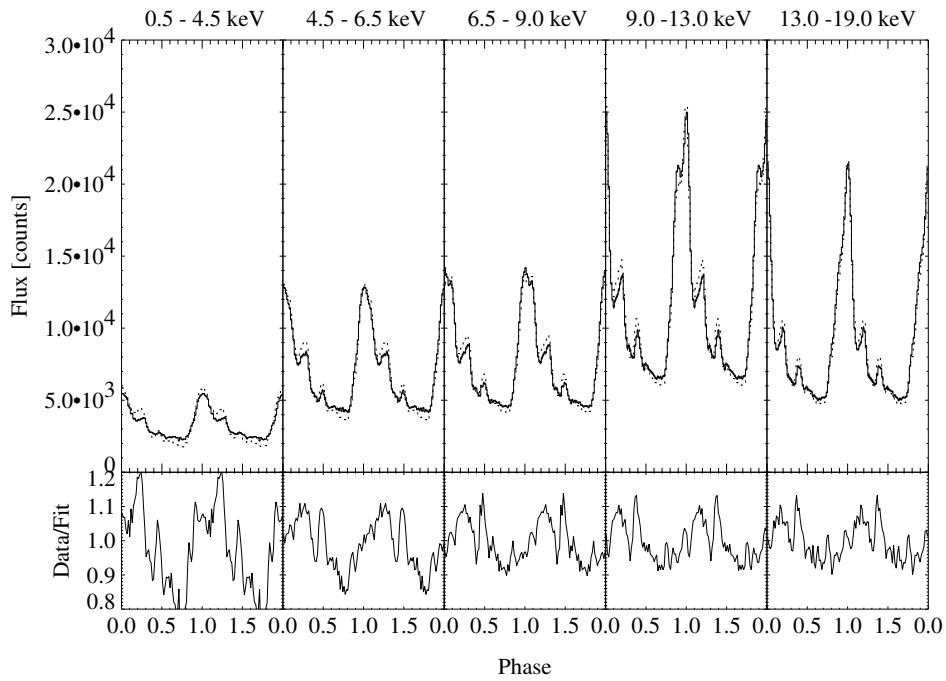
Figure B.11: Limits for N_e: $1.9 \times 10^{24} < N_e < 8.0 \times 10^{25}$ cm^{-2}

Orbit 16
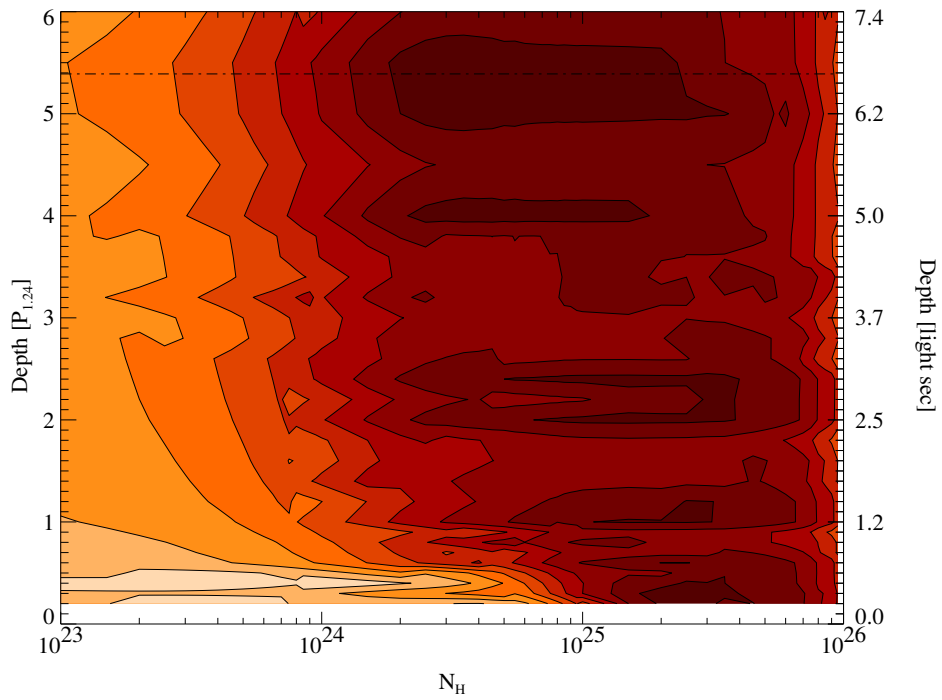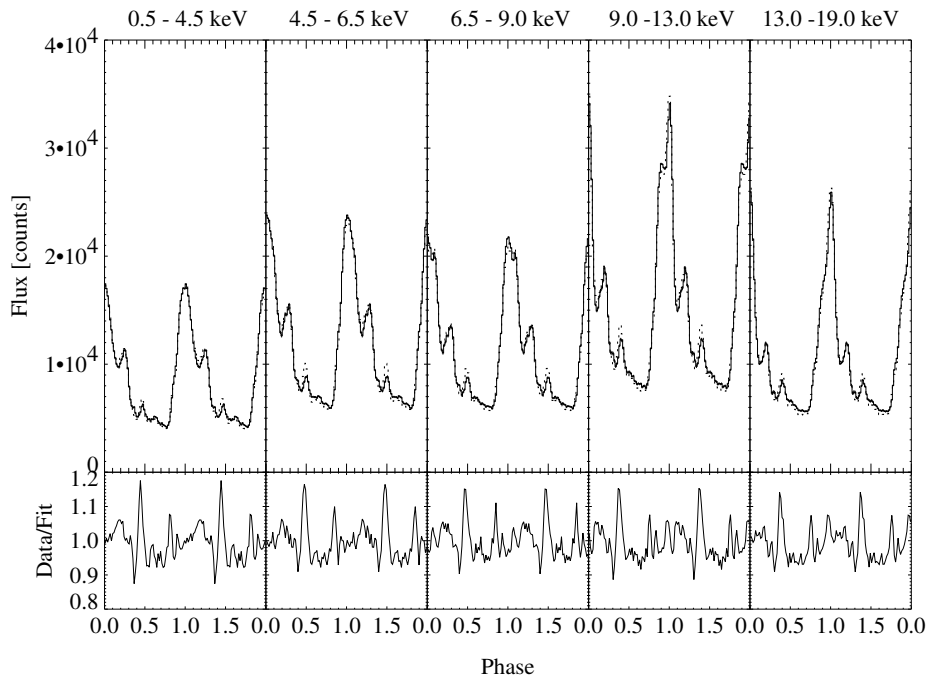
Figure B.12: Limits for N_e: $1.9 \times 10^{24} < N_e < 4.4 \times 10^{25}$ cm^{-2}

Orbit 17
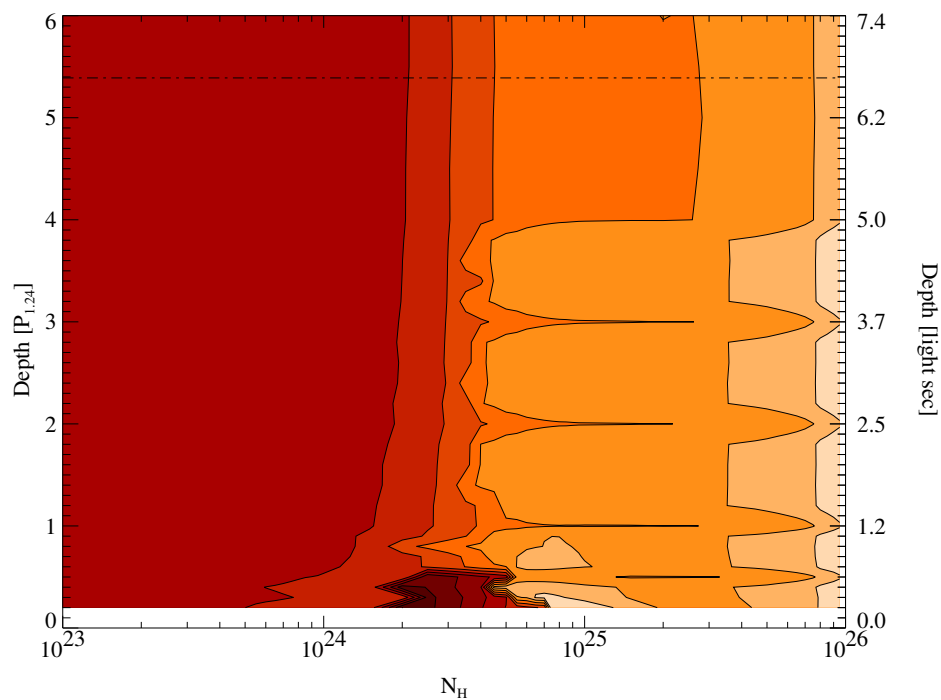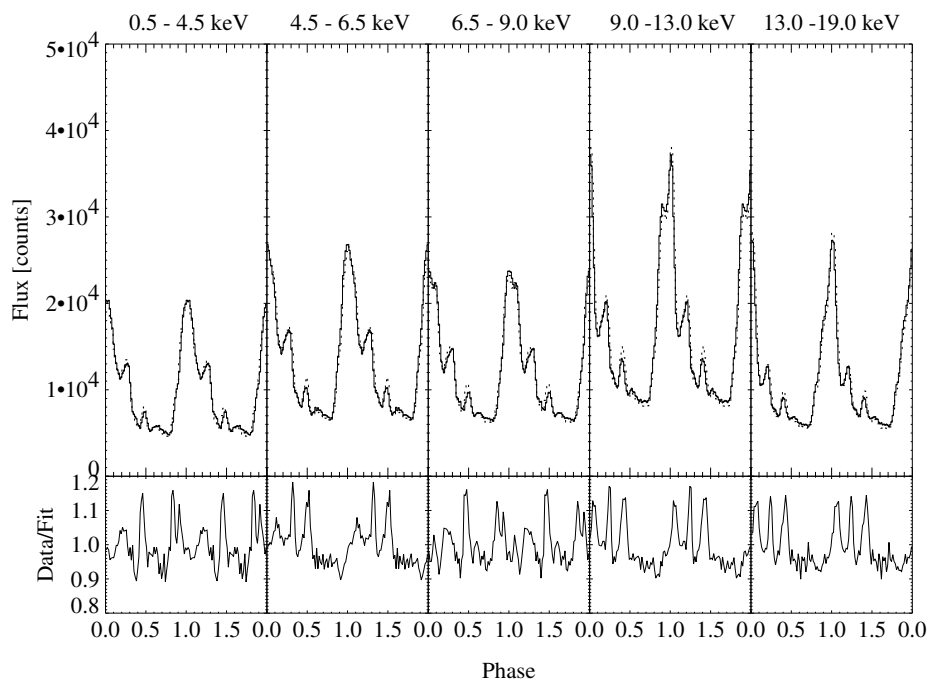
Figure B.13: Limits for N_e: $1.6 \times 10^{24} < N_e < 5.1 \times 10^{24}\ \mathrm{cm}^{-2}$

Orbit 18
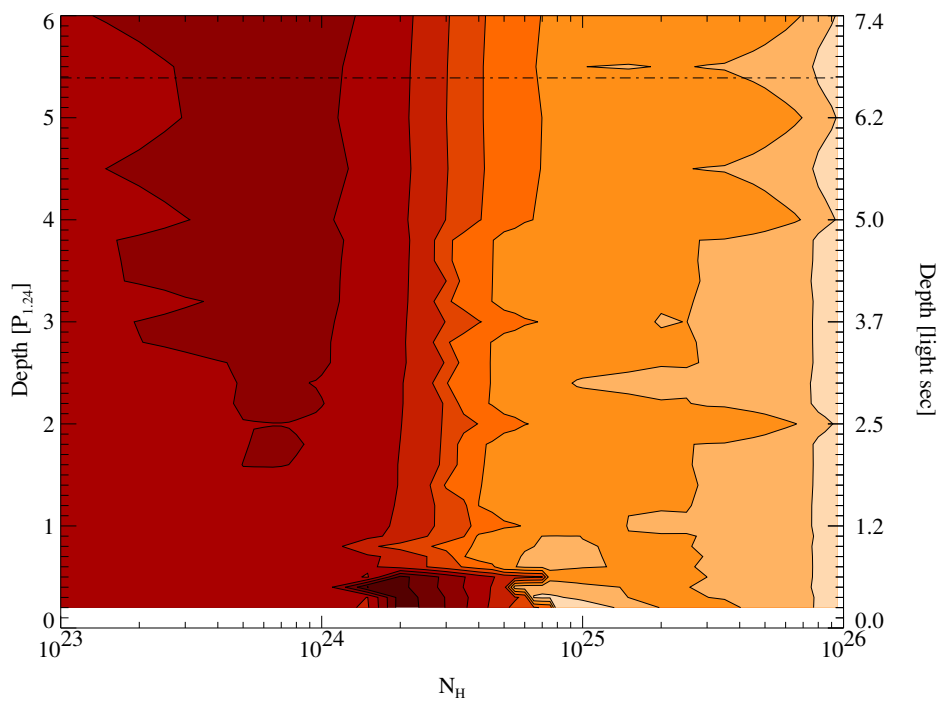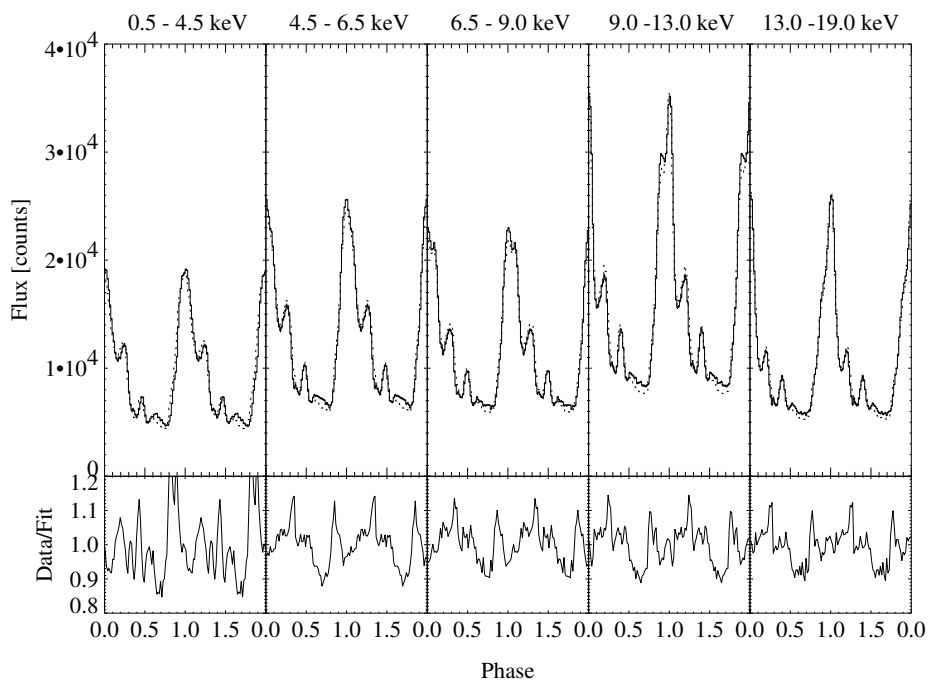
Figure B.14: Limits for N_e: $1.0 \times 10^{24} < N_e < 2.2 \times 10^{24}$ cm^{-2}

Orbit 23
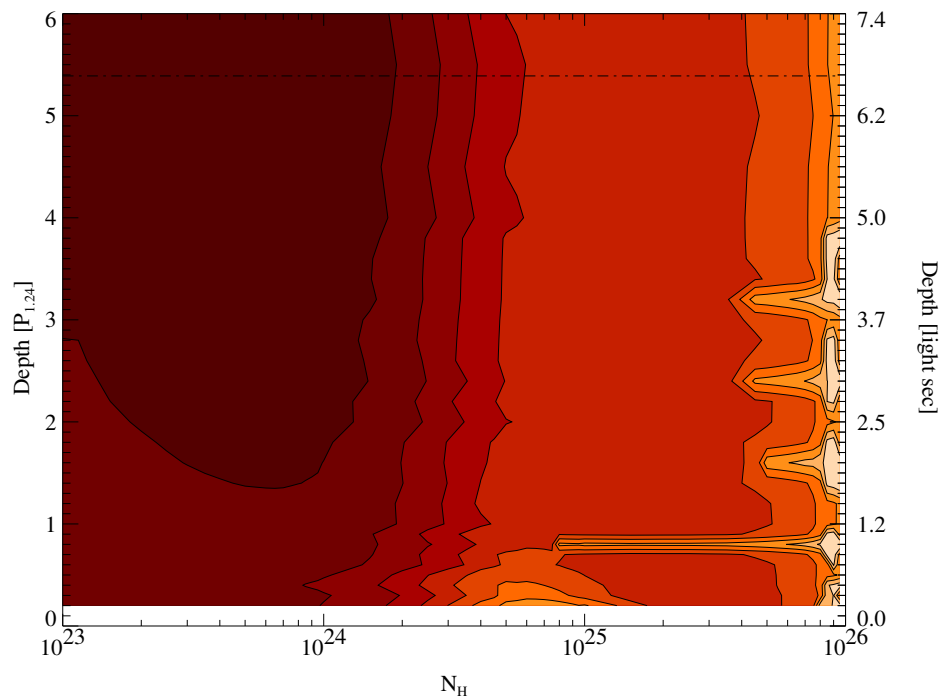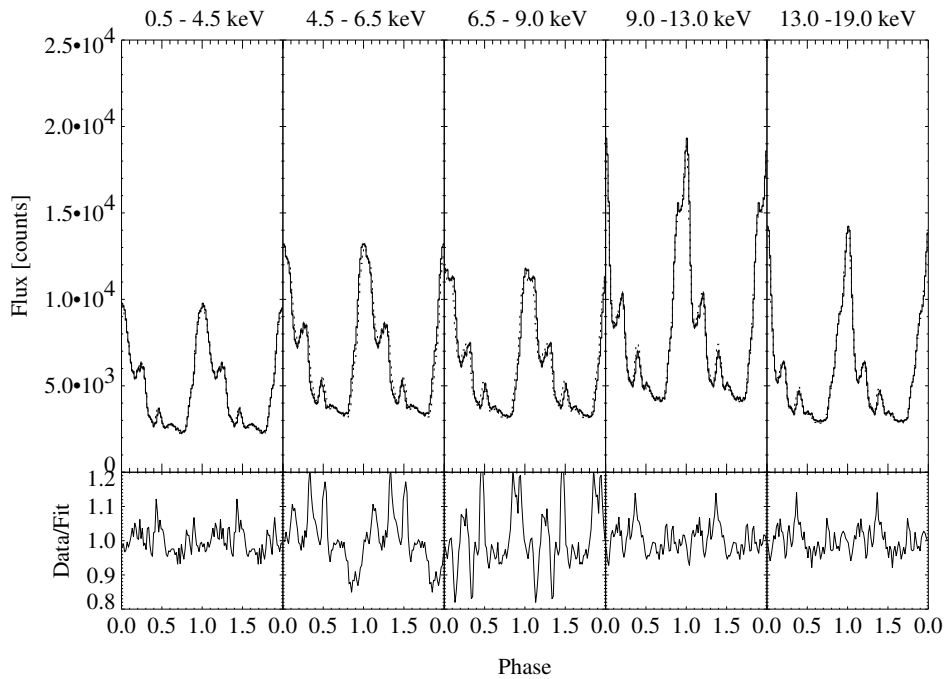
Figure B.15: Limits for N_e: $1.0 \times 10^{23} < N_e < 1.9 \times 10^{24}\ \mathrm{cm^{-2}}$

Orbit 24
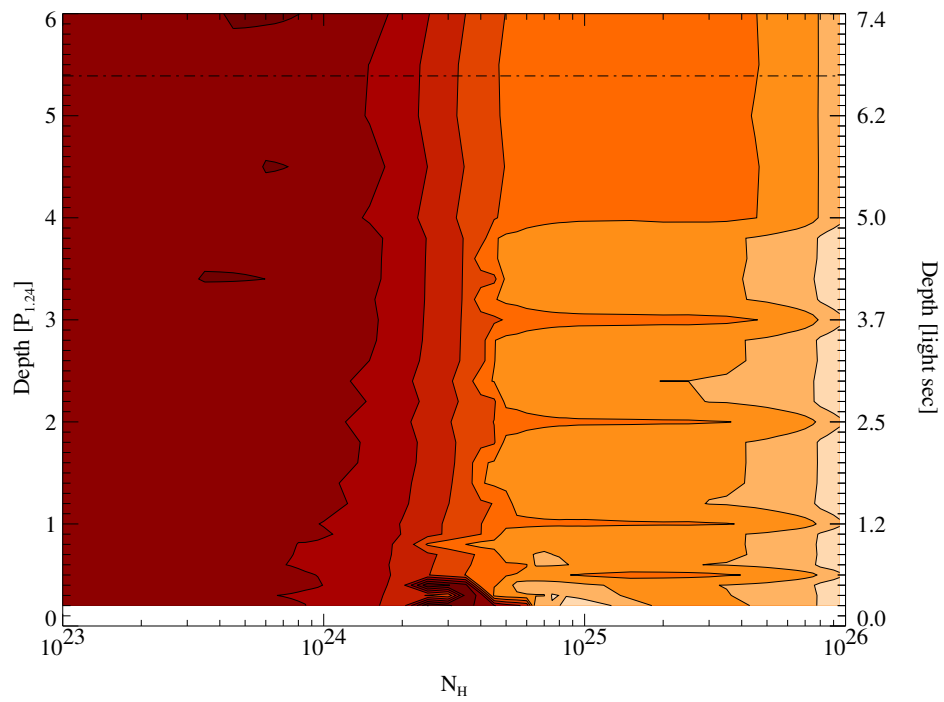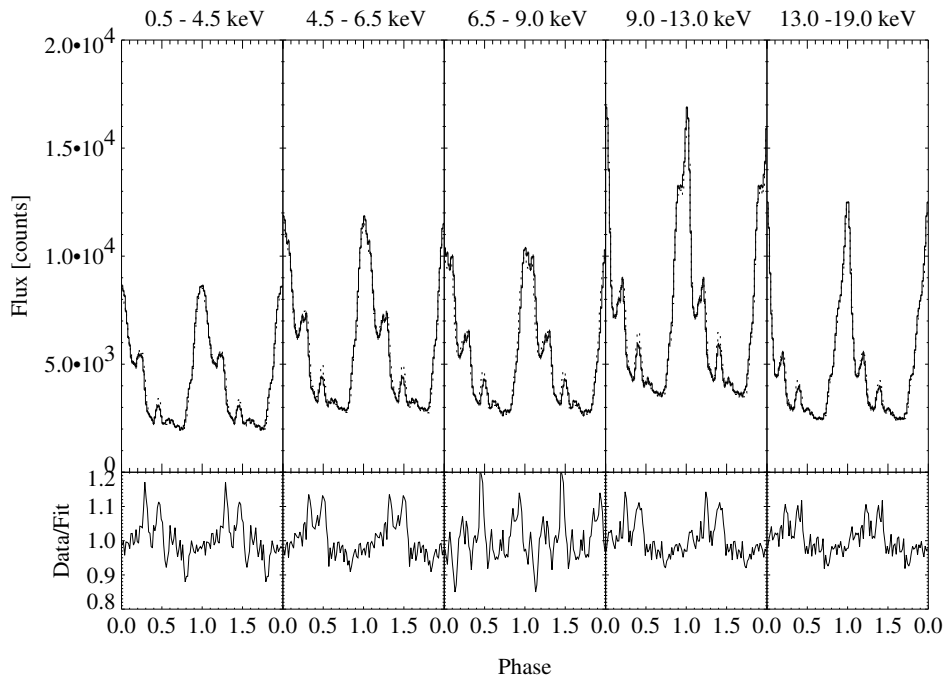
Figure B.16: Limits for N_e: $2.1 \times 10^{24} < N_e < 3.3 \times 10^{24}$ cm^{-2}

Orbit 25
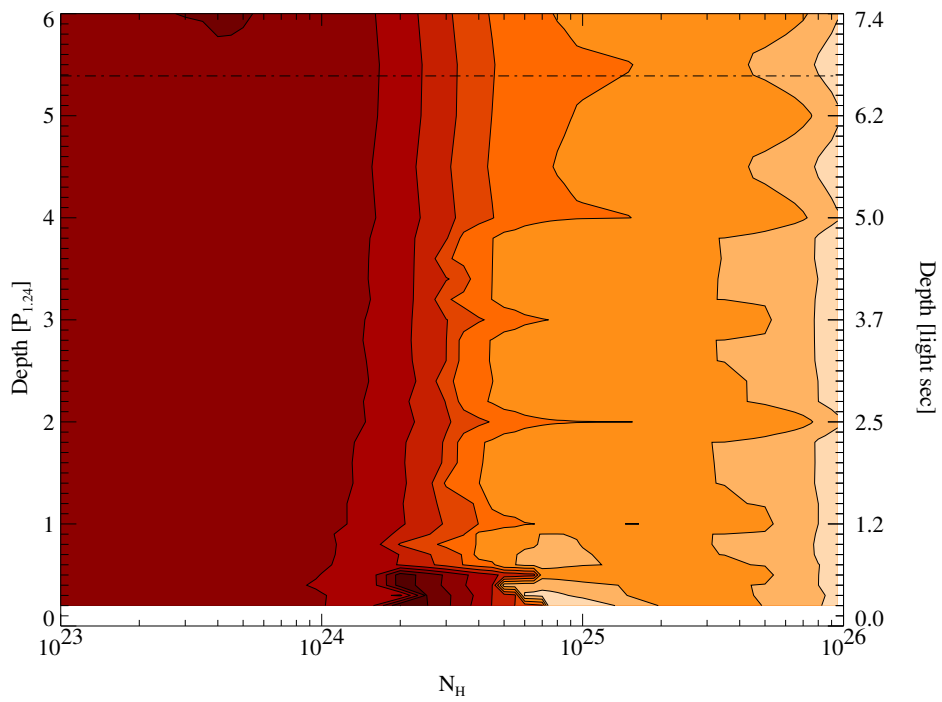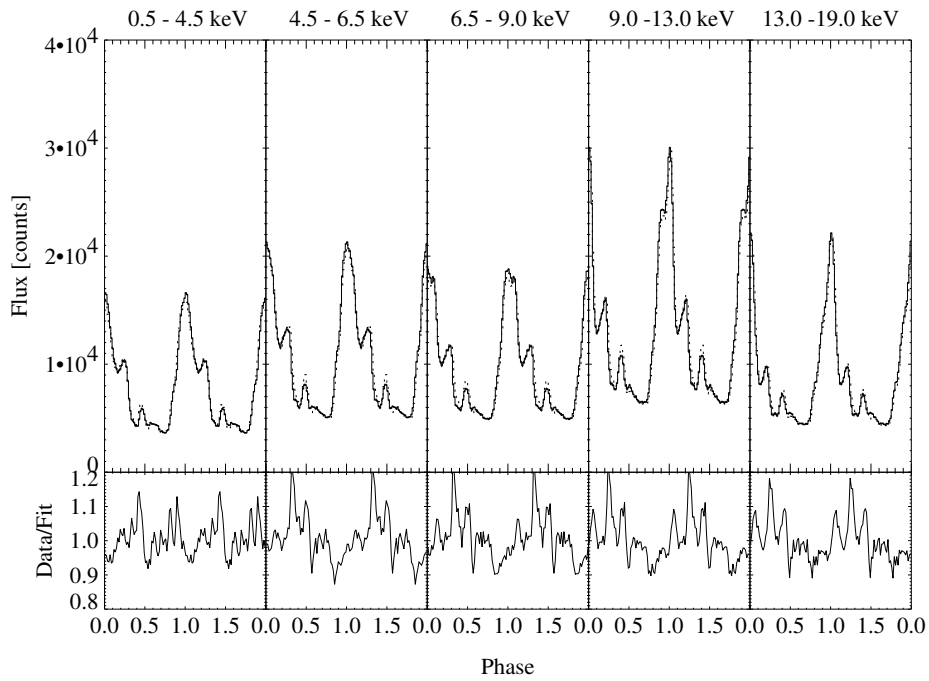
Figure B.17: Limits for N_e: $2.0 \times 10^{24} < N_e < 2.3 \times 10^{24}$ cm^{-2}

Orbit 26
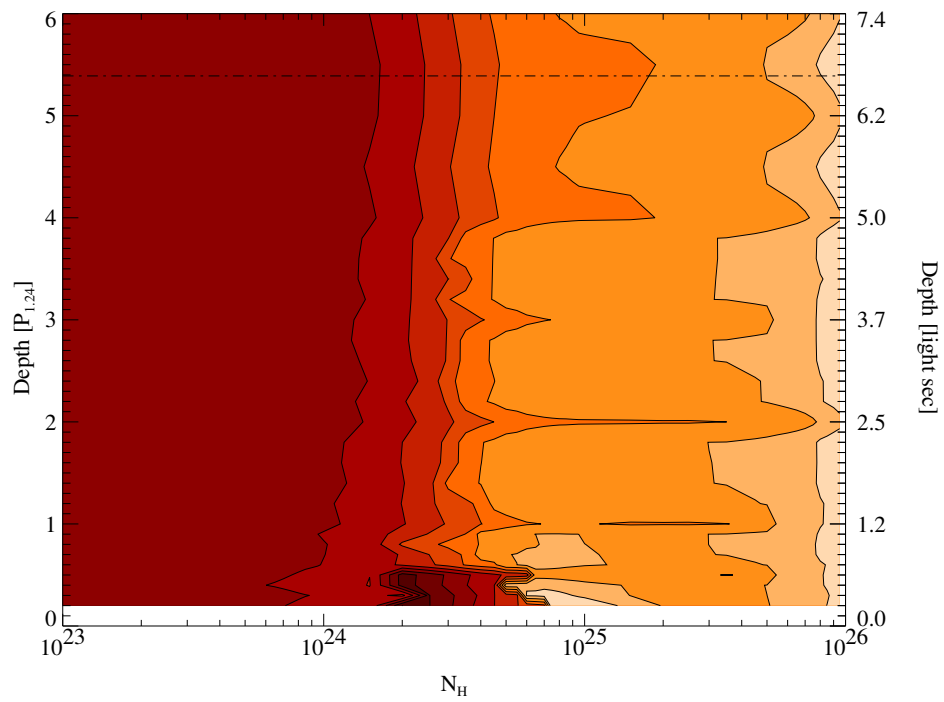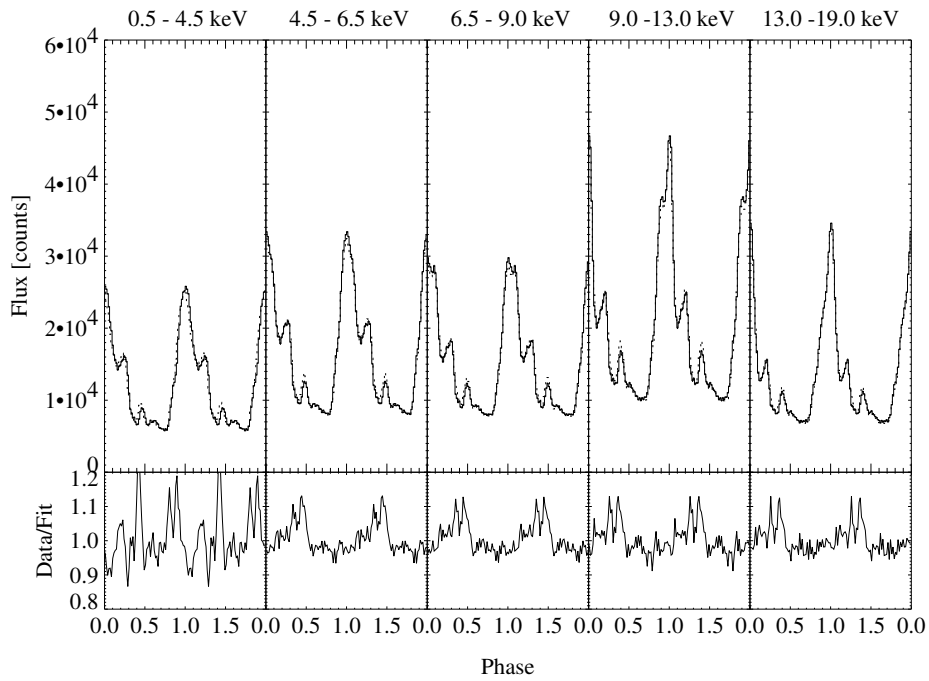
Figure B.18: Limits for N_e: $1.8 \times 10^{24} < N_e < 2.4 \times 10^{24}$ cm^{-2}

Orbit 27
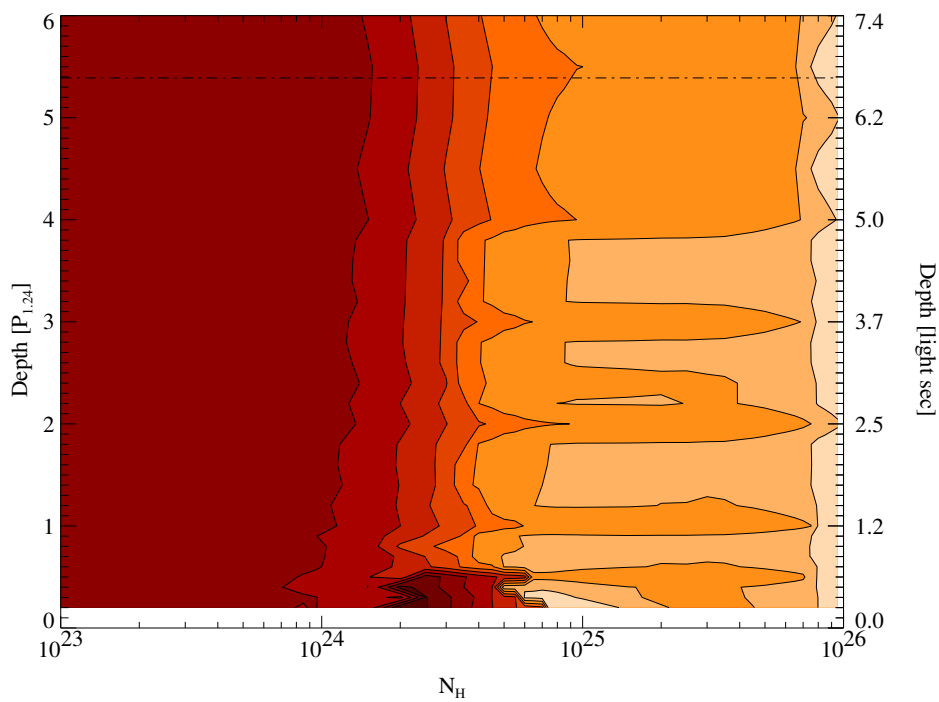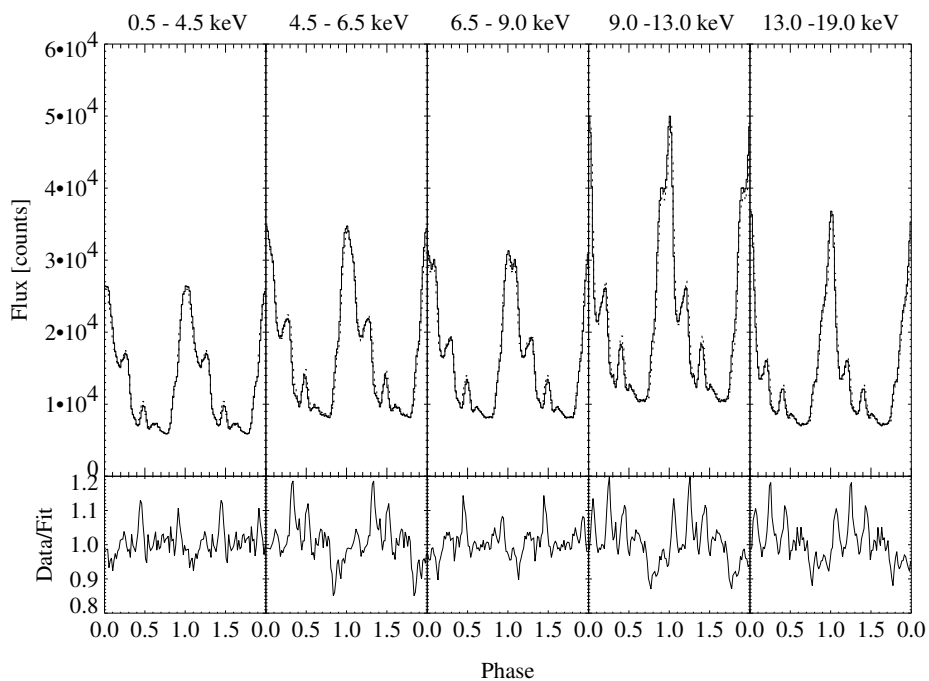
Figure B.19: Limits for N_e: $2.0 \times 10^{24} < N_e < 3.3 \times 10^{24}$ cm^{-2}

Orbit 28
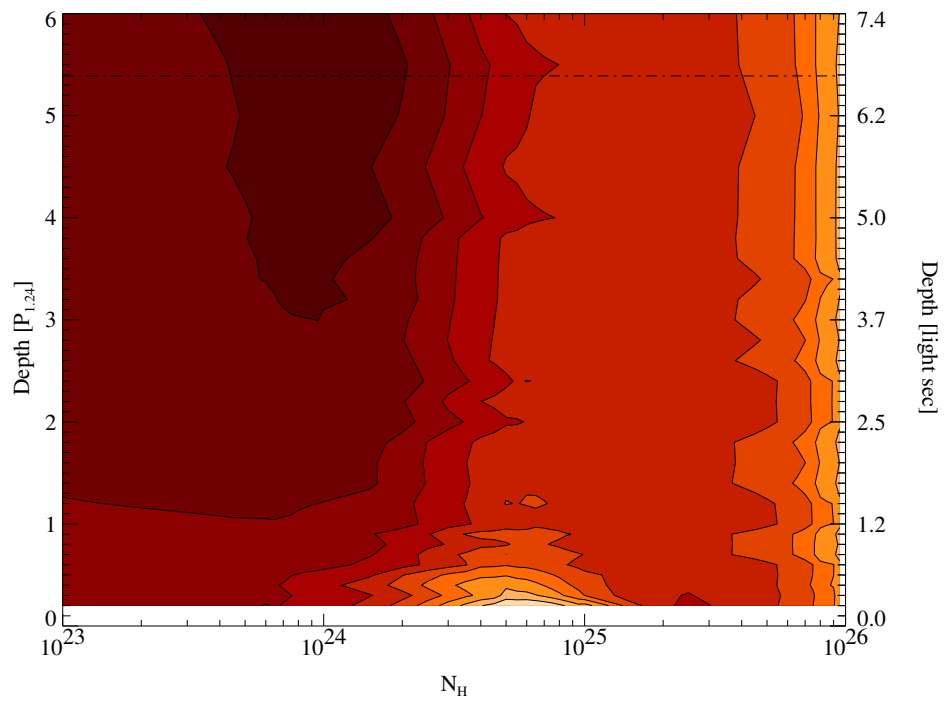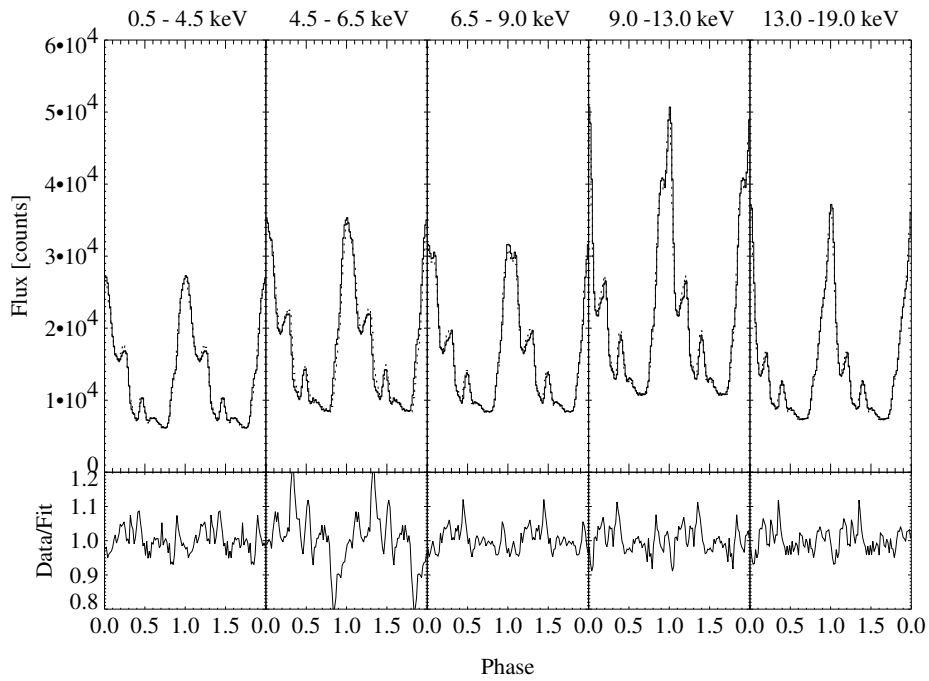
Figure B.20: Limits for N_e: $3.1 \times 10^{23} < N_e < 2.0 \times 10^{24}$ cm^{-2}

Orbit 29
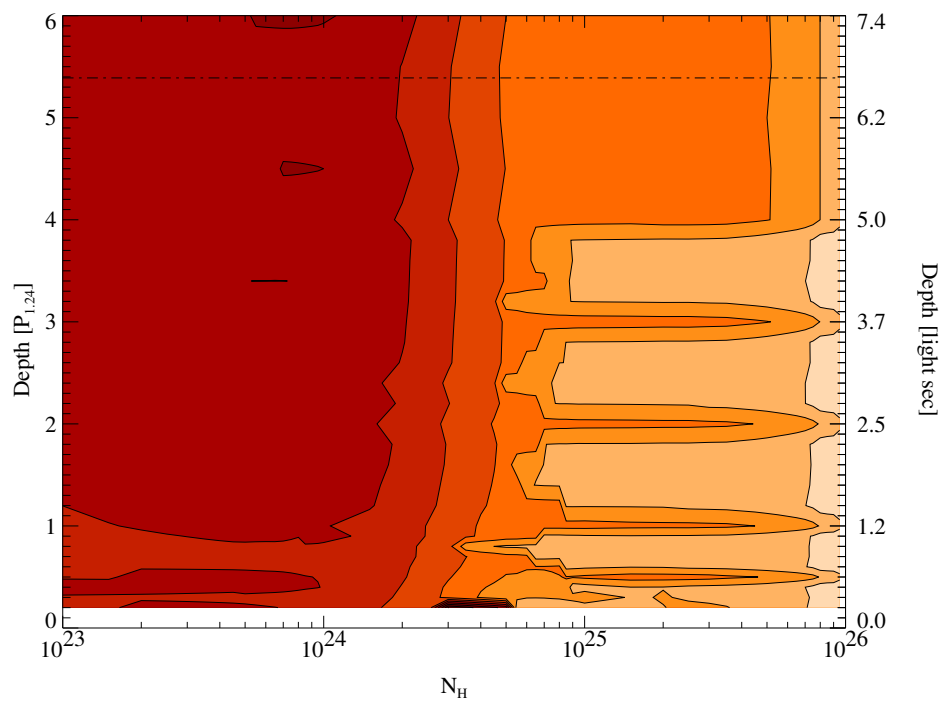
Figure B.21: Limits for N_e: $2.9 \times 10^{24} < N_e < 5.0 \times 10^{24}\,\mathrm{cm}^{-2}$

Orbit 30

Figure B.22: Limits for N_e: $1.9 \times 10^{24} < N_e < 2.8 \times 10^{24}$ cm^{-2}

Danksagung

Lebenslauf
Markus Kuster

09.07.1969	geboren in Ebingen
1976–1980	Grundschule Laufen an der Eyach
1980–1989	Gymnasium Ebingen, Albstadt
1989	Abitur
06.1989–08.1990	Grundwehrdienst
10.1990–06.1997	Eberhard-Karls-Universität Tübingen, Studium der Physik
04.1993–04.1997	Lehrkraft für die Sportart Badminton, Institut für Sportwissenschaften Tübingen Abt. Hochschulsport
01.1995–02.1995	wissenschaftliche Hilfskraft, Institut für Experimental Physik, Universität Tübingen
02.1996–12.1996	wissenschaftliche Hilfskraft, IAA Tübingen Abt. Astronomie, Universität Tübingen
06.1996–06.1997	Diplomarbeit in Physik, unter Anleitung von Herrn Prof. Dr. R. Staubert: "Untersuchung spezieller Effekte eines pn-CCD Arrays für die Röntgensatelliten XMM und ABRIXAS"
06.1997	Diplom in Physik
07.1997–09.1997	wissenschaftliche Hilfskraft, IAA Tübingen Abt. Astronomie, Universität Tübingen
10.1997–06.2002	wissenschaftlicher Angestellter, IAA Tübingen Abt. Astronomie, Universität Tübingen
seit 10.1997	Anfertigung der Dissertation mit dem Titel: "Combined spectral and temporal analysis of a Her X-1 turn-on" an der Universität Tübingen, Institut für Astronomie und Astrophysik Abt. Astronomie, unter Anleitung von Herrn Prof. Dr. R. Staubert
seit 06.2002	wissenschaftlicher Angestellter, Max-Planck-Institut für Extraterrestrische Physik, Max-Planck Halbleiter-Labor, Neuperlach/München

Meine akademischen Lehrer waren die Professoren und Dozenten:

Angewandte Physik: K. Gaukler, H. Plies, R. Schief

Astronomie und Astrophysik: M. Bässgen, H. Mauder, H. Ruder, R. Staubert, K. Werner, J. Wilms

Experimentalphysik: M. Baumann, H. Clement, F. Gönnenwein, P. Grabmayr, W. Hartmann, R. Hübner, W. Nakel, G. Staudt, G. Wagner

Chemie: J. Strähle, H. Ebert

Mathematik: H. Kaul, H. Fischer, M. Mathieu, M. Wolff

Theoretische Physik: A. Fäßler, H. Müther, H. Reinhardt, H. Wittern